BERGISCHE
UNIVERSITÄT
WUPPERTAL

IMAGING TECHNIQUES FOR INVESTIGATION OF FREE-SURFACE FLOWS IN HYDRAULIC LABORATORIES

Habilitationsschrift

zur Erlangung der Lehrbefähigung für das Fachgebiet

WASSERBAU UND WASSERWIRTSCHAFT

von

Daniel B. Bung

aus Düren

Prof. Dr. Daniel B. Bung • Bayernallee 9 • 52066 Aachen • bung@fh-aachen.de

Submission date:	06 January 2021
Examination date:	28 June 2022
Reviewer 1:	Univ.-Prof. Dr.-Ing. Andreas SCHLENKHOFF Chair of Water Management and Hydraulic Engineering Bergische Universität Wuppertal
Reviewer 2:	Univ.-Prof. Dr.-Ing. Robert BOES Laboratory of Hydraulics, Hydrology and Glaciology ETH Zurich
Reviewer 3:	Univ.-Prof. Dr.-Ing. habil. Nils GOSEBERG Dept. of Hydromechanics, Coastal and Ocean Engineering Technische Universität Braunschweig
Chair:	Univ.-Prof. Dr.-Ing. Jörg RINKLEBE Department of Soil and Groundwater Management Bergische Universität Wuppertal

To Leonard
Luisa
Lukas

„I say that the power of vision extends through the visual rays to the surface of non-transparent bodies, while the power possessed by these bodies extends to the power of vision.“

Leonardo da Vinci (1452-1519)

ABSTRACT

This thesis aims at the presentation and discussion of well-accepted and new imaging techniques applied to different types of flow in common hydraulic engineering environments. All studies are conducted in laboratory conditions and focus on flow depth and velocity measurements. Investigated flows cover a wide range of complexity, e.g. propagation of waves, dam-break flows, slightly and fully aerated spillway flows as well as highly turbulent hydraulic jumps.

New imaging methods are compared to different types of sensors which are frequently employed in contemporary laboratory studies. This classical instrumentation as well as the general concept of hydraulic modeling is introduced to give an overview on experimental methods.

Flow depths are commonly measured by means of ultrasonic sensors, also known as acoustic displacement sensors. These sensors may provide accurate data with high sample rates in case of simple flow conditions, e.g. low-turbulent clear water flows. However, with increasing turbulence, higher uncertainty must be considered. Moreover, ultrasonic sensors can provide point data only, while the relatively large acoustic beam footprint may lead to another source of uncertainty in case of relatively short, highly turbulent surface fluctuations (ripples) or free-surface air-water flows. Analysis of turbulent length and time scales of surface fluctuations from point measurements is also difficult. Imaging techniques with different dimensionality, however, may close this gap. It is shown in this thesis that edge detection methods (known from computer vision) may be used for two-dimensional free-surface extraction (i.e. from images taken through transparant sidewalls in laboratory flumes). Another opportunity in hydraulic laboratory studies comes with the application of stereo vision. Low-cost RGB-D sensors can be used to gather instantaneous, three-dimensional free-surface elevations, even in flows with very high complexity (e.g. aerated hydraulic jumps). It will be shown that the uncertainty of these methods is of similar order as for classical instruments.

Particle Image Velocimetry (PIV) is a well-accepted and widespread imaging technique for velocity determination in laboratory conditions. In combination with high-speed cameras, PIV can give time-resolved velocity fields in 2D/3D or even as volumetric flow fields. PIV is based on a cross-correlation technique applied to small subimages of seeded flows. The minimum size of these subimages defines the maximum spatial resolution of resulting velocity fields. A derivative of PIV for aerated flows is also available, i.e. the so-called Bubble Image Velocimetry (BIV). This thesis emphasizes the capacities and limitations of both methods, using relatively simple setups with halogen and LED illuminations. It will be demonstrated that PIV/BIV images may also be processed by means of Optical Flow (OF) techniques. OF is another method originating from the computer vision discipline, based on the assumption of image brightness conservation within a sequence of images. The Horn-Schunck approach, which has been first employed to hydraulic engineering problems in the studies presented herein, yields dense velocity fields, i.e. pixelwise velocity data. As discussed hereinafter, the accuracy of OF competes well with PIV for clear-water flows and even improves results (compared to BIV) for aerated flow conditions. In order to independently benchmark the OF approach, synthetic images with defined turbulence intensitiy are used.

Computer vision offers new opportunities that may help to improve the understanding of fluid mechanics and fluid-structure interactions in laboratory investigations. In prototype environments, it can be employed for obstacle detection (e.g. identification of potential fish migration corridors) and recognition (e.g. fish species for monitoring in a fishway) or surface reconstruction (e.g. inspection of hydraulic structures). It can thus be expected that applications to hydraulic engineering problems will develop rapidly in near future. Current methods have not been developed for fluids in motion. Systematic future developments are needed to improve the results in such difficult conditions.

PREFACE

This manuscript is submitted as a habilitation thesis, compiling several papers being published in international journals or Scopus-indexed conference proceedings. All publications are included as individual sections while variables and figures have been harmonized in order to enhance the legibility of this manuscript[1]. The following table gives an overview of included publications and corresponding sections.

Sec.	Publication
2.1	**Bung, D.B.** (2015): *Laboratory Models of Free-Surface Flows*. In: Rowiński P., Radecki-Pawlik A. (eds) Rivers - Physical, Fluvial and Environmental Processes. GeoPlanet: Earth and Planetary Sciences. Springer, Cham, pp. 213-227 (doi: 10.1007/978-3-319-17719-9_9).
3.2	**Bung, D.B.** (2013): *Non-intrusive detection of air-water surface roughness in self-aerated chute flows*. Journal of Hydraulic Research 51(3), pp. 322-329 (doi: 10.1080/00221686.2013.777373).
4.2	**Bung, D.B.**; Crookston, B.M; Valero, D. (2020): *Turbulent free-surface monitoring with an RGB-D sensor: the hydraulic jump case*. Journal of Hydraulic Research 59(5), pp. 779-790 (doi: 10.1080/00221686.2020.1844810).
6.2	Oertel, M.; **Bung, D.B.** (2012): *Initial stage of two-dimensional dam-break waves: laboratory versus VOF*. Journal of Hydraulic Research 50(1), pp. 89-97 (doi: 10.1080/00221686.2011.639981).
6.3	**Bung, D.B.** (2011): *Non-Intrusive measuring of air-water flow properties in self-aerated stepped spillway flow*. 34th IAHR World Congress - Balance and Uncertainty (Water in a changing world), Brisbane, pp. 2380-2387 (ISBN: 978-0-85825-868-6).
6.4	Leandro, J.; **Bung, D.B.**; Carvalho, R. (2014): *Measuring void fraction and velocity fields of a stepped spillway for skimming flow using non-intrusive methods*. Experiments in Fluids 55(5):1732 (doi: 10.1007/s00348-014-1732-6).
7.2	**Bung, D.B.**; Valero, D. (2016): *Application of the Optical Flow method to velocity determination in hydraulic structure models*. 6th International Symposium on Hydraulic Structures (ISHS 2016), Portland, pp. 240-249 (doi: 10.15142/T3150628160853).
7.3	**Bung, D.B.**; Valero, D. (2016): *Optical flow estimation in aerated flows*. Journal of Hydraulic Research 54(5), pp. 575-580 (doi: 10.1080/00221686.2016.1173600).
8.2	**Bung, D.B.**; Valero, D. (2016): *Image processing techniques for velocity estimation in highly aerated flows: Bubble Image Velocimetry vs. Optical Flow*. 4th IAHR Europe Congress - Sustainable Hydraulics in the Era of Global Change), Liege. CRC Press, pp. 151-157 (ISBN: 978-1-13802-977-4).

[1] Additonally, some sections include materials from other publications. These contents have been modified in order to serve for discussion of specific aspects. Whenever applicable, additional sources are referenced within the particular sections.

CONTENTS

LIST OF FIGURES

LIST OF TABLES

PART I

DATA COLLECTION IN HYDRAULIC ENGINEERING

CHAPTER 1

INTRODUCTION

1.1 THE ROLE OF DATA

In scientific and engineering disciplines, data collection is essential to develop new concepts and theories (explorational experiments), to validate existing methods (validational experiments) and to forecast future developments for varying conditions (variational experiments, cmp. DUNN (2010)). Whenever possible, laboratory data should be compared to field data to preclude laboratory effects (see also Section 2.1) and to validate or improve the significant number of classical, empirical design methods being used in engineering practice.

In hydraulic engineering, the most important quantities are the flow depth and velocity. If a velocity field with sufficient resolution is known, dependent variables, e.g. pressure distributions, may be estimated. In natural water bodies with large cross-sections, combined velocity measurements and water level gauging provide indirect information on the streamflow (MORGENSCHWEIS, 2018). According to BOITEN (2005), water levels may thus be considered the basis for any river study. Indeed, its significance was even known by early civilizations as demonstrated by the still existing nilometers in Egypt (VIOLLET, 2007). Certainly, additional information on different parameters, e.g. the sediment load are important for river basin management as well. However, any phenomenon in hydraulic engineering, such as morphological processes in rivers, depends on the streamflow or flow velocity, respectively, and flow depth (FERREIRA DA SILVA AND YALIN, 2017).

Accurate streamflow estimation is also mandatory for derivation of design discharges of certain return periods which are assumed to guarantee a minimum safety level for water infrastructure and minimze the risk of failure. For this purpose, long-term discharge measurements are necessary. For operational water management, in contrary, immediate information on the streamflow is required (HERSCHY, 2009). This general demand for continuous data collection is enhanced by another challenge of contemporary water management: As MILLY ET AL. (2008) pointed out, "stationarity is dead", i.e. the assumption of stationary hydrological systems is inadequate for future design of water infrastructure (COSGROVE AND LOUCKS, 2015). Instead, climate change and varying hydrologic conditions must be

considered over the lifespan of a hydraulic structures, i.e. in the range of 50 to 100 years. To guarantee proper operation and to ensure structural safety, long-term monitoring becomes more essential than ever and structural design needs to be flexible and allow for adaptation to changing future conditions.

Counterintuitively, another reason for increasing demand for data collection and monitoring is caused by rapidly developing computing capacities and recent advances in Computational Fluid Dynamics (CFD) methods. Numerical modeling may provide high-resolution, three-dimensional data for complex flows (LAURIEN AND OERTEL, 2018; HIRSCH, 2007). To validate resulting, comprehensive information from simulations, experimental data with similar spatial and temporal resolution gains importance (KÄHLER ET AL., 2016) and point data, as obtained by most instrumentation, becomes more and more insufficient.

The increasing demand for data collection leads to ongoing, tremendous efforts in development of new instrumentation for both environments, in laboratory and in the field. In combination with new computer-based data analysis techniques, new or better insight into complex physical processes is reachable.

1.2 NEW CHALLENGES AND DEVELOPMENTS

In hydrology, artificial neural networks (ANN), as an example of the aforementioned new analysis tools, have been employed since some decades to model the non-linearity of hydrologic processes without solving complex differential equations (GOVINDARAJU, 2000). Neural networks belong to the field of deep learning which, in turn, is an approach to machine learning (GOODFELLOW ET AL., 2016) and thus belong to the fast developing artificial intelligence (AI) discipline. It is interesting to note that, according to GOODFELLOW ET AL. (2016), current ANN can reach a size in the order of 10^7 neurons, comparable to the neural network size of a frog. Given the growth of ANN sizes in the last decades and assuming continuous development of computer capacities, ANN could reach the size of human neural networks in the next 40 years. Besides its application to hydrologic problems, ANN may be applied to different hydraulic engineering problems, e.g. in combination with numerical simulations to reduce computation time (CHUA AND HOLZ, 2005) or for calibration of sensors (VALERO AND BUNG, 2018A).

Although significant advances in AI methods have been made in the past, the application to hydro-environmental problems in practice is still relatively low compared to other engineering fields. However, SAVIC (2019) highlights the new opportunities linked with AI methods which are stressed by the increasing number of publications listed in the Web of Science when using keywords like "Genetic algorithms" and "Machine learning" altogether with "Water" (see Fig. 1.2.1).

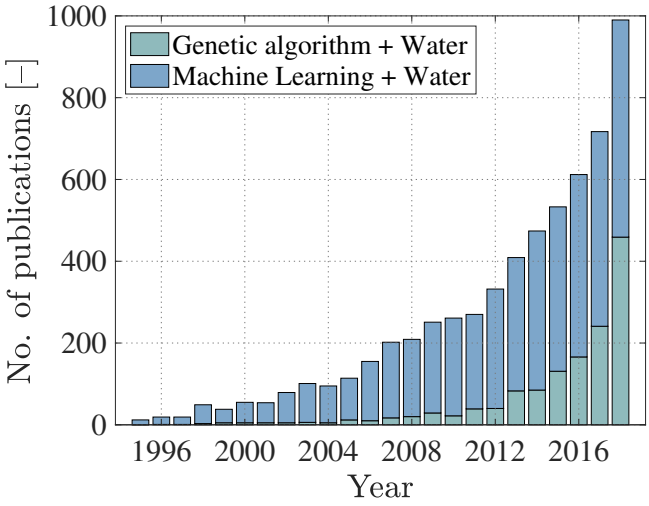

Figure 1.2.1: Water-related publications in combination with genetic algorithms and machine learning according to (SAVIC, 2019) (data digitized from original publication)

NILSSON (2009) provides a broad overview on different AI approaches, including the previously mentioned ANN, genetic programming as well as the so-called robot or computer vision (CV) among others. Computer vision aims at extracting data from images and videos or, in other words, to make a machine see and understand image contents by detecting and recognizing specific features (CIPOLLA ET AL., 2010; DAVIES, 2018). Computer vision methods, which are in the focus of the present thesis, rapidly developed in the recent years, supported by the open source library OpenCV which includes more than 2,500 state-of-the-art computer vision and machine learning algorithms (www.opencv.org).

Computer vision allows for multiple new applications in hydraulic engineering. For instance, the Structure-from-Motion (SfM) method provides detailed three-dimensional surface elevation data with high-spatial resolution by matching features in 2D images (ULLMAN, 1979). SfM may be employed with use of consumer-grade cameras attached to a drone and serve as alternative source of remote sensing data for small areas. BUFFI ET AL. (2017) performed an UAV[1] acquisition study to survey the material conservation status of a dam and provide a metric reconstruction of the structure. BANDINI (2017) demonstrated the applicability of SfM to measure surface elevations along a water body with an accuracy of ± 5 cm. BRENNER ET AL. (2015) employed an image segmentation technique to extract and locate buildings from aerial images which are necessary for 2D flood modeling.

[1] Unmanned Aerial Vehicles

Another CV feature, which may be useful for hydro-environment applications, is object detection and tracking. ALLAMANO ET AL. (2015) presented a study on raindrop detection and estimation of rainfall intensity. Obstacle detection in combination with optical flow methods (see Chapter 7) can be applied for detection of fish in fish passages, classification of fish species and estimation of swim velocities (Fig. 1.2.2, unpublished results from data analysis conducted by the author).

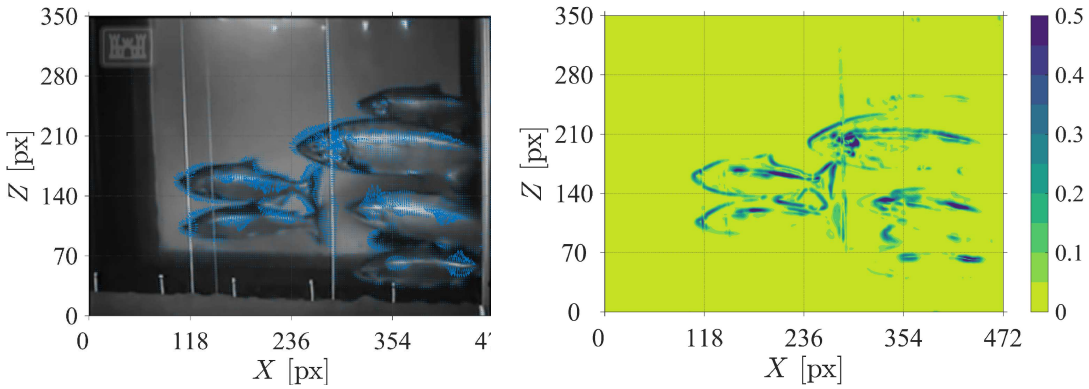

(A) Detected fish bodies and optical flow direction

(B) Velocity field (in fish length per second)

Figure 1.2.2: Optical flow applied to a fish passage observation video from Bonneville dam (courtesy of USACE, video retrieved from www.nwp.usace.army.mil)

As highlighted in the previous section, the need for data collection is increasing and more sophisticated data analysis methods are needed. In turn, artificial intelligence, as the most important example of such new methods, requires tremendous amounts of data to train and validate new models. It may be expected that the fast developing advances in both fields will amplify each other. Fast accessible consumer-grade smart sensors will further enhance monitoring activities. For instance, ZHANG ET AL. (2019A) described the application of low-cost UAV-based smart sensors for catchment monitoring. Non-professional, low budget hand-held devices (e.g. cell phones with LIDAR or depth cameras) include more and more smart technology which may be adapted to be used for hydro-environment data collection. As pointed out by CHEN AND HAN (2016), data from smart sensors and services, remote sensing and earth observation systems will inevitably direct hydroinformatics into the big data era. However, the quality and quantity of data is most essential (GOVINDARAJU, 2000) and dealing with big data in hydro-science becomes yet another challenge (SAVIC, 2019). In this regard, the big data community typically refers to the "V's", i.e. the immense Volume of data (which is gathered with high Velocity) and the Veracity of data. Apart from these criteria, another important issue is Variety, which considers the high number of data sources and formats (DORSCHEL, 2015). The latter is also highlighted by CHEN AND HAN (2016) as a main challenge in hydroinformatics which needs to handle data from different sensors, methods and organizations.

1.3 AIMS AND SCOPE OF THIS THESIS

The presented studies aim at proposing novel experimental instrumentation allowing for simple application to flow depth and velocity measurements in turbulent free-surface flows. It is pointed out that all studies have been limited to laboratory environments. However, most instruments and techniques may be applied at prototype scale as well, providing instantaneous data of turbulent free-surface or (surface) velocities with high temporal or spatial resolution. As mentioned before, imaging methods can be easily conducted with drone-based cameras allowing easy access to inaccessible areas, e.g. stilling basins in operation. All measurements can be performed with consumer-grade hardware and open-source or low-budget software, features that provide an opportunity to make imaging techniques become standard tools for future data collection in hydraulic engineering.

Chapter 2 presents an overview on hydraulic modeling techniques and classical instrumentation.

Free-surface detection methods are introduced in Chapter 3. An edge detection method is used to extract the free-surface from high-speed videos captured through transparent sidewalls of a stepped spillway flume. Moreover, a depth camera is employed to measure the instantaneous 3D free-surface in a highly turbulent hydraulic jump environment (Chapter 4). Both flow conditions are particularly complex due to the large amount of entrained air. Presented depth measuring techniques are discussed in Chapter 5.

In Chapter 6, Particle Image Velocimetry (and its derivative Bubble Image Velocimetry), a well-established method for determination of velocity fields, is applied to clear-water and air-water flows, respectively. Potential image processing methods to improve results are also discussed. Chapter 7 introduces an alternative method for velocity field estimation, based on the optical flow approach. Similar to the previous chapter, both, clear-water and air-water flows, are analyzed and benchmarked against the PIV/BIV method. Capacities and limitations of the presented velocimetry methods are discussed in Chapter 8 and additional benchmarking is achieved by using synthetic particle images.

Chapter 9 summarizes the thesis' contents and conclusions and highlights the original contribution to knowledge. Finally, future research needs are identified in Chapter 10.

CHAPTER 2

CLASSICAL METHODOLOGY IN HYDRAULIC MODELING

2.1 LABORATORY MODELS OF FREE-SURFACE FLOWS

Author: Daniel B. Bung
Book: Rivers – Physical, Fluvial and Environmental Processes
Year: 2015

Abstract: Hydraulic modeling is the classical approach to investigate and describe complex fluid motion. Many empirical formulas in the literature used for the hydraulic design of river training measures and structures have been developed using experimental data from the laboratory. Although computer capacities have increased to a high level which allows to run complex numerical simulations on standard workstation nowadays, non-standard design of structures may still raise the need to perform physical model investigations. These investigations deliver insight into details of flow patterns and the effect of varying boundary conditions. Data from hydraulic model tests may be used for calibration of numerical models as well. As the field of hydraulic modeling is very complex, this chapter intends to give a short overview on capacities and limits of hydraulic modeling in regard to river flows and hydraulic structures only. The reader shall get a first idea of modeling principles and of basic considerations. More detailed information can be found in the references.

Keywords: Physical modeling, similitude, open channels, hydraulic structures

2.1.1 INTRODUCTION

For more than 500 years, people have tried to better understand the nature of complex flows. For instance, several famous records and sketches on flow phenomena were published by Leonardo DaVinci in the late 15th century. Sir Isaac Newton (1642 - 1727) was the first to develop basic approaches on the similitude between a prototype and its scaled reproduction, i.e. the model. These approaches were advanced by other researchers developing modeling laws which are well recognized nowadays. These

model laws were first applied to scaled models at the end of the 19th century. In particular, William Froude (1810 - 1879) and Osborn Reynolds (1842 - 1912) shall be mentioned in the context as representatives of many important individuals of fluid mechanics in these days.

HUGHES (1993) stated that physical modeling is still an important technique to solve hydraulic engineering problems even in a time that computers become more and more powerful and numerical models more reliable. Even two decades later, this statement is still valid.

Hydraulic modeling allows to directly face the effects on flow features induced by changes of boundary conditions. Physical hydraulic models may also be operated to verify theoretical and numerical models or to draw some conclusion in regard to flow phenomena that are still not fully understood to date. Further development of measurement techniques allows for new investigation methods and gives high-precision results. Some up-to-date equipment are illustrated in Fig. 2.1.1.

On the other hand, the setup of a physical model is often relatively expensive and time-intensive. A change of boundary conditions is oftentimes not trivial and needs to be considered in the early stages of planning. Later adaption to other conditions may be difficult.

(A) Ultrasonic displacement sensor for accurate measurement of water levels

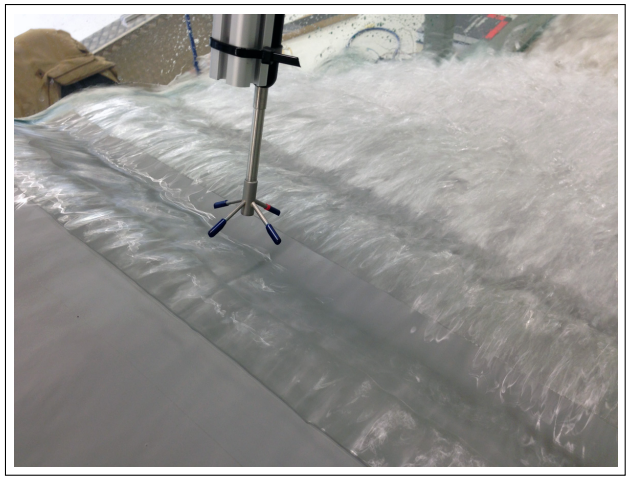

(B) Acoustic Doppler Velocimeter (ADV) for mesasuring of local three-dimensional velocity components (here: installed in the non-aerated part of stepped weir before submerging into water)

Figure 2.1.1: Measuring devices for laboratory studies

2.1.2 SIMILITUDE

In order to extend the findings from a scaled physical model to prototype scale, hydromechanical similitude between both scales must be guaranteed. This means that a geometric, kinematic and dynamic similitude are needed to ensure a similar motion and, by consequence, similar forces acting in the fluid. In a flowing water body, the following forces must be considered (forces due to elasticity are neglected for water as an incompressible fluid):

- a force due to acceleration of the fluid (inertia) F_i,
- a force due to gravity F_g,
- a force due to pressure in the flow field F_p,
- a force due to inner friction (viscosity) F_μ,
- a force due to surface tension at the air-water interface F_σ.

It yields the following balance of forces:

$$F_i = F_g + F_p + F_\mu + F_\sigma \tag{2.1.1}$$

Considering a general length L and time T and neglecting F_p because it is a dependent force, Eq. 2.1.1 becomes:

$$\rho \cdot L^3 \cdot L/T^2 = \rho \cdot L^3 \cdot g + \mu \cdot \frac{L/T}{L} \cdot L^2 + \sigma \cdot L \tag{2.1.2}$$

where ρ is the density of water in [t/m^3], g is the gravity acceleration in [m/s^2], μ is the dynamic viscosity in [kg/(m·s)] and σ is the surface tension in [kN/m]. A dynamic similitude now claims that all forces have the same scale factor:

$$\frac{F_{i,N}}{F_{i,M}} = \frac{F_{g,N}}{F_{g,M}} = \frac{F_{\mu,N}}{F_{\mu,M}} = \frac{F_{\sigma,N}}{F_{\sigma,M}} \tag{2.1.3}$$

and by consequence

$$\frac{\rho_N \cdot L_N^4/T_N^2}{\rho_M \cdot L_M^4/T_M^2} = \frac{\rho_N \cdot L_N^3 \cdot g_N}{\rho_M \cdot L_M^3 \cdot g_M} = \frac{\mu_N \cdot L_N^2/T_N}{\mu_M \cdot L_M^2/T_M} = \frac{\sigma_N \cdot L_N}{\sigma_M \cdot L_M} \tag{2.1.4}$$

with index N referring to prototype scale and index M to model scale, respectively. Full hydromechanical similitude could be achieved if the model would be operated by a fluid with density, viscosity and surface tension that fulfills this constraint. Unfortunately, this fluid does not exist and models are commonly operated by the same fluid as in nature, i.e. water. With the length scale $\lambda_L = L_N/L_M$, the time scale $\lambda_T = T_N/T_M$ as well as $\rho_N/\rho_M = 1$, $\mu_N/\mu_M = 1$, $\sigma_N/\sigma_M = 1$ and $g_N/g_M = 1$, Eq. 2.1.4

becomes:

$$\frac{\lambda_L^4}{\lambda_T^2} = \lambda_L^3 = \frac{\lambda_L^2}{\lambda_T} = \lambda_L \tag{2.1.5}$$

It must be noted that this equation is only valid for $\lambda_L = \lambda_T = 1$, i.e. the prototype scale. It is not possible to properly scale all acting prototype forces in a scaled hydraulic model. Every scaled model implements certain errors. However, this error can be minimized if the most relevant counter-acting force is considered together with the inertia force and properly scaled. For free-surface flows which is dealt with in this chapter, the predominant force is gravity.

2.1.3 FROUDE'S LAW

The relation between the inertia force and the gravity force in open channels is generally expressed by the Froude number:

$$\mathsf{F} = \sqrt{\frac{\text{inertia}}{\text{gravity}}} = \sqrt{\frac{\rho \cdot V \cdot v^2/L}{\rho \cdot V \cdot g}} = \frac{v}{\sqrt{g \cdot L}} \tag{2.1.6}$$

where V is the volume of the water body moving with the velocity v[1].

The basic idea of Froude's law is that the dimensionless Froude number is the same in model and nature for a similar flow condition. This means that a sub-/supercritical flow in nature must be sub-/supercritical in the model as well. The flow may then be described by the same governing differential equations with transferable boundary conditions upstream or downstream. Identical Froude numbers yield:

$$\frac{v_N}{\sqrt{g \cdot L_N}} = \frac{v_M}{\sqrt{g \cdot L_M}} \tag{2.1.7}$$

On this basis, the scaling factors for all physical properties may be derived, e.g.:

- Velocity factor: $\lambda_v = v_N/v_M = \sqrt{L_N/L_M} = \sqrt{\lambda_L}$
- Time factor: $\lambda_T = \lambda_L/\lambda_v = \lambda_L/\sqrt{\lambda_L} = \sqrt{\lambda_L}$
- Discharge: $\lambda_Q = \lambda_v \cdot \lambda_A = \sqrt{\lambda_L} \cdot \lambda_L^2 = \sqrt{\lambda_L^5}$
- etc.

[1] It must be noted that similar considerations yield the Reynolds number (viscosity), Weber number (surface tension) and Mach number (elasticity) if the gravity force is replaced by the other forces.

2.1.3.1 MODEL ACCURACY

Data from the laboratory needs to be scaled to prototype dimensions according to the appropriate model scale factors. However, the modeler must be aware of inaccuracies which may derive from different sources. In detail, model effects and scale effects may occur.

Model effects Model effects may arise from an inappropriate idealization of the prototype conditions in the laboratory. For example, three-dimensional flow patterns in the stilling basin downstream of a weir model (see Fig. 2.1.2) may not fully develop when the model is installed in a narrow flume. Depending on the purpose of such a study, this effect may be more (e.g. stilling basin design) or less (e.g. determination of weir coefficient) severe. Reflections from walls may also lead to some undesired effect as well as incorrect water levels due to wall effects when water levels are visually investigated through a transparent sidewall. On the other hand, some effects being present in the prototype system are difficult to reproduce, e.g. raised water levels by wind. These exemplary problems emphasize that some experience is required by the modeler in order to avoid or at least to recognize such effects and in this case, to evaluate those in regard to not misinterpret the data.

Figure 2.1.2: Model investigation on stilling basin performance downstream of a steep stepped spillway (BUNG ET AL. (2012)), channel width is 1 m to avoid model effects

Scale effects As discussed above, model laws, such as the Froude's law for open channel flows, are based on the idea to just account for the major force counter-acting the inertia force. This assumption is reasonable as long as the model scale does not fall below a critical value where other forces may become significant. A few simple examples shall illustrate this problem:

- If the Froude's law is considered, the scale factor for the dimensionless Reynolds number[2] in a model with identical fluid becomes $\lambda_{\mathsf{R}} = \lambda_v \cdot \lambda_L = \lambda_L^{3/2}$. Thus, the Reynolds number is never properly scaled in a Froude model and viscosity effects may lead to disturbed results. Considering the precondition that the flow resistance f in model and prototype must be equal, it has to be ensured that hydraulic rough conditions are met in the model (i.e. the flow resistance f is no more dependent on R, see Fig. 2.1.3) which in turn is only met in large scale models. Alternatively, the modeler may come up with the idea to chose a smaller surface roughness k in order to ensure a properly scaled f even for a small Reynolds number in the model. However, it must be recognized that scaling of bed roughness is generally difficult, particularly for a small roughness in prototype, e.g. for a concrete surface.

- A small scale weir overflow model becomes more and more affected by surface tension when the water level at the weir crest is low for a given flow velocity.

- Investigations on sediment transport may be affected by scale effects when particles need to be scaled to a smaller size, thus reaching undesired cohesive characteristics.

- Laboratory studies with focus on air-water flows, e.g. hydraulic jump downstream of a weir, must be modeled in large scale as air bubbles in prototype tend to break up when reaching a critical size, particularly in turbulent flows. By consequence, air bubbles have roughly the same size, in model and in prototype, and are thus not properly scalable. Air bubble lift forces may play a more significant role in model as in nature.

[2] note: the Reynolds number is defined as: $\mathsf{R} = \rho \cdot v \cdot D/\mu$

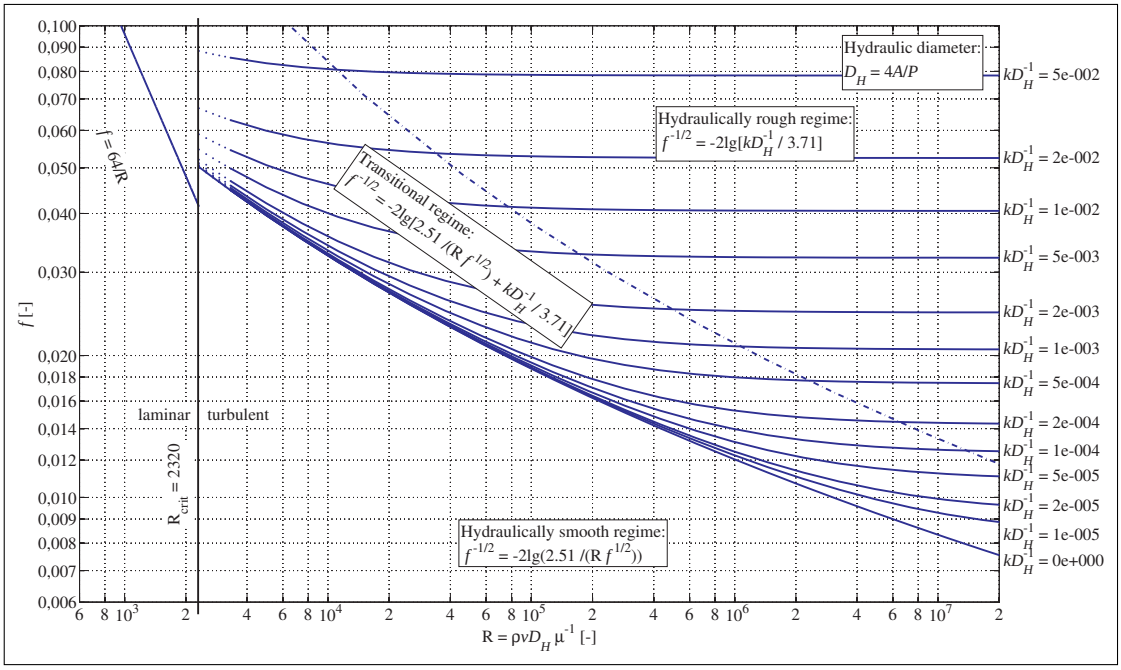

Figure 2.1.3: Moody diagram for determination of flow resistance factor f as a function of relative roughness k/D_H (with $D_H = 4 \cdot A/P$ the hydraulic diameter, A the cross-sectional area and P the wetted perimeter) and Reynolds number R

Numerous studies have been performed to determine the critical scale to prevent scale effects. Several publications on scale effects for models with different focus are included in KOBUS (1984). Recently, a comprehensive review on critical model scales was presented by HELLER (2011). If no information on scale effects and minimum model scales is found in the literature, the modeler should consider evaluating a series of models and differing size scale before setting up the final full model in order to check from which scale on the data lead to differing results when scaled up to prototype scale according to the relevant scale factors. Laminar flows however, where the flow depth is low and the velocity is small, should be modeled in prototype scale to reproduce the viscous effects correctly.

2.1.4 OPEN CHANNELS

2.1.4.1 MODELS WITH FIXED BED

Physical models with fixed beds are used with different focuses. In earlier times, the main interest was to determine water levels and flooded ares for different flood events. Other concerns could be be found in the effects of river training measures or the formation of 2D or 3D flow patterns (e.g. eddy formation in groin fields). It must be confessed that such studies are commonly performed numerically nowadays. Large laboratory capacities in terms of space and discharge are required to operate

physical river models. Consequently, such studies are very cost-intensive while numerical 2D and 3D river models are available for free as open-source codes. However, physical river models are still a useful method to investigate more complex flow situations, which may be caused by e.g. jet formation and mixing procedures at an cooling water outfall structure (see section 2.1.5.4).

2.1.4.2 MODELS WITH MOVABLE BED

River models with movable beds are used for investigation of bed load and sediment transport. Local erosion and deposition processes may be in the focus for waterways modeling and in models of inlet structures to hydropower plants. Such models need to fulfill the same hydraulic similitude as developed above, but further considerations on particle dynamics are needed. These particle dynamics can be described by the particle Froude number

$$\mathsf{F}_p = \frac{\tau_0}{g \cdot (\rho_p - \rho) \cdot d_p} \tag{2.1.8}$$

and the particle Reynolds number

$$\mathsf{R}_p = \frac{\sqrt{\tau_0 \cdot \rho} \cdot d_p}{\mu} \tag{2.1.9}$$

where τ_0 is the bed shear stress, ρ_p the particle density and d_p the particle diameter. Both dimensionless numbers are known from the famous Shields diagram for onset of particle movement and must be the same in model and prototype. With this precondition, relevant scale factors for sediment modeling may be derived, such as the particle size scale and the particle time scale, and a model sediment material (and grain size curve) can be chosen. For further information see ASCE (2000) and KOBUS (1980). One resulting difficulty is caused by the particle time scale which differs from the flow time scale derived above. Sediment movement is faster in the model than in the nature. The modeler may address this issue by comparing the model data with sediment data from the field.

The total bed load or sediment load being transported through the model can be measured by collecting and weighing the material at the model outflow boundary. Depending on the test duration, the model size and the study purpose, it may be necessary to ensure that the same amount of material is added at the inflow boundary in order to provide enough material for the test.

2.1.4.3 DISTORTED MODELS

Model scales for large river models are often limited due to given space and/or discharge capacity in the laboratory. However, too small model scale may result in an

improper scaling of Reynolds numbers and friction factors. One technique to overcome this problem is to set up a distorted model in which the length scale number in vertical direction $\lambda_{L,v}$ is smaller than the length scale number in horizontal direction $\lambda_{L,h}$. By distorting the model, the flow velocity and flow depth is increased compared to an undistorted model with $\lambda_{L,h}$ in all directions and a larger Reynolds number is obtained (the influence of surface tension is decreased as well). By consequence, a hydraulic rough condition can set in. In this case, different scale factors must be regarded for different hydraulic parameters which can be found in KOBUS (1980). It must be noted that the scaling of surface roughness in a distorted model is even more difficult than in an undistorted model. Proper scaling of roughness needs to be achieved by calibration using prototype data. It must also be taken into account that three-dimensional flow patterns, such as vertical eddy formation around a bottom structure, become difficult to transfer to the prototype in a distorted model (ASCE, 2000). The applicability of distorted models must be carefully evaluated. Some model tests, e.g. the three-dimensional mixing procedure in the near field of an outfall structure, do not allow model distortion.

2.1.4.4 VEGETATIONAL FLOW

In the recent past, several studies were conducted which focused on the effects of vegetation in natural channels on the river flow. One major feature which must be addressed is that vegetation may be deformed under hydrodynamic conditions and the absolute roughness becomes a function of discharge. In hydraulic models, the vegetation is often modeled by some artificial plants which must then have a similar geometry and stiffness. Proper scaling of the vegetation characteristics is not trivial. The modeler may also pay attention to river vegetation when a study on sediment transport is planned as some relevant interaction can occur. Vegetational flow features are presented in detail in ABERLE AND JÄRVELÄ (2015) . The flow resistance nature of the vegetation can also change seasonally. For further information on the topic, the reader is referred to ABERLE AND JÄRVELÄ (2015) which also includes some exemplary model studies.

2.1.4.5 DEBRIS AND ICE

Modeling of debris and ice are challenging (and rare) tasks which may come up in early design stages of weirs, locks or hydropower plants and which require correct reproduction of drift and accumulation of ice and debris. For some questions, special attention must be paid to the proper modeling of the material to be used in the laboratory to reproduce the rigidity and eventually the thermal properties in case of ice. Furthermore, wind may play an important role, particularly when the load on a structure is of interest. Debris and ice modeling are no standard problems, see ASCE

(2000) for additional details regarding derivation of relevant scale factors.

2.1.5 HYDRAULIC STRUCTURES

2.1.5.1 AERATED FLOW

Introduction Aeration mainly occurs in highly turbulent flows. The most important causes for aeration in rivers are hydraulic jumps and mixing downstream of weir overflows (see Fig. 2.1.4). For hydraulic jumps, the amount of entrained air depends on the inflow Froude number. In case of a weir, a growing turbulent boundary layer develops at the weir crest. If the structure is high enough, self-aeration sets in at the point of intersection of the boundary layer and water surface. In both cases, the entrainment of air leads to a bulking of the flow depth, i.e. the air bubbles are transported along the whole water column which generates higher water levels than for clear water. Knowledge of the amount of entrained air is thus important for the hydraulic design, e.g. for sidewall heights. Consideration of entrained air is also relevant for energy dissipation calculations when the bulked flow depth is measured in the laboratory.

Some weirs are used specifically to force air entrainment in rivers in order to re-oxygenate the water. Oxygen is transferred across the air-water interface of the bubbles. However, it must be considered that air bubbles are roughly of the same size in model and in prototype. Scale effects are thus very likely when oxygenation tests are performed in scaled model.

(A) Aeration at a weir downstream of Oker dam in Germany; note the strong aeration at the bottom outlet in the background

(B) Aeration on a cross-bar block ramp due to local hydraulic jumps OERTEL AND BUNG (2012A)

Figure 2.1.4: Aeration at hydraulic structures

Air-water mixture Description of the air-water mixture body becomes difficult when the flow is fully aerated. Close to the bottom, the air-water mixture is characterized by air bubbles transported in the water, while in higher elevation larger air pockets being entrapped between surface waves may be found WILHELMS AND GULLIVER (2005). Above this elevation, mainly ejected droplets are found (see Fig. 2.1.5). By consequence, void fraction C is non-uniformly distributed along the water column. A typical void fraction profile for a stepped weir is also presented in Fig. 2.1.5.

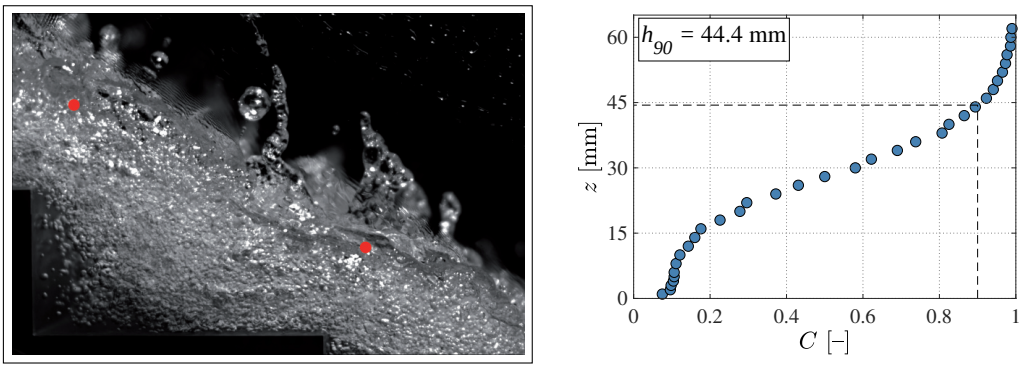

(A) Photograph captured by a high-speed camera with 700 fps; the markers indicate the water level with 90 % time-averaged void fraction which is often taken into account as idealized water surface

(B) Void fraction profile measured at the stepped edges with a conductivity probe

Figure 2.1.5: Air-water mixture in self-aerated high-speed flows on a stepped weir model (width 50 cm, step height 6 cm, slope 1:2, discharge 35 l/s)

In most studies, air-water flow properties were measured by means of intrusive needle probes which consist of fine tips that pierce the air bubbles. These probes work on basis of different conductivity characteristics between air and water (conductivity probe) or different optical refraction characteristics (fiber optical probes). The principle of these probes is discussed in CHANSON (2002A) amongst others. Recent studies show that modern non-intrusive methods may also be applied. LEANDRO ET AL. (2014) present a calibration method which can be used to obtain air concentration profiles and velocity fields from high-speed camera movies. Even the data from ultrasonic displacement sensors, normally known to be inaccurate in flows with irregular surface, can give some reasonable results as demonstrated by CHACHEREAU AND CHANSON (2011) in hydraulic jumps and BUNG (2013) in self-aerated chute flows.

Oxygenation potential Due to the large amount of air-water interface in aerated open channel flows, the oxygenation potential is high. This may be of interest to enrich water from a reservoir with oxygen when discharged to the downstream river.

As mentioned above, scale effects cannot be avoided when investigations are performed on a scaled model due to similar air bubble sizes in the model and in prototype. However, in large-scale models the measured data give at least an idea of relative potentials when different situations are compared. Several recent studies presented direct oxygenation measurements where the water was de-oxygenated by addition of sodium sulfite before the test and the oxygen content recorded over time (AVERY AND NOVAK (1978), BUNG (2011B), ESSERY ET AL. (1978), TOOMBES AND CHANSON (2005) a.o.). The references include more information on the technique, further information may also be found in ASCE (2007).

Scale effects Many publications address the very important topic of scale effects in aerated flows. Accordingly, model tests should be carried out on large-scale models. For self-aerated flows, a minimum scale is often given by 1:10 (e.g. CHANSON (1996)) and a minimum Reynolds number of 10^5 at the aeration point (e.g. KOBUS (1985)). Newer publications identify a minimum Reynolds number of 2 to $3 \cdot 10^5$ to properly represent the turbulent properties (e.g. PFISTER AND CHANSON (2012)).

2.1.5.2 SCOURING

For the modeling of scour processes, the basic considerations on particle dynamics from section 2.1.4.2 dealing with sediment transport models are still valid. Scouring models are typically detailed models of flow at hydraulic structures, i.e. with larger scale than river models with movable beds. For the operation of a scour model, two important aspects are essential:

1. Scouring is a long-term process in nature which takes relatively less time in the model due to different time scales as discussed in section 2.1.4.2. For the safe design of hydraulic structures the maximum values for the scour depth and size are important, i.e. the equilibrium state which sets in after a certain time under steady-state flow conditions. It must thus be ensured that this equilibrium state is obtained in the model. As scour dimensions are usually measured in dry conditions (after the model run), a sensitivity analysis in terms of a series of model runs is required for comparison of results from tests with different duration.

2. As mentioned above, the scour dimensions are measured in dry conditions. It must be ensured by the operator that the scour is not deformed during the run-off process. Seepage through the loose bed may lead to erosion in the scour hole and adulterate the results.

Usually, laser distance meters are used for measuring of scour depth. The measuring spot is tiny and the application in small scour becomes possible. Acoustic displacement meters are characterized by a larger measuring area due to spreading of the acoustic beam. These probes are less accurate for small scour holes where the acoustic beam size is in the range of the scour dimensions.

More information on scouring processes including some exemplary model studies can be found in PAGLIARA AND PALERMO (2015).

2.1.5.3 STRUCTURAL VIBRATION

Knowledge about potential vibrations is essential in early design stages for any regulation structure. Severe damages may happen in case where excitation frequencies coincide with structural frequencies, i.e. the eigenfrequencies which depend on the structure's mass and stiffness. Besides a self-excited vibration which may be induced by a gate movement, flow-induced vibration are the most important vibration source. In this case, flow turbulence leads to fluctuating pressures around the structure. In general, two different ways of modeling are possible for vibration tests.

1. Proper modeling and scaling of all structural parameters, i.e. dimensions, mass and stiffness: Structural vibrations can then be directly inspected. However, scaling of the structure's stiffness is very difficult, particularly for complex structures.

2. Proper modeling of the hydraulic conditions and the structure's dimensions only (see Fig. 2.1.6): The structure's mass and stiffness are disregarded and a fully rigid model is built. In this case, only the external flow fluctuations can be measured in the model. Th excitation potential is then evaluated by comparison of the major frequencies with mathematically derived eigenfrequencies of the structure. The modeler must then decide which eigenfrequencies are relevant for a global vibration. Generally, eigenmodes higher than the 6-7th modes may be considered to lead to local, less severe vibration modes only.

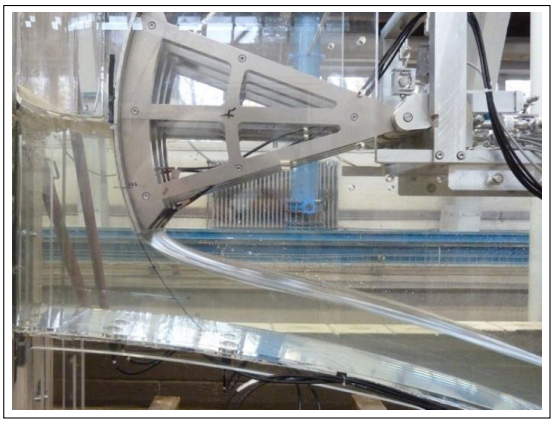

Figure 2.1.6: Rigid physical model (scale 1:35) of a high-head radial gate for vibration test purposes (SCHLURMANN AND BUNG, 2012), note the pressure transducers installed in bottom and at the skin plate of the gate used to measure pressure fluctuations.

The phenomenon of structural vibration in hydraulic engineering is addressed in ICOLD (1996). General information on its modeling is presented by KOBUS (1980) while exemplary studies may be found in CHOWDHURY ET AL. (1997) and SCHLURMANN AND BUNG (2012).

2.1.5.4 OUTFALLS

Effluents from outfall structures often have a different density than the ambient water body. Thus, upward (positive) or downward (negative) directed lift forces due to the different specific weight affect the turbulent diffusion. In this case, a densimetric Froude number[3] becomes relevant TURNER (1966):

$$\mathsf{F}_d = \frac{v}{\sqrt{g \cdot (\Delta\rho/\rho) \cdot L}} \tag{2.1.10}$$

where $\Delta\rho$ is the difference in density between effluent and ambient water.

Generally, the near field around the outfall must be distinguished from the far field. In the near field, the mixing is mainly caused by small-scale turbulence between the jet and the surrounding water body. In the far field, large-scale turbulent diffusion maintains the mixing process. Thus, near field investigations need a detailed reproduction of hydraulic and geometrical conditions at the structure, while for far field investigations proper modeling of the river characteristics is required. However, the transition between near field and field is hard to define. The modeler should therefore ensure correct modeling for all regions.

As the turbulence is the decisive parameter for the mixing, the modeler must pay

[3]For temperature-driven density differences an alternative formulation is given in RIESTER ET AL. (1980).

attention to possible scale effects. As mentioned earlier, the Reynolds number can never be scaled correctly in a Froude model. According to KOBUS (1980), a minimum Reynolds numbers of 2000 for the jet and 3000 for the river, respectively, must be achieved to avoid those scale effects. It must be noted that degradation time scales of pollution due to biological and chemical processes cannot be scaled.

Models are mostly operated by adding some tracers which show a comparable mixing characteristic as the real effluent. For example, the tracer could have a certain salinity leading to a different density. The mixing could then be observed by measuring the decreasing salinity at numerous downstream cross sections. In laboratories with closed water cycles, the modeler must consider the travel time of the tracer to re-arrive at the model to avoid an undesired increase of density at the model inlet.

2.2 CLASSICAL FLOW DEPTH AND VELOCITY SENSORS

2.2.1 GENERAL REMARKS

As highlighted in Section 1.1, measurements of flow depths and flow velocities are of particular importance in free-surface flows. They allow for determination of streamflow, e.g. at a river gauge or using a measuring weir, the estimation of hydrodynamic forces and resulting shear stress as well as the detection of turbulent flow structures of different scales. Nowadays, experimental hydraulic research mainly focuses on measuring of multidimensional data with high spatio-temporal resolution. However, one-dimensional point measurements are still common and may be sufficient for selected applications. Generally, it is emphasized that the selection of instrumentation depends on its availability in the laboratory on the one hand, but on the other hand multidimensional data may increase the complexity of the setup and data analysis in cases where simple, time-averaged 1D data may equally provide relevant information.

This section aims at briefly presenting some state-of-the-art techniques which are commonly employed in contemporary experimental research[4]. Instrumentation, which is mainly employed in the field, will not be discussed herein. For a more complete overview, it is referred to ABERLE ET AL. (2017) instead.

2.2.2 FLOW DEPTH SENSORS

Point gauges represent the most classical device for measurements of steady water levels in laboratory conditions (Fig. 2.2.1(A)). This type of probe consists of a fine needle which is lowered to slightly pierce the free surface from above or from below using a hook-shaped tip (ABERLE, 2017). The corresponding water surface is then visually observed using an attached ruler or elctronically registered. ABERLE (2017) specifies the accuracy of point gauges to be in the order of ~0.1 mm. Application to unsteady flows is difficult and requires automation of the tip positioning system.

Water levels in highly unsteady clear-water flows, e.g. propagating waves, are typically investigated by means of intrusive wave gauges, working either on a resistivity-based or capacitance-based principle. Resistivity gauges consist of two parallel wires with known distance immerging into the water. A voltage passing through the wires cause a varying conductance which is proportional to the submerged length of the sensor (HUGHES, 1993). As pointed out by HUGHES (1993), resistivity gauges have similar accuracy as point gauges and are widely spread due to simple construction and maintenance.

[4]Imaging-based methods are not presented herein as they are in the focus of subsequent chapters.

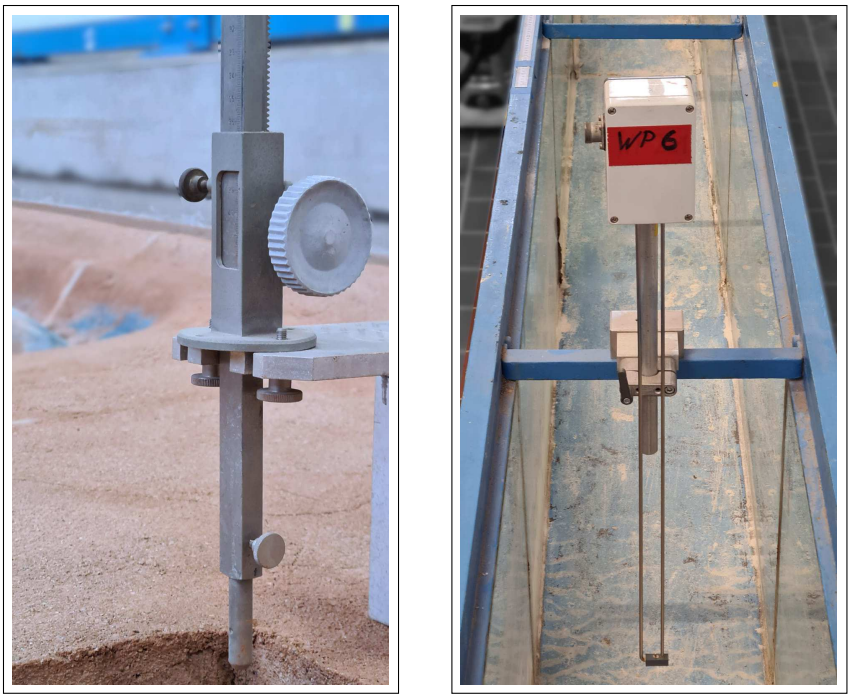

(A) Point gauge **(B)** Capacitance wave gauge

Figure 2.2.1: Water gauges for laboratory applications (courtesy of Dr. Nils Kerpen, Leibniz University Hannover)

Capacitance wave gauges (Fig. 2.2.1(B)) are composed by an insulated wire and a supporting rod. Similar to resistivity sensors, the wire is immerged into the water. The wire insulation serves as capacitor between the conducting wire and the water (HUGHES, 1993). Variation in sensor capacitance is proportional to water level variation. Special care in terms of calibration is needed for both types of wave gauges as any change in water temperature or salinity can significantly affect the measurements.

In the recent past, ultrasonic sensors (USS) have gained a lot of interest in both, hydraulic and coastal engineering communities (Fig. 2.1.1(A)). USS are non-intrusive probes, mounted above the water surface and thus are independent of the water temperature or other water-related parameters. The sensor consists of a membrane generating an acoustic signal which is reflected at surfaces. The distance can be easily calculated for a given celerity of the acoustic wave if the travel time of the original signal and its echo, which is reflected back to sensor, is known. This travel time, i.e. the time of flight, can be determined employing different techniques[5]. It must be noted that the celerity of sound depends on the temperature, thus the sensor should provide a temperature-compensation and any air ventilation in the laboratory should be avoided. The size of the sensor and the distance to the observed surface affect the footprint of the acoustic beam and, consequently, may preclude

[5]The reader is referred to Section 4.1.2 for more information on travel time estimation.

correct measurement or hinder the interpretation of data in case of small-scale free-surface perturbations. In case of higher waves, the acoustic wave may be deflected, limiting the applicability in coastal engineering. ZHANG ET AL. (2018) presented a detailed study on the measuring behavior of USS for typical hydraulic and coastal engineering cases.

2.2.3 FLOW VELOCITY SENSORS

Measuring of flow velocity as an internal flow feature requires special attention. For correct interpretation of data, it must be ensured that the flow field is not affected by intrusive sensors (or that any flow perturbation is of negligible order), the probe head needs to be small enough to provide data with sufficient spatial resolution while sample rates need to be reasonably high if turbulence is of interest. In case of reverse flows, a sensor must be capable to differentiate between forward and backward directed flows.

If spatial and temporal resolution is of minor relevance, a classical Pitot-static tube, also know as Prandtl tube, can be considered adequate. This probe consists of a hollow tube which needs to be aligned with the flow direction. A small opening at the tube head faces the main flow and thus, when a manometer is installed, allows to measure the total head (i.e. the sum of static and dynamic pressure) which is acting at the sensor head. An additional, shielded opening at the shell of the tube allows the measurement of the static pressure alone and thus to calculate the velocity head or flow velocity, respectively (HUGHES, 1993). Pitot-static tubes are robust, low-cost devices. However, the measuring principle and the complex design with two pressure taps in a single housing causes a relatively large diameter which does not allow to measure close to walls or to provide accurate data in flows with high velocity gradients. Interpretation of turbulent properties strongly depends on the correlation of pressure fluctuations within the two measured signals (MCKEON, 2007). The most crucial challenge when using a Pitot-static tube is to properly align the probe with the flow direction. Multihole tubes may be used to directly obtain the flow direction. When properly aligned with the flow, a well-designed Pitot-static tube can achieve an accuracy of ~0.1 % of the dynamic head (MCKEON, 2007).

Propeller anemometers are mechanical velocity sensors working on the principle of proportionality between flow velocity and revolution speed of the wheel. Relatively small sensors, as presented in Fig. 2.2.2(A), are available which allow for application in laboratory scales. Depending on the velocity, a certain voltage is returned which can be converted to a velocity when properly calibrated. It must be noted that propeller anemometers are not capable to distinguish backward from forward directed flow, but provide absolute veocities in both directions instead. Although generally feasible for unsteady flows, the response of a propeller is too slow to reveal turbulent fluctuations (HUGHES, 1993). An exemplary velocity time series obtained

in the non-aerated fow region of a stepped spillway is presented in Fig. 2.2.2(B) highlighting the low frequencies detected by the sensor.

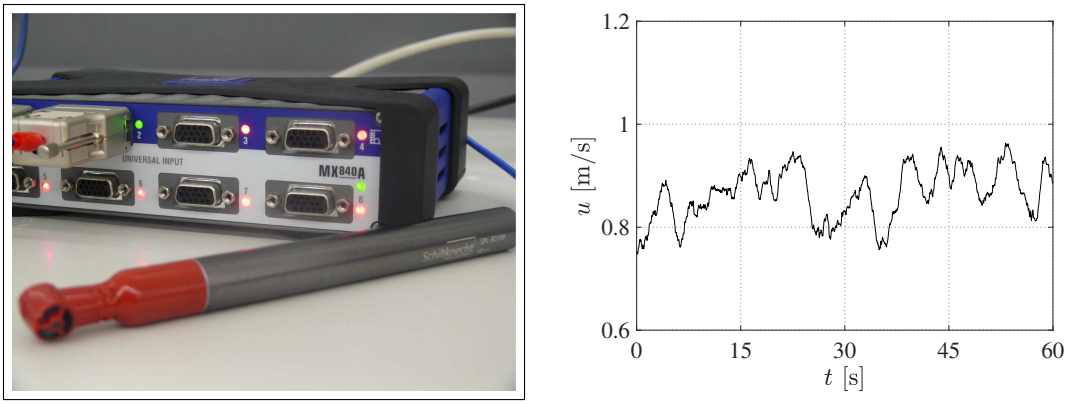

(A) Propeller anemometer plugged to an universal amplifier

(B) Exemplary time series obtained in the non-aerated flow region of a stepped spillway model

Figure 2.2.2: Propeller anemometer and exemplary time series measured in turbulent flows

A well-known approach to determine the velocity of a moving object is the use of the Doppler effect which causes a frequency shift of an emitted signal when reflected from the object. The frequency shift is proportional to the velocity. In order to measure a flow velocity, suspended particles are needed to echo the signal. It is assumed that these particles move with the fluid velocity (HUGHES, 1993) and no slip or positive/negative buoyancy is present. The emitted signal can bei either acoustical (Acoustic Doppler Velocimetry) or optical (Laser Doppler Velocimetry).

In hydraulic laboratories, Acoustic Doppler Velocimeters (ADV) are the most commonly employed acoustic backscattering instruments. ADVs consist of an emitter and mostly two or more separated receivers which are installed in symmetry to the emitter and with a certain inclination to allow for interpretation of flow direction. Bistatic (with two receivers) or multistatic (with three or more receivers) instruments facilitate determination of two or even three velocity components. Figures 2.1.1(B) and 2.2.3 show a four-receiver ADV in operation, which allows for measuring three velocity components plus one redundant measurement of the vertical component which is used for noise removal (LEMMIN, 2017). Figure 2.2.3 further highlights some potential side effects which may arise due to the intrusive measuring principle, i.e. surface perturbations and air entrainment, when measuring close to the free surface. Special attention is needed to ensure high signal quality during data collection (i.e. sufficient signal-to-noise ratio and correlation). In addition, noise filtering during post-processing of the data is essential, particularly for turbulence estimation. Seminal contribution on ADV filtering has been presented by GORING AND NIKORA (2002) and the discussion by WAHL (2003). Recently, a

new methodology for spatial filtering of ADV data in shear flows, obtained with a Vectrino profiler, has been proposed by VALERO AND BUNG (2018C). An ADV profiler provides velocity data within a limited range of ~3 cm. This is achieved by employing wide-angle receiver transducers which can receive the backscattering signal from particles all over the profile (LEMMIN, 2017). LEMMIN (2017) provides a comprehensive presentation and discussion on acoustic backscattering instruments in general.

Figure 2.2.3: ADV operating close to the surface (flow from right to left, note the perturbation and air entrainment in the wake)

In contrast to ADVs, the Laser Doppler Velocimeter[6] (LDV) is a non-intrusive instrument focusing laser light with a lens through a transparent sidewall to a single point in the water (HUGHES, 1993). Modern LDVs work in dual beam mode, focusing two laser beams on the same measuring point where both beams interfere and generate a fringe pattern (SVEEN, 2013). Particles moving through this pattern generate a signal, including the Doppler frequency, which is captured by a photodetector. LDVs provide relatively precise point data as the sample volume is smaller than 1 mm^3 (HUGHES, 1993). Determination of another velocity component can be achieved by using a 2D device emitting another pair of laser beams. Separation of the beams is possible when using different wavelengths, i.e. laser colors. 3D velocity measurements typically require another 1D device and precise focusing of the six beams beams to a single point. The LDV is a calibration-free instrument; velocity measurements depend on the optics geometry and the speed of light only (HUGHES, 1993). Accuracy is in the range of 2 %, although strongly depending on the size of the measuring volume. More detailed information on the LDV principle can be found in TROPEA ET AL. (2007) and FERREIRA AND ALEIXO (2017).

None of the above-mentioned probes is capable to provide reliable data in aerated flows. Air bubbles entering the Pitot-static tube may affect the pressure readings, propeller rotation may be disturbed when a bubble impacts the wheel, optical and

[6] It is also referred to as Laser Doppler Anemometer (LDA).

acoustical signals may be deflected at air bubbles. The most reliable probes in aerated flows are dual-tip phase detection probes. These probes detect phase changes (i.e. water or air) either on the principle of a change of light refraction at air-water interfaces (fiber-optical probes, Fig. 2.2.4) or a change of resistance (conductivity probes) to estimate the time-averaged, local void fraction. Velocity information is obtained by cross-correlating the raw voltage signals from both tip, assuming a slip-free, non-buoyant air bubble transport between both tips. Different tip arrangements have been proposed in the literature. Recently, FELDER ET AL. (2019) presented a detailed comparison of different working principles and setups and identified double-tip conductivity probes with side-by-side arrangement (see Figs. 3.2.1(B) and 6.3.1) as the most suitable for high-velocity air-water flows. Single-tip probes (Fig. 2.2.4) may also provide velocity information by analyzing the rising time of the recorded voltage signal during phase transition. However, this principle requires increased calibration efforts (VALERO AND BUNG, 2018A).

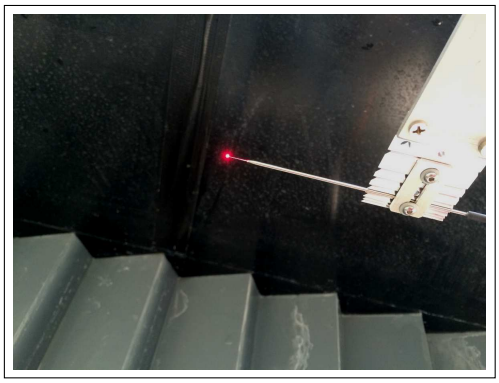

Figure 2.2.4: Single-tip optical fiber probe for void fraction and velocity measurements (from VALERO AND BUNG (2018A))

It must be noted that cross-correlation of full signals, as conventionally performed when analyzing phase detection probe data, yields time-averaged velocity data only and does not allow direct determination of turbulence properties. To overcome this shortcoming, CHANSON AND TOOMBES (2002) introduced an approach for estimation of the turbulence intensity based on the broadening of the cross-correlation function compared to the autocorrelation function of the voltage signals provided by a dual-tip phase-detection probe. More recently, KRAMER ET AL. (2019B) proposed a cross-correlation technique with adaptive time windows to calculate pseudo-instantaneous velocities in order to improve turbulence estimation. KRAMER ET AL. (2020) provide further information on optimum selection of processing parameters. According to BOES (2000), the accuracy of optical fiber probes is in the order of ~5 % for velocities. GONZALEZ (2005) estimates the accuracy of flow velocities obtained with conductivity probes to be ~10 %. The accuracy is, however, difficult to specify due to the complexity of aerated flows and the lack of knowledge of a true value.

2.3 DISCUSSION

Classical flow depth sensors are limited to point measurements. Point data may be sufficient for most applications with smooth water surfaces in low-turbulent flows. However, if turbulent surface fluctuations or multidimensional flows (e.g. 3D wave propagation) are of interest, an array of sensors is required to allow for interpretation of turbulent length and time scales. It must be noted that even with an array of sensors, this interpretation is still challenging. Synchronization and proper calibration of multiple sensors can be difficult and requires a sound setup (which is often time-consuming and expensive) and data analysis procedure.

For determination of flow velocities as well, most available sensors are limited to provide point data. Some sensors, e.g. the ADV profiler may also provide information on velocity profiles; however, these profiles are limited to short ranges. Moreover, most velocity sensors are intrusive and thus potentially disturb the flow. Multidimensional techniques with high-spatial and temporal resolution would help to give a better insight into turbulent flow fields.

The above-mentioned shortcomings of classical measuring devices in hydraulic modeling may be improved by the use of non-intrusive imaging techniques. With increasing camera resolutions and frame rates, even low-cost devices can provide high-density data nowadays. The availability and continuous development and improvement of highly sophisticated, open-source image processing algorithms helped to promote these methods in the recent years. In the following, different imaging approaches for determination of flow depths and velocities will be presented and discussed.

PART II

FREE-SURFACE DETECTION

CHAPTER 3

FREE-SURFACE RECOGNITION BY EDGE DETECTION

3.1 INTRODUCTION TO EDGE DETECTION METHODS

3.1.1 GENERAL REMARKS

Edge detection methods are generally used for image segmentation and are commonly based on the determination of pixel intensity gradients (GONZALEZ AND WOODS, 2018; SONKA ET AL., 2015). The more concentrated such a change of intensity occurs, the more definite is the edge location. Ideally, the transition between two intensity levels, e.g. from 0 to 255, would occur over a distance of a single pixel, resulting in a step pixel intensity profile across this transition. However, in practice, images are characterized by a certain degree of blurring (see the schematic illustration in Fig. 3.1.1), resulting in a ramp (sloped) intensity profile. It may be noted that the ramp slope is directly linked to the degree of blurring. In addition, this blurring is mostly superposed by certain image noise, which may impede the gradient map determination. Thus, edge detection in digital image processing is commonly conducted in combination with preceding image filtering or smoothing. For detailed information on the effects of image noise on determination of first and second order derivatives, the reader is referred to GONZALEZ AND WOODS (2018).

The subsequent sections introduce the principle idea of edge detection and propose different image filtering methods which may be employed to enhance results for free-surface detection in open channel flows. It may be noted that edge detection methods may also be interesting for other applications in hydraulic engineering, e.g. time-variant scour profile determination or (dyed) plume propagation in clear water.

3.1.2 PRINCIPLE OF EDGE DETECTION METHODS

As highlighted above, edge detection is commonly based on identification of sudden (abrupt) changes of pixel intensity within an image I. For the latter, image gradients, i.e. the partial derivatives $I_X = \partial I/\partial X$ in horizontal and $I_Z = \partial I/\partial Z$ in vertical

direction, are required (see Fig. 3.1.1).

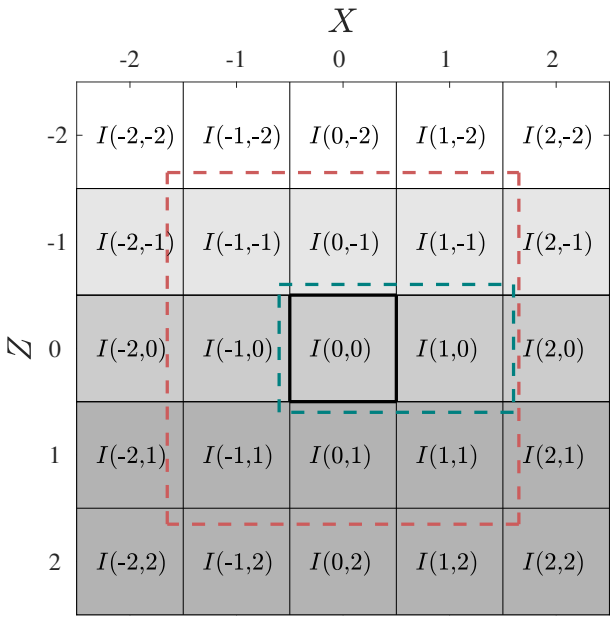

Figure 3.1.1: Schematic image of a blurred, vertical transition from dark gray to white with pixel coordinates in X- and Z-direction relative to the pixel of interest with $(X, Y) = (0, 0)$, blue: pixels used for a simple finite forward difference technique, red: pixels used with 3×3 operators

Numerically, these derivatives can be approximated by finite differences which in general terms may be described as:

$$\text{grad}\,[I(X,Y)] = E \cdot I_{sub} = E \cdot \begin{bmatrix} I(-\Delta x_1, -\Delta y_1) & \cdots & I(\Delta x_2, -\Delta y_1) \\ \vdots & \ddots & \vdots \\ I(-\Delta x_1, \Delta y_2) & \cdots & I(\Delta x_2, \Delta y_2) \end{bmatrix} \tag{3.1.1}$$

with E an operator (also referred to as kernel or edge detector) and I_{sub} a submatrix of the image I which includes the pixel of interest, i.e. $I(0,0)$ as highlighted in Fig. 3.1.1, for which the gradients are to be calculated. Note that the size of I_{sub} is $[m \times n]$ with $m = \Delta y_1 + \Delta y_2$ and $n = \Delta x_1 + \Delta x_2$, while the size of the operator E is $[n \times m]$.

For example, for simple forward finite differences, the image gradients for the central pixel with coordinates $(X, Z) = (0, 0)$ in Fig. 3.1.1 become:

$$\begin{bmatrix} I_X \\ I_Z \end{bmatrix} = \begin{bmatrix} \partial I/\partial X \\ \partial I/\partial Z \end{bmatrix} = \begin{bmatrix} I(1,0) - I(0,0) \\ I(0,1) - I(0,0) \end{bmatrix} \tag{3.1.2}$$

Thus, it yields with $(\Delta x_1, \Delta x_2) = (0, 1)$ and $(\Delta y_1, \Delta y_2) = (0, 0)$

$$I_X = \begin{bmatrix} -1 \\ 1 \end{bmatrix} \cdot \begin{bmatrix} I(0,0) & I(1,0) \end{bmatrix} \tag{3.1.3}$$

and with $(\Delta x_1, \Delta x_2) = (0, 0)$ and $(\Delta y_1, \Delta y_2) = (1, 0)$

$$I_Z = \begin{bmatrix} -1 & 1 \end{bmatrix} \cdot \begin{bmatrix} I(0,0) \\ I(0,1) \end{bmatrix} \tag{3.1.4}$$

The reader may note that the operator in Z-direction equals the transpose of the operator in X-direction. This basic example illustrates the general idea of edge detection and the relevance of the kernel. However, as reported by GONZALEZ AND WOODS (2018), this simple approach is suitable for application in orthogonal direction only while detection of diagonal edges requires higher-order, i.e. two-dimensional kernels.

3.1.3 2D KERNELS

GONZALEZ AND WOODS (2018) state that 3×3 kernels (applied to the pixel neighborhood as illustrated in Fig. 3.1.1) are preferable over 2×2 kernels as they include more information to be used for estimation of the edge direction. Such 3×3 operators have been presented by PREWITT (1970), SOBEL (1970) and SCHARR (2000). While the *Prewitt* operator applies a central differences method using the kernels

$$\begin{bmatrix} -1 & -1 & -1 \\ 0 & 0 & 0 \\ 1 & 1 & 1 \end{bmatrix} \quad \text{and} \quad \begin{bmatrix} -1 & 0 & 1 \\ -1 & 0 & 1 \\ -1 & 0 & 1 \end{bmatrix} \qquad \textit{(Prewitt)}$$

the *Sobel* and *Scharr* operators provide additional image smoothing by increasing the weight of the central location:

$$\begin{bmatrix} -1 & -2 & -1 \\ 0 & 0 & 0 \\ 1 & 2 & 1 \end{bmatrix} \quad \text{and} \quad \begin{bmatrix} -1 & 0 & 1 \\ -2 & 0 & 2 \\ -1 & 0 & 1 \end{bmatrix} \qquad \textit{(Sobel)}$$

$$\begin{bmatrix} -3 & -10 & -3 \\ 0 & 0 & 0 \\ 3 & 10 & 3 \end{bmatrix} \quad \text{and} \quad \begin{bmatrix} -3 & 0 & 3 \\ -10 & 0 & 10 \\ -3 & 0 & 3 \end{bmatrix} \qquad \textit{(Scharr)}$$

GONZALEZ AND WOODS (2018) point out that this feature is essential for noise reduction which could significantly affect edge detection otherwise (as stated earlier). In order to identify physical edges, which are not caused by image noise, image gradient vectors can be classified by their magnitude, which may be approximated by

$$M(X, Z) = |I_X| + |I_Z| \tag{3.1.5}$$

with sufficient accuracy. The direction of the gradient vector is given by:

$$\alpha(X,Z) = \arctan\left(\frac{I_Z(X,Z)}{I_X(X,Z)}\right) \tag{3.1.6}$$

Alternatively, the gradients in all eight possible directions (for a 3×3 operator) can be obtained by simply rotating the kernels and the direction of the gradient is given by the kernel with maximum response (SONKA ET AL., 2015), e.g. for a *Sobel* operator:

$$\begin{bmatrix} -1 & -2 & -1 \\ 0 & 0 & 0 \\ 1 & 2 & 1 \end{bmatrix} \ldots \circlearrowright \ldots \begin{bmatrix} 0 & -1 & -2 \\ 1 & 0 & -1 \\ 2 & 1 & 0 \end{bmatrix} \ldots \circlearrowright \ldots \begin{bmatrix} 1 & 0 & -1 \\ 2 & 0 & -2 \\ 1 & 0 & -1 \end{bmatrix} \ldots$$

It must be noted that with use of two-dimensional matrix convolution, the original kernels (as given above) may be extended to larger sizes, e.g. 7×7, 9×9 etc.. This step may be useful to improve the edge detector performance in case of local noise or low contrast.

3.1.4 IMAGE PREPROCESSING

3.1.4.1 GENERAL REMARKS

Edge detection methods oftentimes produce non-closed contour lines resulting from poor image quality due to e.g. insufficient contrast, non-uniform illumination or light reflections. Image preprocessing can significantly enhance the quality of extracted contour lines by closing the edges, in turn potentially at the cost of accuracy. Some selected image preprocessing techniques which may be applied for edge detection purposes are presented subsequently. Their physical effects on image textures are shown for a close-up of a high-speed image (see Fig. 3.1.2) showing the free-surface of a wave propagating over a horizontal plate (note that the water body is seeded with particles)[1].

[1]This example has been extracted from the FlowCV user manual. FlowCV is an open-source toolbox for computer vision applications in turbulent flows and has been developed by BUNG AND VALERO (2017). The toolbox is distributed under the GNU GPLv3 license and is freely available at https://github.com/FlowCV.

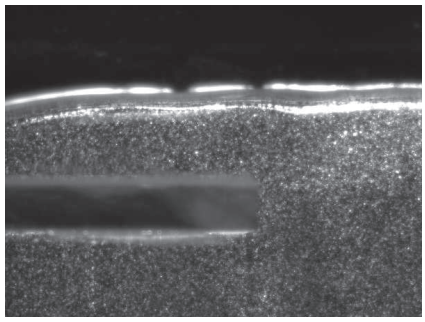

Figure 3.1.2: Original image from a high-speed video of a bore propagation over a submerged plate (close-up of surface region for better illustration of preprocessing effects)

3.1.4.2 BACKGROUND SUBTRACTION

Background subtraction can be useful to remove static contents, i.e. if the images contain some undesired reflections or obstacles, which should not be identified as contours. However, proper illumination and image setup is strongly recommended to avoid detecting spurious edges. For background subtraction, at least two input images are required. A pixel intensity difference threshold needs to be defined, below which the corresponding image coordinate is considered to be static. Note that background subtraction results are affected by particle seeding (Fig. 3.1.3).

Figure 3.1.3: Preprocessed image after background subtraction with 2 px kernel size

3.1.4.3 GAMMA CORRECTION

Gamma correction may intensify reflections at the free water surface and thus assist recognizing the free-surface line. This reflection can be easily separated from the background if a dark rear wall is chosen. Gamma correction can be easily performed by selecting a correction value γ and exponentially scaling of the pixel intensity I. If a 8-bit grayscale image with a maximum pixel intensity of 255 is considered, the

correction may be conducted by:

$$I_{\text{corr}} = 255 \cdot \left(\frac{I}{255}\right)^{1/\gamma} \tag{3.1.7}$$

Figure 3.1.4 illustrates the example image processed with $\gamma = 4.0$.

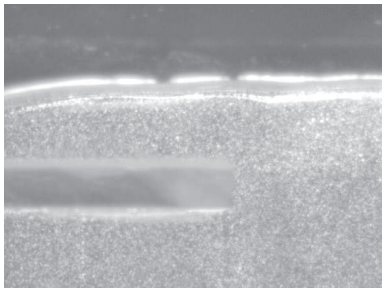

Figure 3.1.4: Preprocessed image after gamma correction with $\gamma = 4.0$

3.1.4.4 DILATION AND EROSION

Dilation and erosion are so-called morphological operations in image processing. These steps may be useful when the brightened free surface does not appear as a closed layer (with some darker gaps in between).

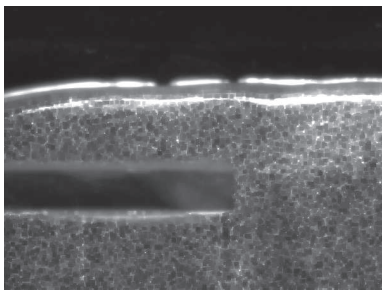

Figure 3.1.5: Preprocessed image after dilation and erosion with 5 px kernel size.

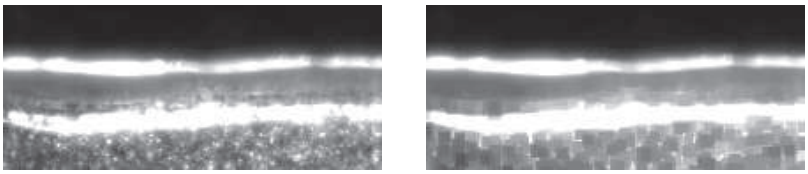

(A) Original image

(B) Image after dilation and erosion (note the closing of the reflecting areas)

Figure 3.1.6: Close-up of preprocessed image after dilation and erosion with 5 px kernel size compared to the original image

Typically, dilation is performed in a first step, followed by an erosion of the brightened areas. Both steps require a certain kernel size, i.e. the length over which each step is conducted. The results from these morphological operations are shown in Fig. 3.1.5. A close-up of the free surface is shown in Fig. 3.1.6.

3.1.4.5 HISTOGRAM EQUALIZATION

Histogram equalization can be performed to improve contrast[2]. This operation basically performs a stretching of the pixel intensity histogram. Besides a standard method (considering the global contrast of the image), a Contrast Limited Adaptive Histogram Equalization (CLAHE, PIZER ET AL. (1987)) is commonly applied. The latter divides the image into small blocks of a predefined size, the histograms of which are then equalized. CLAHE should be preferred if strong intensity variations are noticed within a given image. Both methods are compared in Fig. 3.1.7.

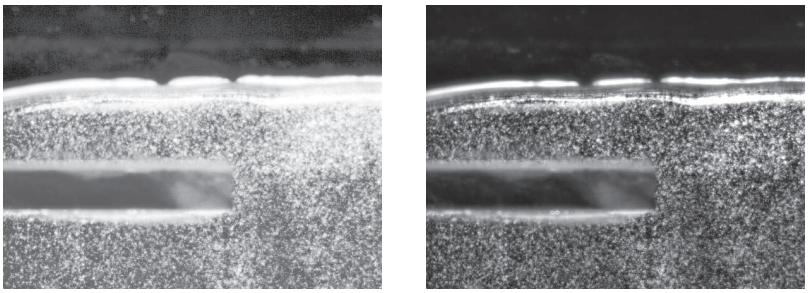

(A) Standard histogram equalization

(B) Contrast Limited Adaptive Histogram Equalization (CLAHE)

Figure 3.1.7: Preprocessed image after histogram equalization

More information on histogram equalization can be found in Section 6.5.3.1.

3.1.4.6 IMAGE FILTERING

In order to close gaps within detected edges, lowpass filters may be applied which typically result in image blurring. One well-known filter method is the so-called Gaussian filter. Wiener filter, in contrary, is a restoring filter method. All filters require the specification of a window size (filter length). Resulting images for above-mentioned, exemplary filter methods are shown in Fig. 3.1.8.

[2]The reader is referred to Section 6.5 and to GONZALEZ ET AL. (2009) for more details on histogram equalization and image filtering.

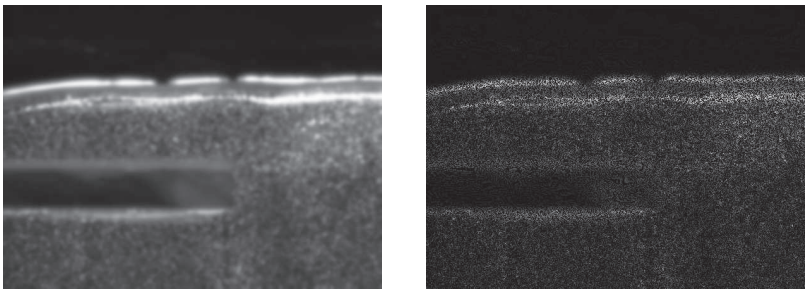

(A) Gaussian filter **(B)** Wiener filter

Figure 3.1.8: Preprocessed image after filtering with 15 px filter window size

3.1.4.7 IMAGE BINARIZATION

Image binarization may be used as a last step in order to obtain a sharp interface (edge) between air and water. Image binarization results in black and white images. Figure 3.1.9 provides an example obtained with the Otsu method (OTSU, 1979). The reader may note the closed edge at the surface which however, is affected by some inaccuracy compared to the original image.

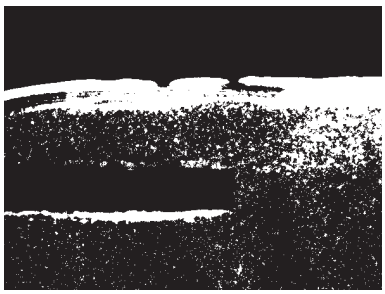

Figure 3.1.9: Preprocessed image after Otsu's binarization

3.1.4.8 EXEMPLARY RESULT

The iterative choice of settings (trial and error) for all preprocessing steps may help to improve the overall results. Fig. 3.1.10 shows the results of edge detection applied to the free water surface in the above given video frame in full resolution (no cropping performed). The time series of the water surface elevation at the end of the submerged plate (x = 830 px) is illustrated for 150 frames in Fig. 3.1.11. This result has been obtained for the following settings:

- Gamma correction with $\gamma = 4.0$,
- dilation and erosion (after gamma correction) with a kernel size of 4 px,
- Sobel edge detection in the Z-direction with a kernel size of 7 px,

- binarization of edges with an intensity threshold of 30,
- dilation and erosion of edges (before contour extraction) with a kernel size of 5 px.

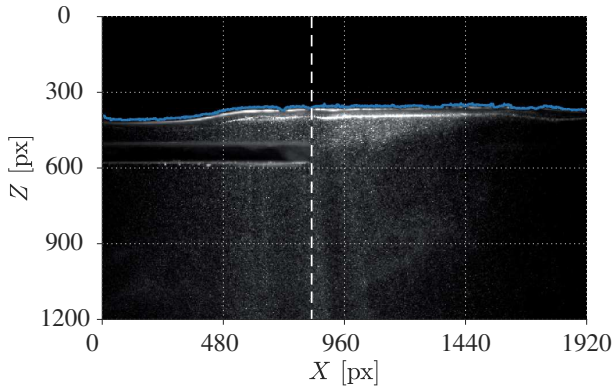

Figure 3.1.10: Resulting instantaneous water surface line for the above listed settings

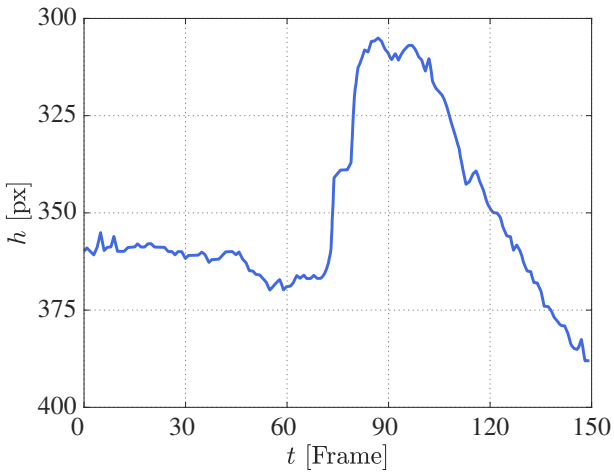

Figure 3.1.11: Resulting water surface time series at x = 830 px (location indicated as a white dashed line in Fig. 3.1.10)

3.2 NON-INTRUSIVE DETECTION OF AIR-WATER SURFACE ROUGHNESS IN SELF-AERATED CHUTE FLOWS

Author: Daniel B. Bung
Journal: Journal of Hydraulic Research 51(3)
Year: 2013

Abstract: Stepped spillways are known to enhance the energy dissipation potential when compared with common smooth invert chutes. In the skimming flow regime, the self-aerated flow becomes more chaotic and surface waves (referred to as air-water surface roughness) are enhanced when the discharge decreases. In this study, experiments on smooth invert and stepped chutes models with a slope of 1 : 2 were conducted to characterize this surface roughness by the use of a high-speed camera and ultrasonic sensor. It was found that the amount of entrapped air – at the water level where the air concentration is 90 % – is reduced when a stepped spillway is considered. With decrease in step height (and on smooth invert chutes), entrapped air became more relevant. Wave heights increased with increase in step height and exceeded significantly the characteristic water level with 90 % air concentration which was detected by a conductivity probe. A wide range of wave frequencies indicated the turbulent structure of stepped spillway flows.

Keywords: Air-water flow, high-speed camera, physical modeling, spillways, surface waves, ultrasonic sensor

3.2.1 INTRODUCTION

Spillways are open or closed channels located at dams that convey water from upstream to downstream during flood events. In order to protect the dams, a large discharge capacity may be required; such high discharge capacity can be achieved by high flow velocity operating steep chutes. Due to growth of the turbulent boundary layer at the crest, a critical point can be found (assumed that the structure is high enough) where self-aeration of the flow occurs. At this point, the turbulent boundary layer reaches the water surface and vertical turbulent velocity components overcome the resistance due to surface tension and bubble rise velocity (ERVINE AND FALVEY, 1987). Once the aeration process sets in, turbulence transports air bubbles along the whole water body (STRAUB AND ANDERSON, 1958; RAO ET AL., 1970). Quasi-uniform flow conditions are found on high structures when the time-averaged flow depth, air content and flow velocity remain unvaried in flow direction (WOOD, 1983; BUNG, 2011A). Two basic types of spillways are generally found in dam engineering, i.e. smooth invert and stepped chutes. In case of stepped chutes, the step-induced macro-roughness leads to a reduction of the length of the non-aerated region, that is, self-aeration occurs upstream of the corresponding location for smooth invert chutes, as turbulence is strongly enhanced down the chute. A number

of fundamental studies on stepped spillway flows have been conducted in the past (e.g. CHANSON, 1993; RUFF AND FRIZELL, 1994; MATOS, 2000; CHANSON AND TOOMBES, 2002; BOES AND HAGER, 2003). The self-aeration process on stepped spillways has been described in-depth by PFISTER AND HAGER (2011). Accordingly, the growing turbulent boundary layer involves a roughening of the water surface and generation of air troughs. Bottom aeration has not set in at this location, but is induced by the occasional expansion of pronounced air troughs impinging the step surface. The air troughs are then separated from the water surface due to the velocity gradient and air bubbles are transported in the upper and lower step and detrained into the black-water flow (PFISTER AND HAGER, 2011).

For engineering purposes, the air-water mixture body may be described as a continuum where the idealized surface is usually referred to as h_{90}, i.e. the elevation with an air concentration C of 90 %. As observed by KILLEN (1968) on smooth invert chutes, a continuous water surface can be found in air-water mixtures, but a significant distortion ("air-water surface roughness") needs to be considered. Similar findings were reported by PEGRAM ET AL. (1999) for stepped spillways. According to RAO AND KOBUS (1975), this distortion leads to a local inception of air bubbles as air is drawn into the flow, broken into bubbles and then released. WILHELMS AND GULLIVER (2005) differentiated between entrapped air (air content between surface waves) and entrained air (air bubbles in water body). As the turbulent flow at the spillway crest exhibits a roughened water surface, the authors stated that the water surface characteristics are directly reflected in the turbulence generated by the spillway. ANDRÉ (2004) stated that h_{90} is located somewhere between the surface wave troughs and crests for a chute angle of $\phi = 30^\circ$. PFISTER AND HAGER (2011) reported that the maximum trough extension of surface waves on stepped spillways with $\phi = 50^\circ$ reaches down to approximately $0.4h_{90} \leqslant z \leqslant 0.5h_{90}$ in uniform flow region. TOOMBES AND CHANSON (2007) developed an empiric surface wave model based on the idealization of sinusoidal random waves. The authors stated that the presence of surface waves has no influence on air concentration profiles, but has significant effects on bubble count rates and chord length distributions. LEANDRO ET AL. (2012) presented water surface and air concentration time series which were observed in a hydraulic jump experiment and obtained by an imaging procedure. A strong surface fluctuation was found although the sample rate was relatively small with 5 fps. The authors concluded that such techniques may provide instantaneous information about flow characteristics within the total flow field and respective time series and that a frequency analysis may be conducted when a high-speed camera is used. Earlier studies on hydraulic jumps also demonstrated the applicability of optical, non-intrusive methods (e.g. MOSSA AND TOLVE, 1998).

In the current study, first results obtained by experiments on a smooth invert and a stepped spillway model with ϕ = 26.6° will be presented with the objective to (i) test the applicability of non-intrusive measuring techniques in highly aerated chute

flows, (ii) to qualitatively compare the surface roughness on smooth invert and stepped chutes and (iii) to describe the wave heights which are important for hydraulic design purposes. The surface wave characteristics were analyzed with both, a high-speed camera and an ultrasonic sensor, in the uniform flow region. Air concentrations were measured with an intrusive conductivity probe to localize the characteristic water levels. Stepped spillway tests were limited to the skimming flow regime setting in for high discharges where the water flows down as a coherent stream above the pseudo-bottom formed by the step edges.

3.2.2 METHODOLOGY

3.2.2.1 EXPERIMENTAL SET-UP

Experiments were carried out on a physical model which was part of a closed water circuit. Water was pumped into an open head tank, while the discharge was regulated by a flap valve and checked with an inductive flow meter. Small tubes in the inlet channel distributed and calmed the flow down before being conveyed. The model had a total drop height of 2.34 m, a chute width of 30 cm and a chute angle of $\phi = 26.6^\circ$. With two different step heights ($s = 3$ cm and $s = 6$ cm) and three specific discharges ($q = 0.07$ m^2/s, 0.09 m^2/s and 0.11 m^2/s), skimming flow regime was found in all the examined stepped spillway model configurations (see BUNG, 2011A). In order to compare the surface wave properties on stepped spillways with those on classical smooth invert spillways, the self-aerated flow on the latter type of structure with identical slope was investigated by attaching a smooth invert to the above-described model set-up (model results subsequently presented by indicating $s = 0$ cm). The chute's PVC (polyvinyl chloride) bottom was equipped with additional micro-roughness elements in the form of an 8 mm high burling installed in a staggered arrangement (Fig. 3.2.1(A)). The burling increased the turbulent boundary layer growth and thus enhanced the self-aeration process which primarily depends on the bottom roughness on smooth spillways (WOOD ET AL., 1983). This high burling was chosen instead of a smoother material (e.g. sand paper) to force the self-aeration process to set in early and to guarantee quasi-uniform, fully-aerated flow conditions near the spillway toe. Although scaling to prototype dimensions becomes unfeasible due to the artificial roughness, the qualitative flow characteristics are unaffected by this model set-up (BUNG, 2010).

Significant dimensionless numbers, i.e. the Froude number F, Reynolds number R and Weber number W were > 5, > $2.3 \cdot 10^5$ and > 100, respectively, for all experiments. It must be noted that, with obtained F and R, W should be > 110 to avoid scale effects regarding the air bubble transport according to PFISTER AND CHANSON (2012). As the Weber number was close to the required value and the study's focus was on the surface waves, it is believed that scale effects are negligible.

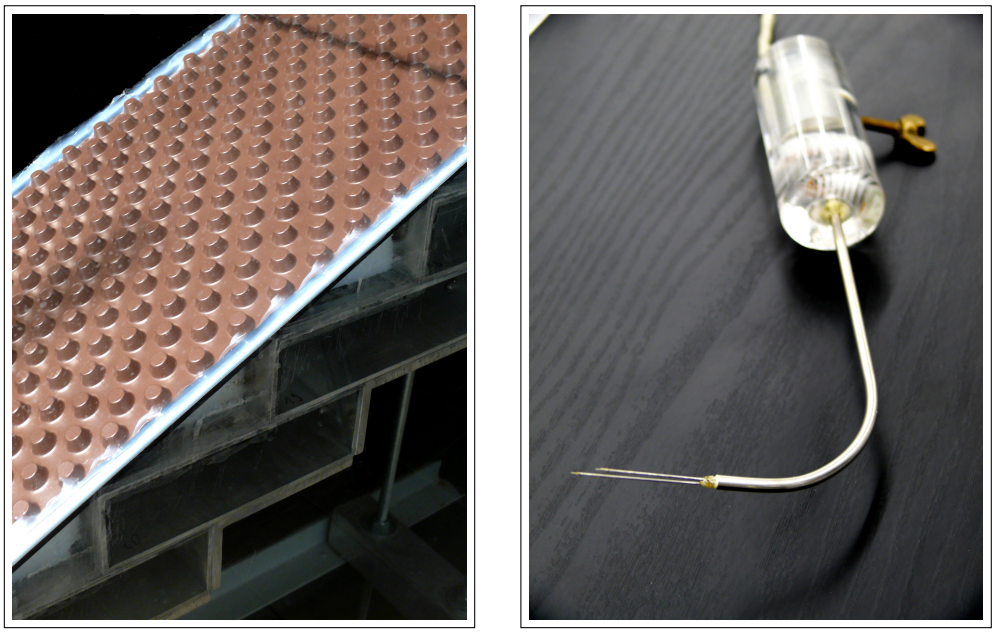

(A) Smooth invert chute model with additional micro-roughness elements in staggered arrangement

(B) Conductivity probe for intrusive measuring of air-water flow properties (note the two tips allow for the determination of flow velocities by cross-correlation of both signals)

Figure 3.2.1: Experimental set-up

3.2.2.2 INTRUSIVE MEASURING OF AIR-WATER FLOW PROPERTIES

Measurements of air-water flow properties were conducted for all model tests by means of a conductivity probe with 130 μm tip diameter (manufactured at IWW, RWTH Aachen, Fig. 3.2.1(B)). Depending on the surrounding medium (i.e. water or air), a high or low voltage was sampled for 25 s with a frequency of 25 kHz. Digitizing the raw signal on the basis of a combined double threshold and gradient method (BUNG, 2012), the air content could be easily derived from the total sample time above the threshold. Exact positioning of the probe was achieved by a two-dimensional linear computerized numerical control (CNC) system.

3.2.3 NON-INTRUSIVE DETECTION OF THE AIR-WATER MIXTURE SURFACE

3.2.3.1 HIGH-SPEED CAMERA

The flow field in uniform flow region was captured with a high-speed camera (sample rate 1220 fps, resolution 256 $\times$ 256 pixel) for all model configurations. In order to enhance the contrast, the backside of the flume was equipped with a black PVC wall.

The flow was illuminated with white light from halogen spots. After capturing the movies, the surface of the air-water mixture was numerically extracted by means of an image processing technique (Fig. 3.2.2) consisting of

1. highlighting of the air-water mixture body (achieved by enhancing the brightness and contrast of the raw images) and removing of spurious droplets,
2. numerical detection of edges and finding of surface edge,
3. rotation to a horizontal bottom and scaling from pixel to model dimensions (cm).

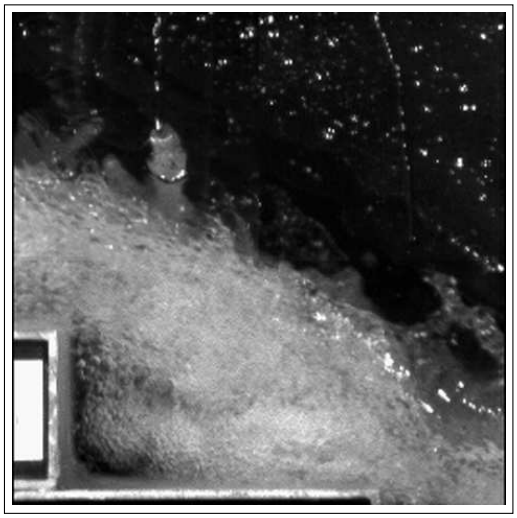

(A) Step 0: raw image captured by camera

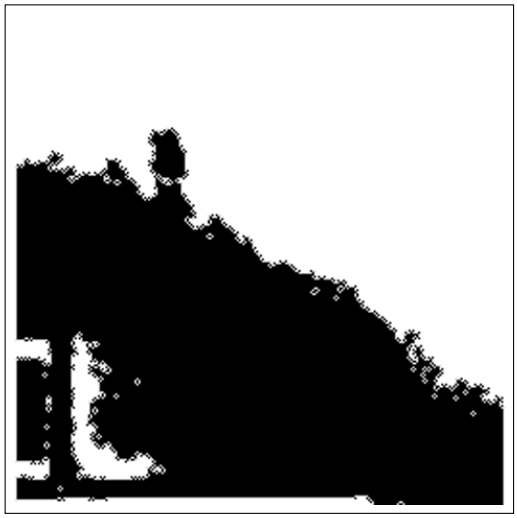

(B) Step 1: highlighting of the air-water mixture body and removing of spurious droplets

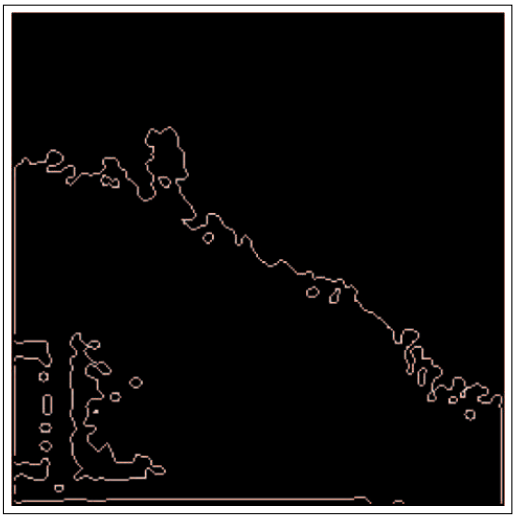

(C) Step 2: edge detection

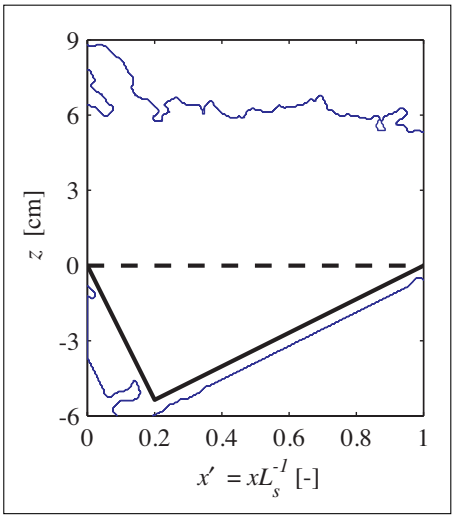

(D) Step 3: scaling from pixel dimensions to model dimensions and rotation

Figure 3.2.2: Exemplary image processing for surface extraction

This is an **Author's Accepted Manuscript** of an article published by Taylor & Francis Group in Journal of Hydraulic Research on 24 April 2013, available online: HTTPS://WWW.TANDFONLINE.COM/DOI/ABS/10.1080/00221686.2013.777373

The results will be compared with the conductivity probe measurements subsequently and will give further information about the air-water surface roughness. Due to a limited storage capacity, the sampling time was chosen as 1 s. In order to validate the results, reproduction tests were carried out. It is worth mentioning that the conductivity probe's results differed in the range of only ± 5 % when the sample time was reduced from 25 to 1 s.

It must be acknowledged that sidewall effects cannot be avoided but are assumed to be small. KRAMER (2004) presented detailed results on sidewall effects. Accordingly, air concentration distributions were nearly unaffected in the uniform flow region, while flow velocities were reduced in the range of ~10 %. In the current study, water droplets, which have been ejected from the water body or which were attached to the sidewall, were neglected by the above-described method. The number of detected waves in the 30 cm wide channel is higher than in a well-defined plane. But due to the small channel width, deviations are believed to be rather small.

3.2.4 ULTRASONIC SENSOR

An ultrasonic sensor (measuring range: 60 - 350 mm, resolution: 0.18 mm) was used for comparison of the high-speed data. The acoustic displacement measurements were limited to the stepped spillway configurations. During the measurements, the ultrasonic sensor was approximately 15 cm above the air-water surface. Data were sampled for 60 s with 30 Hz. The recorded signal was disturbed due to surface waves and ejected droplets from the air-water mixture. An unknown penetration depth of the acoustic beam into the air-water mixture needs to be considered (MURZYN AND CHANSON, 2009A) and the acoustic beam may not be reflected exactly back to the receiver in the case of very steep surface waves. In this study, raw data were smoothed by the use of a moving average filter. Evident measuring errors (outliers) were identified and eliminated by setting a threshold defined as the mean value $\pm$ three times the standard deviation of the raw signal. Please note that the influence of these measuring inaccuracies was found to be negligible as the number of detected outliers was rather small.

3.2.5 RESULTS

3.2.5.1 HIGH-SPEED CAMERA

Extracted surface wave time series for $q = 0.07$ m^2/s and 0.11 m^2/s are illustrated in Fig. 3.2.3 and compared with the characteristic flow depths h_{75}, h_{90} and h_{99} where C is 75, 90 and 99 %, respectively, measured with the use of the conductivity probe in the channel centerline (where sidewall effects do not occur) as an installation of the probe directly at the wall was not possible. For stepped spillway configurations, the results

obtained at step edges are given.

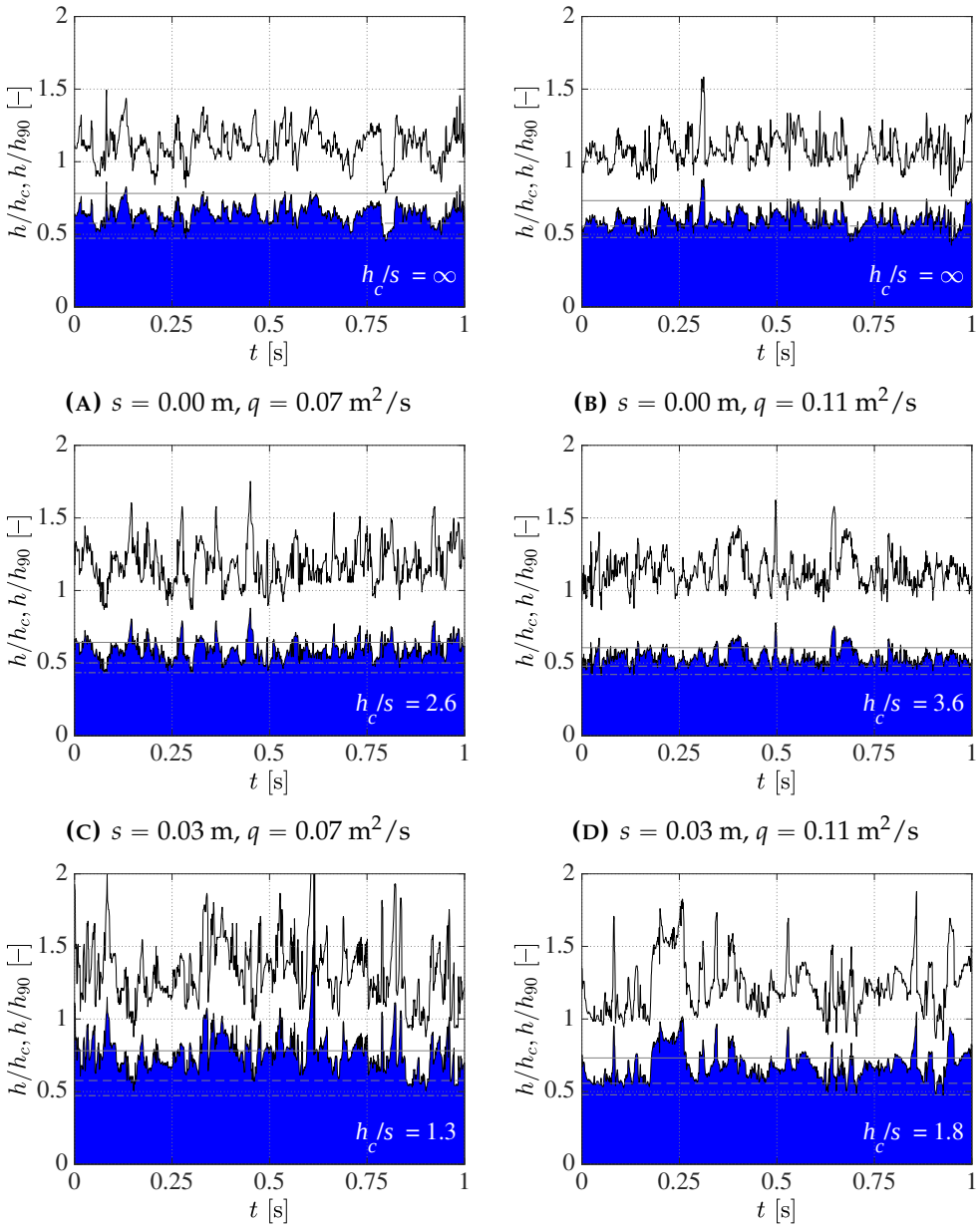

(A) $s = 0.00$ m, $q = 0.07$ m^2/s **(B)** $s = 0.00$ m, $q = 0.11$ m^2/s

(C) $s = 0.03$ m, $q = 0.07$ m^2/s **(D)** $s = 0.03$ m, $q = 0.11$ m^2/s

(E) $s = 0.06$ m, $q = 0.07$ m^2/s **(F)** $s = 0.06$ m, $q = 0.11$ m^2/s

Figure 3.2.3: Surface wave characteristics in the uniform flow region detected by a high-speed camera at step edges (sample rate 1220 fps, sample time 1 s) for $q = 0.07$ m^2/s (left) and $q = 0.11$ m^2/s (right), solid (blue) area: h/h_c; black line: h/h_{90}; grey chain-dotted line: h_{75}/h_c; grey dashed line: h_{90}/h_c and grey solid line: h_{99}/h_c

Figure 3.2.3 shows that the maximum trough extension of the surface waves can be found at the water depth h_{75} for all illustrated time series. The height of the continuous air-water layer below the surface waves found in this study thus confirms the order of the effective homogeneous flow depth given by ANDRÉ (2004) for stepped spillways ($C < 70 - 75$ %) and the findings presented by CAIN (1978) for

smooth invert chutes ($C < 70$ %). Yet, even the characteristic water depth h_{90}, usually referred to as the idealized air-water mixture surface, compares well with the wave troughs. As a consequence, the time-averaged amount of entrapped air at h_{90} (determined by the time where $h < h_{90}$) is likewise small but found to increase with increasing h_c/s (up to 23 % for $s = 0$ cm, 12 % for $s = 3$ cm, 8 % for $s = 6$ cm), where h_c is the critical water depth. It must be noted that the artificial roughness may lead to model effects, but the qualitative result comparing the different set-ups is assumed to be unaffected. On the other hand, the presented camera technique tends to underestimate the entrapped air as a well-defined measuring plane is not given. Low wave troughs in the centerline (where air concentration measurements were conducted) may thus be covered by higher wave troughs near the acrylic glass wall, but this effect is assumed to be small due to the narrow model chute. More studies with different set-ups (bottom roughness, chute width and camera) are needed to evaluate these findings.

The maximum wave height rarely exceeds the water depth h_{99} for $h_c/s > 3.6$. For lower h_c/s, the number of surface waves exceeding this characteristic water depth becomes larger. A higher flow depth than h_{99} must thus be taken into account in the design of stepped spillways operating with relatively low discharges. Maximum wave heights roughly correspond to $2h_{90}$, similar results were presented by MEIRELES ET AL. (2007) for steeply sloping stepped chutes. Surface wave heights are generally lower on smooth invert chutes than on stepped chutes. For a stepped spillway, the wave heights increase for low h_c/s and thus with increasing turbulence.

The results presented herein hypothesize that the common continuum concept with h_{90} as idealized air-water mixture surface does not significantly differ from other concepts differentiating between entrapped and entrained air. The observation by PFISTER AND HAGER (2011) that the maximum trough extension reaches down to roughly $0.5h_{90}$ on steep stepped spillways with $\phi = 50^\circ$ cannot be confirmed for milder slopes in spite of similar ranges of h_c/s. This finding may indicate that the generally known increase in the mean air concentration on steeper slopes, when compared with moderately sloped chutes, may be primarily a result of more entrapped air pockets.

It must be noted that the presented imaging technique allows determining surface waves higher than h_{99}. In this case, the surface wave must transport a high amount of entrained air to justify a total air concentration of 99 % measured by the conductivity probe. Other procedures are based on interpreting h_{99} or user-defined pixel grey values to represent the air-water surface level (e.g. LEANDRO ET AL., 2012) and may thus ignore higher elevations.

3.2.5.2 ULTRASONIC SENSOR

Figure 3.2.4 illustrates the ultrasonic signals which have been measured on the stepped spillway models at the step edges in the uniform flow region. The characteristic of a high surface roughness – which was described above – is again observed. For the configurations with higher steps or lower h_c/s, respectively, the more chaotic flow regime becomes manifest in the stronger surface fluctuations. The maximum surface elevation is here limited to ~1.5h_{90} (Fig. 3.2.4(C)).

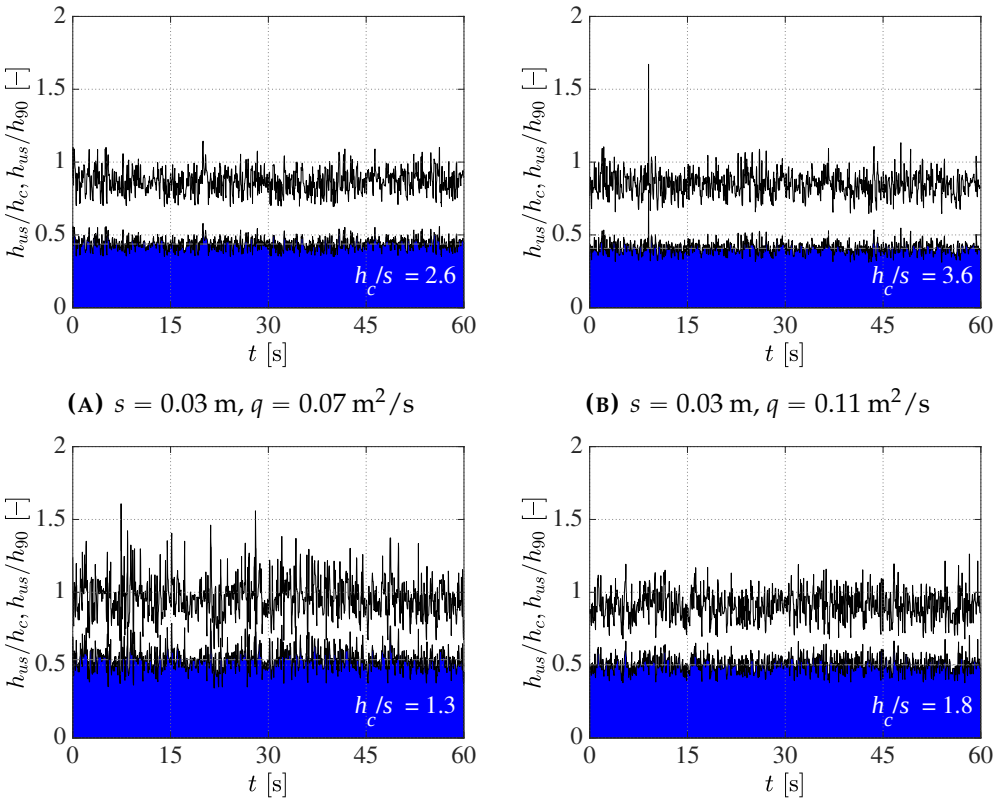

(A) $s = 0.03$ m, $q = 0.07$ m^2/s **(B)** $s = 0.03$ m, $q = 0.11$ m^2/s

(C) $s = 0.06$ m, $q = 0.07$ m^2/s **(D)** $s = 0.06$ m, $q = 0.11$ m^2/s

Figure 3.2.4: Ultrasonic signals in the uniform flow region at step edges (sample rate 30 Hz, sample time 60 s) for $q = 0.07$ m^2/s (left) and $q = 0.11$ m^2/s (right), solid (blue) area: h_{us}/h_c; black line: h_{us}/h_{90}; grey dashed line: $h_{us,mean}/h_c$, note the obvious outlier in (B) which was not eliminated by the applied filtering method

The reason for the difference compared with the high-speed camera results are caused by a generally lower flow depth h_{us} detected by the use of the ultrasonic sensor. In detail, the mean flow depth $h_{us,mean}$ roughly corresponds to a water level close to h_{75} and thus to the maximum trough extension of the surface waves. As h_{us} is equally distributed around $h_{us,mean}$, the acoustic signal must penetrate the air-water mixture to an extent of the same order as the surface wave heights. Although the sampling frequency could not be varied within this study, it is assumed that it affects

the penetration depth. The sensor diameter is believed to have an influence as well as the distance between the sensor and the surface influencing the present diameter of the expanding ultrasonic beam cone. Due to the strongly limited measuring range of only 29 cm, a variation of the beam diameter could not be performed. The minimum water depths found in these experiments must thus be considered to be governed by the applied sensor.

A certain penetration depth of ultrasonic sensors in bubbly flows was also observed by MURZYN AND CHANSON (2009A) when investigating hydraulic jumps. The authors stated that the time-averaged value corresponds to an elevation within the upper free-surface region (i.e. above the air-water shear layer) where the air concentration is generally > 20 %, rapidly reaching 90 % and more. CHACHEREAU AND CHANSON (2011) complement this result finding that $h_{us,mean}$ roughly corresponds to the clear water depth h_w:

$$h_w = \int_0^{h_{90}} (1 - C)\,\mathrm{d}z \tag{3.2.1}$$

In the present study, deviations in the range from 14 to 37 % between h_w and $h_{us,mean}$ were observed.

3.2.6 SURFACE WAVE FREQUENCIES

Significant surface wave frequencies can be determined from the water level signals. Figure 3.2.5 illustrates the normalized power spectral density PSD' = PSD/max(PSD) for the stepped spillway configurations.

Analysis of the high-speed camera results measured with 1220 fps indicates that significant frequencies range from 1 to 20 Hz. For $q = 0.11$ m^2/s, the highest PSD' is found for low frequencies, while for $q = 0.07$ m^2/s single peaks in the range of 20 Hz occur. Generally, the wide range of frequencies emphasizes the chaotic nature of stepped spillway flow. For comparison, the significant frequencies obtained by the ultrasonic sensor are included. The sample rate of 30 Hz is too low to detect the significant higher frequencies identified by the high-speed camera.

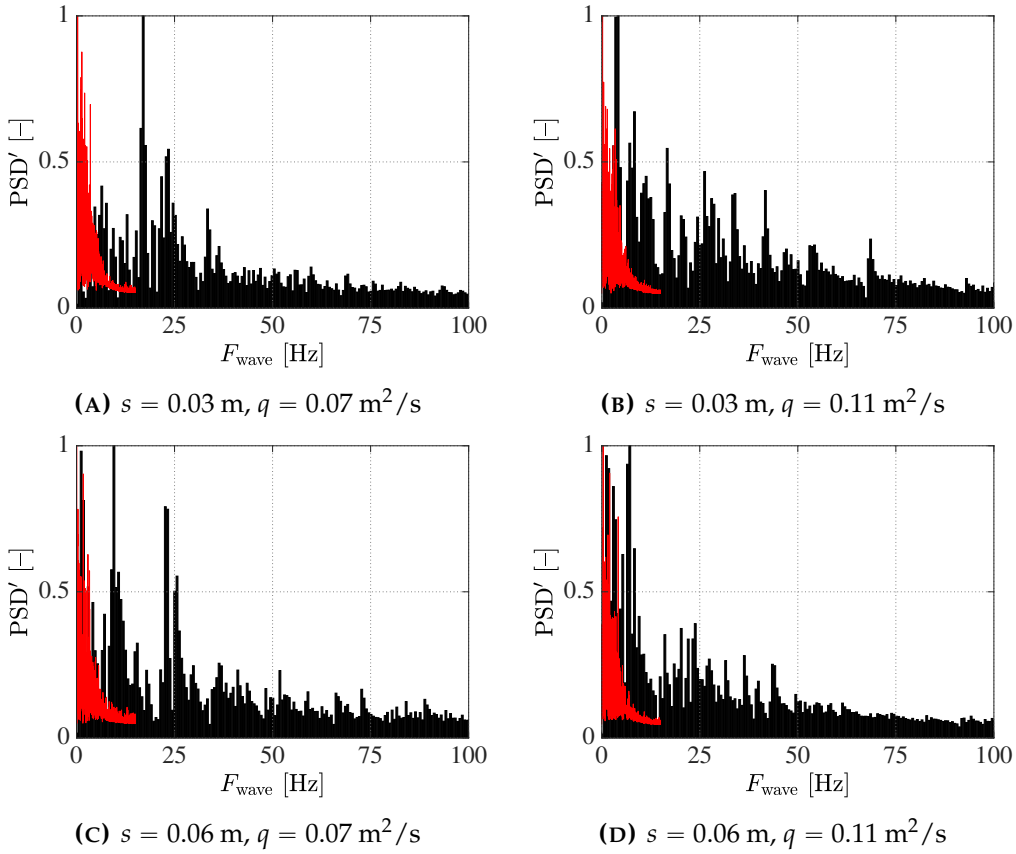

(A) $s = 0.03$ m, $q = 0.07$ m^2/s **(B)** $s = 0.03$ m, $q = 0.11$ m^2/s

(C) $s = 0.06$ m, $q = 0.07$ m^2/s **(D)** $s = 0.06$ m, $q = 0.11$ m^2/s

Figure 3.2.5: Normalized power spectral density PSD′ = PSD/max(PSD) of significant surface wave frequencies F_{wave} determined by the high-speed camera (black bars) and ultrasonic sensor (red bars) for all stepped spillway configurations in the uniform flow region

3.2.7 CONCLUSIONS

A comparative study focusing on the air-water surface roughness in self-aerated chute flows was presented. The applicability of non-intrusive measuring techniques, i.e. a high-speed camera and an ultrasonic sensor, was demonstrated. When comparing the air concentration data obtained by a conductivity probe with high-speed movies and considering the continuum concept with h_{90} as the idealized surface, the amount of air entrapped between the surface waves was found to be small on investigated stepped spillways with moderate slopes. With decreasing step height (and on smooth invert chutes), entrapped air becomes more and more relevant. Surface wave heights are lower on smooth invert chutes than on stepped chutes as shown by both applied methods. In the case of stepped spillways, the wave heights increase for low h_c/s and may then significantly exceed the characteristic flow depth h_{99}. Even if stepped spillways are designed for high design discharges, structures must properly work for lower discharges as well and the transition should be considered by the designing engineers. Besides the evaluation of flow depths, the

extracted time series may be used to characterize the surface waves in terms of wave frequency. A frequency analysis indicated a wide range of frequencies, particularly for low h_c/s, which may be caused by the high degree of turbulence. For the detection of these frequencies, a sufficient high sample rate as provided by the high-speed camera is required. As the sample time of the high-speed camera could not be extended due to limited storage capacity, future investigations with larger memory are required to validate the presented findings. Besides the extension of the sample time, the camera's resolution and the channel width need to be varied to detect possible influences on the results.

CHAPTER 4

3D FREE-SURFACE RECONSTRUCTION

4.1 INTRODUCTION TO DEPTH CAMERAS

4.1.1 GENERAL REMARKS

Depth cameras are sensors providing information on the distance between the camera and observed features. Nowadays, consumer-grade sensors with different working principles are available. Generally, depth sensing may be differentiated between passive and active methods (ZOLLHÖFER, 2019). While passive depth sensing techniques aim to reconstruct 3D features from the original, non-modified scene, active depth sensing techniques typically use additional light projected on the scene. Furthermore, depending on the number of cameras, monoscopic (one camera) and stereoscopic (two cameras) devices are available. A common technology using a monoscopic approach is LiDAR (Light Detection and Ranging), based on the time-of-flight principle. Stereoscopic systems try to match physical image features (passive system) or, in order to enhance the number of features and improve the results, to estimate the disparity from a detected light to its original projection (active stereo system). It is noteworthy that light projection methods also allow for depth ranging using a single camera. It is then referred to as structured light methods. Infrared domain is typically chosen for light projections to not interfer with the scene of interest. Fig. 4.1.1 presents a classification of available depth sensing techniques.

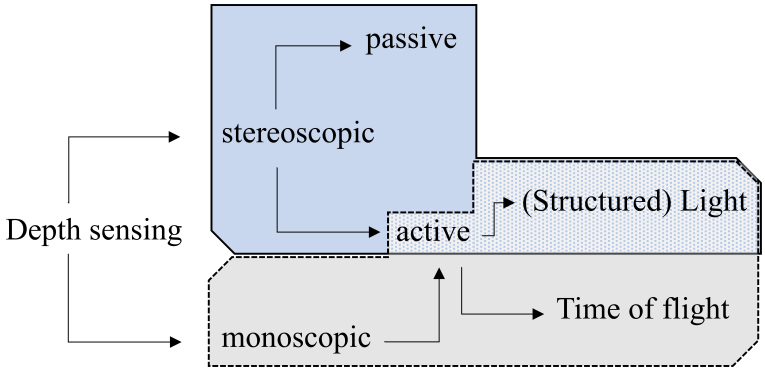

Figure 4.1.1: Classification of depth sensing techniques

It must be noted that none of the subsequently presented techniques is applicable to transparent surfaces. In order to measure free water surfaces, a sufficient texture is mandatory. Such texture may be obtained by adding surface tracers (with limited spatial resolution) or by dyeing the water in low-turbulent flows. In white waters, i.e. highly-aerated flows, the required texture is given by the rough surface (as discussed in Section 3.2).

4.1.2 TIME OF FLIGHT

Time-of-flight cameras measure the travel time of an emitted light signal which is reflected at a surface and captured by the image sensor. The travel time and thus, the distance, are proportional to the speed of light (i.e. $c \approx 3 \cdot 10^8$ m/s). Accordingly, extremely fast sensors would be required to measure distances with sufficient accuracy based on a single light pulse. Alternatively, the travel time Δt can be determined by the phase shift between a modulated illumination (typically sinusoidal or square wave) and its reflection (BRASINGTON, 2017):

$$\Delta t = \left(\frac{\varphi}{2\pi} + n\right) \cdot \frac{1}{f} \tag{4.1.1}$$

with φ the phase angle, n the integer number of wavelengths and f the modulation frequency.

LI (2014) discusses different techniques of measuring electrical charges by sampling every pixel by

- using two sampling windows which are out-of-phase to the reflected light or
- taking four samples per measurement with 90 degrees phase shifts.

To avoid aliasing at a critical distance, which depends on the modulation frequency, multiple-frequency techniques may be considered.

The time-of-flight method has been proven to be applicable for most complex flows, i.e. aerated stepped spillway flows and hydraulic jumps, respectively, as demonstrated by KRAMER ET AL. (2019A) and MONTANO AND FELDER (2020) using a two-dimensional LIDAR system. Time-of-flight sensors are, however, susceptible to other light sources, impeding the use in outdoor environments.

4.1.3 STRUCTURED LIGHT

Structured-light cameras illuminate the scene with a defined coded pattern. This pattern is subject to distortion depending on the shape of an observed obstacle or its distance to the camera. The disparity between the original and observed patterns is

correlated to the distance to a particular pixel. The depth is then obtained by triangulation between the lense, the projector and the observed surface point (GIANCOLA ET AL., 2018). For this purpose, the distance between the lens and projector, i.e. the so-called baseline, must be known. Different spatial distributions may be considered, e.g. pseudo-random, binary, trapezoidal or sinusoidal phase codification (BELL ET AL., 2016).

Codification methods have different resolution and perform differently depending on noise (which may be caused by surrounding light sources) and shape of the observed obstacle. Accuracy also decreases with increasing distance. To increase the accuracy of a single depth frame, successive projections can be employed (LI, 2014). However, in this case, the achievable frame rate and thus the applicability of structured-light methods to unsteady (or even highly turbulent) motions are limited.

4.1.4 STEREO VISION

Stereo vision methods use two cameras to capture a scene from different perspectives. Disparity between both images is obtained by matching both images. Similar to the structured-light sensors, both cameras must have a known baseline to determine the distance by triangulation:

$$D = \frac{Bf}{d} \tag{4.1.2}$$

where D the distance, B the camera baseline, f the focal length, $d = x_r - x_l$ the disparity, x_l and x_r the locations of the observed obstacle on the left and right camera sensor (see Fig. 4.1.2).

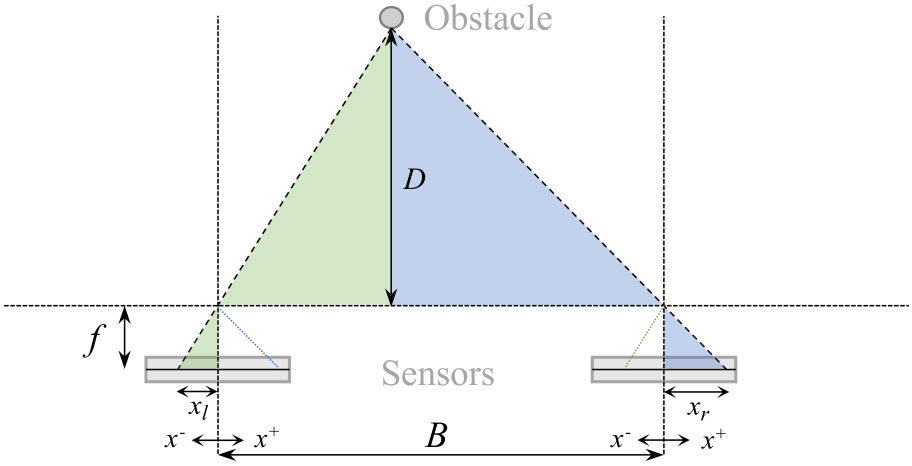

Figure 4.1.2: Triangulation in stereo vision applications (note that $x_l < 0$ in this illustration)

Apparently, the challenge in stereo vision is to identify sufficient matches of image features in a reasonable computation time (LI, 2014; GIANCOLA ET AL., 2018). This is the so-called correspondence problem which is commonly solved by

- *intensity-based* (also known as *area-based)* techniques, i.e. cross-correlation of pixel intensity distributions in small interrogation windows[1] or least-squares matching (LMS);
- *feature-based* techniques, i.e. extraction of image features, such as edges or corners[2].

A detailed overview on image matching in photogrammetry is given by GRUEN (2012), highlighting the superior performance of LMS. Intensity-based methods generally yield denser range maps while feature-based methods depend on the number of good features. Additional features may be added by projection of light patterns (active stereo), if physical texture is insufficient. The advantage of feature-based methods is, however, the relatively low computational cost and its robustness against changes in illumination.

A significant drawback of stereo vision, in comparison to time-of-flight techniques, is its limited accuracy for far-range applications as the error grows quadratically with the distance (GALLUP ET AL., 2008). However, as demonstrated in the next section, consumer-grade stereo vision sensors, set up at short-range in laboratory conditions, can yield similar accuracy as classical instrumentation in complex, aerated flows.

[1] This technique is similar to processing in Particle Image Velocimetry as described in Section 6.1.
[2] See Sections 3.1 and 7.1 on edge detection and corner detection, respectively.

4.2 TURBULENT FREE-SURFACE MONITORING WITH AN RGB-D SENSOR: THE HYDRAULIC JUMP CASE

Author: Daniel B. Bung; Brian M. Crookston; Daniel Valero
Journal: Journal of Hydraulic Research 59(5)
Year: 2020

Abstract: Measuring flow depths in free-surface turbulent flows can be challenging due to their fast dynamics and the presence of aeration. This study analyzes the suitability of a low-cost sensor, the Intel® RealSense™ D435 RGB-D camera, for characterization of a highly aerated case study: the hydraulic jump. As with all instrumentation, special care must be taken to ensure accurate measurements. In this case, two different methods to calibrate depth estimations (accounting for setup and any instrument precision) are presented, both leading to similar results. The main advantage of the presented instrumentation is its capability to measure 3D surfaces with high temporal and spatial resolution. Results are presented primarily in 2D in order to evaluate the flow depth estimation quality of this new technique with 2D data available in literature. The employed sensor showed a similar level of uncertainty as previous, well-established instrumentation for the study of free-surface elevations, amplitudes and frequencies of turbulent fluctuations.

Keywords: Aerated flows, flow visualization and imaging, hydraulic jumps, Intel® RealSense™ D435 depth camera, RGB-D vision

4.2.1 INTRODUCTION

4.2.1.1 TURBULENT FREE-SURFACE FLOW: THE HYDRAULIC JUMP CASE

A hydraulic jump (Fig. 4.2.1) is the abrupt transition from supercritical to subcritical flow, which may involve a turbulent water surface, large amounts of air entrained through the toe perimeter and the roller region, and significant energy dissipation, the latter being the primary reason why this hydraulic phenomenon has been extensively studied and implemented in a wide variety of hydraulic structures (CHANSON, 2015; MONTES, 1998; RAJARATNAM, 1967). Hydraulic jumps are commonly classified in terms of the impinging flow Froude number $\mathsf{F}_1 = v_1/(g \cdot h_1)^{1/2}$, with v_1 being the upstream mean flow velocity, g the gravity acceleration and h_1 the upstream flow depth.

With increasing F_1, a larger downstream depth is required as per momentum compatibility. When the high-velocity inlet jet impacts the slower downstream flow region, the occurring velocity difference leads to an inflexion point in the mean velocity profile and, consequently, an inviscid instability (DRAZIN, 2002). The high velocity jet is dissipated inside the jump in a wall-jet type manner (CHANSON AND

BRATTBERG, 2000; LIU ET AL., 2004; RAJARATNAM, 1967). Vortex shedding is generated at the impingement point (MISRA ET AL., 2008), which can resemble the structures observed in von Kármán streets although involving large quantities of entrained air. Likewise, at the impinging point large turbulence intensities are produced, overpassing those of common single-phase shear layers (KRAMER AND VALERO, 2020; LIN ET AL., 2012). The gradient in the streamwise velocity, together with symmetry in the transverse direction, leads to another gradient for the vertical velocity component, which motivates the roller motion to satisfy continuity. Whereas turbulence is largely anisotropic in the jet region (streamwise-predominant), turbulence tends to become isotropic inside the roller region and the fluid surface between jet and roller holds the largest rates of shearing (KRAMER AND VALERO, 2020; LIN ET AL., 2012), which should be primarily responsible for air bubble breakup.

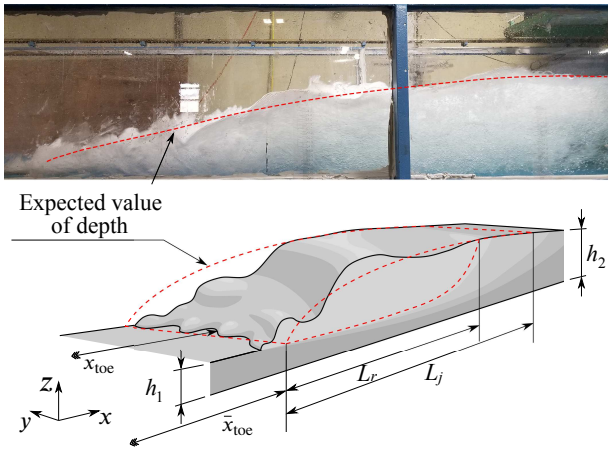

Figure 4.2.1: Hydraulic jump, top: photograph with mean surface profile, bottom: overview sketch with parameters; h_1: inflow depth, h_2: subcritical depth, x_{toe}: instantaneous jump toe position, $\bar{x}_{toe}$: mean jump toe location, L_r: roller length, L_j: jump length.

The described hydrodynamics impress a footprint in the free-surface. In the supercritical flow, before the impinging point, fluctuations in the free-surface are related to boundary layer turbulent properties (VALERO AND BUNG, 2018B). Length scales are limited by the flow depth and fluctuations occur rapidly over short time scales. At the impact, compatibility between the impinging jet and the backwards – slower flowing – roller is enforced, producing fluctuations commonly in the range of 1 to 4 Hz at laboratory scale (CHACHEREAU AND CHANSON, 2011; MONTANO ET AL., 2018; MURZYN AND CHANSON, 2009A; WANG, 2014) with largest amplitudes near this jet impact region, as most energy is still undissipated at this point. This can be readily observed as it is the region with larger splashing for higher F_1 values. Energy is dissipated through the shear layer and fluctuations reduce further downstream. In essence, short and fast waves can be observed close to the impingement, mixed with the abovementioned dominating frequency peak at

roughly 1 to 4 Hz coupled with vortex shedding. Larger and slower waves can be observed while advancing in the streamwise direction; although these waves may travel a considerable distance, there is negligible wave production downstream of the roller end.

4.2.1.2 PAST INVESTIGATION TECHNOLOGIES

The classic hydraulic jump serves as a canonical case study with horizontal channel and rectangular cross-section. Given its model simplicity, it has been reproduced in numerous laboratories and experimental studies that used different types of instrumentation, including the following for free-surface depiction: point gauges (HAGER, 1993), video cameras (MOSSA, 1999), wire gauges (MURZYN ET AL., 2007), ultrasonic sensors (WANG, 2014), and Light Detection and Ranging (MONTANO ET AL., 2018). Depending on the setup and instrumentation, the accuracy for a static measurement can range from 0.1 mm to a few centimetres, whereas the spatial resolution can span from a point measurement ($\approx$ 1 mm) or averaging in a small region (5 - 10 cm) intending to approximate a point measurement, to two-dimensional mapping of a surface of a few squared meters. A summary of selected studies is provided in Table 4.2.1, including upstream Froude number, sample frequency and duration, as well as details regarding the measurement precision and spatial resolution.

Table 4.2.1: Summary of technologies implemented in previous hydraulic jump free-surface research and present study

Instrument type	**Code**	F_1 [–]	**Sample frequency [Hz]**	**Sample duration [s]**	**Precision / Spatial resolution**	**Reference**
Point Gage	PG	4.3 - 8.9	-	-	$\pm$0.02 mm	HAGER (1993)
Wire Gage	WG	1.9 - 4.8	128	5	1 mm	MURZYN ET AL. (2007)
Video Camera	VC	1.9 - 4.8	120	-	240 $\times$ 192 px	MURZYN ET AL. (2007)
		1.3 - 9.9	25	120	-	MOSSA (1999)
Ultrasonic Sensor	USS	2.8 - 7.2	50	540		WANG (2014)
		4.6	44	60		Present Study
Light Detection and Ranging	LiDAR	2.1 - 4.7	35		24 mm / 195 px	MONTANO ET AL. (2018)
Intel® RealSense™ D435	RS	4.6	90	60	848 $\times$ 480 px	Present Study

4.2.1.3 THREE-DIMENSIONAL DIGITAL CAMERAS

Traditional digital cameras are, in simplest terms, image sensors providing a two-dimensional projection of a three-dimensional reality. Three-dimensional (3D) cameras augment conventional images with depth estimates made by coupling image sensors with software, thus providing detecting, scanning, and recognition capabilities without any physical intrusion. Recently, this technology has been leveraged in many and diverse applications such as robotics, health care, cinema, video games, communications, security, etc. (CARFAGNI ET AL., 2019). Furthermore, various non-intrusive depth acquisition techniques are available, which can be divided into two general 3D shape acquisition groups: transmissive or reflective. Reflective techniques are non-optical (e.g. RADAR, SONAR) or optical; the latter being subdivided into: 1) passive methods (e.g. stereoscopy, depth from focus, depth from shading, etc.) and 2) active methods (time-of-flight, interferometry, structured light, and active stereoscopy) (GIANCOLA ET AL., 2018). Active methods enhance optical depth estimations by using an external light source to achieve 3D shape acquisition. In particular, 3D or depth cameras coupled with red-green-blue (RGB) sensors that add color to an image are known as RGB-D cameras.

The Intel® RealSense™ D435 camera module is a low-cost non-scientific calibre (consumer grade) camera that uses active stereoscoping to estimate the distance from the camera (i.e. module) to the surface of an object. For reference, this camera is compared to previous technologies in Table 4.2.1. This module was released in 2018 (building upon the Microsoft Kinect and previous Intel RealSense series cameras) and includes vision processors, depth and tracking modules, and depth cameras comprised of an RGB digital camera, two infrared (IR) cameras, and an IR laser (CARFAGNI ET AL., 2019; GIANCOLA ET AL., 2018). Stereoscopy triangulation of static and dynamic scenes is implemented via the two IR (to reduce sensitivity to ambient light) cameras coupled with the IR laser that projects a random dot pattern over the scene if enabled (i.e. providing additional features if sufficient physical texture is not available), thus reconstructing depth (assigned to each pixel in the digital image) via the disparity between the two IR cameras' points of view using the onboard D4 processor implementing feature (geometric shape) and correlation (textured surfaces) algorithms. This package is supported by the open-source LibRealSense (formerly, Software Development Kit 2.0) that includes a variety of tools (https://github.com/IntelRealSense/librealsense/tree/master/tools) such as the RealSense Viewer (v2.23.0) for visualization, settings, and renderings, a depth quality tool, and debug tools. Metrological data of the RS400 cameras (a group of cameras that includes the D415 and D435 models), including planarity test, is reported in GIANCOLA ET AL. (2018) and CARFAGNI ET AL. (2019) with a summary reported herein (Section 4.2.2).

This depth sensor technology enables simultaneous high time and spatial resolution over relatively large domains, hence arising as a potential alternative for the study of unsteady and turbulent free-surface flows. Similar depth sensor technology has previously been implemented in various studies focused on scanning topography (BUTKIEWICZ, 2014; LACHAT ET AL., 2015), sediment and scour monitoring (e.g. AHMED ET AL., 2017; NOACK ET AL., 2018; ZHANG ET AL., 2017), and transient granular flows (CAVIEDES-VOULLIÈME ET AL., 2014). Indeed, the characteristics of RGB-D sensors could support investigations of a wide range of water-flow applications. Nonetheless, of particular interest is the accuracy of this technology for free-surface estimations and its reliability under extreme flow conditions, such as turbulent aerated flows. Therefore, this study explores the suitability of the consumer-grade Intel® RealSense™ D435 camera module for the investigation of one such group: complex free-surface flows. For convenience, the classic hydraulic jump has been chosen as a case study. This objective is achieved by investigating this RealSense™ D435 instrument sensitivities and analyzing the acquired image properties. Camera settings and postprocessing techniques are reported. Furthermore, the camera-acquired data are compared to hydraulic jump data acquired using several well-established instruments (Table 4.2.1). The main advantage of the presented sensor, compared to the other instrumentation, is its capability to instantaneously measure 3D surfaces with high temporal and spatial resolution. However, as the main objective of the current study is to evaluate the camera's performance in such difficult conditions, data analysis is limited to the centerline and compared with two-dimensional (2D) datasets available in the literature. In detail, the results include:

- hydraulic jump expected surface profile, and
- free-surface fluctuation amplitudes and spectrum.

4.2.2 EXPERIMENTAL SETUP

4.2.2.1 PHYSICAL SETUP

Experiments were conducted at the Utah Water Research Laboratory (UWRL) at Utah State University (USU) in a horizontal rectangular flume (7.32 m long, 0.933 m wide, 0.610 m deep). The flume was equipped with an upstream headbox, baffle (flow straightener), and vertical sluice gate with an opening measurable to $\pm$ 1 mm. The flume also featured a downstream flap gate that could be adjusted to influence the position of the hydraulic jump. Flow measurements were time-averaged over 10 or more minutes using a pressure transducer and a calibrated orifice meter (located in the 305 mm diameter supply piping). The orifice meter was calibrated previously using National Institute of Standards Technology (NIST) traceable instrumentation

with a 136,000 kg weight tank. For this study, flow measurement accuracy was estimated to be $\pm$ 0.2 %. Additional instrumentation included the Intel® RealSense™ D435 camera and a single microsonic™ mic+130 ultrasonic sensor (USS). A thorough analysis of the USS performance can be found in ZHANG ET AL. (2018). The experimental setup is presented in Fig. 4.2.2. A Froude number of $F_1 = 4.6$ was obtained using a sluice gate opening of 10.5 cm and a discharge of $Q = 224\,\mathrm{l\,s^{-1}}$. The flap gate was lifted to keep the mean jump toe location at $\bar{x}_{toe} = 3.5$ m from the inlet section.

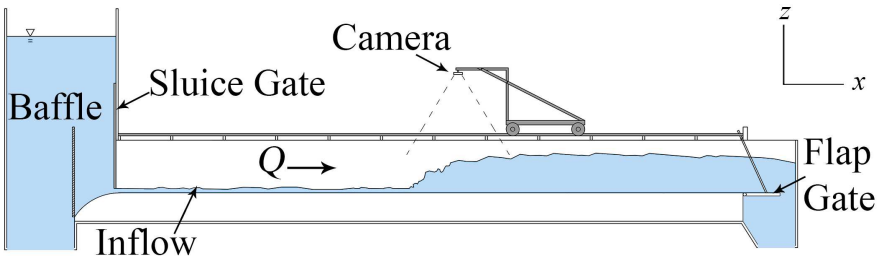

Figure 4.2.2: Experimental setup and camera mounting

4.2.2.2 RGB-D CAMERA OVERVIEW

The Intel® RealSense™ D435 was selected over the alternative D415 model as it has a wider field of view (FOV), a global shutter sensor, and the D415 is advertised by Intel to be less accurate in dynamic scenes, which would include aerated flows. A summary of camera characteristics, as reported by the manufacturer, is provided in Table 4.2.2 .

Table 4.2.2: Overview of the RGB-D (Intel® RealSense™ D435) camera characteristics

Characteristics	**Specifications**
IR camera resolution (max)	1280 × 720 px
RGB camera output resolution (max)	1280 × 720 px
Output frame rate (max)	90 Hz
Baseline	50 mm
FOV (H × V) at 8:5	91.2° × 65.5° ($\pm$3°)
FOV (H × V) at 16:9 in HD	85.2° × 58.0° ($\pm$3°)
Range (z axis)	0.2 to 4.5+ m
Depth technology	Active IR Stereo
Image sensor	Global shutter: $3\mu \times 3\mu$

The camera was mounted to a rolling instrument carriage that could be moved in the streamwise direction. The camera was located along the center of the flume at 129.9 cm

above the flume bottom and was leveled in the x and y planes within 0.1° by using an electronic level (with x the streamwise and y the crosswise direction). The camera position along the streamwise direction was carefully selected and documented for postprocessing.

For the RS400 series cameras, systematic frame random errors at 0.5 m and 1.0 m, along with central pixel standard deviation of a static plane (as a function of distance) are reported in GIANCOLA ET AL. (2018) and CARFAGNI ET AL. (2019) with errors of about 2 mm with the distance of the camera from the object between 0.5 m and 1.0 m, based upon VDI (2012), a German Standard on 3D Optical Measurement. In this study, it was noted that when observing the hydraulic jump, there was a discrepancy (described in detail in Section 4.2.2.4), particularly at the edges of the frame, meriting calibration and postprocessing efforts. Although the camera does not require structured light or particular lighting schemes, efforts were made to reduce any glare on the water surface caused by sunlight and overhead LED lighting as strong glares or light reflections were found to have an impact on measurements.

4.2.2.3 RGB-D CAMERA WORKING PRINCIPLE

As previously noted, the technology employed in this camera is active stereoscopy (BARNARD AND FISCHLER, 1982; KANADE AND OKUTOMI, 1991). The camera includes the Intel® RealSense™ Vision Processor D4 (specifications available at https://www.mouser.com/pdfdocs/Intel_Vision_Processor_D4_ProductBrief.pdf) with a proprietary depth algorithm (that receives input from the optical module comprised of the two IR cameras, the infrared projector, and the RBG camera for color). Fundamentally, the device uses two cameras with a fixed separation distance (known as the *baseline*) to capture at a precise moment a left and right image pair, which is compared for correspondence. This process involves two images taken along epipolar lines, image rectification where left and right images are reprojected on a common virtual plane, a proprietary filtering algorithm to remove failed matching due to occlusion, and computing disparity throughout the FOV. This means that any shifts required to properly match the right image to the left image are computed (number of pixels shifted = *disparity*). Through triangulation, a depth per pixel is derived from:

$$\text{Depth} = \frac{\text{baseline}}{\text{disparity}} \cdot \frac{X_{res}}{2\tan\left(H_{FOV}/2\right)} \tag{4.2.1}$$

where X_{res} = horizontal image resolution, and H_{FOV} = the horizontal FOV ($\approx 90°$). In order to compute depth resolution, Eq. 4.2.1 can be differentiated with respect to disparity. Intel (GRUNNET-JEPSEN ET AL., 2019B) notes that depth resolution is a function of the smallest disparity step or subpixel. Because this algorithm is proprietary, specific details are not available; however, documentation

(https://dev.intelrealsense.com/docs) provided by the manufacturer describes various aspects of performance, setup, sensitivities, and camera settings users may adjust and select in the user interface (RealSense Viewer and LibRealSense). LibRealSense also includes a selection of preset parameter combinations or setting profiles that are also available in the user interface (see RGB-D Camera Settings).

The D435 is capable of detecting subtle texture variations in well-lit environments including outdoor applications. Although the system was specifically developed for applications with a variety of lighting conditions, guidance for optical projector overlays for poor lighting conditions or untextured scenes is provided in GRUNNET-JEPSEN ET AL. (2019A). The onboard IR laser is an AMS Princeton Optronics projector located between the left and right stereo imagers and, if used, it overlays a random dot pattern (approximately 5,000 dots) on the scene. Since Intel employs an active stereo depth system, this IR projection (often unnecessary in many applications) and the pattern, number of dots, and projection stability do not have strict requirements (Intel employees Jesus Garcia and Mauricio Umana, personal communications, 11 February 2020). Indeed, these IR projections are intended to add texture for texture-lacking scenes. Furthermore, the camera has no difficulty estimating depths through clear substances such as acrylic and clear water unless the substance is highly reflective or creates optical distortion through refraction. Note that for turbulent flows with sufficient lighting and reflectivity, this is not an issue as shall be shown herein. Furthermore, air bubbles within water flows cause light diffraction thus producing an opaque white visual effect. Tinting water with synthetic or natural dyes or materials (e.g. common flow visualization techniques) may be considered on a case-by-case basis. Thus, the camera is fairly robust but accuracy may vary depending on the application or scene, camera settings, and lighting conditions. Lighting, reflections, and light diffusion should be considered on a case-by-case basis through calibration and postprocessing. However, the RealSense Viewer does provide a live view of the scene with some initial indications to users regarding the depth measurements and if there are any significant issues with an experimental setup.

4.2.2.4 RGB-D CAMERA SETTINGS

Extensive control of the D435 are available through the RealSense™ Viewer and LibRealSense software to allow various adjustments to system parameters by users for different applications. Parameters and selection of parameters are discussed in detail at GRUNNET-JEPSEN ET AL. (2019C). Visual presets are defined at "D400 Series Visual Presets" (2019) with a brief summary and discussion herein.

Intel includes within the LibRealSense software six camera presets or setting profiles for specific purposes, identified as default, high density, medium density, high accuracy, hand, and left imager color w/o IR pattern. Only high density, medium

density, and high accuracy presets are resolution based and are recommended by Intel to enhance object recognition and measurement accuracy. The general performance difference between the high and medium density presets and the high accuracy preset is the fill factor; Intel recommends the latter for manufacturing applications such as object scanning, collision avoidance, and robot guidance systems (Intel, personal communication, 11 February 2020). Furthermore, the high density preset adjusts camera settings to maximize fill factor, which maximizes the camera's ability to detect the most detail with maximum accuracy in a scene (preferred preset used as a basis followed by individual parameter adjustments for this study).

(A) RGB image

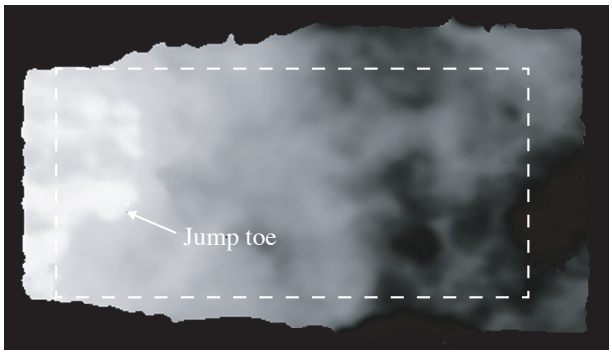

(B) Depth image (white to black for decreasing distance to the water surface), dashed line indicates the field of view of the RGB-D camera (note the different field of view dimensions)

Figure 4.2.3: Snapshots of a single instant taken with RGB-D camera (flow from left to right)

Beyond these camera presets, this study followed individual camera parameter tuning guidance provided by Intel, presented in GRUNNET-JEPSEN ET AL. (2018). In this study, the High Density and High Accuracy settings were investigated. At a first glimpse in the Viewer, the High Density setting seems to provide a more continuous free-surface detection, with only localized data omissions. Notwithstanding, a sensitivity analysis proved that more favorable results were obtained using a user-modified High Accuracy setting profile (details provided under Results). A

sampling resolution of 848 × 480 px at 90 Hz was selected, which is comparable to other instrumentation noted in Table 1. Higher spatial resolution with this sensor is not supported for the given sample rate. The FOV had a length of ≈200 cm, resulting in pixel density of roughly 4 px cm^{-1} in the flow direction. The sample time was 60 s resulting in 5,400 frames. The autoexposure setting functioned satisfactorily for this experiment with a depth exposure of 8,500 μs and a UVC (USB Video Class) image gain of 16 (minimum) and a mean intensity setpoint of 1536. The depth units setting was specified at 1 mm. Multiple laser powers were tested; a laser power of 250 mW was selected for final tests based upon results reported by CARFAGNI ET AL. (2019) and observations herein for this specific application. An example frame captured during data acquisition with the RealSense™ Viewer with specified settings is provided in Fig. 4.2.3.

4.2.2.5 POSTPROCESSING

Data correction

Each camera unit is pre-calibrated for immediate use. Nevertheless, users may perform a calibration either within the camera software or as part of data postprocessing such as the one here performed. In preliminary tests, it was noted that the accuracy of the measured depth was variant within the FOV and non-symmetrical, which may have been caused by shipping or associated with manufacturing tolerances. In a first step, to overcome this issue and determine the pixelwise deviation (Fig. 4.2.4(A)) for in situ conditions, a wooden construction dimensioned based upon USS measurements of the flow depths was fabricated and placed in the flume as a simplified, mean hydraulic jump profile (with time-averaged upstream and downstream elevations h_1 = 85 mm and h_2 = 347 mm, as well as the hydraulic jump length L_j = 170 cm). The main purpose of this construction is to establish reference depths at different positions, which are similar to those to be estimated in the turbulent hydraulic jump. The resulting deviation matrix from this dry-bottom test and a 3D fit are illustrated in Fig. 4.2.4(B). With this method, an average discrepancy of 26 mm was obtained with an average standard deviation of 1.7 mm. Significant local differences (up to 78 mm) were observed at the edges of the FOV and adjacent to the sidewalls due to distortion of the increasing surface level (see Fig. 4.2.3). However, as mentioned earlier, the present study presents data from the centerline only, for which moderate discrepancy was observed. It is assumed that the specified characteristics are dependent upon this specific device, variations between sensor units may occur, and specific corrections may be necessary for other cameras.

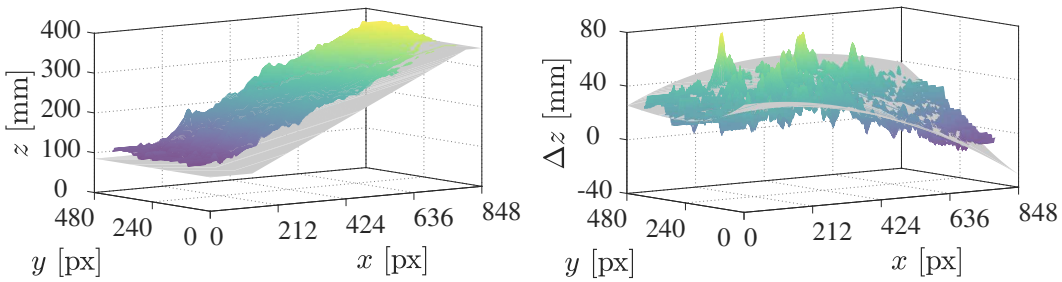

(A) Measured elevation (upper) compared to target elevation (lower)

(B) Resulting depth discrepancy and fitted 3D curve (note the non-symmetric deviation in both, x- and y-direction)

Figure 4.2.4: Results of the dry-bottom test using a simplified hydraulic jump profile (90 fps and 5 s sample time)

In a second step, to validate the measuring error from in situ (dry-bottom) calibration, additional pre-tests in dry conditions were conducted in which the camera was placed in front of a white plane and its distance to the plane incrementally increased. The results for the centerline data are illustrated in Fig. 4.2.5. In Fig. 4.2.5(A), the range of measured distances are illustrated for tests with 10 s sample time as well as the median distances for target distances between 500 mm and 1400 mm. Apparently deviations are smaller for shorter distances, which is in agreement with the results from the dry-bottom test in Fig. 4.2.4. Also, the unsymmetrical shape of the deviations is detected. To highlight the linearity of the deviations, Fig. 4.2.5(B) compares the measured median distances from selected centerline pixels (i.e. x = 120, 240, 360, 480, 600 and 720 px) with the target values. Figure 4.2.5(B) also includes the measured centerline distances to the dry bottom from Fig. 4.2.4 to demonstrate that the linear trend of this offset is independent of the installation and surrounding conditions.

Finally, the subsequent results have been obtained by instantaneously subtracting the offset from the dry-bottom test, i.e. the known error from the measured data. A similar calibration method has been applied by NOACK ET AL. (2018) to account for distortion to different refraction through transparent surfaces. It is noteworthy that almost identical results have been obtained by considering the pixelwise, instantaneous offset from the wall tests, which suggests that future studies might be conveniently conducted simply using an out-of-the-channel calibration.

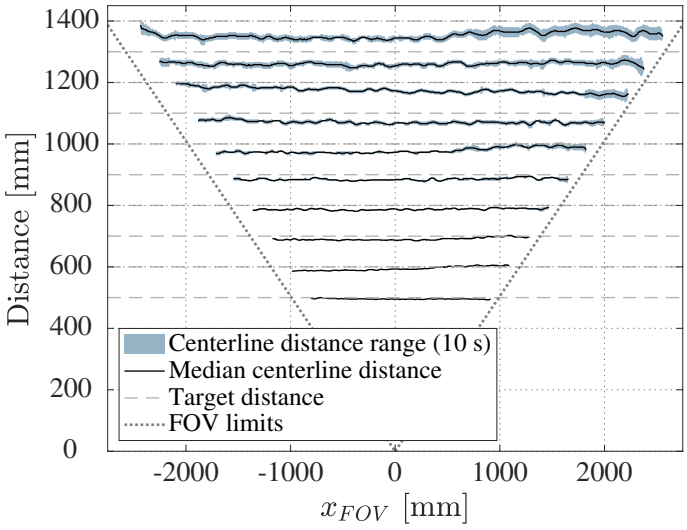

(A) Centerline data along the width of field of view (FOV)

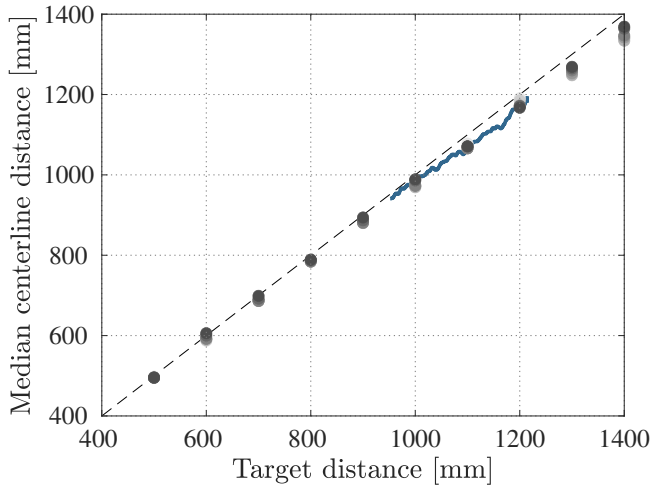

(B) Comparison of measured distance and target distance for selected centerline pixels (i.e. x = 120, 240, 360, 480, 600 and 720 px), bright to dark markers for increasing x (the solid line shows the centerline data from the dry bottom test)

Figure 4.2.5: Results from wall tests showing the linearity between measuring discrepancy and distance

Data filtering

At a given x, y location, the corrected depth data has been filtered to remove outliers as follows (subscript: *raw* for raw data, *filt* for filtered):

$$P_{filt} = \begin{cases} \text{NaN} & P(t) < P_{\min} \text{ and } P(t) > P_{\max} \\ P_{raw} & \text{otherwise} \end{cases} \tag{4.2.2}$$

where $P_{\min} = \text{MED}(P(t)) - 1.4832[2\ln(N)]^{1/2}\text{MAD}(P(t))$ and $P_{\max} = \text{MED}(P(t)) + 1.4832[2\ln(N)]^{1/2}\text{MAD}(P(t))$, where $P(t)$ is a data point at instant t, $\text{MED}(P(t))$ is the median of the time series at pixel with coordinates x and y, N is the total number of samples and $\text{MAD}(P(t))$ is the median absolute deviation of $P(t)$ (see also GORING AND NIKORA (2002); WAHL (2003)). Equation 4.2.2 implies that data within some acceptable bounds are admitted as potentially correct whereas data unreasonably far from the median are discarded. Further discussion on turbulent free surface data filtering can be found in VALERO ET AL. (2020).

4.2.2.6 ULTRASONIC SENSORS

For completeness, free-surface measurements were taken using the microsonic mic+130 ultrasonic sensor (USS) connected via the LinkControl Adapter (v7.7.6.0). The sensor was mounted at about 0.7 m above the flume bottom. Transducer frequency was 200 kHz with an acoustic sensing range of 0.2-2.0 m with tolerances ranging between 0.18 mm and 0.57 mm, respectively. The sensor has internal thermal compensation; however, it was left operational overnight ($>\approx$12 h) to minimize any thermal changes during daytime testing. The sensor was positioned along the centerline of the flume and measurements were taken at 44 Hz for 60 s every 50 cm, except in the vicinity of the hydraulic jump where measurements were taken every 10 cm. All data were filtered using the same method, presented in Eq. 4.2.2.

4.2.3 RESULTS

4.2.3.1 GENERAL REMARKS

The data from the present study are compared to 2D data sets from the selected references in Table 4.2.1. Data points were either received by the respective authors or digitized from plots with an observed accuracy of $\pm$ 1 %. For the purpose of using a homogeneous dimensionless form of the data, the empirical expression of HAGER (1992) for the hydraulic jump length was used to process the data of HAGER (1993), the empirical expression of WANG AND CHANSON (2015) for the hydraulic jump length (roller in the original study) was used to process the data of MONTANO ET AL. (2018), and the Bélanger equation was used for the estimation of the sequent depth h_2 to process the data of MONTANO ET AL. (2018).

4.2.3.2 MEAN FREE-SURFACE PROFILE

The time-averaged free-surface profile is known to be self-similar for stable hydraulic jumps with a wide range of Froude numbers (F_1), as shown in Fig. 4.2.6(A), where h is the local mean water depth along the jump. Different measuring techniques may

result in detecting different characteristic water levels within the highly aerated region of the roller. Note that the roller length was visually determined as L_r = 1.16 m, which corresponds to 68 % of the jump length L_j. In this study, the roller length is defined as the distance between the mean toe location and the section where recirculation usually stops occurring, and the jump length as the distance from toe to the section where free surface becomes, on mean terms, horizontal.

While point gauges generally provide the highest observed water elevation at a given measuring location, ultrasonic sensors are known to penetrate into the air-water mixture (BUNG, 2013), resulting in slightly lower water depths (representing a characteristic water depth) as supported by the data of WANG (2014). Similar characteristics are found for both techniques applied in this study. For $x/L_j \leqslant 0.6$, the ultrasonic sensor gives lower water depths than the RGB-D camera, which is assumed to provide a characteristic water level close to the upper boundary of the air-water mixture (a detailed determination of the exact characteristic water level would require intrusive phase-detection probes which were not available for the current study). It is clearly visible that this new RGB-D technique is capable to accurately measure time-averaged water levels. It must be noted that a similar result was obtained with a much shorter sample time of only 10 s. Figure 4.2.6(B) illustrates the discrepancy of different measuring techniques compared to an empirical equation for the jump profile proposed by WANG AND CHANSON (2015). Again, it is shown that the RGB-D data, after the proposed calibration was carried out, leads to similar (or even lower) data spread than the classical point gauge data by HAGER (1992) and WANG (2014), the latter at the downstream end of the jump. The observation that point gauge data are also providing such a lower spread is remarkable, as one may assume that this simplistic instrumentation is handicapped for turbulent or fluctuating free surface measurements.

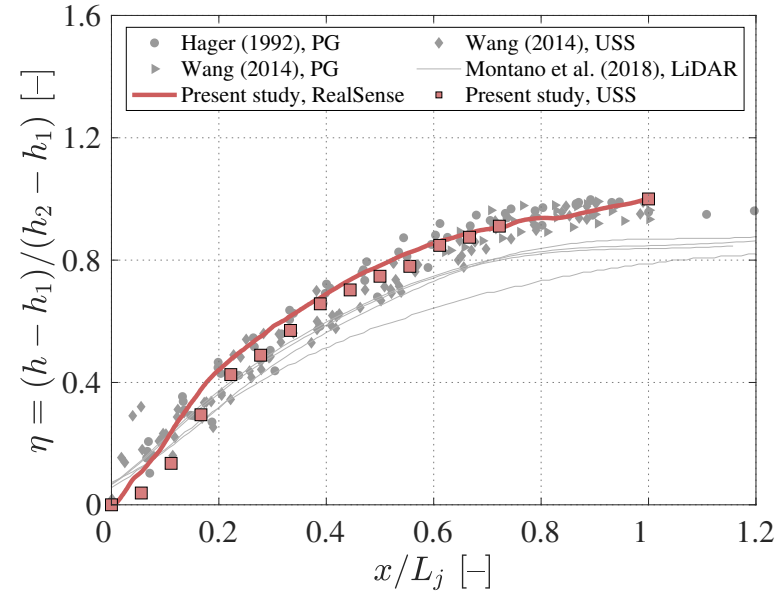

(A) Dimensionless, mean / median free-surface profile obtained through different measuring systems (Table 4.2.1): point gauge (PG), ultrasonic sensors (USS), and Light Detection And Ranging (LiDAR)

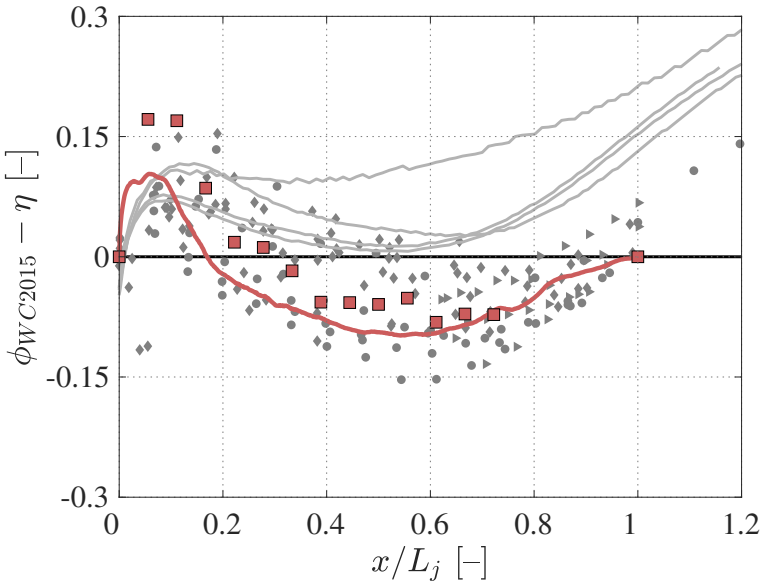

(B) Spread of each measuring technique when compared to empirical relationship of WANG AND CHANSON (2015)

Figure 4.2.6: Time-averaged free-surface results

4.2.3.3 FREE-SURFACE FLUCTUATIONS

The standard deviation of the flow depth (h') may be considered to describe the amplitude of the turbulent, vertical fluctuations. Strongest surface fluctuations are found within the aerated roller of the jump. As shown in Fig. 4.2.7, the standard

deviation may reach up to 15 % of the mean water depth difference $h_2 - h_1$. Both the USS and RGB-D data compare well to literature data, while the USS is observed to estimate higher fluctuations in the aerated region. In particular, for $0.4 \leqslant x/L_j \leqslant 0.8$ a deeper analysis of the instantaneous measurements revealed that the USS probability distributions are slightly wider with a tendency to provide minimum flow depths that are roughly 10 mm lower than those obtained from the camera (while maximum flow depth are of the same order, Fig. 4.2.8(A)). This finding may be explained with the known characteristic of USS providing flow depth data in the order of h_{60} to h_{85}, i.e. flow depths corresponding to a level with 60 to 85 % void fraction (BUNG, 2013; KUCUKALI AND CHANSON, 2008; ZHANG ET AL., 2018). The larger spread in the histograms leads to a higher standard deviation in this region. In the upstream region, the RGB-D camera data marks significantly higher fluctuations than the USS. This phenomenon may be explained in part by the generally lower accuracy near the boundaries of the camera's FOV as previously described. Moreover, it was noted that a sufficiently turbulent surface was needed to be properly recognized by the camera. As with the LiDAR data of MONTANO ET AL. (2018), an upstream shift of the curve is noticed in comparison to all point measurements. However, this discrepancy could be attributed more to the definition of the fluctuating jump toe location rather than to the measuring principle. Figure 4.2.8(B) presents the dynamic fluctuations around the mean value, i.e. $h_{inst} - h$ with h_{inst} the instantaneous water depth, for the same cases as in Fig. 4.2.8(A) . For both locations, the camera and the USS show identical probability distributions. It may thus be assumed that the dynamic response of the camera is comparable to the response of the USS.

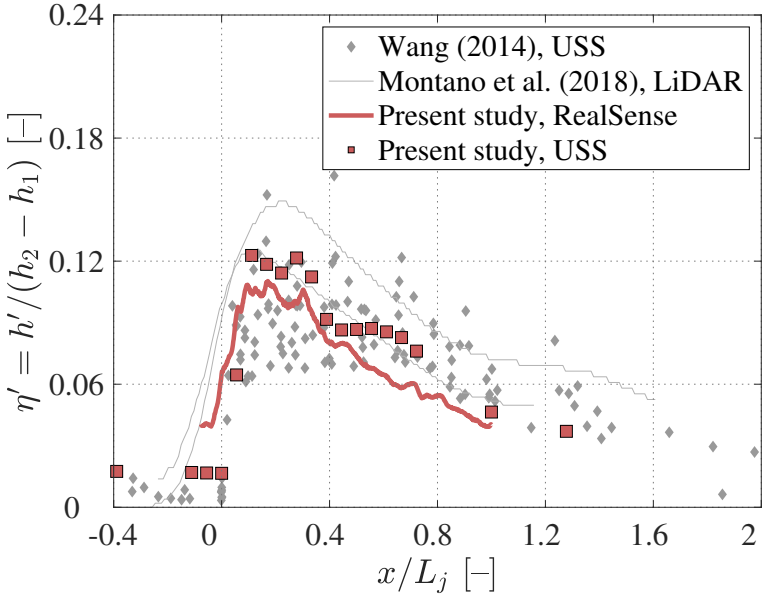

Figure 4.2.7: Dimensionless standard deviations obtained through different measuring systems: point gauge (PG), ultrasonic sensors (USS), and Light Detection And Ranging (LiDAR)

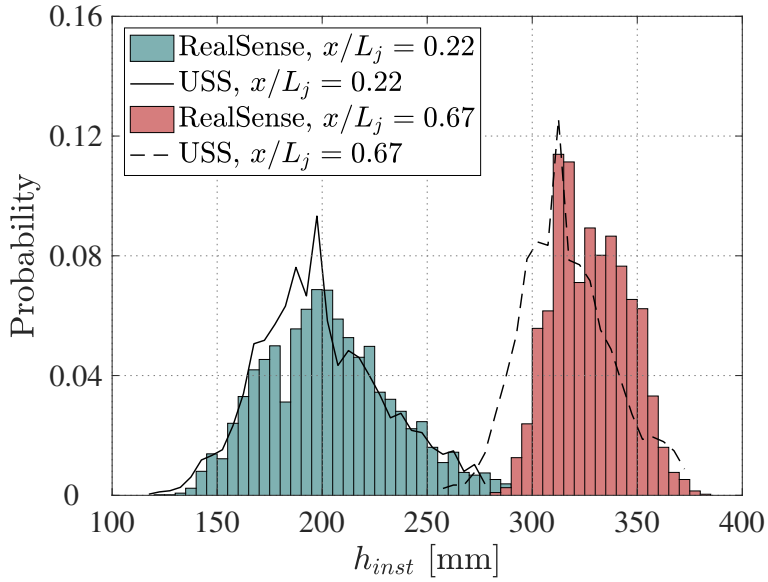

(A) Absolute, instantaneous flow depth

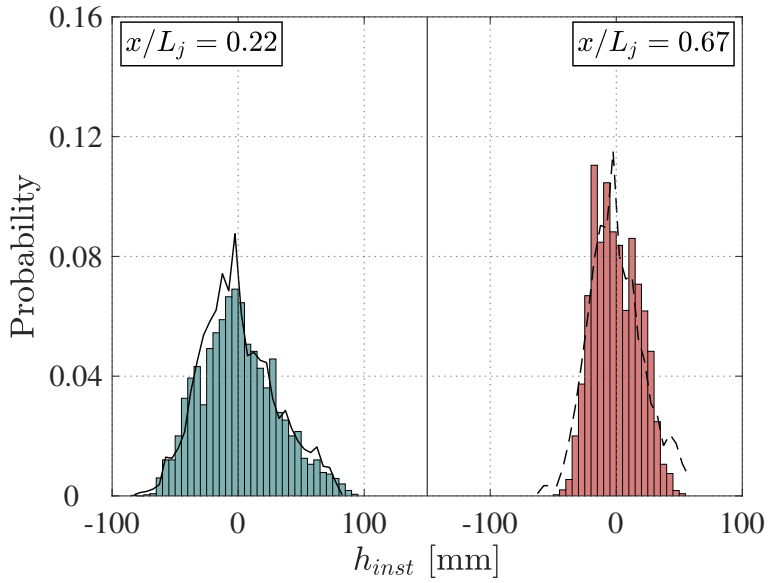

(B) Fluctuations around the mean value

Figure 4.2.8: Normalized histograms (probability distributions) of measured data from both devices at two different locations

Furthermore, spectral analysis can be used to quantify free-surface fluctuations. Turbulent exchanges within the hydraulic jump can leave a mark in the flow depth that results in waves of different amplitudes over a wide range of frequencies. High-frequency free-surface fluctuations tend to absorb the -5/3 power slope from the velocity spectrum (VALERO AND BUNG, 2018B) whereas for lower frequencies, energies tend to spread at similar energy levels when large amplitudes occur (VALERO, 2018).

This is an **Author's Accepted Manuscript** of an article published by Taylor & Francis Group in Journal of Hydraulic Research on 18 December 2020, available online: HTTPS://WWW.TANDFONLINE.COM/DOI/ABS/10.1080/00221686.2020.1844810

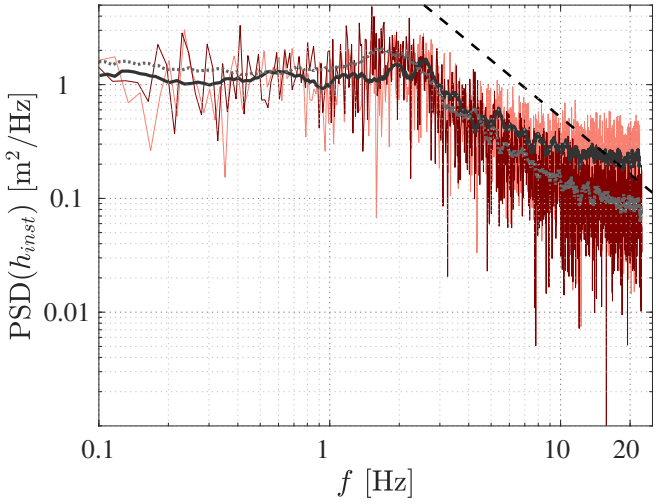

(A) $x/L_j = 0.28$

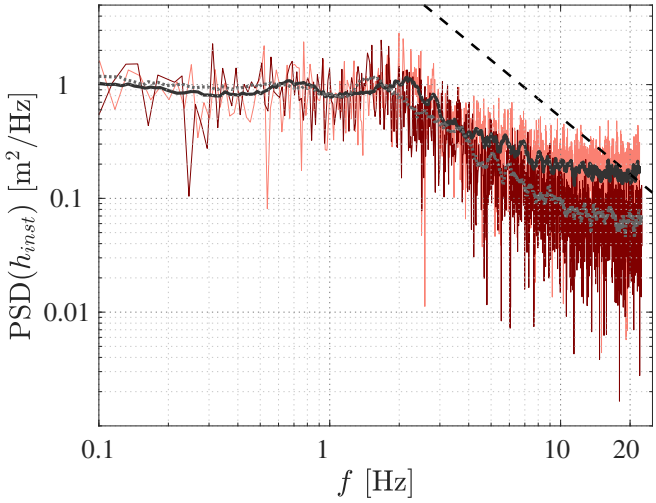

(B) $x/L_j = 0.50$

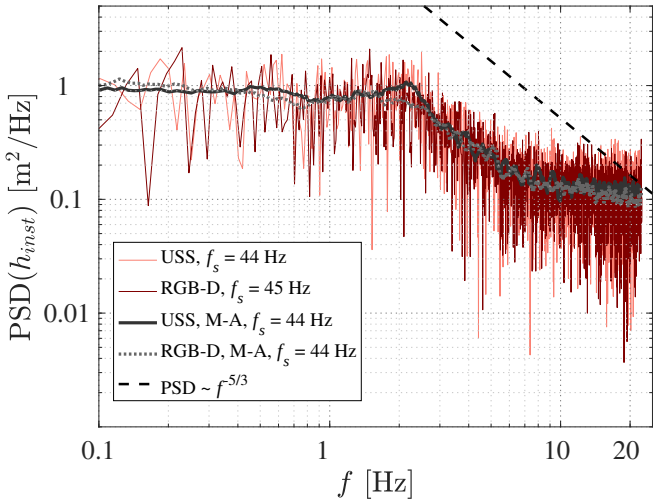

(C) $x/L_j = 0.72$

Figure 4.2.9: Spectra of the free-surface fluctuations for different jump locations (M-A for moving-averaged spectrum, backward and forward window over 10 frequency points)

Instantaneous flow depths were recorded at 90 Hz with the RGB-D sensor, which roughly corresponds to twice the sampling frequency of the USS (i.e. 44 Hz). For comparison, depth time series of the RGB-D sensor were downsampled to 45 Hz, which does not require any interpolation and facilitates an assessment of the datasets. Figure 4.2.9 presents the Power Spectral Density (PSD) obtained from both datasets at three different locations along the jump centerline, i.e. at x/L_j = 0.28, 0.50 and 0.72. Depth time series were again processed using data filtered with the method in Eq. 4.2.2. Figure 4.2.9(A) corresponds to the most turbulent flow location while Fig. 4.2.9(C) show less intense fluctuations (see Fig. 4.2.7 for comparison). For clarity, a moving-averaged spectrum (over the 10 neighboring frequencies) is superposed to the spectrum obtained from the direct fast Fourier transformation, hence smoothing the crests and troughs resulting from limited sampled time.

A subtle peak can be observed in the spectra of Fig. 4.2.9 at around 1.5 to 3 Hz, with larger frequencies observed in the USS data. The peak in USS data sometimes shows neighboring secondary peaks that can be readily mistaken as other dominant frequencies. These double, or even triple peaks are not present in the RGB-D spectrum, which show a more consistent shape with the peak frequency appearing more stable across jump locations. All spectra from USS data shown tend to a flat slope after frequencies over 6 - 10 Hz. However, the spectra obtained from RGB-D data series respond better at larger frequencies (up to 10 - 20 Hz). This flattening at large frequencies for USS data was already observed by ZHANG ET AL. (2018). When amplitudes are more intense, the signal remains clearly above the noise and thus the sampled data can be better discerned. This is also consistent with the data shown in Fig. 4.2.7 , which depicted larger turbulent intensities in the USS data. It must be noted that noise – as such shown in the high-frequencies plateaus of USS spectra – translate into larger intensity fluctuations, mimicking a flawed larger turbulent level. Thus, RGB-D spectra suggest that this sensor may be better suited than USS for the study of time-resolved free-surface turbulence.

4.2.4 DISCUSSION

As demonstrated above, calibration of the camera is essential. Two different methods have been proposed, both leading to similar results. It is acknowledged that the final selected calibration method, i.e. the correction with subtraction of a 3D fitted offset matrix of the dry-bottom, may involve some smaller errors as a constant offset is considered regardless of the instantaneous measurement. However, the range of measurements for a given location is in the order of up to 100 mm (4.2.8(A)) and thus the effect on the real, instantaneous offset is negligibly small.

The accuracy of the RealSense^{TM} D435 sensor and the offset matrix depend on the particular device employed and need to be checked before first use and should be regularly checked afterwards. Incontrovertibly, the calibration with a dry-bottom is

unwieldy but the calibration happens within the experimental setup. The accuracy check over a plane (such as the wall test in this study) is easy to conduct but requires the sensor to be placed in the experiment following calibration. The sensor performance seemed to be unaffected by the surrounding conditions (i.e. installation over a flume with artificial lighting against installation in front of a white wall with daylight conditions).

It must be noted that when exploring camera limitations, a still water surface was not detected by the camera; preliminary tests showed that introduction of water coloring improved drastically the detection of non-turbulent water surfaces for still water levels. This, however, falls out of the scope of this work and has little impact on the study of aerated flows.

4.2.5 CONCLUSIONS

This study examined the capacity of an RGB-D camera (Intel® RealSense™ D435) to investigate water surface elevations in highly turbulent and aerated open channel flows. A hydraulic jump was chosen as a case study given that it has been previously examined via numerous experimental techniques. This camera was used to measure and calculate mean free surface depths, amplitudes and frequencies of its turbulent fluctuations. Special care must be taken on calibration of depth estimations, with two calibration techniques presented in this study.

The difficulty to validate the detected turbulent water surface levels is acknowledged, as all existing instrumentation suffers from different limitations in this complex environment. However, the authors believe through the study results juxtaposed with 2D high-quality published data sets that the tested RGB-D camera is as reliable as other technology currently employed (at the time of this study) to investigate highly turbulent aerated open channel flows including LiDAR, ultrasonic sensors, wire gauges, and point gauges. To further evaluate and better understand which characteristic level is being detected by the RGB-D camera, a combined study with intrusive air-water flow measurements is required. Future studies may also consider the installation of a camera array to increase the study area. Due to its ease of installation, the camera may be considered for field measurements although the question of range and position must be addressed.

CHAPTER 5

DISCUSSION

5.1 CAPACITIES AND LIMITATIONS OF OPTICAL WATER DEPTH MEASUREMENTS

Two different approaches to determine flow depths by imaging techniques have been presented. The first approach, namely the identification of free-surface levels by edge detection, requires transparent sidewalls for visual inspection and yields two-dimensional information in a longitudinal section. It was demonstrated that edge detection can provide valuable information, even in most difficult flow conditions such as aerated spillway flows being characterized by intense surface roughness. In this case, some uncertainty needs to be accepted as the three-dimensional nature of the aerated surface waves can not be correctly recognized by this technique. However, in well-defined, two-dimensional flows, adequate accuracy may be achievable. ZHANG ET AL. (2018) proved the good agreement between edge detection and ultrasonic sensors applied to a propagating wave experiment. ZHANG ET AL. (2018) further showed that the detection of the free surface becomes more difficult with increasing aeration. At the inception point of self-aeration of a spillway, the uncertainty was found to be mainly caused by a thickening of the reflecting water surface line and three-dimensional artefacts in the background that may corrupt the edge detection algorithm. These artefacts, e.g. droplets and background perturbations, become more significant for stronger aeration. Despite the limited accuracy, but promoted by its simplicity, edge detection as a flow depth measuring technique has gained increasing interest in the recent past, particularly in relation to wave experiments in laboratory environments. DOUGLAS ET AL. (2020) applied an edge detection approach to investigate the wave interactions with rubble mound breakwaters. DU ET AL. (2017) proposed an improved edge detection algorithm to speed up processing. For this purpose, determination of unsteady flow depths was carried out by employing a moving interrogation window which is shifted based on results from a previous time step.

The second approach, which was presented herein, is based on direct depth estimation through cameras installed above the water surface. Different sensors, i.e. LiDAR and the proposed RGB-D sensor, have been applied to free-surface flows so

far. Depth cameras require appropriate texture at the surface to be recognized. Such texture may be obtained by dye or surface tracers. Alternatively, flow aeration can provide sufficient texture with the drawback of implicating significant disturbances and thus increasing the uncertainty. However, it could be demonstrated that this uncertainty is in the same order as for classical air-water flows instrumentation. LiDAR and stereo vision can provide instantaneous 2D or 3D data, respectively, which is a significant improvement to commonly employed sensors (e.g. ultrasonic sensors). An important feature of aerated flows, which is in the focus of contemporary studies, are turbulent length and time scales. Improving the knowledge about these scales may help to better understand the complex flow in spillways, hydraulic jumps and other flow conditions involving aeration. Three-dimensional techniques, in particular, will help to close this gap of knowledge. However, it was shown that special care is required to properly calibrate the cameras and to correctly rectify distorted images.

5.2 POTENTIAL PROTOTYPE APPLICATIONS

In the recent years, first attempts have been made to apply edge detection methods to field observations. In this case, the camera is positioned with a known perspective to the water body and the flow depth is estimated by a case-specific calibration. Alternatively, physical dimensions of objects in the image, e.g. bridge piers, can help to scale the water level if a reference level is known (BHOLA ET AL., 2019). For instance, ELTNER ET AL. (2018) used the Canny edge detector in combination with image filtering methods for automatic image-based water stage measurements. A similar study has been presented by ZHANG ET AL. (2019B) suggesting that camera-based gauging may provide a similar accuracy as classical float-type automatic water level gauges. Compared to these classical gauges, non-intrusive, cameras are relatively low-maintenance and low-cost devices. BHOLA ET AL. (2019) suggest to continuously process images from cameras to regularly validate water levels and improve flood inundation forecasts.

As pointed out by ERPICUM ET AL. (2020), making use of new techniques to collect prototype data is one of the biggest challenges in the hydraulic structures community. Prototype data is of utmost importance for the safe design of hydraulic structures, but is still rare to date. Optical depth sensors can help gathering such data at spillways and stilling basins (e.g. for quantification of scale effects in physical models). Installation of intrusive probes is generally difficult in high-velocity flows and structures are often hardly accessible. An array of multiple cameras or RGB-D sensors can be installed on top of a spillway or stilling basin without difficulty[1]. Alternatively, attaching compact RGB-D sensors to a drone may be considered.

[1]It is noteworthy that similar methodology is used in coastal engineering since the 1980's (GUIMARÃES ET AL., 2020; MOLFETTA ET AL., 2020).

PART III

VELOCITY DETERMINATION

CHAPTER 6

PARTICLE (BUBBLE) IMAGE VELOCIMETRY

6.1 INTRODUCTION

Particle Image Velocimetry (PIV) is an image-based technique allowing for determination of full instantaneous velocity fields (ADRIAN AND WESTERWEEL, 2011). For this purpose, the fluid is seeded with small particles (see. Fig. 6.1.1(A)), i.e. so-called tracers, and the scene is captured with a camera. The particle material should have a density close to one and a spherical shape to allow for a slip-free transport within the fluid. Moreover, the particles should have a reflective surface to enhance the visibility when illuminated with a light source.

If available, a laser light sheet, forming a plane perpendicular to the view direction of the camera, is preferred. Particles which are located outside of this plane are not visible for the camera and ignored by the image analysis. Consequently, only the two-dimensional flow within the plane is detected and it is referred to as planar PIV. It must be noted that three-dimensional flows may be investigated using a stereoscopic PIV system, i.e. with use of two synchronized cameras detecting the flow over the width of the laser plane, or a volumetric PIV system, i.e. with use of multiple cameras detecting the flow within a defined volume. In any case, the light source should be pulsed with the camera(s) to ensure constant illumination.

With a specified sample rate F_{im} of the camera or separation time $\Delta t_{im} = 1/F_{im}$ of the images, respectively, one may be able to calculate the particle velocities $\vec{v}$ if their displacements $\vec{d}$ are known:

$$\vec{v} = \frac{\vec{d}}{\Delta t_{im}} \tag{6.1.1}$$

For estimation of the particle displacements, the frames are divided into interrogation windows with smaller size and the most likely motion within a window is determined by Direct Cross-Correlation (DCC) in spatial domain or in frequency domain using a Fast Fourier Transform (FFT). Special attention is needed as the particle movement must not exceed the window size. Thus, a minimum interrogation window size is essential which in turn limits the maximum resolution of velocity fields. Alternatively, for a given camera resolution, the field of view (FOV) needs to be reduced to increase

the velocity data resolution or interrogation windows may overlap. It is pointed out that PIV provides one single velocity vector per each interrogation window.

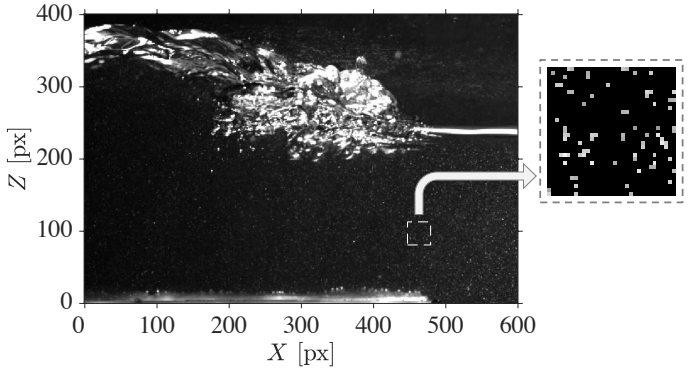

(A) Frame 1 with tracer particles and interrogation window (32 × 32 px) after contrast and gamma correction, wave propagation from left to right

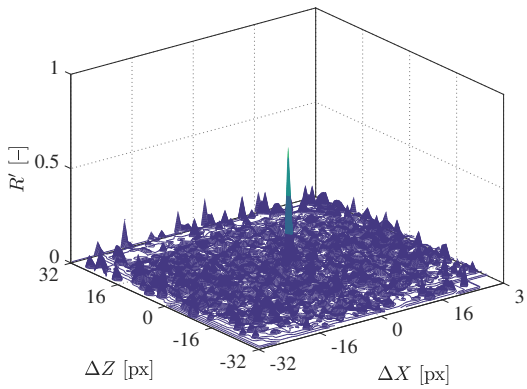

(B) Normalized cross-correlation matrix

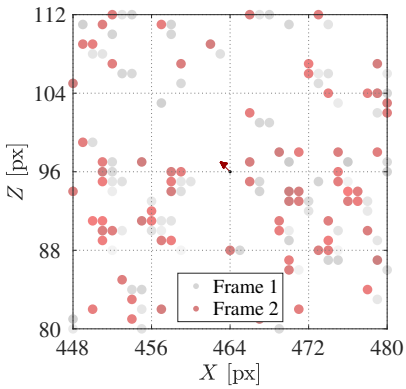

(C) Extracted tracer particles from both interrogation windows

Figure 6.1.1: General PIV procedure for the case of a wave propagating over a submerged plate

Figure 6.1.1 illustrates the general PIV procedure for a wave propagating and breaking over a submerged plate[1] (image taken from BUNG AND OERTEL (2019) and cropped to an image size of 600 × 400 px) . In Fig. 6.1.1(A), an interrogation window with a typical size of 32 × 32 px is shown and zoomed out to highlight transported tracer particles and their pixel representation. A 2D cross-correlation (see Eq. 8.2.1) has been performed using the interrogation window pixel intensity matrices from two subsequent frames. The normalized 2D-cross-correlation matrix in Fig. 6.1.1(B) highlights a clear peak suggesting a most likely, mean particle displacement of $\Delta X = -1$ px and $\Delta Z = 1$ px, respectively. This result is supported by Fig. 6.1.1(C) showing the particles from both subsequent interrogation windows (marker

[1] This case is identical to the case considered in Section 3.1.

brightness corresponds to the pixel intensity from both original grayscale image frames). The displacement vector in the window center illustrates the cross-correlation result. The reader may note that detected pixel clusters representing a single tracer particle can change appearance from one frame to another leading due to image noise and thus to a reduced correlation coefficient.

Nowadays, pulsed LED light sources are also available as an alternative to laser illumination. LED's may be used to 1) form a light plane with use of a lens, similar to a laser, but with a wider, less accurate plane, or 2) to illuminate the full scene through the inspection window of a flume. In the latter case, particle displacements perpendicular to the interrogation plane as well as particles out of focal plane may adulterate calculated displacements.

However, some applications in the field of hydraulic engineering (DI CRISTO, 2011) may justify the use of diffusive light sources. In aerated flows, for instance, application of a laser may lead to unacceptable reflections and thus to eye injuries for attending staff. Furthermore, as even smallest air bubbles are about one dimension larger than a typical laser plane thickness, the general idea of limiting the image interrogation to only those particles in focal plane is not transferable to air-water flows. It must be noted that, in such flows (so-called white waters), classical seeding with tracers is mostly insufficient as the particles are difficult to recognize between air bubbles (Fig. 6.1.1(A)). Instead, the physical image texture due to entrained air may be considered for image analysis. The method is then commonly referred to as Bubble Image Velocimetry (BIV).

It is acknowledged that the principle of PIV is more suitable for discrete particle images. Aerated flows, in turn, lead to a continuous image texture, depending on the spatial image resolution. Some lack in accuracy must thus be expected when performing a BIV analysis as shown in subsequent sections. However, extensive calibration efforts and image preprocessing may help to improve the results, but still significant differences may occur when compared to intrusive measurements.

6.2 INITIAL STAGE OF TWO-DIMENSIONAL DAM-BREAK WAVES: LABORATORY VS. VOF

Authors: Mario Oertel; Daniel B. Bung
Journal: Journal of Hydraulic Research 50(1)
Year: 2012

Abstract: Since several decades, dam-break waves have been of main research interest. Mathematical approaches have been developed by analytical, physical and numerical models within the past 120 years. During the past 10 years, the number of research investigations has increased due to improved measurement techniques as well as significantly increased computer memories and performances. In this context, the present research deals with the initial stage of two-dimensional dam-break waves by comparing physical and numerical model results as well as analytical approaches. High-speed images and resulting particle image velocimetry calculations are thereby compared with the numerical volume-of-fluid (VOF) method, included in the commercial code FLOW-3D. Wave profiles and drag forces on placed obstacles are analyzed in detail. Generally, a good agreement between the laboratory and VOF results is found.

Keywords: Dam-break, drag force, numerical model, physical model, PIV, VOF

6.2.1 INTRODUCTION

Dam-break waves have been investigated for various boundary conditions during the past 120 years. Research studies are available for two-dimensional (2D) and three-dimensional (3D) dam-break waves in flumes or on planes. Their main focus concerned the wave front velocity and the flow depth. With improved imaging techniques, visualization studies and numerical computations became available in the last decade.

RITTER (1892) studied 2D dam-break waves presenting analytical solutions for the wave velocity and the flow depth. Since his approach considers an idealized wave tip region, studies were conducted to improve Ritter's wave profile (e.g. DRESSLER, 1952; WHITHAM, 1955; LAUBER AND HAGER, 1998A). The effects of channel slope or initial water depth on the dam-break wave were also studied (e.g. HUNT, 1982; LAUBER AND HAGER, 1998B; STANSBY ET AL., 1998). The first 3D analyses for dike-break propagations on a horizontal plate were made by AURELI AND MIGNOSA (2002). OERTEL AND SCHLENKHOFF (2008) analyzed dike-break waves along with the resulting tailwater flooding processes. ROGER ET AL. (2009) presented experimental and numerical results for a large-scaled dike-break model. Research projects on fluid-structure interactions after a dam break were also initiated (e.g. SOARES-FRAZÃO, 2007; SOARES-FRAZÃO AND ZECH, 2007; YANG ET AL., 2010).

For the simple 2D dam-break wave, CHANSON (2009) gave a simple solution to determine the wave tip profile based on the St.-Venant equations. OZMEN-CAGATAY AND KOCAMAN (2010) compared the solutions of the shallow-water equations and the Reynolds-Averaged Navier-Stokes equation, indicating a better wave reproduction by using the latter.

With increasing computer processing capacity, numerical simulations for hydrodynamic processes become attractive, including dam-break problems. A comparison of these numerical results with experimental model or prototype data is still required for calibration and validation. This study deals with the initial stage of 2D dam-break waves comparing physical and numerical data as well as analytical approaches. High-speed images and the resulting Particle Image Velocimetry (PIV) calculations are thereby compared with those of the numerical Volume-of-Fluid (VOF) method. For various placed obstacles in the propagation area, drag forces are also analyzed and compared.

6.2.2 THEORETICAL BACKGROUND

6.2.2.1 RITTER'S SOLUTION

Ritter's analytical solution for the idealized frictionless dam-break wave within a rectangular channel is based on mass and energy conservation, resulting in the horizontal wave speed:

$$u = 2\sqrt{gh_0} - 3\sqrt{gh} \tag{6.2.1}$$

where u = horizontal velocity, g = acceleration due to gravity, h_0 = initial flow depth and h = flow depth at point of interest. If the flow depth at the wave front is $h = 0$, then the front velocity is

$$u = 2\sqrt{gh_0} \tag{6.2.2}$$

while for the negative wave into the reservoir of depth of $h = h_0$, the down-surge velocity is

$$u = -\sqrt{gh_0} \tag{6.2.3}$$

For the range $-(gh_0)^{0.5}t \leqslant x \leqslant 2(gh_0)^{0.5}t$ or time $t \geqslant x/(2(gh_0)^{0.5})$ if $x \geqslant 0$, and $t \geqslant x/(gh_0)^{0.5}$ if $x < 0$, respectively, the wave profile results in

$$h = \frac{1}{9g}\left(2\sqrt{gh_0} - \frac{x}{t}\right)^2 \tag{6.2.4}$$

with x = streamwise distance from original dam location and t = time from dam removal. Figure 6.2.1(A) shows the wave front profile for various time steps based on Eq. 6.2.4. Note that Ritter's solution yields a single curve (Fig. 6.2.1(B)) when using the dimensionless parameter X/T, with $X = x/h_0$ and $T = t(gh_0^{-1}))^{0.5}$.

6.2.2.2 WAVE TIP SOLUTION

Viscosity and friction obviously affect the dam-break wave tip region. Analytical solutions to describe this region were proposed depending on flow resistance. CHANSON (2009) introduced a simple solution based on the St.-Venant equations to predict the wave tip profile and compared it with experimental and numerical data. The resulting wave front location is

$$X_s = (3U - 1)\,T + \frac{(1-U)^4}{fU^2} \tag{6.2.5}$$

where X_s = dimensionless wave or surge front position (subscript s), $U = u/(4gh_0)^{0.5}$ = dimensionless wave front velocity and f = Darcy-Weisbach friction factor. For $-T \leqslant X \leqslant (3U-1)T$, Ritter's idealized fluid assumption is accurate, and the wave profile satisfies his solution:

$$\frac{h}{h_0} = \frac{1}{9}\left(2 - \frac{X}{T}\right)^2 \tag{6.2.6}$$

while for the tip region $(3U-1)T \leqslant x/h_0 \leqslant X$,

$$\frac{h}{h_0} = \sqrt{fU^2(X_s - X)} \tag{6.2.7}$$

CHANSON (2009) assumed a constant friction factor in the wave tip region. Its shape is described by

$$\frac{h}{h_0} = \left(\frac{9}{8}\left(3.65 \cdot 10^{-5}\frac{k}{d_0} + \frac{1.25^{\cdot -3}}{\mathrm{R}_d U}\right)^{1/4} U^2(X_s - X)\right)^{4/9} \tag{6.2.8}$$

Note that Eq. 6.2.8 was developed for wide channels, which is applicable for the wave tip region due to small flow depths compared to the channel width. In Fig. 6.2.1(A), the wave tip region is identified. For an idealized breach with the dam instantaneously removed, the wave front velocity is doubled when compared with the down-surge velocity. The wave profile thereby rotates about $4/9h_0$. Plotting the results versus X/T (Fig. 6.2.1(B)), the wave tip region changes its shape with time due to bottom resistance following CHANSON (2009), in contrast with Ritter's solution. Herein, the dimensionless front velocity U was calculated iteratively by Eq. 6.2.8. For increasing time steps, the wave tip region becomes steeper and the influenced wave tip length and wave height increase.

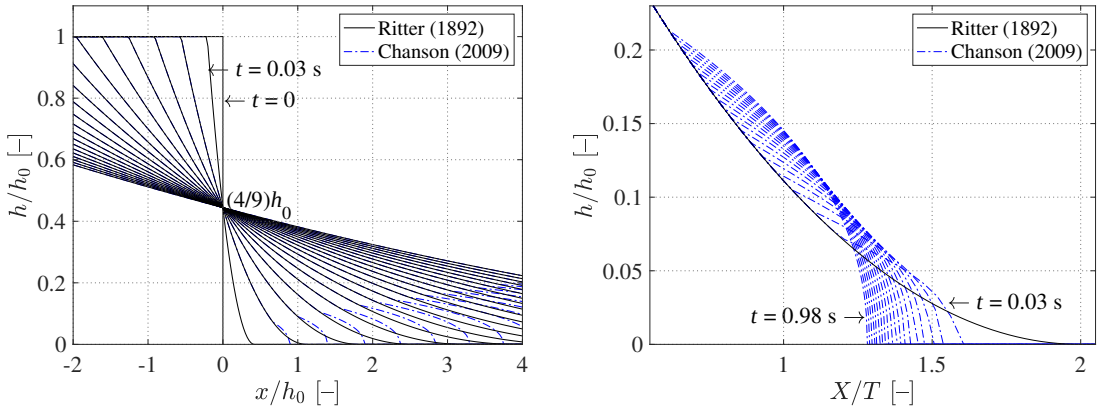

(A) Wave profile as a function of x/h_0 **(B)** Wave tip profile as a function of X/T

Figure 6.2.1: Dimensionless dam-break wave profile from Ritter's solution and analytical wave tip approach for various time steps for $t = 0.03$ to 0.9 s, $\Delta t = 0.03$ s, $h_0 = 0.2$ m, $\mu = 1 \cdot 10^{-3}$ kg/(ms) and $k = 0.001$ m

Other influences next to bottom friction are not included in the wave profile. When dealing with experimental models, it is difficult to remove a dam within a small time period. Hence, an effect on the wave front shape and velocity results. In nature, dams will not collapse immediately as well, so that the breach formation needs to be analyzed, which, however, is not discussed herein.

6.2.3 EXPERIMENTAL SETUP AND NUMERICAL MODEL

6.2.3.1 PHYSICAL MODEL

Physical model tests were conducted in a rectangular flume that was 22 m long, 0.30 m wide and 0.50 m high (Fig. 6.2.2). Both the bottom and the walls were made of Plexiglas with a surface roughness of k ~0.0015 mm. At a distance of 9 m from its downstream end, a vertical gate was installed, dividing the flume into two reaches; of which, the longer served as reservoir, while the other was dry before each test. The gate of 0.015 m thickness was guided by grooves within the flume sidewalls. A rubber seal avoided water leakage before lifting the gate by dropping a weight attached to a cable and guided by a pulley (Figs. 6.2.2(A) and 6.2.2(B)). Weights of 7.8, 9.6, 11.4 and 12.8 kg were used. The resulting dimensionless gate lift times, T_L, determined by a high-speed camera are described subsequently. It was found that the lift velocity is generally a function of the gate position. As the effect of the drop weight on the wave front velocity was found to be negligibly small, all tests were conducted using a weight of 11.4 kg and a drop height of 0.45 m. To minimize wave reflection and splashing at the downstream flume end, it was equipped with a screen acting as a filter (Fig. 6.2.2(C)). No data were taken after wave reflection from the screen.

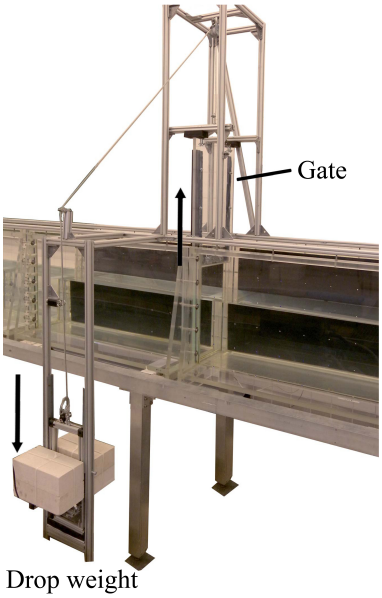

(A) Photograph of gate and towing apparatus

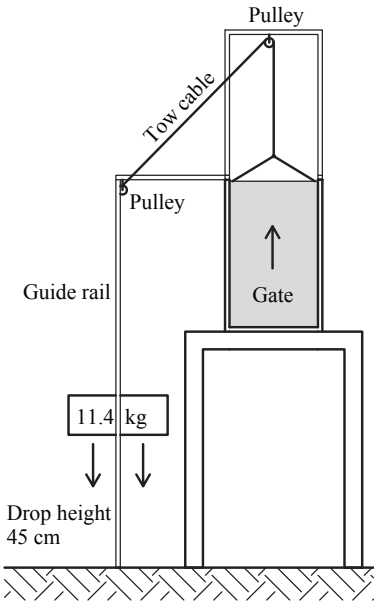

(B) Sectional sketch of towing apparatus

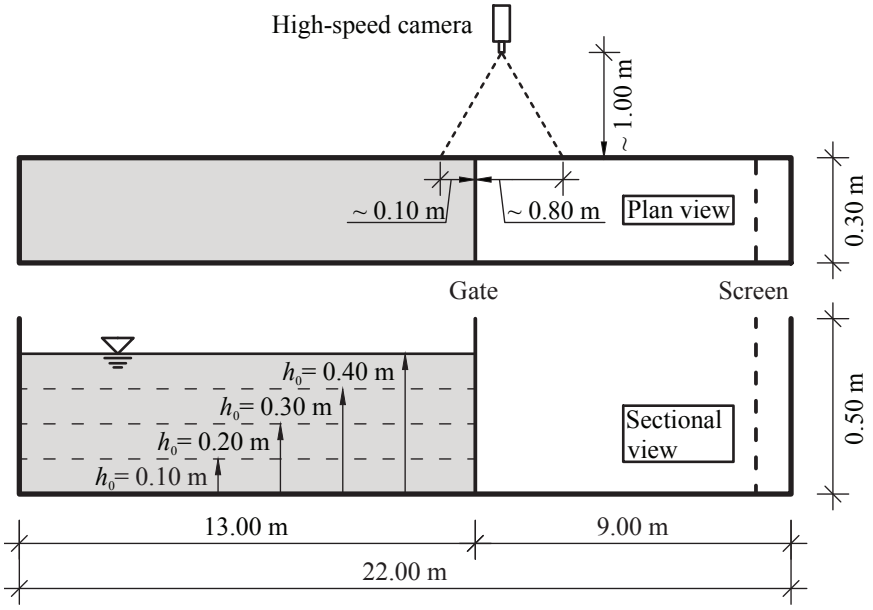

(C) Plan view and sectional view of flume facility (distorted)

Figure 6.2.2: Experimental setup

A high-speed camera was used to record the dam-break waves. The MotionScope M3 camera, Imaging Solutions, has a maximum sensor resolution of 1280 × 1024 pixels, each being 12 μm × 12 μm in physical size. The sample frequency (fps = frames per second) depends on the resolution, with 517 fps for maximum resolution. With decreasing resolution, the sample frequency increases up to 33,000 fps. Tests were carried out with a camera resolution of up to 1280 × 576 pixels and a sample rate of 1,000 fps (shutter time ~0.0009 s). The flow field was illuminated by halogen spot

lights. Additionally, the free surface was measured using seven ultrasonic probes at six positions downstream and one position upstream from the gate (General Acoustics, type USS 635, sample rate 75 Hz, accuracy ± 1 mm). The results were used to validate the free surface profile resulting from high-speed imaging.

6.2.3.2 PIV METHOD

The PIV method was applied to the high-speed images, seeding the water with fine polyamide tracers along the flume axis. After gate release, the particles mainly moved in the streamwise direction and particle spreading over the flume width was small so that wall effects may be neglected. Two subsequent frames with the constant time increment of 1 ms showed the movement of tracer particles within the observational area. A cross-correlation algorithm identified the best fit and determined the velocity field by $u = s_x \Delta t^{-1}$ and $w = s_z \Delta t^{-1}$, where s_x and s_z are particle movements in the x-direction and the z-direction, respectively. As the tracers have density nearly the same as that of the fluid, a slip-free particle movement was assumed. Data analysis was conducted using the open-source MATLAB® code MatPIV (V1.6.1) of SVEEN (2004). Besides the basic operation steps, that is, cross- and auto-correlation PIV and minimum quadratic difference calculations, a signal-to-noise ratio filter, a global histogram filter, a local filter and a masking mode for neglecting regions out of flow were applied with user-defined threshold values. The present correlations were performed with a variable interrogation window size of 32×32 pixels and 16×16 pixels, respectively, and an overlap of 50 %. To reduce computational time, areas which are not part of the flow field were masked. Note that near the gate, no information was available as the flume sidewalls were non-transparent (Fig. 6.2.2(A)). As no laser sheet was applied herein, the camera focused on a weakly-defined plane, assuming that similar particles are illuminated and focused in subsequent images so that errors remain small. A successful application of MatPIV combined with white light illumination was demonstrated by BUNG ET AL. (2008) and SRIRAM ET AL. (2010).

6.2.3.3 NUMERICAL MODEL

The VOF method as developed by HIRT AND NICHOLS (1981) for free boundary problems was applied. The commercial code FLOW-3D, version V9.4, was used to simulate the dam-break waves herein, along with the renormalized group turbulence model (RNG $k - \epsilon$). Previous investigations show its good applicability for free surface flows (e.g. BUNG ET AL., 2008). The 2D numerical model representing the physical model was simulated with 100,000 actively used cells of 0.005 m. The flume length was shortened to reduce calculation times. The dam-break process was simulated by a moving obstacle with a pre-defined lift velocity, found in the physical

model by use of the high-speed camera. The flume boundaries were thereby set slip free.

Table 6.2.1: Summary of model runs

No.	h_0 [m]	lab/num	wall	x_{ob} [m]	s_{ob} [m]
1	0.10	lab	yes	–	–
2	0.20	lab	yes	–	–
3	0.30	lab	yes	–	–
4	0.40	lab	yes	–	–
5	0.10	num	yes	–	–
6	0.20	num	yes	–	–
7	0.30	num	yes	–	–
8	0.40	num	yes	–	–
9	0.10	num	no	–	–
10	0.20	num	no	–	–
11	0.30	num	no	–	–
12	0.40	num	no	–	–
13	0.20	lab	yes	0.20	0.02
14	0.20	lab	yes	0.40	0.02
15	0.20	lab	yes	0.20	0.06
16	0.20	lab	yes	0.40	0.06
17	0.20	num	yes	0.20	0.02
18	0.20	num	yes	0.40	0.02
19	0.20	num	yes	0.20	0.06
20	0.20	num	yes	0.40	0.06
21	0.10	num	yes	0.10	0.02
22	0.10	num	yes	0.20	0.02
23	0.10	num	yes	0.30	0.02
24	0.10	num	yes	0.40	0.02
25	0.10	num	yes	0.10	0.06
26	0.10	num	yes	0.20	0.06
27	0.10	num	yes	0.30	0.06
28	0.10	num	yes	0.40	0.06
29	0.20	num	yes	0.10	0.02
30	0.20	num	yes	0.30	0.02
31	0.20	num	yes	0.10	0.06
32	0.20	num	yes	0.30	0.06
33	0.30	num	yes	0.10	0.02
34	0.30	num	yes	0.20	0.02
35	0.30	num	yes	0.30	0.02
36	0.30	num	yes	0.40	0.02
37	0.30	num	yes	0.10	0.06
38	0.30	num	yes	0.20	0.06
39	0.30	num	yes	0.30	0.06
40	0.30	num	yes	0.40	0.06
41	0.40	num	yes	0.10	0.02
42	0.40	num	yes	0.20	0.02
43	0.40	num	yes	0.30	0.02
44	0.40	num	yes	0.40	0.02
45	0.40	num	yes	0.10	0.06
46	0.40	num	yes	0.20	0.06
47	0.40	num	yes	0.30	0.06
48	0.40	num	yes	0.40	0.06

6.2.3.4 MODEL RUNS

More than 40 model tests have been conducted with the physical and numerical models (Table 6.2.1), in which the numerical tests were analyzed with and without moving obstacles as dam walls. The initial water depths included $h_0 = 0.1, 0.2, 0.3$ and 0.4 m ($T_L = 0.93, 1.12, 1.33$ and 1.43). Four configurations with rectangular obstacles (subscript *ob*) of height $s_{ob} = 0.02$ and 0.06 m, placed in the wave propagation area of obstacle distance to gate $x_{ob} = 0.2$ and 0.4 m, were tested with the physical model at $h_0 = 0.20$ m. For these cases, the drag forces were measured with load cells. The reproduced model tests for all physical model configurations involved an accuracy of ± 5 %. Once the numerical model was in agreement with the physical model data, additional numerical tests were arranged for combinations of x_{ob} and h_0 for $s_{ob} = 0.02$ and 0.06 m. The forces from the numerical model were determined by integrating the upstream (subscript *us*) and downstream (subscript *ds*) pressures as

$$F_D = \int_{z=0}^{z=s_{ob}} p_{us}(z) - p_{ds}(z) \mathrm{d}z \tag{6.2.9}$$

with F_D as the drag force in the x-direction, z = vertical coordinate above flume bottom and p = pressure.

6.2.4 RESULTS AND DISCUSSION

6.2.4.1 REFERENCE CASE WITHOUT OBSTACLES

When comparing the physical model wave tip region with that determined by the analytical and numerical approaches, several phenomena are identified. The main difference results for the wave front velocity. The velocity reduces as a function of the equivalent bottom sand roughness height k and the dynamic viscosity μ. Hence, the tip region is curved as shown by, for example, LAUBER AND HAGER (1998A). Generating dam-break waves within a physical model, the wave tip velocity and shape also depend on the gate lift velocity. Figure 6.2.3 compares the high-speed images and ultrasonic sensor results (USS) with the approach of CHANSON (2009) and the VOF model for $h_0 = 0.40$ m. Comparing the wave profile with the USS results, a maximum error of 3-5 % is found. The analytical approach does not satisfy the experimental data since the gate opening time exceeded the critical limit $T_L = 1$ (e.g. LAUBER AND HAGER, 1998A). However, since identical opening times were used in the numerical and experimental tests, validation of VOF and PIV results is possible. Focusing on the high-speed images, the effect of the gate velocity is identified especially for $T \leqslant 1.49$. Since the gate has not released all the water within this time, wave propagation is delayed. The first time steps ($T \leqslant 0.50$) indicate that the wave generation starts with a high turbulent splash.

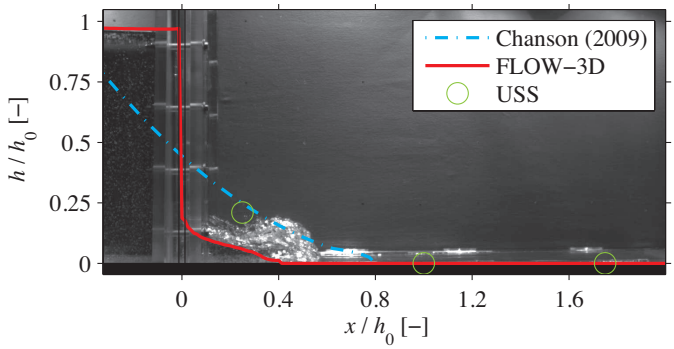

(A) $T = t(gh_0^{-1})^{0.5} = 0.50$

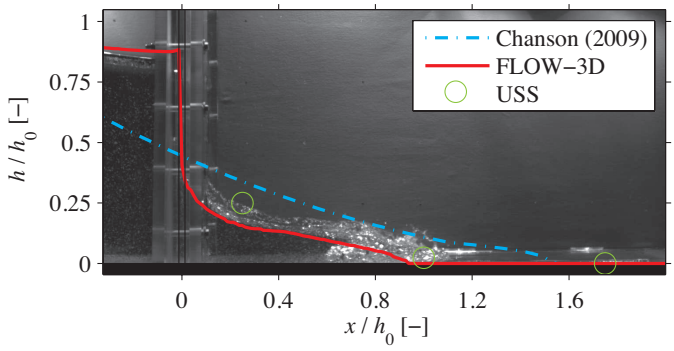

(B) $T = t(gh_0^{-1})^{0.5} = 0.99$

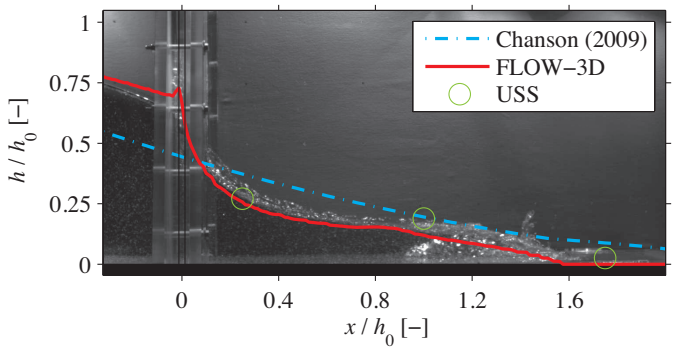

(C) $T = t(gh_0^{-1})^{0.5} = 1.49$

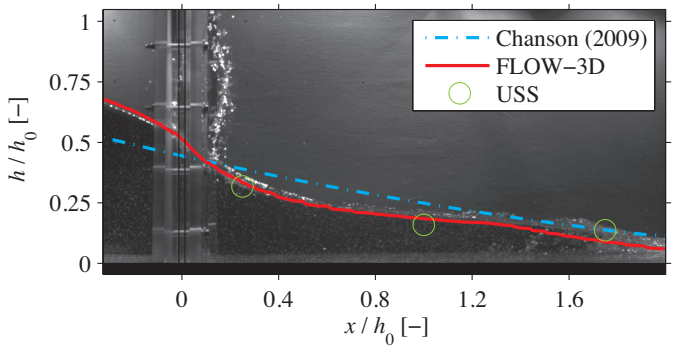

(D) $T = t(gh_0^{-1})^{0.5} = 1.98$

Figure 6.2.3: Physical model, numerical VOF model and analytical results for $\mu = 10^{-3}$ kg/(ms), $k = 0.001$ m and various dimensionless times

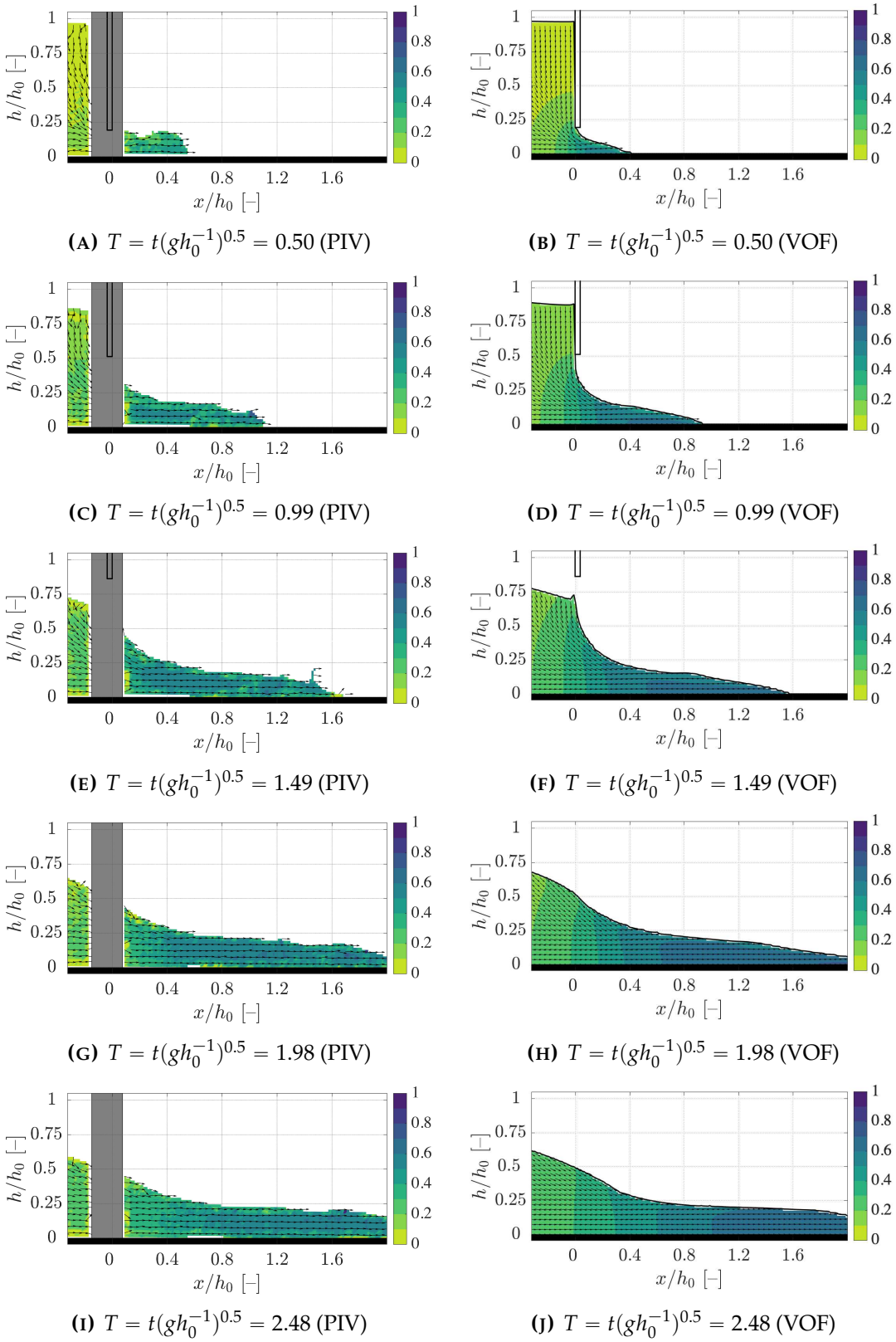

(A) $T = t(gh_0^{-1})^{0.5} = 0.50$ (PIV)

(B) $T = t(gh_0^{-1})^{0.5} = 0.50$ (VOF)

(C) $T = t(gh_0^{-1})^{0.5} = 0.99$ (PIV)

(D) $T = t(gh_0^{-1})^{0.5} = 0.99$ (VOF)

(E) $T = t(gh_0^{-1})^{0.5} = 1.49$ (PIV)

(F) $T = t(gh_0^{-1})^{0.5} = 1.49$ (VOF)

(G) $T = t(gh_0^{-1})^{0.5} = 1.98$ (PIV)

(H) $T = t(gh_0^{-1})^{0.5} = 1.98$ (VOF)

(I) $T = t(gh_0^{-1})^{0.5} = 2.48$ (PIV)

(J) $T = t(gh_0^{-1})^{0.5} = 2.48$ (VOF)

Figure 6.2.4: Dimensionless velocity $U = u/(4gh_0)^{0.5}$ for $h_0 = 0.40$ m, PIV from physical model compared to VOF

After the complete water body moves ($T > 1.49$), the wave propagation proceeds with a concave surface profile. The velocities below the wave surface are determined by the PIV method. Figure 6.2.4 shows these velocities up to $T = 2.48$ using the masked calculation area. Dimensionless velocities of $U \leqslant 0.75$ occur below the dam-break wave, that is, less than that obtained from Eq. 6.2.2. Their main direction is longitudinal in the wave tip area. Near the gate, the reduction of the reservoir flow depth leads to mainly vertical velocity components. Analyses were limited to $-0.2 < x/h_0 < 2.0$ for dam-break waves without obstacles.

Compared with the numerical results, the initial flow aeration at $T = 0.50$ and the resulting increase in flow depth at the wave front are not well reproduced (Figs. 6.2.4(A) and 6.2.4(B)). Moreover, the corresponding wave velocities are higher and closer to Ritter's solution for all times. This discrepancy appears to be due to the strong aeration at the wave front leading to strong light reflections and thus affecting the PIV results (Fig. 6.2.5). The maximum aerated flow depth at the wave front is roughly $0.2h_0$.With further wave propagation, the aeration reduces and the velocities tend towards those of an idealized theoretical solution. A detailed analysis on these characteristics (e.g. CHANSON, 2004) was not attempted herein. Generally, the wave profile is accurately predicted with the numerical model.

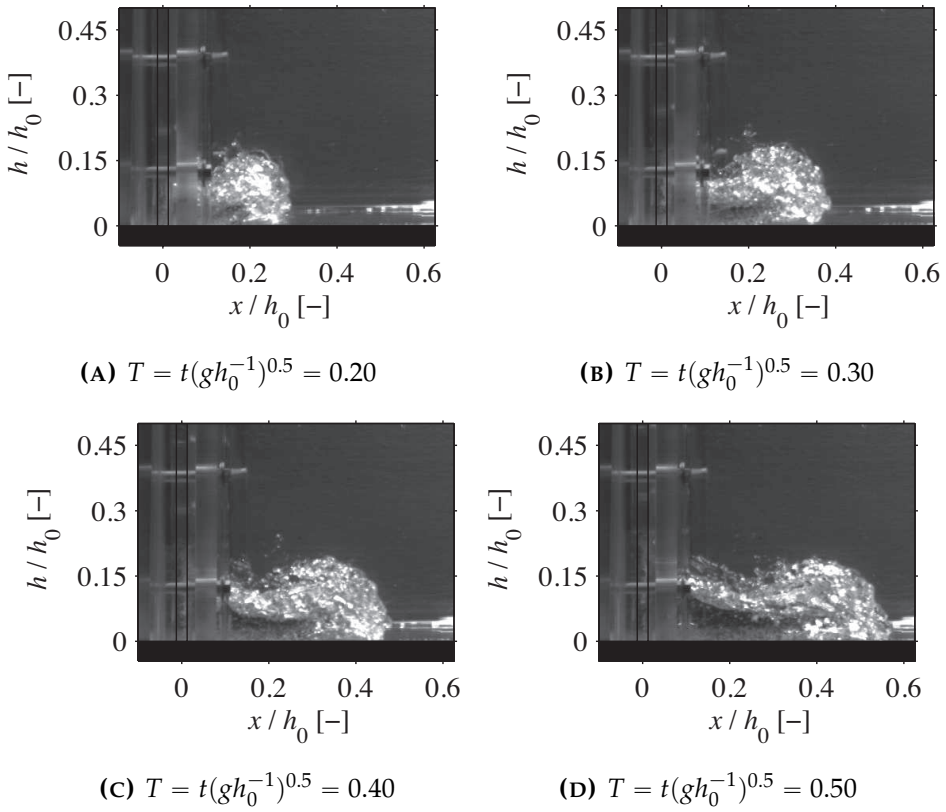

(A) $T = t(gh_0^{-1})^{0.5} = 0.20$ **(B)** $T = t(gh_0^{-1})^{0.5} = 0.30$

(C) $T = t(gh_0^{-1})^{0.5} = 0.40$ **(D)** $T = t(gh_0^{-1})^{0.5} = 0.50$

Figure 6.2.5: Wave front aeration in the physical model

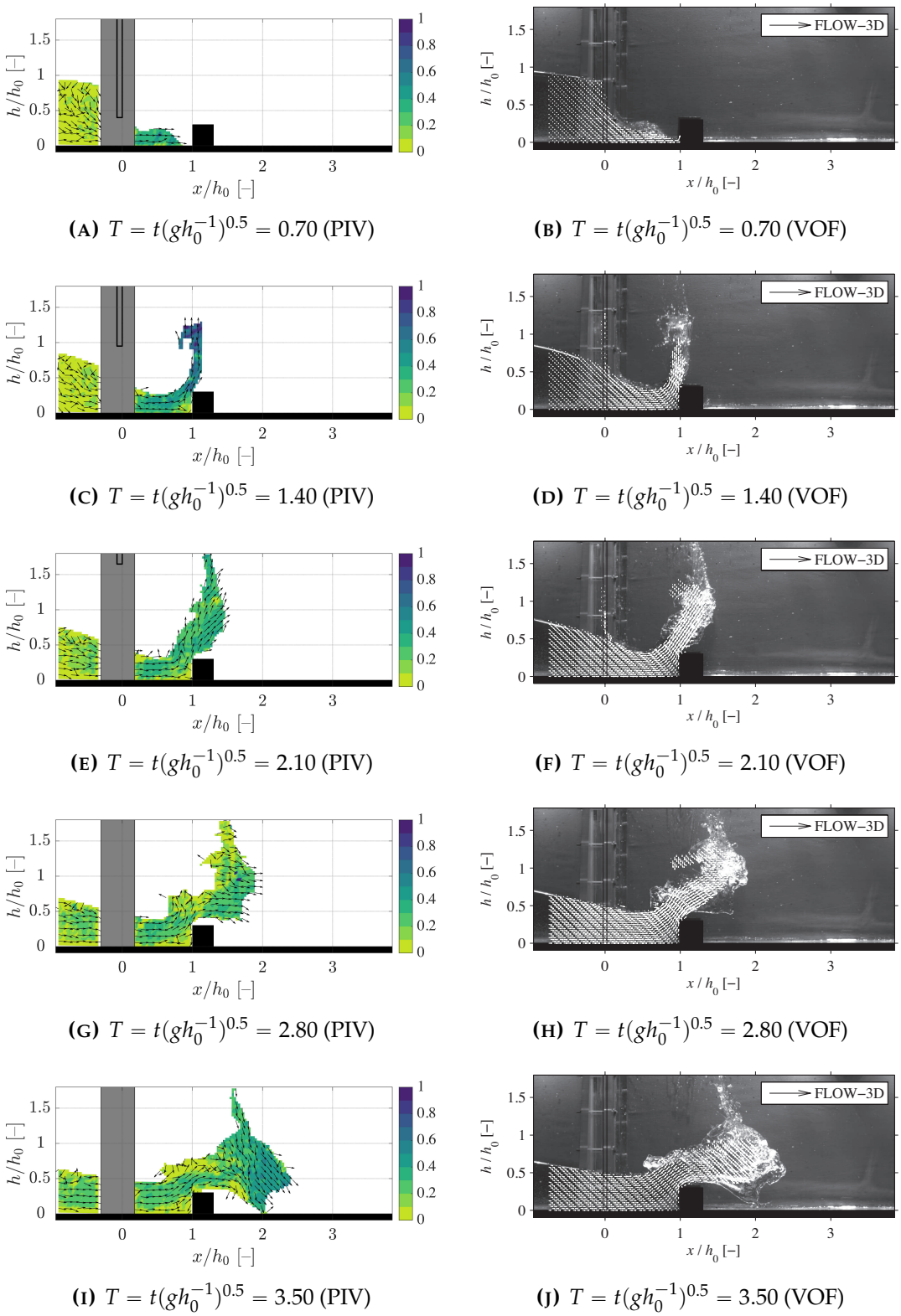

(A) $T = t(gh_0^{-1})^{0.5} = 0.70$ (PIV) **(B)** $T = t(gh_0^{-1})^{0.5} = 0.70$ (VOF)

(C) $T = t(gh_0^{-1})^{0.5} = 1.40$ (PIV) **(D)** $T = t(gh_0^{-1})^{0.5} = 1.40$ (VOF)

(E) $T = t(gh_0^{-1})^{0.5} = 2.10$ (PIV) **(F)** $T = t(gh_0^{-1})^{0.5} = 2.10$ (VOF)

(G) $T = t(gh_0^{-1})^{0.5} = 2.80$ (PIV) **(H)** $T = t(gh_0^{-1})^{0.5} = 2.80$ (VOF)

(I) $T = t(gh_0^{-1})^{0.5} = 3.50$ (PIV) **(J)** $T = t(gh_0^{-1})^{0.5} = 3.50$ (VOF)

Figure 6.2.6: Velocities for a dam-break wave with obstacle at propagation area for $h_0 = 0.20$ m, $x_{ob} = 0.20$ m, $s_{ob} = 0.06$ m, PIV from physical model compared to VOF

6.2.4.2 EFFECT OF OBSTACLES

Placing obstacles in the wave propagation area results in a fundamentally different dam-break wave (compare Fig. 6.2.4 with Fig. 6.2.6). The wave impacts the obstacle and is redirected in the upstream direction. While the reservoir continues to empty, the flow changes its horizontal direction again and overflows the obstacle with decelerated velocities. Figure 6.2.6 compares the physical and numerical models. The VOF model reproduces the obstacle-affected dam-break wave with the same accuracy as the standard dam-break wave.

The maximum redirected splash height after the wave front has impacted the obstacle is nearly unaffected by the obstacle distance from the gate. Due to the smooth bottom, the momentum reduction remains small. Thus, the resulting forces acting on the obstacle are also not greatly affected by the spacing between the gate and the obstacle. On comparing the measured and computed drag forces on the obstacles, two typical phenomena emerge. The initial water impact on the obstacle is characterized by a high force (the first peak in Fig. 6.2.7). During obstacle overflow, the air accumulation upstream from the obstacle is fully removed, leading to reduced drag and a quasi-steady-state situation (Fig. 6.2.7). The maximum drag forces are shown in Fig. 6.2.8. Herein, analyses were limited to $-1.0 < x/h_0 < 4.0$ for dam-break waves with obstacles.

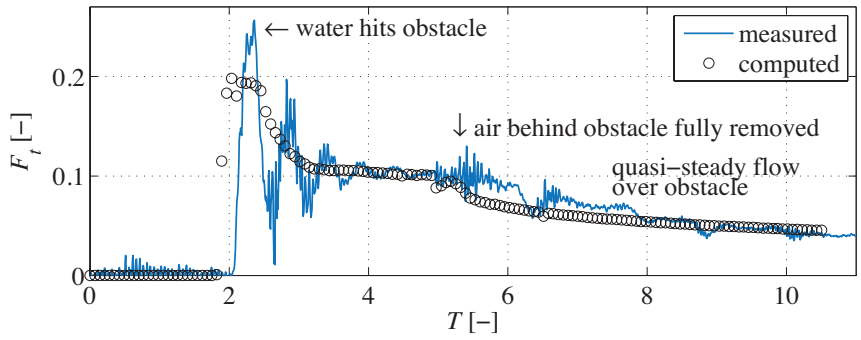

Figure 6.2.7: Typical dimensionless temporal drag force F_t acting on obstacle (laboratory vs. numerical simulation)

The maximum dimensionless drag force $F = F_{D\max}/(0.5\rho g h_0^2)$ follows the fit with $R^2 = 0.97$ (Fig. 6.2.8):

$$F = 1.38 \left(\frac{h_0}{s_{ob}} \right)^{-0.4} - 0.35 \tag{6.2.10}$$

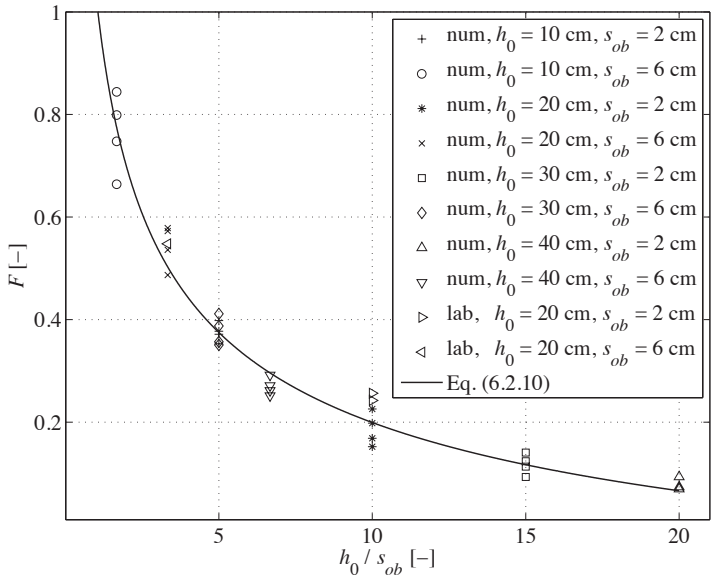

Figure 6.2.8: Dimensionless drag force F versus dimensionless obstacle height h_0/s_{ob} compared with Eq. 6.2.10

Equation 6.2.10 applies for $1.6 \leqslant h_0/s_{ob} \leqslant 20$. Note that this approach is independent from the distance between the gate and the obstacle, as described previously. For rough prototype bottoms, a decrease in the drag force is assumed to occur along the wave propagation.

6.2.5 CONCLUSIONS

The understanding of dam-break wave hydraulics is important to develop flood protection measures. In this regard, this research dealt with the physical and numerical model results of 2D dam-break waves comparing, among others, the PIV method with the VOF method, included in the commercial code FLOW-3D. It was found that the numerical simulations fit the physical model data of the wave surface and the velocity profiles including gate effects, whereas the analytical approaches are unable to include the gate effect. When placing an obstacle in the dam-break propagation area, the wave is redirected in the vertical direction after impacting the obstacle. With continuing wave propagation, streamwise velocities are reduced due to the obstacle. The maximum dimensionless drag force was also determined, with the VOF method again indicating a good comparability with the physical model data, leading to the conclusion that VOF simulations apply well for dam-break waves with and without obstacles in the propagation area. Limitations of this research were pointed out.

6.3 NON-INTRUSIVE MEASURING OF AIR-WATER FLOW PROPERTIES IN SELF-AERATED STEPPED SPILLWAY FLOW

Authors: Daniel B. Bung
Conference: 34th IAHR World Congress, Brisbane
Year: 2011

Abstract: For hydraulic design of stepped spillways, knowledge of flow properties as flow depth and velocity of the air-water mixture is essential. Generally, these parameters are measured on large-scale models by use of an intrusive probe (i.e. double-tip conductivity or fiber-optical probe) and scaled to prototype dimensions. In this paper, the capability and limitation of non-intrusive measuring devices are analyzed by comparison with a large model data set measured with a double-tip conductivity probe in skimming flow regime. In fact, flow depths are measured with an ultrasonic sensor and velocity fields are determined by use of a modified high-speed PIV method (Bubble Image Velocimetry). The results indicate that non-intrusive devices may be applied for a first estimation of flow properties with sufficient accuracy. The flow field above the pseudo-bottom and within the cavity of the steps can be visualized in high resolution.

Keywords: Stepped spillway flow, air-water flow, non-intrusive measuring methods, Bubble Image Velocimetry, ultrasonic sensors

6.3.1 INTRODUCTION

Numerous research studies on self-aerated spillway and stepped spillway flows have been conducted in recent years. Typically, the air concentration, the air-water mixture depth and the flow velocity are of particular interest. Various measuring systems have been applied for determination of these parameters. For instance, double-tip needle probes detecting both, phase transition and air-water mixture velocity, on basis of a conductivity or fiber-optic principle, respectively, have been successfully used in laboratory studies (CHANSON, 2002A; KRAMER, 2004). Alternatively, the velocity may be determined by means of backflushing pitot tubes for air concentrations up to 70-80 % and ADV probes (Acoustic Doppler Velocimeter) if the air content is less than 8 % (MATOS ET AL., 2002).

These methods require a complex setup and long measuring time in order to calculate time-averaged values of the highly turbulent flow parameters in various heights. Moreover, intrusion of measuring devices may generally affect the flow field and hence, lead to distorted results.

In this paper, comparative investigations with intrusive and non-intrusive measuring methods are presented. For this purpose, experiments on a stepped spillway model with two moderate slopes ($\phi = 18.4^\circ$ and $\phi = 26.6^\circ$), two step heights ($s = 3$ cm and

$s = 6$ cm) and three specific discharges ($q = 0.07$ m^2/s, $q = 0.09$ m^2/s and $q = 0.11$ m^2/s) are conducted. With these geometry and discharge combinations, skimming flow regime sets in with all configurations. In this flow regime, water flows down as a coherent stream above the imaginary pseudo-bottom formed by the step edges (OHTSU ET AL., 2004).

On the one hand, air concentration, flow velocity and air-water mixture depth are determined with a classical, intrusive double-tip conductivity probe. On the other hand, the surface of the air-water mixture body along the non-uniform flow region is detected with a non-intrusive ultrasonic sensor and the flow and velocity field in uniform flow region is visualized by application of the BIV method. This method was introduced by RYU ET AL. (2005) focussing on aeration due to breaking waves and adopted to open channel cavity flows by LIN ET AL. (2008). The procedure is a modified PIV method (Particle Image Velocimetry) which directly uses the bubbles illuminated by white light as tracers and measures the bubble velocity by correlating the texture of subsequent snapshots of the air-water flow. In air-water flows, the original PIV method is limited to low air concentrations (e.g. undular hydraulic jumps with low Froude numbers) as air bubbles distort the optical rays between the image and the acquisition plane (LENNON AND HILL, 2006). The applicability of ultrasonic sensors for surface detection in highly turbulent, aerated flows, e.g. hydraulic jumps, has been proven by MURZYN AND CHANSON (2009B).

Adaptability to stepped spillway flows and limitation of both methods, the ultrasonic measurements and the BIV procedure, will be discussed subsequently.

6.3.2 METHODOLOGY

All investigations are carried out on a physical model scaled 1:10 with a total drop height of 2.34 m and a chute width of 30 cm. Two spillway slopes ($\phi = 18.4^\circ$ and $\phi = 26.6^\circ$), two step heights ($s = 3$ cm and $s = 6$ cm) and three specific discharges ($q = 0.07$ m^2/s, $q = 0.09$ m^2/s and $q = 0.11$ m^2/s) are taken into account. The parameter variation leads to 12 examined configurations involving skimming flow regime. The modeled structure is part of a closed water circuit. Water is pumped into a system of two open head tanks. Small tubes are installed in the approaching channel in order to distribute and calm down the flow before being conveyed. Two pumps generate the examined discharges controlled by a flap valve. Discharge is checked with an IDM system and verified with an ultrasonic sensor and an appropriate rating curve installed in the approaching channel.

This is an **Author's Accepted Manuscript** of a conference paper published in the Proceedings of the 34th IAHR World Congress (Brisbane, 2011) by Engineers Australia, ISBN:978-0-8582-5868-6.

6.3.2.1 DOUBLE-TIP CONDUCTIVITY PROBE

Intrusive measurements of air-water flow properties are conducted by means of a double-tip conductivity probe. This probe is characterized by two electrodes with diameters of 130 μm which are arranged back-to-back in flow direction (manufactured at IWW, RWTH Aachen, Fig. 6.3.1). Depending on the surrounding medium (i.e. water or air) a high or low voltage is sampled for 25 s with a sample rate of 25 kHz. Phase detection is realized by application of a combined dual-threshold and slope criterion applied to the raw data (THORWARTH, 2008). By cross-correlating both signals, the time lag which results in a maximum correlation factor may be interpreted as the traveling time Δt_e of air bubbles between both tips. With knowledge of the distance Δx_e in flow direction of the two electrodes (which is 5.1 mm here) the flow velocity $u = \Delta x_e / \Delta t_e$ of the air-water mixture can be calculated. This method assumes that no slip occurs between air bubbles and water on the one hand and that both tips pierce the same bubbles despite the distance of 1 mm in cross-direction.

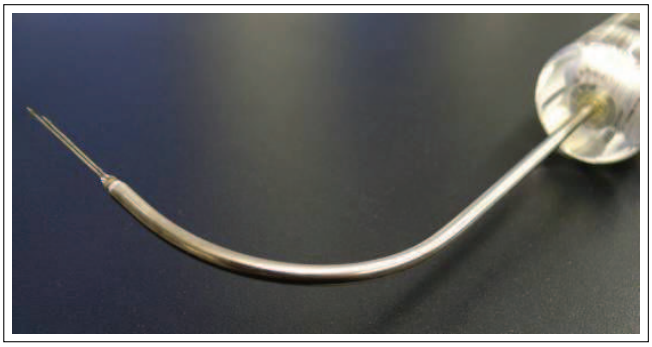

Figure 6.3.1: Double-tip conductivity probe for determination of air concentration and flow velocity (note: 2 electrodes with a distance of 5.1 mm in flow direction and 1 mm in cross-direction)

Exact positioning of the probe is achieved by a two-dimensional linear guide system operated by a CNC controller (isel). Since the probe allows for measurement of one-dimensional flows only, all experiments are limited to the skimming water body ($z > 0$). The cavity flow fields, characterized by large vortices, are disregarded. For both step heights, measurements are carried out in the centerline of the flume at the step edges ($x/L_s = 0$) and additionally at the middle of the step niches ($x/L_s = 0.5$) in case of the larger steps. L_s is the distance between two step edges along the pseudo-bottom.

6.3.2.2 ULTRASONIC SENSOR

An ultrasonic sensor (General Acoustics, USS60350) with a measuring range of 60 to 350 mm is used for non-intrusive determination of the flow depth. According to the

This is an **Author's Accepted Manuscript** of a conference paper published in the Proceedings of the 34th IAHR World Congress (Brisbane, 2011) by Engineers Australia, ISBN:978-0-8582-5868-6.

producer the resolution is 0.18 mm. The sensor is mounted exactly above the double-tip conductivity probe in order to ensure identical measuring locations (Fig. 6.3.2). The probe calibration, carried out before each measurement in dry conditions, refers to the pseudo-bottom formed by the step edges. For calibration a rigid smooth invert plate is installed in the channel. After starting the pumps and attaining steady-state flow conditions, data at each location is sampled for 60 s with a rate of 15 Hz.

Figure 6.3.2: Ultrasonic sensor for determination of air-water mixture depth (note: double-tip conductivity probe below during measurement)

Data analysis is conducted by means of a smoothed sample using a moving average filter. Evident measurement errors are identified by a threshold defined as the mean value +/- two times the standard deviation of the raw signal and detected outliers are eliminated. However, the influence of these measuring inaccuracies is found to be negligible. Figure 6.3.3 illustrates two exemplary samples in comparison to the smoothed signals.

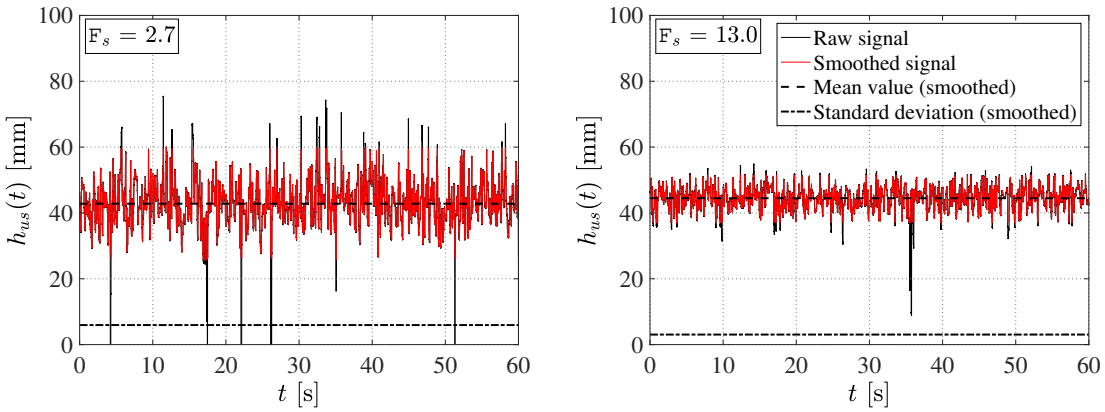

(A) $\phi = 26.6°$, $s = 6$ cm, $q = 0.07$ m^2/s **(B)** $\phi = 18.8°$, $s = 3$ cm, $q = 0.11$ m^2/s

Figure 6.3.3: Exemplary ultrasonic sensor samples (raw and smoothed) in uniform flow region

This is an **Author's Accepted Manuscript** of a conference paper published in the Proceedings of the 34th IAHR World Congress (Brisbane, 2011) by Engineers Australia, ISBN:978-0-8582-5868-6.

Obviously, the accuracy of the sample strongly depends on the step Froude number

$$F_s = \frac{q}{\sqrt{g \cdot \sin\phi \cdot K^3}} \tag{6.3.1}$$

with q the specific discharge, g the gravity constant, ϕ the spillway slope and K the step-induced macro-roughness $K = s \cdot \cos\phi$. Low step Froude numbers are involved by low discharges or high steps, respectively, and describe a more chaotic, unstable flow regime.

6.3.2.3 BUBBLE IMAGE VELOCIMETRY (BIV)

The Bubble Image Velocimetry technique (BIV) is comparable to the classical Particle Image Velocimetry except that the flow field is illuminated by halogen spot lights producing white light instead of using a laser sheet. Due to the strong aeration in stepped spillway flows the visibility of the laser sheet would be significantly reduced. Further, laser reflections on air bubble surfaces are uncontrollable and may damage the camera lens or lead to severe injuries for the personnel. Assuming a slip-free air bubble transport, the flow velocity can be calculated by correlating the textures of two subsequent air bubble snapshots taken with a defined time shift. The bubbles act then as tracers. Since the illuminated bubbles are not limited to a well-defined plane as in case of PIV, the results become less accurate. Air bubbles, which are out of focus, may be included in calculations and distort the resulting velocity field. However, the technique allows a first estimation of velocity distributions and flow field characteristics.

In this study, high speed movies of the stepped spillway flow in uniform flow region are taken with a frequency of 1220 fps. This sample rate is required in order to capture the high-speed flow characteristics. The resolution of the camera (KSV Instruments, HiSiS2000) is 256 × 256 px. In dependence of the examined configurations, the width of the field of view is about 16 to 22 cm resulting in a pixel density of about 12 to 16 px/cm. With a maximum velocity of approximately 400 cm/s, the maximum movement of a single bubble between two subsequent frames is then about 4 to 5 px. The flow field is illuminated by means of halogen spot lights with a total power of 1300 W. BIV calculations are performed with use of the open-source Matlab® toolbox MatPIV in its latest version 1.6.1 (SVEEN, 2004). Besides the basic operation steps, i.e. cross- and auto-correlation PIV and MQD (Minimum Quadratic Difference) calculations, several filters like a signal-to-noise ratio filter, global histogram filter, local filter and a masking mode for neglecting regions out of flow can be applied with user defined threshold values. Further, the correlation process can be easily integrated in a loop in order to repeat the calculation.

This is an **Author's Accepted Manuscript** of a conference paper published in the Proceedings of the 34th IAHR World Congress (Brisbane, 2011) by Engineers Australia, ISBN:978-0-8582-5868-6.

In this study, the correlation has been performed for 1200 subsequent frame pairs with an interrogation window size of 16 × 16 px and 75 % overlap. The filtered results obtained by these 1199 PIV calculations are then superposed and averaged by taking the median of all single values. With this procedure a more robust description of the time-averaged velocity field is obtained. In order to reduce the calculation time, the step contour is masked as shown in Fig. 6.3.4. The figure further illustrates the interrogation window size and overlap in comparison to the total picture size and the maximum air bubble movement.

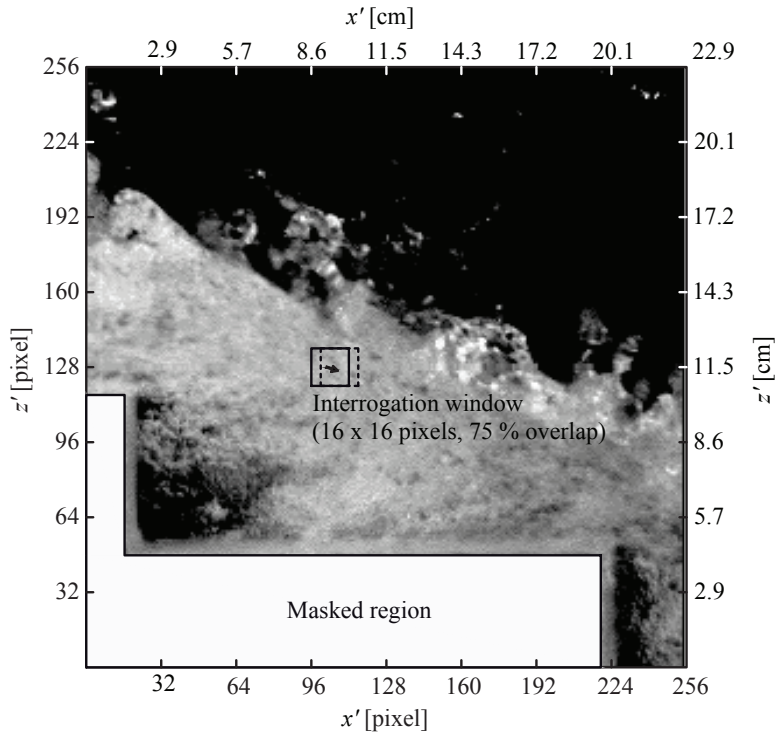

Figure 6.3.4: High-speed frame with 256 x 256 px, interrogation window with 16 x 16 px and 75 % overlap, masked region for reduction of calculation time (exemplarily for $\phi = 18.4°$, $s = 6$ cm, $q = 0.09$ m^2/s, arrow illustrates maximum air bubble movement of approx. 4 px)

The applicability of MatPIV in combination with white light illumination has been successfully demonstrated by BUNG ET AL. (2008) focussing on the visualization of the unaerated flow field behind a submerged plate under a propagating bore.

6.3.3 RESULTS

6.3.3.1 FLOW DEPTH

It is found that h_{us}, which is the time-averaged value of the flow depth measured by use of the ultrasonic sensor, is correlated to a specific present air concentration. This air concentration may be specified to 80 % (approximately 75 % in case of the

This is an **Author's Accepted Manuscript** of a conference paper published in the Proceedings of the 34th IAHR World Congress (Brisbane, 2011) by Engineers Australia, ISBN:978-0-8582-5868-6.

smaller steps and 85 % for the higher steps). The characteristic water depth h_{us} can be interpreted as obstruction water depth for the ultrasonic signal. Below this depth the air-water mixture density precludes the signal from penetrating.

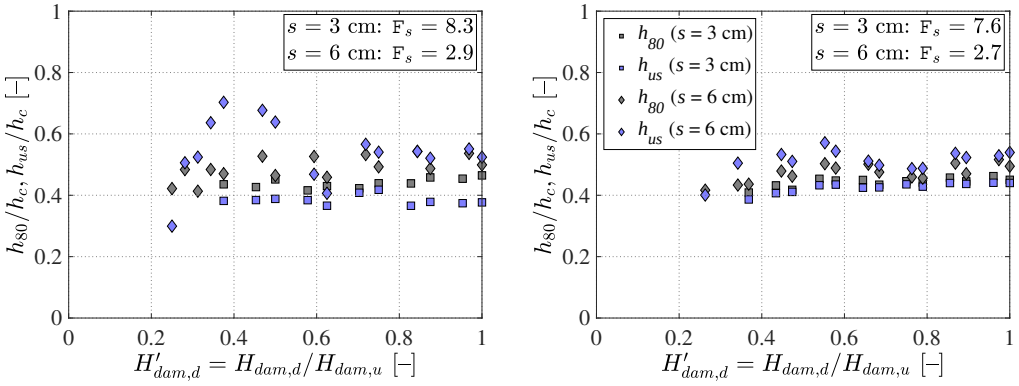

(A) $\phi = 18.4°$, $q = 0.07\ \mathrm{m^2/s}$

(B) $\phi = 26.6°$, $q = 0.07\ \mathrm{m^2/s}$

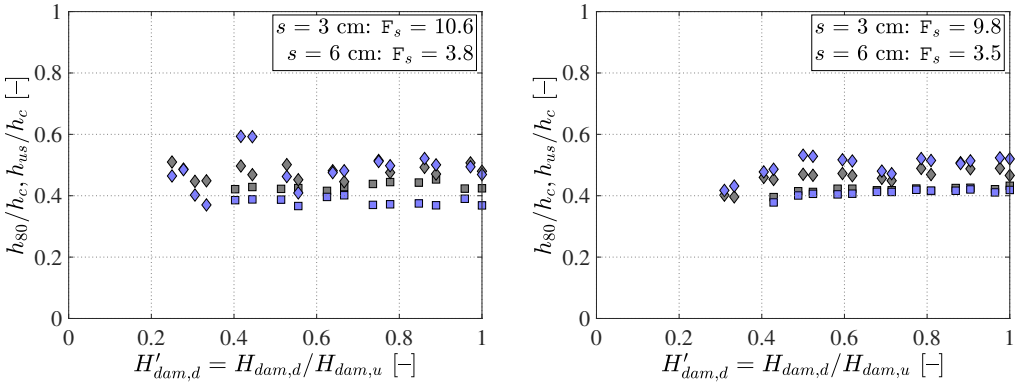

(C) $\phi = 18.4°$, $q = 0.09\ \mathrm{m^2/s}$

(D) $\phi = 26.6°$, $q = 0.09\ \mathrm{m^2/s}$

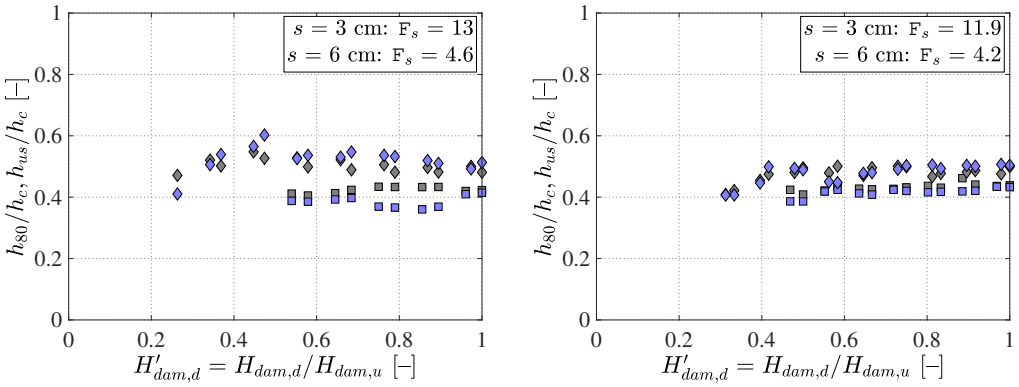

(E) $\phi = 18.4°$, $q = 0.11\ \mathrm{m^2/s}$

(F) $\phi = 26.6°$, $q = 0.11\ \mathrm{m^2/s}$

Figure 6.3.5: Comparison of the development of dimensionless characteristic flow depth h_{80}/h_c and dimensionless mean flow depth h_{us}/h_c measured with ultrasonic sensor in non-uniform flow region for all investigated configurations

This finding is illustrated in Fig. 6.3.5 comparing the characteristic flow depth h_{80} measured by use of the conductivity probe with h_{us} obtained by averaging the

This is an **Author's Accepted Manuscript** of a conference paper published in the Proceedings of the 34th IAHR World Congress (Brisbane, 2011) by Engineers Australia, ISBN:978-0-8582-5868-6.

filtered ultrasonic signal along the non-uniform flow region. The dimensionless drop height $H'_{dam,d}$ relates the total drop height $H_{dam,d}$ to the drop height $H_{dam,u}$ where uniform flow conditions have been attained. Generally, a good agreement between both quantities is found. However, larger deviations must be noted for model configurations with the smallest discharge $q = 0.07$ m^2/s and the step height $s = 6$ cm. Especially near the inception point of self-aeration, a more chaotic flow regime is present as it is in case of higher discharges or lower step heights leading to a stabilization of the flow. Although the sampling frequency could not be varied within this study, it is assumed that it affects the obstruction depth. Hence, the water depth h_{80} found in these experiments must be considered to be fixed by the applied sensor. However, the other way round it is assumed that ultrasonic sensors may be calibrated for a certain water depth by variation of the sampling frequency. If so, it could be possible to calibrate a second sensor to a water depth h_{90} with $C = 90$ % which is generally defined to be the idealized water depth of air-water mixtures on spillways. With knowledge of h_{90} and any second characteristic water depth below (e.g. h_{80} as detected in this study) the air concentration distribution $C(z)$ between the pseudo-bottom and h_{90} is clearly defined as illustrated in Fig. 6.3.6. Moreover, the air concentration distribution is a function of the mean air content C_{mean} only (CHANSON AND TOOMBES, 2001), which may indirectly be determined.

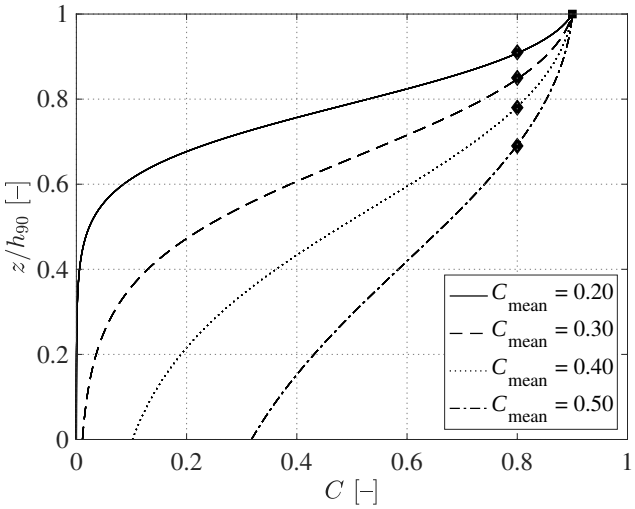

Figure 6.3.6: Air concentration distribution $C(z/h_{90})$ according to advective air bubble diffusion model developed by CHANSON AND TOOMBES (2001) for varying mean air contents C_{mean} (note: h_{90} and an additional characteristic water depth below h_{90} clearly define the corresponding air concentration distribution and the mean air content)

6.3.3.2 FLOW VELOCITY

Exemplary velocity fields calculated with the BIV method for uniform flow conditions are illustrated below. Figure 6.3.7(A) presents the result for the model configuration

This is an **Author's Accepted Manuscript** of a conference paper published in the Proceedings of the 34th IAHR World Congress (Brisbane, 2011) by Engineers Australia, ISBN:978-0-8582-5868-6.

with $\phi = 18.4°$, $s = 6$ cm and $q = 0.07$ m^2/s where the skimming flow regime is about to set in. Instead of fully skimming above the pseudo-bottom, a jet impacting on the downstream part of the tread is generated. The large step vortex which is characteristic for the skimming flow regime is clearly visible. Figure 6.3.7(B) presents the velocity distribution measured with the double-tip conductivity probe at a step edge for comparison.

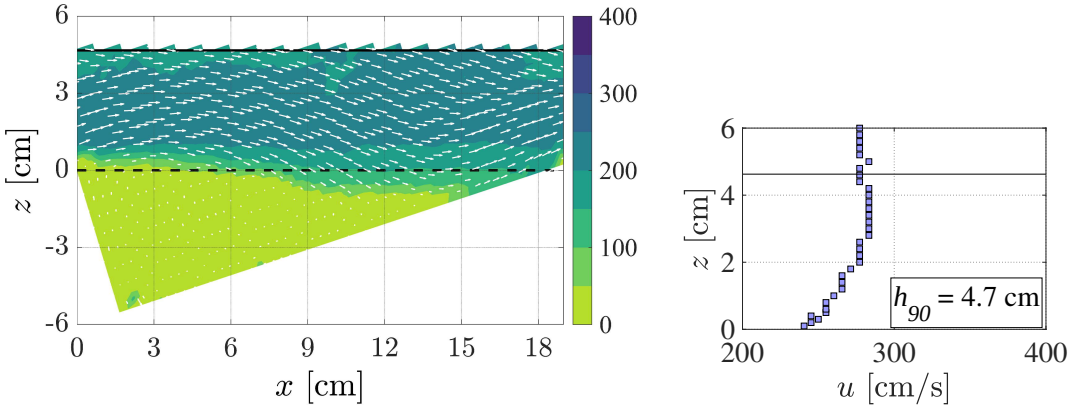

(A) BIV method

(B) Double-tip conductivity probe (step edge)

Figure 6.3.7: Air-water mixture velocity in uniform flow region ($\phi = 18.4°$, $s = 0.06$ m, $q = 0.07$ m^2/s, $F_s = 2.9$, dashed line: pseudo-bottom, solid lines: h_{90})

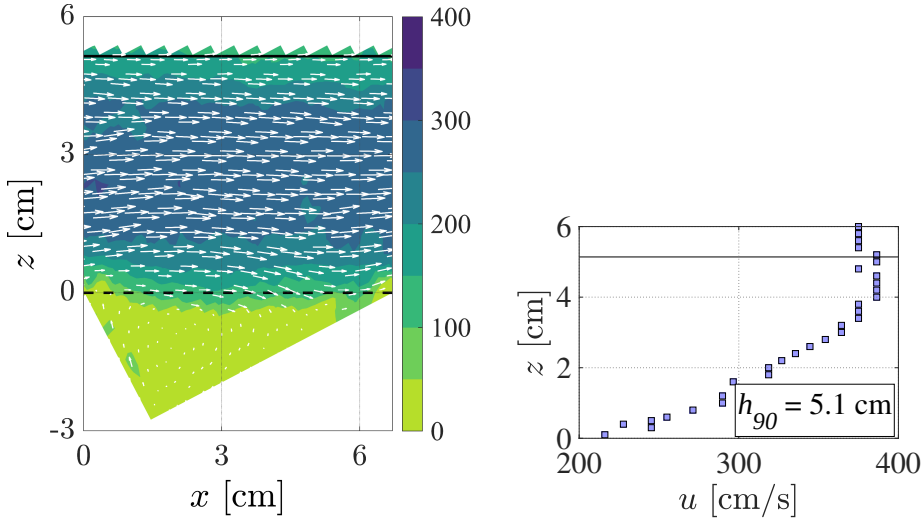

(A) BIV method

(B) Double-tip conductivity probe (step edge)

Figure 6.3.8: Air-water mixture velocity in uniform flow region ($\phi = 26.6°$, $s = 0.03$ m, $q = 0.11$ m^2/s, $F_s = 11.9$, dashed line: pseudo-bottom, solid lines: h_{90})

This is an **Author's Accepted Manuscript** of a conference paper published in the Proceedings of the 34th IAHR World Congress (Brisbane, 2011) by Engineers Australia, ISBN:978-0-8582-5868-6.

It is found that the result obtained by the intrusive measurement is slightly higher. However, it must be noted that the accuracy of the needle probe in regard to the determination of flow velocities is about 10 %. In fact, the double-tip probe tends to overestimate the velocity in the same range. Further, the velocity obtained by the BIV method decreases near the surface. It is well-known that this is not the case in spillway flows. In contrary, the maximum flow velocity is generally found below h_{90} and remains constant for higher z as illustrated in Fig. 6.3.7(B). It is assumed that this velocity decrease given by the BIV method is due to the low number of droplets near the surface available for the correlation calculation (cmp. Fig. 6.3.4). The described characteristics can be found for all other configurations. For instance, Fig. 6.3.8 presents the flow velocity for the model configuration with $\phi = 26.6°$, $s = 3$ cm and $q = 0.11$ m^2/s resulting in a higher step Froude number and hence, in a more stable skimming flow regime. Independent of the model configuration, the flow velocity in the cavity, which is generally difficult to determine with intrusive probes, is approximately 50 cm/s.

It must be further noted that the sampling time significantly differs for both methods (i.e. 1 s for BIV and 25 s for double-tip probe). This difference may affect the detected air-water mixture velocity. For example, Fig. 6.3.9 illustrates the uncertainty of calculated air-water mixture velocity (determined by correlating the raw signals of both electrodes of the double-tip probe as explained above) based on a sampling duration of 1 s. For this purpose, a moving correlation window with a length of 1 s is shifted across the total sample length of 25 s. Obviously, deviations in the range of 20 % must be considered for a shorter sampling time of 1 s. Analogously, a longer capture time may enhance the resulting BIV flow velocity. However, the effect of a longer record time cannot be investigated due to limitation of the fixed camera memory.

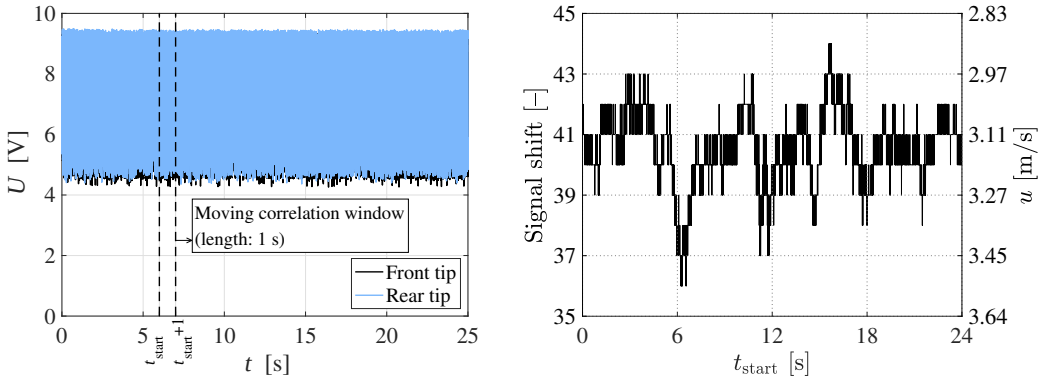

(A) Raw data and correlation window

(B) Signal shift (yielding max. correlation factor) and resulting flow velocity u

Figure 6.3.9: Exemplary uncertainty of air-water mixture velocity measured with a double-tip conductivity probe applying a sampling duration of 1 s (based on a 1 s window moving across the full 25 s raw signal, correlation of signals from both electrodes)

This is an **Author's Accepted Manuscript** of a conference paper published in the Proceedings of the 34th IAHR World Congress (Brisbane, 2011) by Engineers Australia, ISBN:978-0-8582-5868-6.

6.3.4 SUMMARY AND OUTLOOK

A comparative study of intrusive and non-intrusive measuring methods for stepped spillway flows has been presented.

It is found that ultrasonic sensors are capable for the determination of flow depths. An obstruction depth of the signal corresponds to a characteristic flow depth with a certain air concentration. Future investigations are needed to specify the influence of the sample rate and a possible indirect determination of the air content.

The Bubble Image Velocimetry method can be used for the visualization of the flow field and determination of the velocity field. The current experiments show that the BIV method results in lower flow velocities than the intrusive measurement with a double-tip conductivity probe. More experiments with use of a camera with a higher sample rate and resolution and a larger memory for extension of the sampling time are needed to possibly improve the results (particularly near the surface).

This is an **Author's Accepted Manuscript** of a conference paper published in the Proceedings of the 34th IAHR World Congress (Brisbane, 2011) by Engineers Australia, ISBN:978-0-8582-5868-6.

6.4 MEASURING VOID FRACTION AND VELOCITY FIELDS OF A STEPPED SPILLWAY FOR SKIMMING FLOW USING NON-INTRUSIVE METHODS

Authors: Jorge Leandro; Daniel B. Bung; Rita Carvalho
Journal: Experiments in Fluids 55(5)
Year: 2014

Abstract: Stepped spillways have higher energy dissipation than smoother hydraulic structures used to divert flood discharges. The inception point related to air entrainment is, however, located further upstream causing an undesired bulking of the flow depth. For large discharge rates and for straight stepped spillways, the skimming flow regime may be assumed two dimensional; this is an attractive feature for the application of non-intrusive flow visualization techniques because these methods measure the flow characteristics in the vicinity of the sidewalls which are likely to correlate with the flow at the center of the flume. This paper tests the hypothesis that such techniques can be used to measure the flow inside the flume. The hypothesis is tested against measurements taken with an intrusive probe. Void fraction contour lines and velocity fields are obtained in 12 different stepped spillway configurations using the image processing procedure and the Bubble Image Velocimetry, respectively. The void fraction and velocity results are overall consistent with the probe measurements. The velocity fields show a persistent underestimation of the probe measurements which can at least be partially explained by sidewall effects and possible probe's overestimation.

Keywords: Imaging techniques, void fraction, Bubble Image Velocimetry, high-speed camera

6.4.1 INTRODUCTION

Stepped spillways are commonly used to divert flood discharges from a reservoir dam. When compared with other spillway types, stepped spillways have the advantage of producing higher energy dissipation, due to the stepped geometry, and requiring a smaller stilling basin downstream. The inception point of air entrainment is, on the contrary, located further upstream on stepped spillways than on smoother spillways (PFISTER AND HAGER, 2011). The inception of air and increase in void fraction result in an undesired bulked flow depth and therefore a raise in the spillway construction costs. Depending on the discharge rate, step height and slope, three flow regimes can be identified: nappe, transition and skimming flow. The first, occurs for relatively low discharge rates and/or lower slopes, is characterized by a complex three-dimensional void fraction and velocity field (TOOMBES AND CHANSON, 2008). The second has the stronger void fraction values and a chaotic flow motion with intense splashing (CHANSON AND TOOMBES, 2004). The third,

occurs for relatively higher discharge rates and steeper slopes, is characterized by a flow over the pseudo-bottom formed by small vortices between edges; in addition, the flow may be assumed two dimensional whereby velocity profiles become a function of the slope (CHANSON, 1993) and void fraction depends on the slope and step height (BUNG, 2011A).

Void fraction and velocity have been mostly measured by intrusive methods, e.g. single- (CHANSON, 2007) and dual-tip probes (CHANSON AND FELDER, 2010; BUNG, 2011A). The first measurements were obtained by RAJARATNAM (1962) using electric resistive probes and RESCH ET AL. (1974) using hot-film anemometry in hydraulic jumps. In stepped spillways, MURILLO (2006) used hot-film anemometry and KRAMER (2004) used fiber-optic probes. Intrusive methods allow the measurement of points inside the flow; however, they do not allow multiple points readings. Nonintrusive methods based on imagery can produce simultaneous points readings, and it is nonetheless acknowledged that the results are likely to be more representative in the vicinity of the sidewall where the images are taken (LEANDRO ET AL., 2012). Earlier works on estimating void fraction based on visualization techniques were calibrated based on the global average (MOSSA AND TOLVE, 1998; KIMMOUN AND BRANGER, 2007), and recently LEANDRO ET AL. (2012) calibrated such a technique for a vertical profile of void fraction. To the authors knowledge, void fraction visualization techniques have not yet been applied to stepped spillways. For accessing the velocity fields, PIV (CARVALHO AND AMADOR, 2008; AMADOR ET AL., 2004) in non-aerated region and BIV methods (BUNG (2011C) in aerated regions) have been applied.

The aim of this study is to estimate average void fraction and velocity fields based upon non-intrusive visualization techniques for skimming flows in a stepped spillway at the center of the flume. The hypothesis is that for skimming flows, the results of visualization techniques can be indirectly calibrated to adequately measure the flow inside the flume. This is supported by evidence that skimming flow is presumably 2D and not a function of the transversal direction (CHANSON, 1993), and therefore, visualization techniques (which are more representative in the vicinity of side walls) are likely to remain representative. The experimental facility is presented in Section 6.4.2 along with the model set-up, the high-speed camera and the dual-tip conductivity probe. Section 6.4.3 describes the re-coding of the image processing procedure used for estimating the void fraction for stepped spillways. Section 6.4.4 describes the bubble image velocimetry for stepped spillways. Sections 6.4.5 and 6.4.6 describe the calibration routine and validation used for both non-intrusive methods. Section 6.4.7 presents the results, and Section 6.4.8 discusses the image processing procedure and the bubble image velocimetry results.

6.4.2 EXPERIMENTAL FACILITY

6.4.2.1 MODEL SETUP

The experimental investigations are performed on a physical stepped spillway scaled model 1:10 (Fig. 6.4.1). The structure, with a total drop height of 2.34 m and width of 0.3 m, is integrated in a closed water circuit. Water is pumped into open head tanks and then conveyed through an approaching channel with a length of 1 m width where small tubes at the inlet reduce the flow turbulence. In total, 12 different configurations are tested by varying the chute angle (ϕ = 18.4° and ϕ = 26.6°), the step height ($s = 3$ and $s = 6$ cm) and the specific discharge ($q = 0.07$, $q = 0.09$ and $q = 0.11$ m^2/s). For the selected configuration and discharges, skimming flow was always observed. The different configurations are referred to as RunID 1 to RunID 12 in Table 6.4.1. Each RunID refers to a particular configuration that can be summarized as ($\tan^{-1}(\phi)$-s-q), e.g. RunID1 refers to (2-03-07), meaning $\tan^{-1}(\phi)$ = 2 (i.e. $\phi = 26.6°$), $s = 3$ cm and $q = 0.07$ m^2/s. Due to the large drop height, the flow was fully developed (i.e. uniform flow set in) during all experiments. The discharge is regulated by a flap valve and checked with an inductive flow meter. In addition, an ultrasonic gauge installed in the approaching channel in combination with a calibrated rating curve is used for verification. One chute sidewall is made of Plexiglas allowing for visual investigations, while the rear wall is made of black PVC enhancing the contrast of the images.

Figure 6.4.1: Experimental facility of the stepped spillway located at the University of Wuppertal, Germany (here: configuration with $\phi = 26.6°$, $s = 6$ cm)

All parameter combinations involve the skimming flow regime which sets in for relative large discharges or relative small step heights. In this flow regime, water flows down as coherent stream above the pseudo-bottom formed by the step edges. Within the step niches, large vortices are generated and maintained by the shear stress between the main flow above and the cavity flow below the pseudo-bottom (Fig. 6.4.2).

Table 6.4.1: Summary of the experimental flow conditions in the stepped spillways ($F_s = q/(g \sin\phi (s\cos\phi)^3)^{0.5}$ is a Froude number defined in terms of the step-induced macro-roughness height (CHANSON, 1993))

RunID	1	2	3	4	5	6	7	8	9	10	11	12
q [m^2/s]	0.07	0.09	0.11	0.07	0.09	0.11	0.07	0.09	0.11	0.07	0.09	0.11
ϕ [°]	26.6	26.6	26.6	26.6	26.6	26.6	18.4	18.4	18.4	18.4	18.4	18.4
s [cm]	3	3	3	6	6	6	3	3	3	6	6	6
F_s [–]	7.6	9.8	11.9	2.7	3.5	4.2	8.3	10.6	13.0	2.9	3.8	4.6

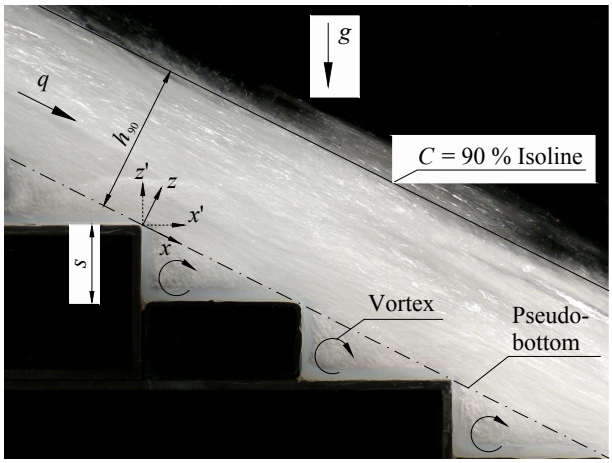

Figure 6.4.2: Illustration of skimming flow regime (note that the isoline with void fraction $C = 90$ % isoline (h_{90}) is often interpreted as the idealized air-water mixture surface

6.4.2.2 HIGH-SPEED CAMERA

High-speed movies of the stepped spillway flow in uniform flow region are taken with a frequency of 1,220 fps. The resolution of the camera (KSV Instruments, HiSiS2000) is 256 × 256 px. In dependence of the examined configurations, the width of the field of view is about 16-22 cm resulting in a pixel density of about 12-16 px/cm. The camera sensor is placed 0.50 m away from the side wall. The flow field is illuminated by means of halogen spot lights with a total power of 1,300 W. Three spots with 300 W each were installed above the channel in a distance of 80 cm above the pseudo-bottom. Two more spot lights with 200 W each were installed near the sidewall (in a distance of 50 cm) with an angle of ~45°. The use of artificial light assured that the light intensity remained constant in all images regardless of the day each configuration measurement took place.

One second high-speed movies are recorded per run. BUNG (2011C) showed in this experimental setup that for skimming flow, the 1 s average velocity had an error smaller than 3 % when compared with a full 25 s measurement using the dual-tip conductivity probe (3.03 m/s instead of 3.11 m/s). Ideally one would still prefer to

have longer recordings; however, 3 % error is considered acceptable given that it is smaller than the conductivity probe's overestimation error of 5 % (BOES, 2000; GONZALEZ, 2005) and the considerable gain in storage capacity.

6.4.2.3 DUAL-TIP CONDUCTIVITY PROBE

Air-water flow properties are measured with a dual-tip conductivity probe. The probe is placed on the channel centerline (CL) because it is where we are interested in characterizing the void fraction and velocity. In addition, as discussed in LEANDRO ET AL. (2012), the conductivity probe cannot be placed next to the wall in order to avoid errors in the measurements due to splashes near the sidewall (KUCUKALI AND CHANSON, 2008) and possible enhancement/ interference with the sidewall effects.

This probe consists of two electrodes of 130 μm diameter which are arranged back-to-back in flow direction (manufactured at IWW, RWTH Aachen, Fig. 6.3.1). In dependence of the surrounding medium (i.e. water or air), a high or low voltage is recorded and digitized with means of a combined dual-threshold and slope criterion to obtain a proper sawtooth signal (THORWARTH, 2008). Sample rate and duration are set to 25 kHz and 25 s, respectively. The total duration t_{air} where the signal equals the characteristic voltage for air gives information about the local void fraction ($C = t_{\text{air}}/25$ s).

By cross-correlating the signals of both tips, the time lag resulting in the maximum correlation factor is the traveling time Δt_e of detected air bubbles from the front to the rear tip. As the distance Δx_e in flow direction of the two electrodes is known to be 5.1 mm in this study, the flow velocity $u = \Delta x_e/\Delta t_e$ of the air-water mixture can be easily calculated. It must be noted that this method assumes a no-slip transport of air bubbles on the one hand. On the other hand, it is assumed that both tips pierce the same bubbles despite the distance of 1 mm in cross-direction.

A CNC controller (fabricate: isel) operates a two-dimensional linear guiding system guaranteeing exact positioning of the probe in x-direction along the chute and in z-direction at the step edges. All experiments are limited to the skimming water body ($z > 0$).

6.4.3 RE-CODING OF THE IMAGE PROCESSING PROCEDURE (IPP) FOR STEPPED SPILLWAYS

The image processing procedure IPP in LEANDRO ET AL. (2012) is a generic tool developed for obtaining time-averaged void fractions from images ($PI_{i,j}$). The IPP consists of two algorithms written in Matlab: (1) image editing (IE) and (2) pixel intensity matrix (PIM) algorithms. The first algorithm allows the calibration of the IPP using void fraction data. The second algorithm calculates the averaged pixel

intensity matrix ($PI^{f}_{i,j}$) necessary for calculating the vertical profiles of time-averaged void fraction. Earlier tests applying the IPP in the stepped spillway produced images with low contrast which PIM did not translate back into the correct void fraction profiles. A possible reason was the low resolution of the stepped spillway images of 256×256 px which produced images with a lower contrast than the high-resolution images of $3,072 \times 2,048$ px used in the hydraulic jump experiment (LEANDRO ET AL., 2012). This low resolution is nonetheless justified by the storage capacity required for the higher resolution (a $3,072 \times 2,048$ px image requires 4 MB of memory while a 256×256 px requires 65 kB), and the gain in fps from 751 to 1,220. Hence, a re-coded version of the IE algorithm to further enhance the images contrast was sought.

One of the drawbacks of the original IPP was the necessity of manually adjusting the location of the water surface defined by its upper and lower limit. Given the exceptional large number of files in this particular experiment, we developed a simple algorithm (Sst) to determine automatically the water upper ($\lim S$) and lower limit ($\lim St$), which will now be discussed. The Sst first step is to determine the average pixel intensity per row of the $PI_{i,j}$ matrix, $\mathrm{med}PI_i$:

$$\mathrm{med}PI_i = \overline{PI_{i,j}(\mathrm{row})} \tag{6.4.1}$$

Next the Sst builds a vector $\mathrm{vect}PI_i$ with the differences between every two $\mathrm{med}PI_i$ (Eq. 6.4.1) values distancing k rows apart:

$$\mathrm{vect}PI_i = \mathrm{med}PI_i - \mathrm{med}PI_{i-k} \tag{6.4.2}$$

In Eq. 6.4.2, k was set equal to 10; this value was found to give good results by test-and-try. $\lim S$ is set as the maximum value of $\mathrm{vect}PI_i$, i.e. the average row in which air first contacts with the water surface. Because we are dealing with an oscillating surface, Sst sets a band width defined as the first value following the first maximum which relative difference does not exceed 15 %. $\lim St$ is then set as the first row which $\mathrm{vect}PI_i$ value is lower than the lower end of the band width (Fig. 6.4.3). This last procedure avoids the existence of a second peak lying within our water upper and lower limit. This procedure can be applied in both the original and the re-coded IE form (Fig. 6.4.4).

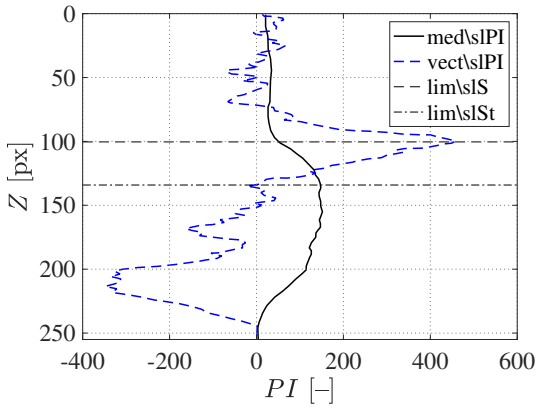

Figure 6.4.3: Illustration of the vectors medPI and vectPI used to estimate lim$S$ and limSt using an original image with 256 × 256 px

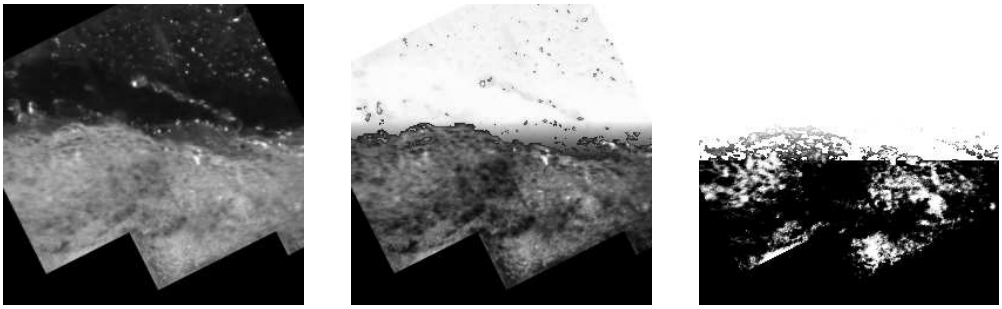

(A) Original image with 256 × 256 px

(B) Outputs from the originally developed IE

(C) Outputs from the re-coded IER

Figure 6.4.4: Image editing (IE) results (black areas surrounding image (A) is defined by the steps geometry and the limits of the original image before rotation

Alike the original IE version, the IER is a three-step algorithm (IE-1 to -3) defined by three equations, as shown in Table 6.4.2. Each equation allows us to edit the original image ($PI_{i,j}$) to obtain one final image ($PI^{f}_{i,j}$) in three distinct areas: (1) the area below the water surface identified by $i \geqslant \lim St$ (Eq. 6.4.3), (2) the area above the water surface identified by $i < \lim S$ (Eq. 6.4.6) and (3) the transitional area identified by $\lim S \leqslant i < \lim St$ (Eq. 6.4.8). To assist, IE uses threshold functions (IT) to include or neglect different edited images, and fuzzy logic equations to enhance the images contrast (namely Smf a fuzzy logic "S" function and lmf, a fuzzy logic linear function as defined in LEANDRO ET AL. (2012); e.g. the edit image $PI^{n}_{i,j}$ is the n^{th} editing of $PI_{i,j}$ and I_{Tn} is the n^{th} threshold function.

Now we will explain in detail the changes in the re-coded version of the IE algorithm. For the sake of clarity, IE and IER algorithms are summarized in Table 6.4.2. There are two main changes in the algorithm; a first is in step IE-1 and a second in step IE-2 which must then be included in IE-3. The first change is done because the fuzzy logic

Eq. 6.4.4 (Smf in IE-1) only allows the image to be darkened. As discussed before, we now need to enhance that contrast, i.e. darker and brighter areas. In Eq. 6.4.4, $PI_{i,j}$ is replaced by 255 (the upper range of the grey-scale), with this change $PI^1_{i,j}$ can now have values larger than the original image. In order to control the amount of contrast, the minimum and maximum limits of Smf become now calibration parameters.

In step IE-2 (Eq. 6.4.6), $PI^2_{i,j}$ is replaced by 255, thus clearing out the noise above the water upper limit (as seen in Figs. 6.4.4(B) and 6.4.4(C)). A high threshold value ($Ptr3$) is nonetheless kept in case there is a clear air-water content, identified by I_{T5}, whereby the original image remains unchanged. The image in Eq. 6.4.2, found in IE-1, is kept for the remaining threshold values in order to keep continuity of the air-water interface.

Step IE-3 is changed accordingly with the changes in the two previous steps. First, IE-3 keeps the $PI^1_{i,j}$ image and the PI unchanged image found in IE-2. Second, IE-3 linear transition between upper and lower layer is done between IE-1-enhanced contrast image ($PI^1_{i,j}$) and the 100 % air content defined in IE-2 (255). Figure 6.4.5 shows the effect of the three steps described in the IER algorithm on an image sample.

The re-coded IER algorithm has now five calibration parameters, i.e. three more than the original version IE. This number can be nonetheless reduced to three, if one considers that Ptr must be a small value and can therefore be kept constant (e.g. in the range of 0-10) and $Ptr3$ must be a high value and thus can also be assumed constant (e.g. in the range of 250-255). In sum, IER has two parameters to regulate the amount of enhanced contrast ($smfLL$, $smfUL$), and one for deciding the limit where the enhanced contrast is applied ($Ptr2$). This will be further discussed in the calibration section.

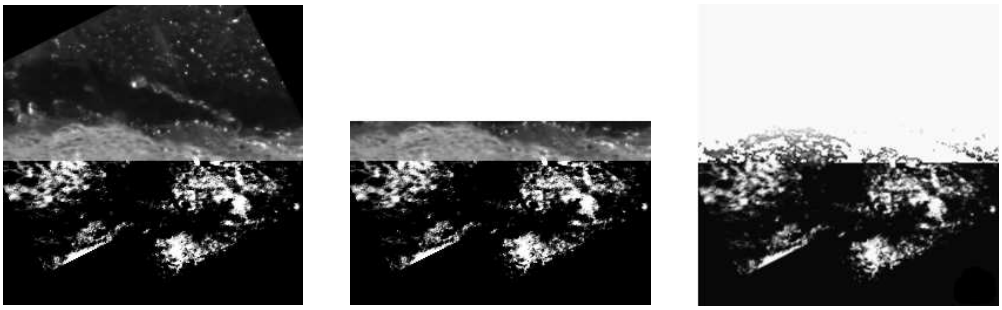

(A) IER-step 1 **(B)** IER-step 2 **(C)** IER-step 3

Figure 6.4.5: Application of the three steps in the IER algorithm on an image with 256×256 px for configuration 1

Step	IER (re-coded)	IE (original)	
IE-1	$PI_{ij}^{f} = \underbrace{I_{T1} \cdot PI_{ij}^{1}}_{\text{Enhance contrast}}$	$PI_{ij}^{f} = \underbrace{I_{T1}(PI_{ij}) \cdot PI_{ij}^{1}}_{\text{Darken } PI_{ij}}$	(6.4.3)
PI	$PI_{ij}^{1} = 255 \cdot Smf(PI_{ij}, [smfLL, smfUL])$	$PI_{ij}^{1} = PI_{ij} \cdot Smf(PI_{ij}, [0, 255])$	(6.4.4)
IT	$I_{T1}(x) = \begin{cases} 1, & x \geqslant Ptr \\ 0, & x < Ptr \end{cases}$	$I_{T1}(x) = \begin{cases} 1, & x \geqslant Ptr \\ 0, & x < Ptr \end{cases}$	(6.4.5)
IE-2	$PI_{ij}^{f} = \underbrace{I_{T4} \cdot PI_{ij}^{1} + I_{T2} \cdot 255}_{\text{IE step 1}} + \underbrace{I_{T5} \cdot PI}_{\text{unchanged}}$	$PI_{ij}^{f} = \underbrace{I_{T3}(PI_{ij}) \cdot PI_{ij}^{3}}_{\substack{\text{Linear transition } (PI_{ij} - PI_{ij}^{1}) \\ \text{for } (i<\lim S)}} + \underbrace{I_{T2}(PI_{ij}) \cdot PI_{ij}^{2}}_{\text{Lighten } (PI_{ij})}$	(6.4.6)
IT	$I_{T2}(x) = \begin{cases} 1, & x \leqslant Ptr2 \\ 0, & x > Ptr2 \end{cases}$ $I_{T4}(x) = \begin{cases} 1, & Ptr2 \leqslant x \leqslant Ptr3 \\ 0, & x > Ptr3 \vee < Ptr2 \end{cases}$ $I_{T5}(x) = \begin{cases} 1, & x \geqslant Ptr3 \\ 0, & x < Ptr3 \end{cases}$	$I_{T2}(x) = \begin{cases} 1, & x \leqslant Ptr2 \\ 0, & x > Ptr2 \end{cases}$ $I_{T3}(x) = \begin{cases} 1, & x > Ptr2 \\ 0, & x \leqslant Ptr2 \end{cases}$	(6.4.7)
IE-3	$PI_{ij}^{f} = I_{T1} \cdot (I_{T4} \cdot PI_{ij}^{1} + \underbrace{I_{T2} \cdot PI_{ij}^{4}}_{\substack{\text{Linear transition} \\ (255 - PI_{ij}^{1})}} + I_{T5} \cdot PI)$	$PI_{ij}^{f} = \underbrace{I_{T3}(PI_{ij}) \cdot I_{T1}(PI_{ij}) \cdot PI_{ij}^{1}}_{\text{Darken } (PI_{ij})}$	(6.4.8)
PI	$PI_{ij}^{4} = lmf(i, [\lim S, \lim St, 255, PI_{ij}^{1}])$	$PI_{ij}^{4} = lmf(i, [\lim S, \lim St, PI_{ij}^{2}, PI_{ij}^{1}])$	(6.4.9)

Table 6.4.2: Definition of threshold functions (IT), images (PI) and the three steps in the EI and EIR algorithm: IE-step1 (edition of the area below water surface), IE-step 2 (edition of the area above the water surface) and IE-step 3 (edition of the transitional area)

6.4.4 BUBBLE IMAGE VELOCIMETRY FOR STEPPED SPILLWAYS

The Bubble Image Velocimetry (BIV) method, introduced by RYU ET AL. (2005) focusing on aeration due to breaking waves and adopted to open channel cavity flows by LIN ET AL. (2008), is applied in this study to investigate the velocity fields in uniform flow region. This technique is a modified PIV method (Particle Image Velocimetry) where the entrained and transported air bubbles are illuminated by halogen spot lights instead of using a laser sheet. In aerated flows, the PIV method is limited to low void fractions (e.g. undular hydraulic jumps with low Froude numbers) as air bubbles distort the optical rays between the image and the acquisition plane (LENNON AND HILL, 2006). Moreover, laser light reflected from the air bubble surface could lead to significant damage of the camera sensor and severe injuries for the personnel.

Assuming a slip-free air bubble transport, the velocity field may be determined by cross-correlating the textures of two subsequent high-speed frames with known time shift when the air bubbles are considered as tracers. A general loss of accuracy must be acknowledged, because no well-defined plane as in case of PIV is given due to the missing laser sheet. Air bubbles being out of focus are included in calculations and probably distort the resulting velocity field.

The BIV calculations are performed on basis of the open-source Matlab® toolbox MatPIV in its latest version 1.6.1 (SVEEN, 2004). Besides the basic correlation steps, several filters like a signal-to-noise ratio filter (SNR) and a peak height filter can be applied with user-defined threshold values as well as a masking mode for neglecting regions out of flow. Moreover, the BIV process can be easily integrated in a series of calculation loops to perform a sensitivity study or calibration. In order to reduce the calculation time, the step contour is masked as shown in Fig. 6.3.4. The figure further illustrates an exemplary interrogation window size and overlap in comparison with the total picture size and the maximum air bubble movement.

6.4.5 CALIBRATION ROUTINE FOR IPP AND BIV

The calibration routine developed herein is applicable for both the image processing procedure (IPP) and the BIV. The IPP was calibrated by using measured vertical profiles of void fraction similarly to the work in LEANDRO ET AL. (2012), while BIV used vertical velocity profiles at upstream step edges. For the sake of clarity and space, the calibration routine will be only explained for the IPP. The corresponding BIV parameters will be given as footnotes.

Equation 6.4.10 defines the objective function as the summation of the absolute difference between the void fraction using the dual-tip conductivity probe (Co) and the IPP (Cp), divided by the number of points measured along the void fraction

profile (np):

$$\text{for IPP : objective function (OF)} \overset{\min}{\rightarrow} \frac{\sum^{np} |Co - Cp|}{np} \tag{6.4.10}$$

For BIV, the objective function is related to the mean velocity detected by the conductivity probe ($\bar{u}p$) in order to take into account the varying range of flow velocities for the different RunIDs:

$$\text{for BIV : objective function (OF)} \overset{\min}{\rightarrow} \frac{\sum^{np} |Uo - Up|}{np \cdot \bar{u}p} \tag{6.4.11}$$

As discussed in the previous section out of the five possible calibration parameters, it is possible to reduce it to two parameters by assuming Ptr and $Ptr3$ constant and equal to 5 and 250 (i.e. within the limits suggested in the IPP subsection), and using $Ptr2$, $smfUL$ and $smfLL$ as calibration parameters[2]. The calibration parameters are regarded as discrete with a step dx and constrained by upper and lower limits. The limits were found by manual inspection of the outcome results looking that the best visual fit would lie within those limits and the spacing magnitude in order to keep the domain size manageable. Equation 6.4.12 defines the domain of the calibration parameters[3]:

$$\text{Parameters} \begin{cases} PTR2 & \underset{\mathrm{d}x=20}{\rightarrow} & [160 : 240] \\ smfUL & \underset{\mathrm{d}x=20}{\rightarrow} & [180 : 220] \\ smfLL & \underset{\mathrm{d}x=20}{\rightarrow} & [80 : 140] \end{cases} \tag{6.4.12}$$

Because we had 12 configurations, in principle, any of the 12 could be selected for calibration and the remaining 11 for validation. However, the calibrated set of parameters would then be dependent on the selected configuration. In order to obtain an overall optimum set of parameters, a program was written whereby all 12 configurations are individually calibrated and the corresponding set of calibrated parameters saved. For each set of parameters, we obtain the so-called built validation matrices (BVM) and use them to judge on the calibration quality to obtain the overall optimum set of parameters. The program flow chart (Fig. 6.4.6) and concepts will now be explained in more detail. For the sake of clarity, we will first introduce the subprogram to calculate the individual optimum set of parameters and only after the subprogram to calculate the overall optimum.

[2]For BIV replace: $Ptr2$, $smfUL$ and $smfLL$ by overlap (OL), SNR threshold (SNR) and peak height filter (Peak)

[3]For BIV replace $\begin{cases} PTR2 & \underset{\mathrm{d}x=20}{\rightarrow} & [160 : 240] \\ smfUL & \underset{\mathrm{d}x=20}{\rightarrow} & [180 : 220] \\ smfLL & \underset{\mathrm{d}x=20}{\rightarrow} & [80 : 140] \end{cases}$ by $\begin{cases} OL & \underset{\mathrm{d}x=0.25}{\rightarrow} & [0.25 : 0.75] \\ SNR & \underset{\mathrm{d}x=0.1}{\rightarrow} & [1.1 : 1.5] \\ Peak & \underset{\mathrm{d}x=0.1}{\rightarrow} & [0.2 : 0.5] \end{cases}$

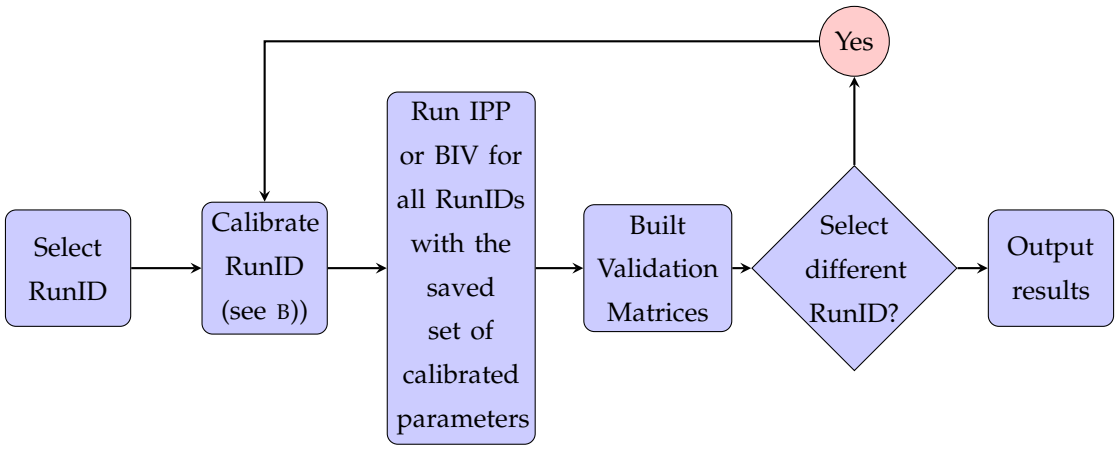

(A) Evaluation of resulting built validation matrices

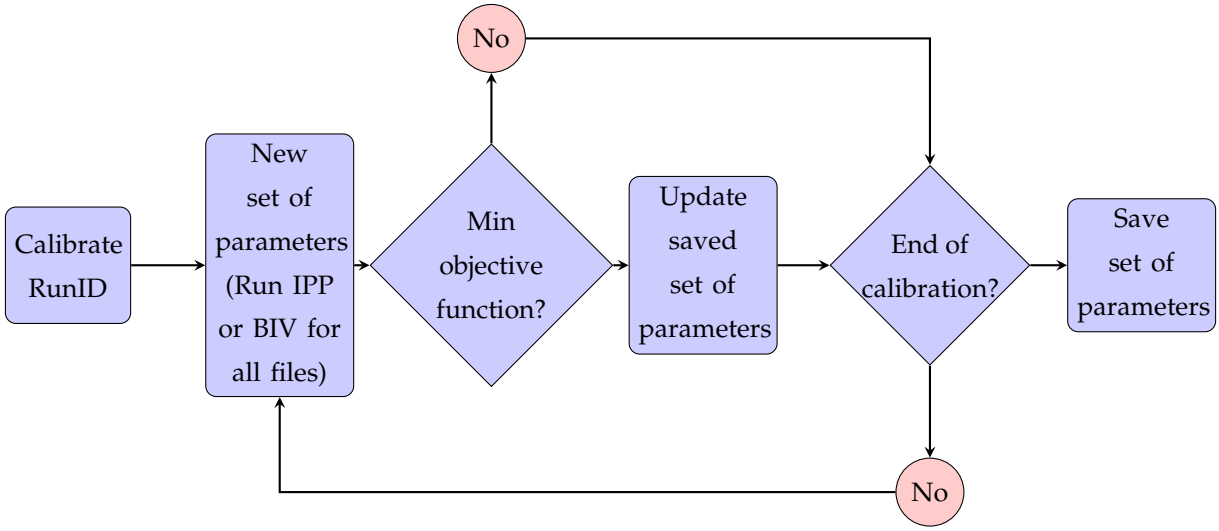

(B) Evaluation of individual optimum set of parameters for each configuration

Figure 6.4.6: Program flow chart for obtaining the overall optimum

6.4.5.1 SUBPROGRAM TO CALCULATE THE INDIVIDUAL OPTIMUM

After selection of a RunID (one of the possible 12 configurations), the subprogram runs all the elements in the parameters domain Eq. 6.4.12 to select the best set of parameters, i.e. the set that minimizes Eq. 6.4.10. In total, the image processing procedure (IPP) needs to run $5 \cdot 3 \cdot 4 = 60$ times for a selected RunID ($Ptr2 \cdot smfUL \cdot smfLL$). To keep accuracy high, we specify for calibration purposes the highest grid resolution, i.e. $gr = 2$ (pi), and to avoid a high computational burden, we select the number of files (nf) equal to 400, i.e. below the maximum of 1,200 (note that this only done during the calibration stage, Fig. 6.4.5(B)). Since each calibration will be repeated in the overall optimum subprogram for each RunID, this will total $60 \cdot 400 = 24,000$ image editions (Fig. 6.4.6(B)).

6.4.5.2 SUBPROGRAM TO CALCULATE THE OVERALL OPTIMUM

This subprogram calls the subprogram that calculates the individual optimum and builds the BVM for each set of individual optimal set of parameters. The BVM stores the values of the normalized Eq. 6.4.10[4] obtained for all configurations using the individual optimal set of parameters.

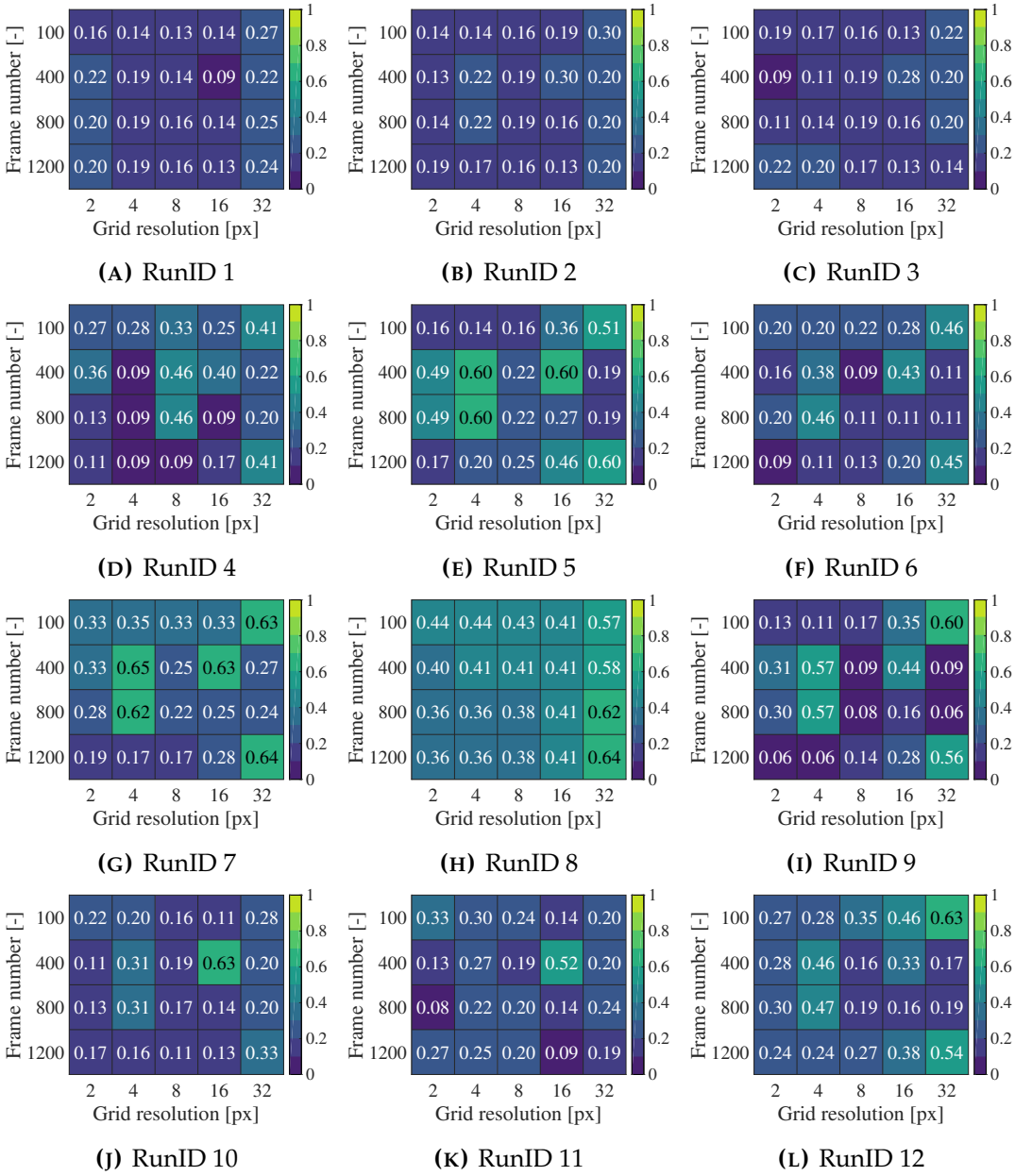

(A) RunID 1 **(B)** RunID 2 **(C)** RunID 3

(D) RunID 4 **(E)** RunID 5 **(F)** RunID 6

(G) RunID 7 **(H)** RunID 8 **(I)** RunID 9

(J) RunID 10 **(K)** RunID 11 **(L)** RunID 12

Figure 6.4.7: The 12 built validation matrices for each RunID using RunID 7 for calibration, ordered by RunID from left to right (during calibration it was used $nf = 400$ and $gr = 2$ for each BVM)

[4]Normalization is only done at the end with the maximum value obtained from all matrices. The normalization enables an easier cross-comparison between matrices.

BVM is defined by a two-dimensional array where rows are the number of files (nF) used (100, 400, 800, 1,200) and columns are the different grid (gr) resolutions (2, 4, 8, 16, 32)[5]; thus, the gain of reducing the number of files and resolution can be compared (including using all files with highest resolution). Figure 6.4.7 shows an example for the IPP calibration of the 12 BMV matrices obtained with RunID7. This procedure is repeated for all 12 configurations (similar matrices were produced for BIV).

6.4.6 VALIDATION

In order to validate the calibration and summarize the BVM information, we build histograms for each calibration run. Each histogram is divided into the same 10 classes (to ease the cross-comparison, the limit was set after all histograms were calculated). The histogram represents the number of times each element in the BVM rests within each class. The closer the histogram is to left side, the better is our global fitting. For example, for IPP, Fig. 6.4.8(A) shows that the use of RunID 1, 6 or 10 for calibration resulted in 55 counts of BVM values to rest in the first class, in contrast by selecting RunID 2 or 3, the same first class had a counting lower than 30 (Fig. 6.4.8(B)). A score defined as $S(c.c) = \sum(\text{class} \cdot \text{counts})$ is used to rank the optimal calibration. The overall optimal is identified by the lowest score. Parameters obtained with RunID4 were used for producing the final void fraction profiles (Fig. 6.4.8(C)).

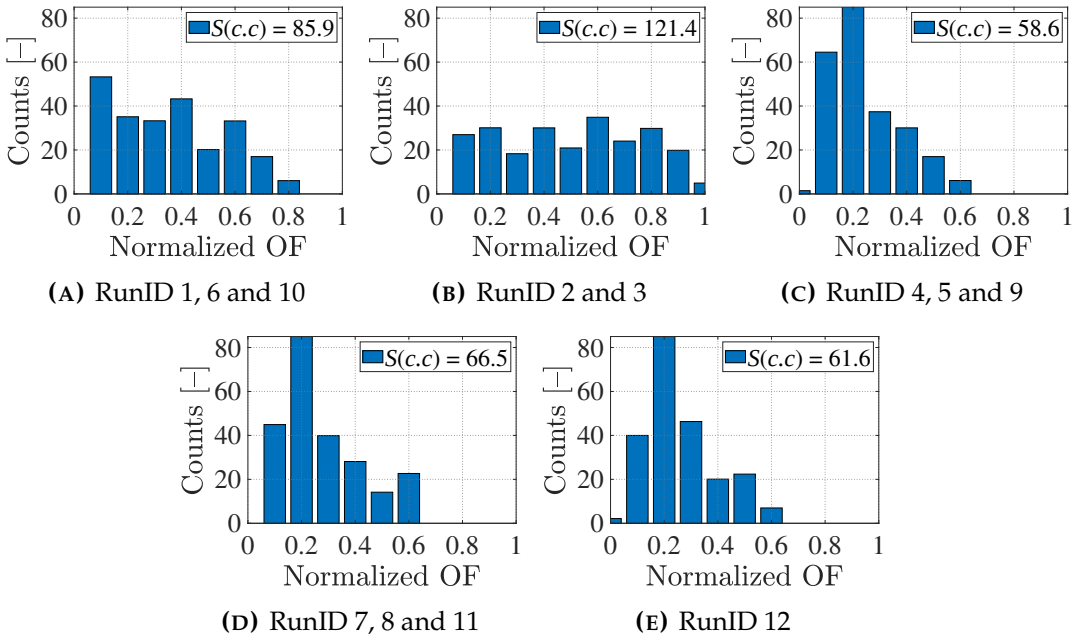

(A) RunID 1, 6 and 10 **(B)** RunID 2 and 3 **(C)** RunID 4, 5 and 9

(D) RunID 7, 8 and 11 **(E)** RunID 12

Figure 6.4.8: Histograms summarizing the validation results of the BVM for each calibration run with corresponding score $S(c.c)$

[5]For BIV replace: nf = (100, 400, 800, 1,200) and gr = (2, 4, 8, 16, 32) by nf = (50, 100, 200, 400, 800, 1,200) and interrogation window size iws = (12, 16, 24, 32, 40).

Table 6.4.3 shows a summary of the optimal parameters obtained during the BIV and IPP calibration. Figure 6.4.9 shows the average BVM matrices of IPP and BIV where the average normalized objective function (NOF) is shown for each matrix element. In addition, it is also shown in highlighting the number of files, grid resolution and information window size used to produce the void fraction and velocity final results.

Table 6.4.3: Summary of the optimal parameters obtained during the BIV and IPP calibration for each of the 12 RunIDs

RunID	**1, 6 & 10**	**2 & 3**	**4, 5 & 9**	**7, 8 & 11**	**12**				
$Ptr2$	180	180	200	180	160				
$smfUL$	180	180	200	180	200				
$smfLL$	120	100	140	140	140				
RunID	**1**	**2**	**3**	**4**	**5 & 7**	**6**	**8**	**9, 11 & 12**	**10**
OL	0.50	0.75	0.75	0.75	0.25	0.25	0.25	0.50	0.75
SNR	1.40	1.20	1.50	1.30	1.50	1.20	1.40	1.50	1.3
$Peak$	0.50	0.50	0.50	0.50	0.50	0.50	0.50	0.50	0.3

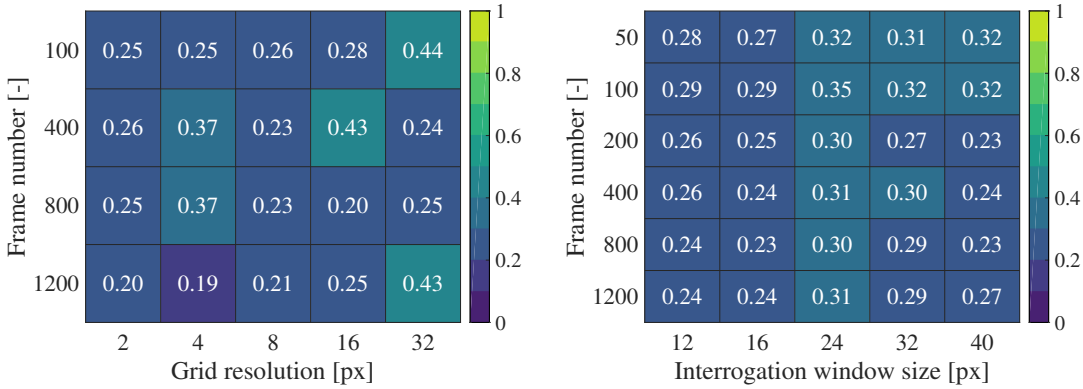

(A) Void fraction results for RunID4 (minimum normalized OF = 0.20 found for $nf = 1,200$ and $gr = 2$)

(B) Velocity results for RunID3 (minimum normalized OF = 0.23 found for $nf = 800$ and $iws = 16$)

Figure 6.4.9: Average built validation matrices

6.4.7 RESULTS

Once the image processing procedure (IPP) and the bubble image velocimetry (BIV) have been validated (Fig. 6.4.7), the best set of parameters can be used to produce complete maps of void fraction and velocity fields covering the water profiles. Figure 6.4.10 shows three examples of calibrated profiles of void fraction for the calibrated RunID4 and corresponding 95 % confidence intervals (CI), and Fig. 6.4.11 shows similar examples for the velocity profiles for the calibrated RunID3. Table 6.4.4 shows the summary of the objective function for both methods, for the final run. Figure 6.4.12 shows the average void fraction contour lines for all configurations using the

image processing procedure (IPP). For sake of the velocity fields' visualization, these figures are zoomed in around the first step and oriented along the pseudo-bottom (Fig. 6.4.13). Figure 6.4.14 shows the average velocity vector fields and magnitudes for all configurations using BIV.

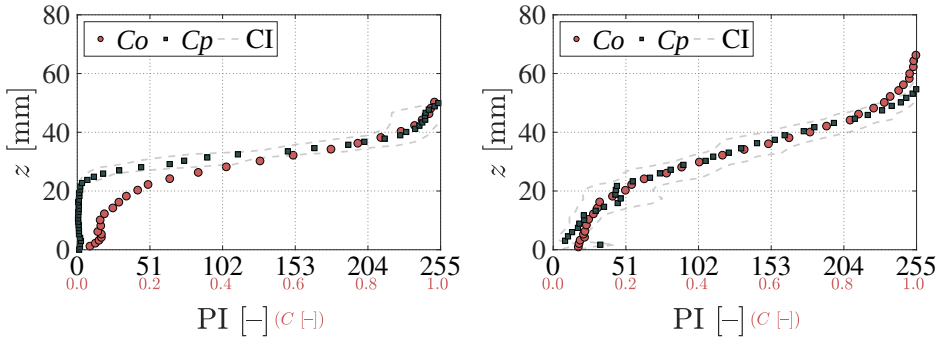

(A) Average profile fit with objective function (OF) = 0.083 (RunID 1)

(B) Best profile with OF = 0.024 (RunID 5)

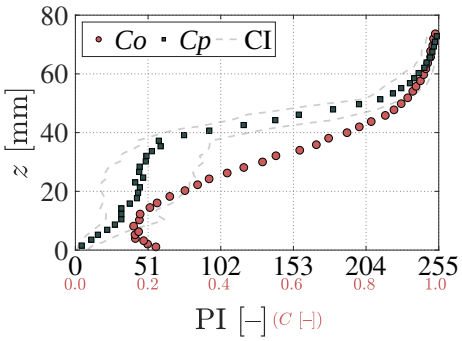

(C) Worst profile with OF = 0.153 (RunID 11)

Figure 6.4.10: Three examples (out of 12 possible RunID) of calibrated profiles of air concentration using dual-tip conductivity probes (Co) and the image processing procedure (Cp) with 95 % confidence intervals (CI) using RunID 4 as calibration run (see parameters in Fig. 6.4.9 and Table 6.4.3)

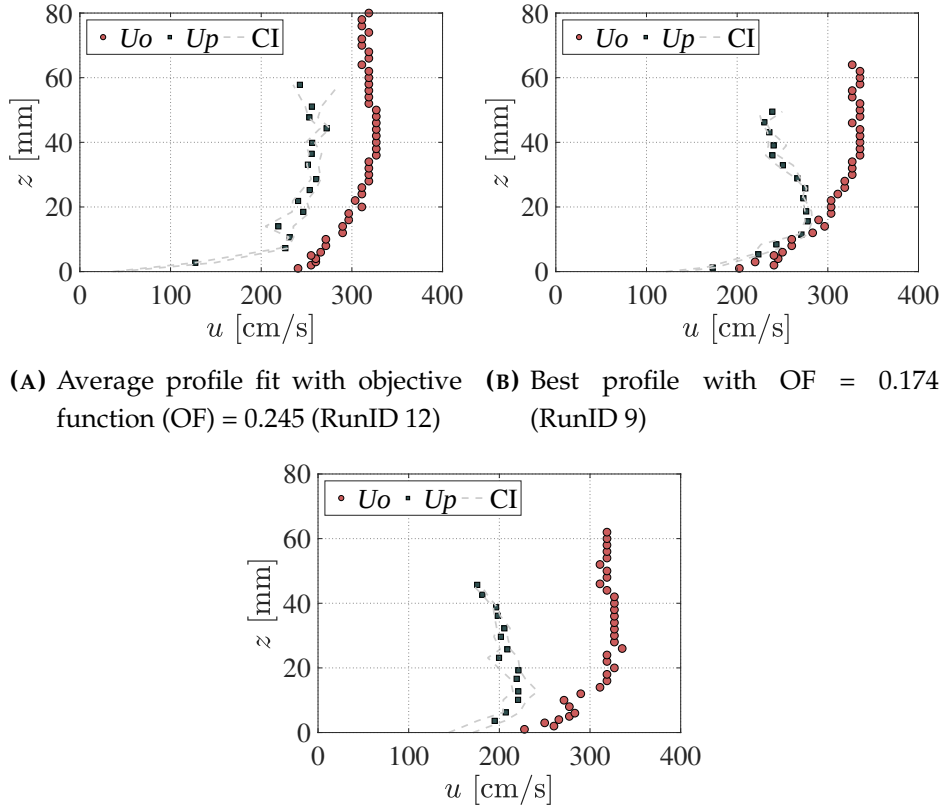

(A) Average profile fit with objective function (OF) = 0.245 (RunID 12)

(B) Best profile with OF = 0.174 (RunID 9)

(C) Worst profile with OF = 0.335 (RunID 4)

Figure 6.4.11: Three examples (out of 12 possible RunID) of velocity profiles using conductivity probe ($U0$) and the BIV (Up) with 95 % confidence intervals (CI) using RunID 3 as calibration run (see parameters in Fig. 6.4.9 and Table 6.4.3)

Table 6.4.4: Summary of the Objective Function OF according to Eq. 6.4.10 and 6.4.11 (average absolute error, +/-) for the average profile and the 95 % confidence intervals (CI), for each profile and for both the IPP and BIV methods

RunID	1	2	3	4	5	6	7	8	9	10	11	12
IPP	0.08	0.08	0.08	0.04	0.02	0.04	0.08	0.13	0.03	0.07	0.15	0.06
CI95	0.13	0.11	0.10	0.09	0.06	0.12	0.14	0.16	0.08	0.11	0.21	0.08
CI05	0.08	0.06	0.08	0.05	0.07	0.08	0.09	0.11	0.04	0.05	0.08	0.12
BIV	0.29	0.22	0.18	0.34	0.31	0.25	0.21	0.18	0.17	0.22	0.33	0.24
CI95	0.27	0.20	0.16	0.30	0.29	0.22	0.19	0.16	0.15	0.18	0.29	0.21
CI05	0.34	0.26	0.21	0.37	0.35	0.28	0.22	0.20	0.19	0.27	0.34	0.26

6.4.8 DISCUSSION

6.4.8.1 EXPERIMENTAL FACILITY AND HYPOTHESIS

The tests were carried out for step Froude numbers ranging from 2.7 to 13, two possible slopes and step heights (Table 6.4.1). Measurements of void fraction and velocity profiles were made at the step edges (Fig. 6.4.2). The dual-tip conductivity probe sample rate and duration were set to 25 kHz and 25 s, well within the values of 20 kHz and 20 s suggested in the literature (CHANSON AND FELDER, 2010). While the frequency of acquisition of 1,220 fps is within the acceptable range for obtaining velocity fields with PIV techniques (AMADOR ET AL., 2004), the number of images is also well in excess of previous experiments which applied visualization techniques for obtaining void fraction data (MOSSA AND TOLVE, 1998; KIMMOUN AND BRANGER, 2007; LEANDRO ET AL., 2012).

All tests were conducted for skimming flow. As discussed in the introduction, skimming flow can be assumed two dimensional (2D) whereby dimensionless void fraction profiles depend only on the slope, and step height and dimensionless velocity profiles depend only on the slope. This is a much desired assumption when using visualization techniques, because these techniques are likely to be more representative in the vicinity of the sidewalls; if the flow is presumably 2D and not a function of the transversal direction (CHANSON, 1993), then the initial hypothesis that the results of such techniques can adequately measure the flow inside the flume, where probe measurements were taken, is indeed plausible. Nonetheless, it is acknowledged that in laboratory tests, sidewall effects must be present. KRAMER (2004) showed that in a 50 cm wide flume for uniform flow region, the void fraction of self-aerated chute flows near the side wall and at the centerline are indeed similar, while the velocity near the sidewall is approximately 15 % lower than at the centerline. The profiles shown in Figs. 6.4.10 and 6.4.11 support our hypothesis and KRAMER 's findings; the profiles' shape is well captured in both void fraction and velocity profiles with the BIV consistently underestimating the probe profiles. As discussed in Section 6.4.2.2, increasing the 1 s recording period of the high-speed camera would at the most improve 3 % the BIV underestimation. However, this error is smaller than the 5 % conductivity probe's own overestimation error. Thus, the error is considered acceptable as it is unlikely to change the findings in this study.

6.4.8.2 RE-CODING OF THE IMAGE PROCESSING PROCEDURE (IPP)

In relation to the re-coding of the IPP, two issues need to be discussed. First is the need to expand the calibration capabilities of the IPP procedure, and second is the automatic detecting of the water surface upper and lower limits (Fig. 6.4.3). The soft images used in this experiment highlighted the need to add a parameter to allow

enhancement of brighter areas, i.e. where higher contents of air are expected. Figure 6.4.4(C) shows that it can be achieved with the Smf parameter in Eq. 6.4.4. This first issue was in previous experiment (hydraulic jump) not highlighted because the images used had a higher contrast between pixels (LEANDRO ET AL., 2012). Thus, it is not expected that the re-coded version of IPP would have any additional benefit on that study.

As for the second issue, the automatic detection of the water surface upper and lower limits was achieved with a simple algorithm. This can be explained by the type of flow studied. In the skimming flow regime, the external edges of the steps form a pseudo-bottom over which the flow passes. The time-averaged water surface above becomes parallel to the pseudo-bottom. Thus, one only needs to look for the average values of the water upper ($\lim S$) and lower limit ($\lim St$) per image, as there will be only natural oscillations across different images for the same flow rate (Fig. 6.4.4). Figure 6.4.10 shows that the void fraction profiles around the surface h_{90} are in very good agreement. Again comparing with the hydraulic jump experiment, these limits are dependent not only on the flow rate plus/minus some natural oscillations but also on the distance to the jump toe. Thus, such a simple algorithm may not provide such good results.

6.4.8.3 CALIBRATION AND VALIDATION PROCEDURE

The calibration and validation procedure developed allows overall optimum set of parameters (as defined in Section 6.4.5.2) to be obtained instead of occurring an overfitting for a single experiment. The histograms summarizing the validation results of the BVM for each calibration (Fig. 6.4.8) show that depending on the RunID selected for calibration, the validation will necessarily produce better or worst results. In principle, this can be explained by the choice of the domain spacing in Eq. 6.4.12. In order to limit the computation burden, a manageable domain size was chosen. It can, nonetheless, occur that for a specific RunID, a better solution could be found outside this domain (BAZARAA ET AL., 1993).

The set of overall optimal parameters are taken from Table 6.4.3 having in mind the best scores in Fig. 6.4.8. Parameters obtained with RunID4 and RunID3 were used for producing the final void fraction profiles (Fig. 6.4.8(C)) and velocity profiles, respectively. The histograms provide an easy measure for comparing across different calibrations, as they visually suggest which calibration performed best. The validation matrices in Fig. 6.4.9 show that the normalized objective function generally improves as the number of frames and the resolution increases. These variations are often small suggesting that selecting a different pair of values around the selected number of frames and px (highlighted in grey) would not likely show a large variability in the outcome results of Figs. 6.4.12 and 6.4.14.

6.4.8.4 VOID FRACTION CONTOUR LINES

Perhaps the most striking outcome of Fig. 6.4.12 is the actual quantification of the void fraction along the stepped spillway in particular in the corner eddies found in skimming flows, often discussed in the literature (YASUDA AND OHTSU, 1999). These eddies have been described as large transverse air-water vortices (FELDER ET AL., 2012) maintained through the transmission of shear stress from the fluid flowing above the pseudo-bottom (CHANSON, 1993) and believed to be responsible for the energy dissipation found in skimming flows (MURILLO, 2006).

Figure 6.4.12 highlights that there are two main factors regulating the void fraction inside the eddies, namely the ratio of the water surface (h) to the step height (s) and the slope. The former (related to the eddies driving force) is responsible for the transmission of shear stress to the eddies, sustaining the air trapped within the steps long enough to raise the average void fraction. If this ratio is increased (moving from left to right in Fig. 6.4.12), the high void fraction values inside the eddies tend to reduce until they reaches values similar to the surrounding flow. The latter constrains the size and shape of the eddies identified by the void fraction; from an almost circular shape (experiments 1-6, slope 1:2, top row, Fig. 6.4.12), to an elongated form (experiments 7-12, slope 1:3, bottom row, Fig. 6.4.12). The elongated shape may be also influenced by the relatively low discharge rates (see Section 6.4.8 on the velocity fields), whereby for early stages of skimming flow, the flow is not yet absolutely parallel to the pseudo-bottom, thus adding to the elongated shape of the eddies identified by the void fraction.

The results seem overall consistent across different geometries and flow rates, except for experiments 4-6 inside the eddies. The experiment with slope 1:2 and step height 6 cm exhibits an exceptional high values of void fraction at the center of the eddies. In the authors' opinion, having in mind the care taken in setting up the experiment (Section 6.4.2.2), the only reasonable explanation might be on a possible overexposure of the film for this particular set of experiments given the reduced dark area of the steps within each frame when compared with the remaining experiments (particularly obvious in experiment 4). Assuming a possible drawback of the IPP, this could explain a possible higher than normal pixel intensity in these images which enhanced the already high values of the void fraction at the center of the eddies.

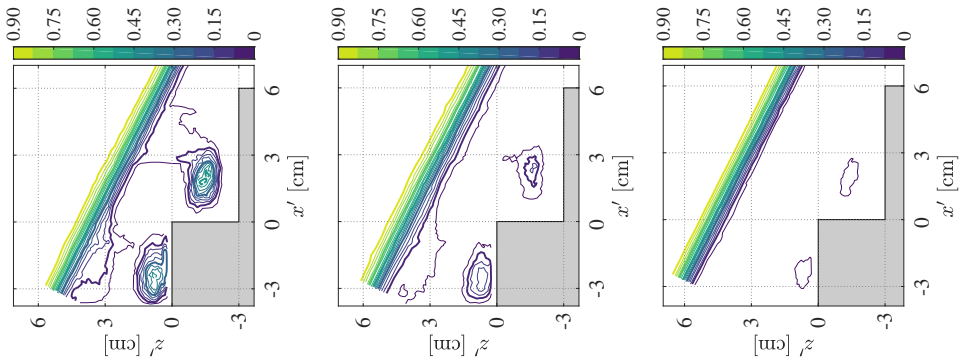

(A) RunID 1 (B) RunID 2 (C) RunID 3

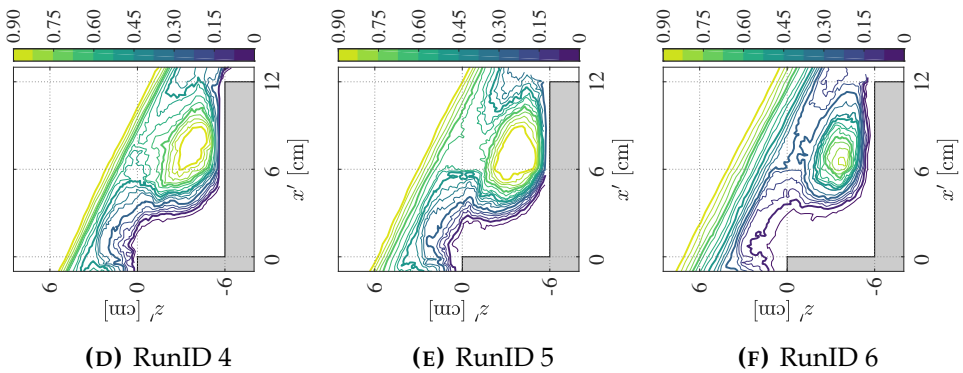

(D) RunID 4 (E) RunID 5 (F) RunID 6

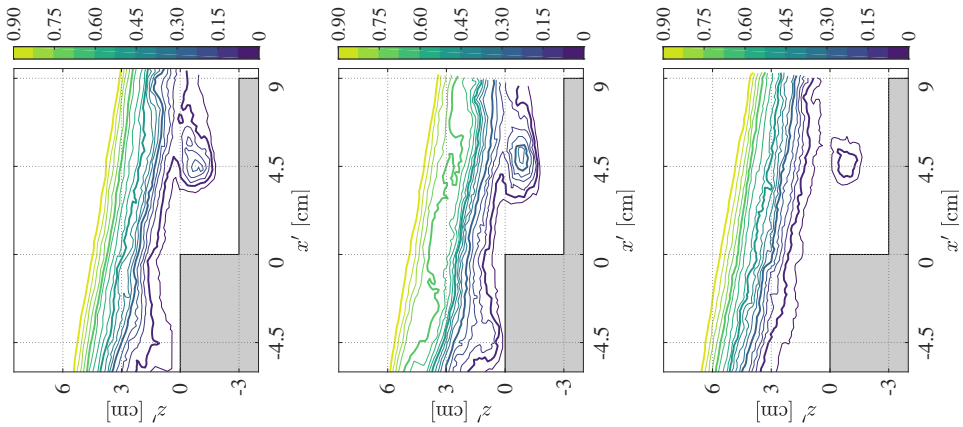

(G) RunID 7 (H) RunID 8 (I) RunID 9

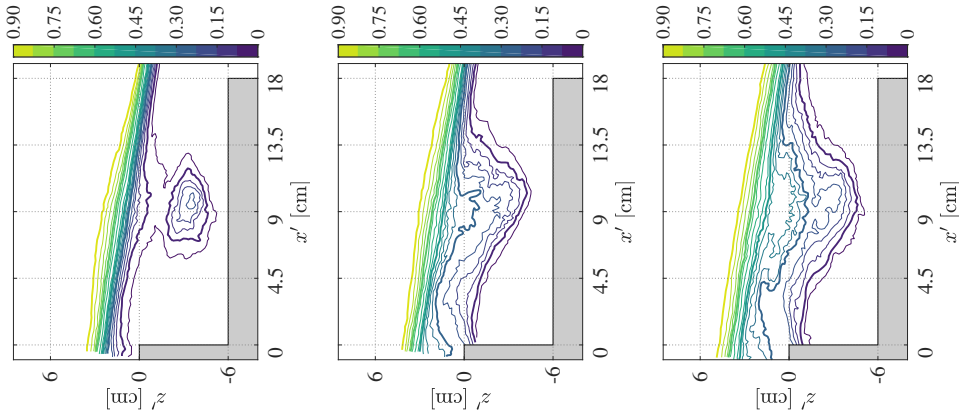

(J) RunID 10 (K) RunID 11 (L) RunID 12

Figure 6.4.12: Average void fraction contour lines (0 % to 90 %, in 5 % increments) for all 12 configurations using the image processing procedure (IPP)

6.4.8.5 VELOCITY FIELDS

The velocity fields obtained by the BIV method (Fig. 6.4.14) allow a qualitative description of stepped spillway flows. The main characteristics of a skimming flow regime, i.e. the eddy within the step niche and a high-speed flow above the pseudo-bottom, are well represented in all experiments, for example, the BIV is able to clearly capture the "left-to-right" velocities near the cavity bottom (experiments 1-3, top row, Fig. 6.4.14), or the descending velocities crossing the pseudo-bottom (experiments 7-9, middle bottom row, Fig. 6.4.14). With the BIV images, it is now clear that for early stages of skimming flow, the flow is not absolutely parallel to the pseudo-bottom (experiments 7-10, Fig. 6.4.14), thus producing the elongated void fraction profiles discussed earlier.

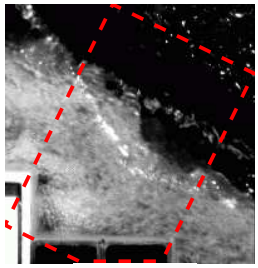

Figure 6.4.13: Orientation of the BIV results crop (here for RunID 1)

Following the exhaustive calibration procedure discussed in the calibration/validation sections, it is the authors' opinion that the flow velocities near the sidewalls are indeed lower than those measured by the conductivity probe which was installed in the flume's centerline. This is in agreement with other authors that found that the sidewall effects can lead to a reduction in flow velocities of approximately 15 % (see Section 6.4.1). This range of deviations can also be found in Fig. 6.4.11 for the flow region near the pseudo-bottom, i.e. for $z/h_{90} < 0.6$. Two further reasons for enhancing those differences could be the conductivity probe's overestimation of the flow velocities which is estimated in the range of 5 % (BOES, 2000; GONZALEZ, 2005) and fluctuations on the surface air-water mixture, particularly in the higher flow regions. As described by BUNG (2013), the maximum trough extensions of the surface waves reach down to approx. h_{75}, i.e. the water level with 75 % void fraction.

Overall, the BIV method provides valuable information about flow velocities within the step niche where measurements using an intrusive probe are generally difficult, particularly within the vortex region. Dual-tip probes need to be aligned with the flow direction in order to receive reliable results and thus be rotated to be aligned with the vortex direction. Further applications of the velocity fields may see the determination of shear stresses and the development of turbulent shear layers along the pseudo-bottom downstream of the step edges.

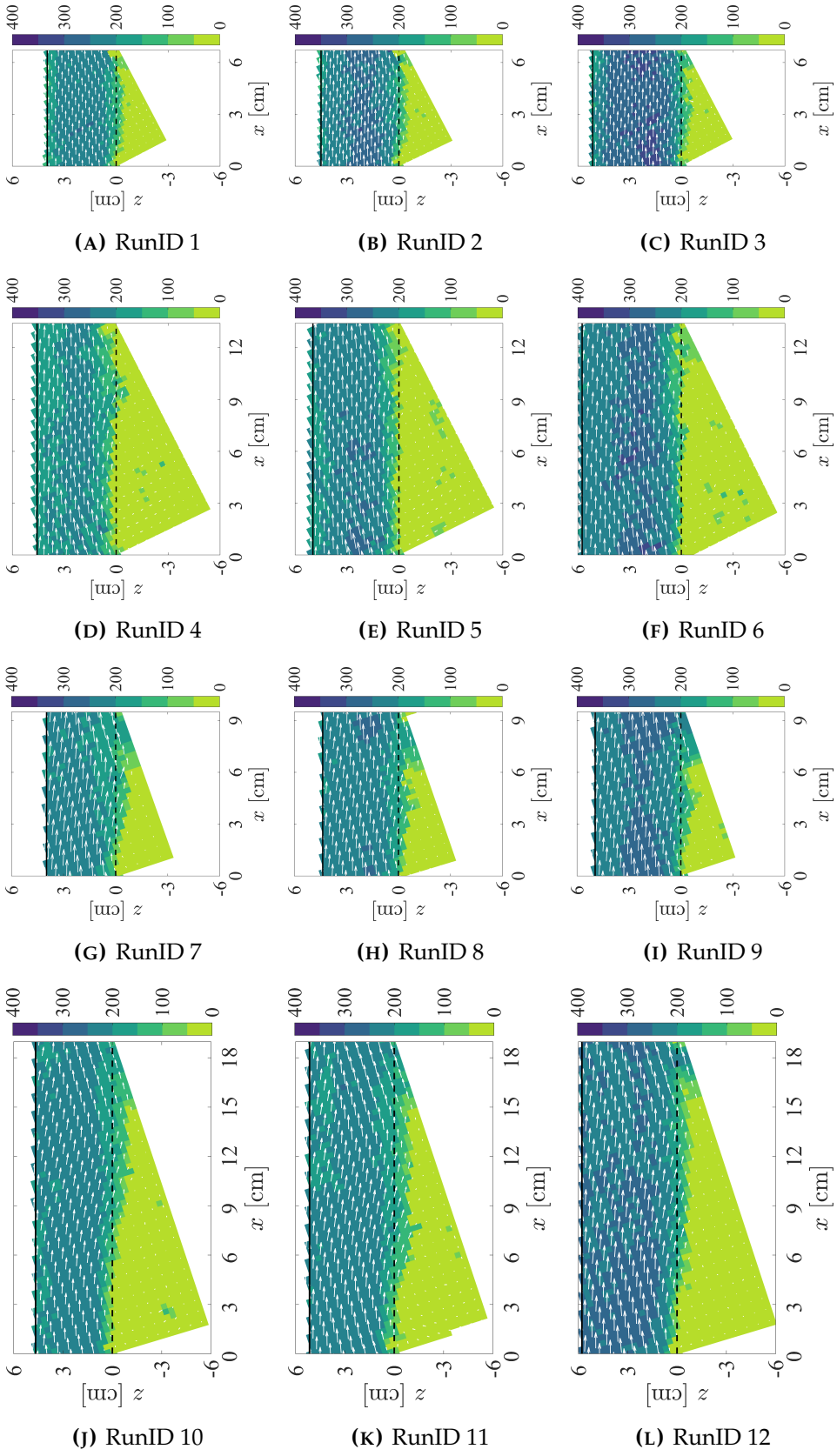

(A) RunID 1 **(B)** RunID 2 **(C)** RunID 3

(D) RunID 4 **(E)** RunID 5 **(F)** RunID 6

(G) RunID 7 **(H)** RunID 8 **(I)** RunID 9

(J) RunID 10 **(K)** RunID 11 **(L)** RunID 12

Figure 6.4.14: Average velocity field distributions and magnitude scale in cm/s, for all 12 configurations using the BIV, ordered by RunID (every 2nd vector displayed)

6.4.9 CONCLUSION

This paper presented the application of non-intrusive methods to measure the void fraction and velocity fields of a stepped spillway for skimming flow, namely the Image Processing Procedure (IPP) and the Bubble Image Velocimetry (BIV). The good agreement found between probe measurements and the non-intrusive methods with an adequate calibration showed that the hypothesis was indeed plausible; non-intrusive methods can with sufficient accuracy measure the flow inside the flume for stepped spillways with large flow rates, i.e. for skimming flow. Nonetheless, void fraction results had a better adjustment to the probe measurements than the velocity profiles; the latter showed a consistent underestimation that may be explained by sidewall effects (up to 15 %) and possible probe's recognized overestimation (up to 5 %).

A calibration and validation procedure was developed and applied to both the IPP and the BIV methods. This procedure enabled an optimum set of parameters to be found within a defined domain of calibration parameters, and it is expected to be valid also for other type of experiments. The original IPP procedure was re-coded in order to expand its calibration capabilities and to automatically detect the water surface upper and lower limits.

Void fraction contour lines and velocity profiles were presented for 12 different stepped spillway configurations. Analyzing in particular the void fraction contours, it was shown that there are two main factors regulating the void fraction inside the eddies found in skimming flows, namely the ratio of the water surface (h) to the step height (s) and the slope. If the ratio increases, the high void fraction values inside eddies tend to reduce. The slope constrains the size and shape of eddies identified by the void fraction values. In regard to the velocity fields, valuable information was obtained within the step niche where measurements using an intrusive probe are generally difficult. In particular, both the eddy within the step niche and a high-speed flow above the pseudo-bottom were well identified.

6.5 IMPROVING BIV RESULTS THROUGH IMAGE PREPROCESSING

6.5.1 MOTIVATION

It was demonstrated in previous sections that the BIV method is capable to provide reasonable data for complete velocity fields in aerated flows which may help to support or even to better understand data from intrusive air-water measurements. However, the accuracy of this method strongly depends on the air concentration (velocity data in regions of low void fraction was found to be closer to the conductivity probe data) although wall effects, which are difficult to quantify, most likely play an additional role. As presented before, some improvements can be obtained by extensive calibration efforts. Another aspect that needs to be addressed is certainly the effect of image quality. While the results for different image resolution will be discussed at a later stage (see Section 8.2), potential improvement by image preprocessing will be discussed subsequently.

For this purpose, different filtering and image processing techniques are evaluated with the aim to test if a preceding image processing may enhance the BIV results for the exemplary case of a skimming flow in a stepped spillway model. Therefore, constant settings for BIV calculations are applied (i.e. interrogation window size, overlap, correlation method) although it was shown by LEANDRO ET AL. (2014) that these settings are of high significance for BIV accuracy. It is thus not intended in the present study to optimize the absolute BIV results but to evaluate the relative effect of the different image processing techniques.

6.5.2 METHODOLOGY

A new set of high-speed videos has been recorded with a Phantom M120 camera supplied by LaVision. The camera's maximum resolution is 1920 × 1200 px while the maximum frame rate is 730 Hz. All experiments were run at a physical model with a fixed but identical geometry as the one employed in previous sections, i.e. a slope of 1V:2H, step height s = 6 cm and specific discharge $q = 0.07$ m^2/s. Flow features were studied at step number 21, being located in the aerated, quasi-uniform flow region. All presented data is extracted at the downstream step edge. In order to enhance the contrast, the backside of the flume was equipped with a black PVC wall. Flow illumination was again achieved by white light from halogen spots.

For comparison of BIV results, the conductivity probe data from the previous studies (taken from the previous studies) was used. It is pointed out that some differences between both setups may occur. However, as the focus is put on the relative effects of image preprocessing, these differences become irrelevant. Differences, if any, arise

Selected contents from: Deltas of the future and what happens upstream - Proceedings of the 36th IAHR World Congress (The Hague, 2015), Ed: A. Mynett. Reproduced with permission from IAHR.

most likely from different inlet conditions, but become smaller in the uniform flow region.

BIV calculations were performed by use of the open-source Matlab® toolbox PIVlab (THIELICKE AND STAMHUIS, 2014B). However, different image preprocessing techniques were added based on the Matlab® Image Processing toolbox. More information about the applied algorithms can be found in GONZALEZ ET AL. (2009). The single-pass cross-correlations of subsequent frames in the BIV code have been carried out taking advantage of 2D Fourier transformation.

Previous BIV calculations, performed with the original images (without any preprocessing technique), have shown that 128 px window size for single-pass cross-correlation with 75 % overlapping (step: 32 px) give acceptable results. Larger window sizes resulted in a larger number of outliers while higher overlapping increased considerably the calculation time without improving the results. Consequently, the same settings are employed hereinafter.

Masking of regions out of flow helped to speed up calculations. In order to get a robust result, BIV was performed in a loop over 249 frame pairs with maximum resolution and frame rate and the mean results are subsequently considered for comparison to the conductivity probe results.

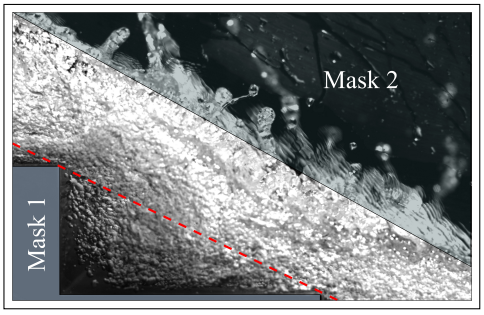

Figure 6.5.1: Non-preprocessed high-speed camera frame used in the BIV calculations (note: gray areas mark the masked flow regions, the red dashed line indicates the pseudo-bottom of the flume).

6.5.3 IMAGE PROCESSING TECHNIQUES

6.5.3.1 SPATIAL DOMAIN PROCESSING

Spatial domain refers to the image plane, in which each pixel is identified by a fixed coordinate originating from its row and column. Thus, in spatial domain processing techniques, image pixels are directly manipulated. The spatial domain processes can be defined in a general way as:

$$g(X,Z) = T\left[f\left(X,Z\right)\right] \tag{6.5.1}$$

Selected contents from: Deltas of the future and what happens upstream - Proceedings of the 36th IAHR World Congress (The Hague, 2015), Ed: A. Mynett. Reproduced with permission from IAHR.

where X and Z are pixels coordinates, $f(X, Z)$ the input image, $g(X, Z)$ the output image and T an operator which works upon f. This operator T will vary depending on the employed method. The operator can be both, a linear or nonlinear function, which can employ the value of the pixel intensity only or altogether with the neighbor pixel intensities.

Histogram equalization techniques are the most commonly used techniques when dealing with spatial domain processing methods. With histogram equalization, the intensity values of the histogram are spread out to the extreme values enhancing the contrast of the image. These techniques can be applied to the whole image at once or sectionwise. The latter method is known as Adaptive Histogram Equalization (AHE).

Histogram equalization It is noted that the values in a normalized histogram are approximations to the probability of occurrence of each intensity level in the image. Then, with $p_r(r_j)$, j = 1, 2, ..., L, with L the total number of possible levels in the input image, the histogram can be defined as a Probability Density Function (PDF). The histogram equalization can be expressed as follows:

$$s_k = T(r_k) = \sum_{j=1}^{k} p_r(r_j) \tag{6.5.2}$$

for k = 1,2, ..., L, where s_k is the intensity value in the output image corresponding to value r_k in the input image. Note that the transformation function $T(r_k)$ is simply the cumulative sum of normalized histogram values. In a normalized histogram, the values associated with the intensity levels are the probability of occurrence of each intensity level in the image as defined before.

More advanced techniques consist of matching the histogram of the input image to a template histogram so the intensity values are spread in a specified way (histogram matching). Another possibility is to perform different histogram equalizations in different small sections of the image so that a dark background in remote part of the original image is not affecting all pixels equalization. Then, this method is more suitable for improving local contrast. After performing this operation section boundaries must be linked, usually with an interpolation technique. This technique is called Adaptive Histogram Equalization (AHE). If we limit the contrast of the original image, then this technique can be called Contrast-Limited Adaptive Histogram Equalization (CLAHE). By definition, these adaptive methods fit better with the correlation algorithms in the BIV technique, which are applied in small sections as well.

Selected contents from: Deltas of the future and what happens upstream - Proceedings of the 36th IAHR World Congress (The Hague, 2015), Ed: A. Mynett. Reproduced with permission from IAHR.

6.5.3.2 FREQUENCY DOMAIN PROCESSING

Frequency domain processing is not a substitute to spatial domain processing; it is indeed complementary and some preprocessing techniques can be implemented both in the spatial or the frequency domain. Nevertheless frequency domain filtering can provide some advantages given the properties of Fourier transforms. Thereby, 2D discrete Fourier transform (DFT) can be defined as:

$$F(m,n) = \sum_{X=0}^{M-1} \sum_{Z=0}^{N-1} f(X,Z) e^{-j2\pi\left(\frac{mX}{M}+\frac{nZ}{N}\right)} \tag{6.5.3}$$

for m = 0,1,2, ...,$M-1$ and n = 0,1,2, ...,$N-1$; j refers to the imaginary number and M, N are the size of the input image f. Thus, filtering can be applied to $F(m,n)$ just multiplying by $H(m,n)$ (the filter or transfer function) obtaining the modified Fourier transform $G(m,n)$. In order to obtain the filtered spatial domain image $g(X,Z)$, inverse discrete Fourier transform can be applied as follows:

$$g(X,Z) = \frac{1}{MN} \sum_{X=0}^{M-1} \sum_{Z=0}^{N-1} G(m,n) e^{j2\pi\left(\frac{mX}{M}+\frac{nZ}{N}\right)} \tag{6.5.4}$$

for X = 0,1,2, ...,$M-1$ and Z = 0,1,2, ...,$N-1$. Additional considerations must be made with the assumption of periodicity of the image for the Fourier transform. More information about this issue can be found in GONZALEZ ET AL. (2009).

Lowpass filtering Some lowpass and highpass filtering techniques can be carried out easily in both, the spatial and the frequency domain. Lowpass filtering usually blurs the images eliminating some noise. The simplest way of conducting a lowpass filtering is averaging the value of a pixel with the rest of the neighborhood pixel values, which would be a spatial domain preprocessing technique. In the frequency domain, an Ideal Lowpass Filter (ILPF) is defined by the transfer function:

$$H(m,n) = \begin{cases} 1 & D(m,n) \leqslant D_0 \\ 0 & D(m,n) > D_0 \end{cases} \tag{6.5.5}$$

where D_0 is a specified non-negative number and $D(m,n)$ is the distance from point (m,n) to the center of the filter. Thus, D_0 could be defined as a masking distance for the Fourier transform $F(m,n)$. The geometrical location of the points where $D(m,n) = D_0$ is a circle. A Butterworth Lowpass Filter (BLPF) of order r, with a cutoff frequency at a distance D_0 from the origin, has the transfer function:

$$H(m,n) = \frac{1}{1+[D(m,n)/D_0]^{2r}} \tag{6.5.6}$$

Selected contents from: Deltas of the future and what happens upstream - Proceedings of the 36th IAHR World Congress (The Hague, 2015), Ed: A. Mynett. Reproduced with permission from IAHR.

Additionally, the Gaussian Lowpass Filter (GLPF) transfer function can be defined as:

$$H(m,n) = e^{-D^2(m,n)/2D_0^2} \tag{6.5.7}$$

Highpass filtering Highpass filtering sharpens the image by attenuating the low frequencies and leaving the high frequencies of the Fourier transform relatively unchanged. It is usually defined as the complementary technique to the lowpass filtering. Given the transfer function $H_{lp}(m,n)$ of a lowpass filter, the transfer function for a highpass filter (H_{hp}) is obtained as:

$$H_{hp} = 1 - H_{lp}(m,n) \tag{6.5.8}$$

Thus, the Ideal Highpass Filter (IHPF), the Butterworth Highpass Filter (BHPF) or the Gaussian Highpass Filter (GHPF) can be defined as for the lowpass filtering.

Wiener filtering This is one of the earliest and best known approaches to linear image restoration (GONZALEZ ET AL., 2009). A Wiener filter seeks an estimate $\hat{f}$ that minimizes the statistical error function:

$$e^2 = E\left\{\left(f - \hat{f}\right)^2\right\} \tag{6.5.9}$$

where E is the expected value operator and f is the undegraded image. The solution to this expression in the frequency domain is:

$$\hat{F}(m,n) = \left[\frac{1}{H(m,n)}\frac{|H(m,n)|^2}{|H(m,n)|^2 + |N(m,n)|^2/|F(m,n)|^2}\right][H(m,n)F(m,n) + N(m,n)] \tag{6.5.10}$$

where $|H(m,n)|^2 = H^*(m,n)H(m,n)$, being $H^*(m,n)$ the complex conjugate of the degradation function $H(m,n)$, $F(m,n)$ the frequency domain image and $N(m,n)$ the Fourier transform of the noise. Note that $|N(m,n)|^2$ is the power spectrum of the noise and $|F(m,n)|^2$ the power spectrum of the undegraded image. Thus, $|N(m,n)|^2/|F(m,n)|^2$ can be defined as the signal-to-noise ratio. If no information is known about the noise, white noise can be assumed. Further assumptions may be done about the degradation function $H(m,n)$.

6.5.4 RESULTS

6.5.4.1 CONTRAST ADJUSTMENT

Contrast adjustment has been carried out by means of Contrast-Limited Adaptive Histogram Equalization (CLAHE), as described before. The main variable in this

Selected contents from: Deltas of the future and what happens upstream - Proceedings of the 36th IAHR World Congress (The Hague, 2015), Ed: A. Mynett. Reproduced with permission from IAHR.

method is the application window size. Once the histogram equalization is performed in every window, the windows are merged using an interpolation procedure. Different window sizes have been tested ranging from 4 to 128 px (3 to 100 % of the interrogation window size in the BIV correlation algorithm). The results are presented in Fig. 6.5.2. Apparently, even small window sizes (i.e. 4 px) improve the results, particularly in higher elevations with larger void fraction. Higher values for the window size produce similar results, not leading to a significant difference. Best results were obtained for 16 px and 32 px windows sizes; which corresponds to 12.5 and 25 % of the BIV interrogation window size, respectively.

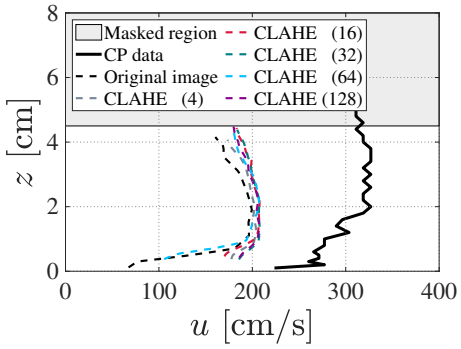

Figure 6.5.2: Velocity profiles obtained using CLAHE algorithm

6.5.4.2 LOWPASS FILTERING

As described before, different lowpass filtering techniques can be defined depending on the transfer function. Ideal Lowpass Filter (ILPF), Butterworth Lowpass Filter (BLPF) and Gaussian Lowpass Filter (GLPF) have been employed with different D_0 values. For BLPF, n was additionally set to 1 to reduce the number of tests.

As a general result, lowpass filtering of the images - by its nature - produced excessive blurring of the images (see Fig. 3.1.8(A)). This effect is unfavorable for the PIV (or BIV) method which is known to perform better for discrete particles. Blurring of images results in loss of texture information and thus yields a decrease of BIV accuracy (Fig. 6.5.3, left column). It may be assumed that higher values of D_0, producing lower blurring, may result in similar results as the non-preprocessed images. However, no clear trend can be observed in the results. In any case, this method may not to be recommended for preprocessing BIV images.

6.5.4.3 HIGHPASS FILTERING

Similar highpass filtering techniques can be defined, as done for the lowpass filters, i.e. Ideal Highpass Filter (IHPF), Butterworth Highpass Filter (BHPF) and Gaussian Highpass Filter (GHPF).

Selected contents from: Deltas of the future and what happens upstream - Proceedings of the 36th IAHR World Congress (The Hague, 2015), Ed: A. Mynett. Reproduced with permission from IAHR.

Highpass filters enhance the main features of the image by sharpening image textures, yielding a more white-over-black look alike image. Results obtained with images, preprocessed with beforementioned methods, are presented in Fig. 6.5.3 (right column). It is found that similar results are obtained for all techniques with optimum D_0 values between 18 px and 30 px. As a main feature, highpass filtering improves the shape of the velocity profile in the highly aerated region were the correlation performance fails more.

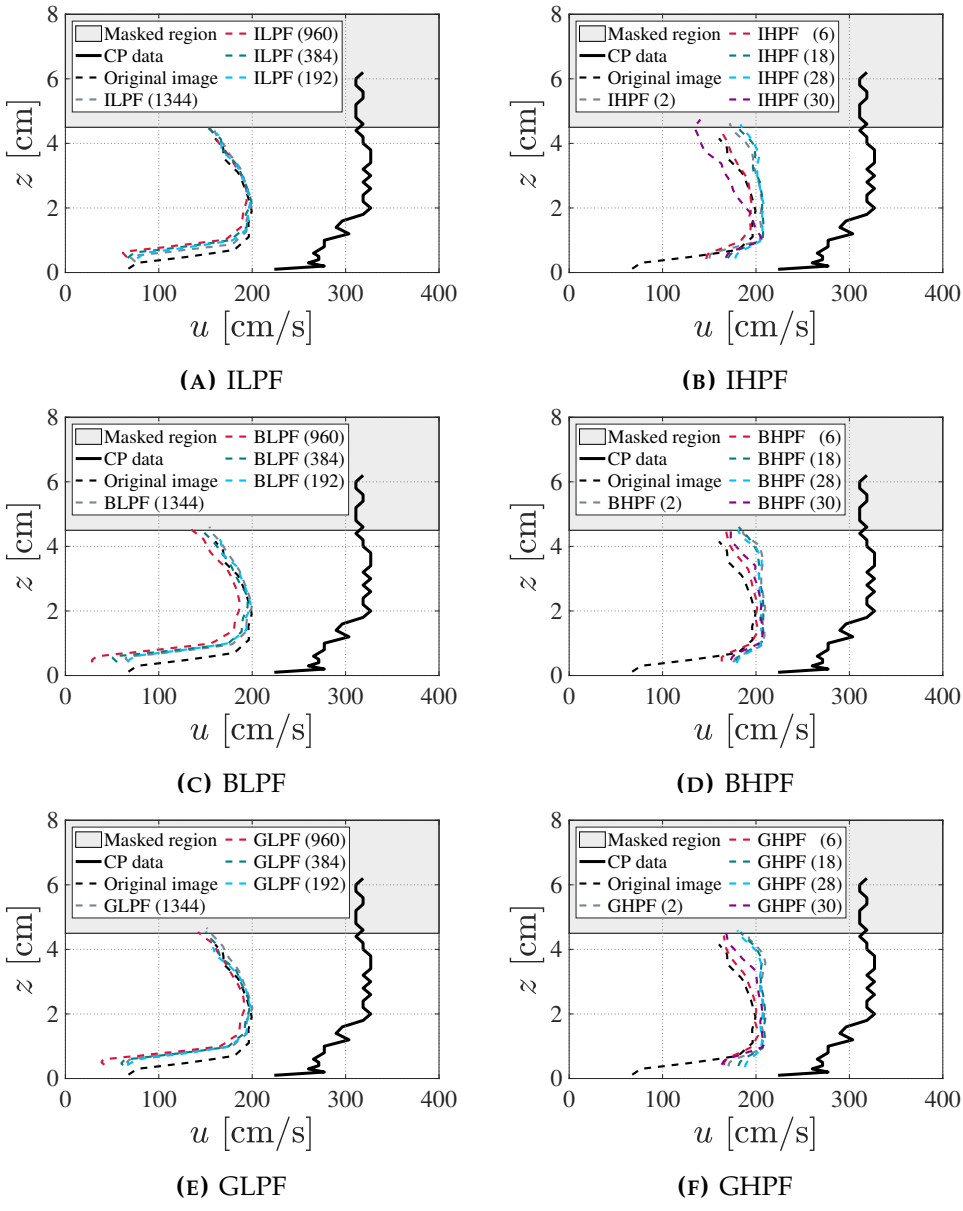

(A) ILPF (B) IHPF

(C) BLPF (D) BHPF

(E) GLPF (F) GHPF

Figure 6.5.3: Velocity profiles obtained using Lowpass and Highpass filtering with different D_0 values

Selected contents from: Deltas of the future and what happens upstream - Proceedings of the 36th IAHR World Congress (The Hague, 2015), Ed: A. Mynett. Reproduced with permission from IAHR.

6.5.4.4 WIENER FILTERING

Fig. 6.5.4 presents the results using a Wiener filter. It is highlighted that this method does not yield any improvement in the BIV calculations. It must be noted that original images are densely populated with edges (see Fig. 3.1.8) and fast changing gradients and Wiener filter produced some blurring even for smaller values of the windows size of application. However, a lower value of the Wiener filter window size (i.e. 3 px), was found to improve the BIV calculation when working in combination with other methods.

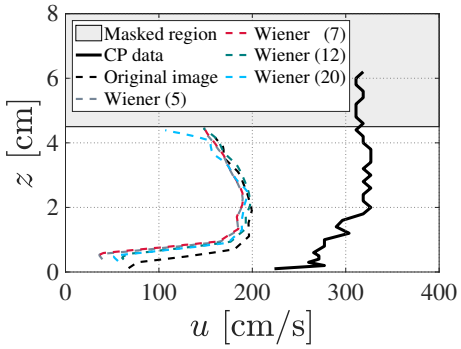

Figure 6.5.4: Velocity profiles obtained using Wiener filtering algorithm

6.5.4.5 PREPROCESSING TECHNIQUES COMBINATIONS

The option of combining different filtering techniques is analyzed subsequently. Two preprocessing techniques combinations are presented. Combination A includes 1: CLAHE(32), 2: GHPF(24) and 3: Wiener(3) and corresponds to the best standalone options obtained previously, combined with the Wiener method. Combination B is arranged by 1: CLAHE(16), 2: BHPF(18) and 3: Wiener(3) which corresponds to the second best options and again the Wiener method. Although Wiener filter has shown to blur the images when working individually, combined with these other two preprocessing operations has shown to slightly enhance the BIV performance with small window sizes. In any case, it is pointed out that the effect of different filtering combinations strongly depend on the order of single filters. Both combinations applied to the original images are shown in Fig. 6.5.5; the BIV obtained results are presented in Fig. 6.5.6.

As shown in Fig. 6.5.6, similar results have been obtained with both combinations. Thus, it is not mandatory to obtain an optimum value of the preprocessing techniques parameters but to generally tune the image quality in a proper range. Best improvements have been obtained in the highly aerated region and close to the pseudo-bottom, as illustrated in Fig. 6.5.6. The accuracy enhancement in the upper region (calculated over the raw original images BIV result) is about 23 %. It has been also observed that the number of outliers is significantly reduced. However, accuracy

improvements obtained with every method separately does not add to the improvement of other methods when combined, thus a non-linear result is obtained when combining different preprocessing techniques. Hence, one technique which may reduce the accuracy when applied solely, may enhance the quality of the BIV result when combined with a different technique.

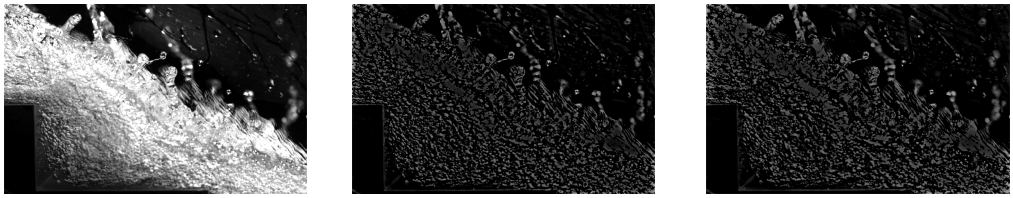

(A) Original image **(B)** Combination A **(C)** Combination B

Figure 6.5.5: Resulting images from Combinations A and B compared the original image

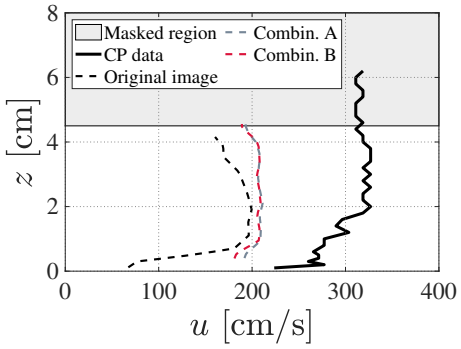

Figure 6.5.6: Velocity profiles obtained using combinations A and B

6.5.5 CONCLUSIONS

Contrast enhancement is effective for all window sizes. It enhances the difference between extreme intensity values and helps the correlation algorithm detecting maximum intensity values. Lowpass filtering has shown excessive blurring, which is unsuitable for BIV. Highpass filtering, however, was found to be very effective, producing a new set of images with enhanced bubble features and thus producing better BIV results. Combinations of the studied preprocessing methods can improve the results as well when employing the optimum values obtained working standalone. However, the combination does not necessarily produce an additive effect over the performance improvement obtained for every technique.

Image preprocessing in general may help identifying key features of the images by eliminating unnecessary features for the correlation algorithm. They may also considerably reduce the number of outliers in the BIV calculations. Filtering techniques seems to be more important for BIV than for PIV, where particles are

Selected contents from: Deltas of the future and what happens upstream - Proceedings of the 36th IAHR World Congress (The Hague, 2015), Ed: A. Mynett. Reproduced with permission from IAHR.

smaller and of constant shape and appearance. BIV has to deal with bubble blobs and light reflections, bubble shape changes and high number of bubbles which are a handicap for any BIV computation. In future, improved peak finding algorithms and cross-correlation setups altogether with more advanced postprocessing techniques could help to get more accurate results from BIV in highly-aerated flows.

CHAPTER 7

OPTICAL FLOW

7.1 INTRODUCTION

Optical flow may be understood as the motion of intensity patterns in a series of images and it is sometimes referred to as the image velocity (BARRON ET AL., 1994). For its original application in computer vision, i.e. object recognition and tracking, optical flow generally estimates a 2D motion field as a result of a projection of 3D motion to the image plane. In experimental fluid mechanics, only a few attempts have been made to apply optical flow for velocity field estimation and to compete with PIV (CORPETTI ET AL., 2006; LIU AND SHEN, 2008; LIU ET AL., 2015; RUHNAU ET AL., 2005; SEONG ET AL., 2019), although many flow cases may be considered two-dimensional with sufficient accuracy and thus optimal cases for application of optical flow methods.

Seminal works on optical flow estimation have been presented in the early 1980's by HORN AND SCHUNCK (1981) and LUCAS AND KANADE (1981). Following the same idea of object tracking, both methods are fundamentally different in one aspect: While the Lucas-Kanade technique identifies image features in motion and estimates velocities for the corresponding pixel neighborhoods only, the Horn-Schunck method provides velocity data for every pixel, regardless of any physical motion. For the latter, the computer vision community refers to as a dense motion or velocity field. According to FORTUN ET AL. (2015), estimation of a dense motion field is the most low-level optical flow characterization as it provides dispensable data. This drawback for general applications, however, may be a significant benefit for fluid mechanics cases. A dense velocity field, i.e. velocity information at every pixel, may help to identify turbulent flow structures (although idealized as two-dimensional) with very high spatial resolution. Certainly, sparse motion data may be sufficient in some hydraulic engineering cases, e.g. fish detection and tracking (Fig. 1.2.2).

Both, the Lucas-Kanade and Horn-Schunck methods, are so-called gradient-based algorithms (ATCHESON ET AL., 2009) or differential techniques (BARRON ET AL., 1994). With the assumption of intensity conservation of pixels in motion, i.e.

$$\frac{\mathrm{d}I}{\mathrm{d}t} = 0 \tag{7.1.1}$$

with I the pixel intensity and t the time, the *optical flow constraint* may be obtained through first-order Taylor series expansion:

$$\frac{\partial I}{\partial t} + \frac{\partial I}{\partial X}\frac{\partial X}{\partial t} + \frac{\partial I}{\partial Z}\frac{\partial Z}{\partial t} = 0 \tag{7.1.2}$$

with X and Z the pixel coordinates in horizontal and vertical direction. Higher-order derivatives are ignored with the assumption of small and non-rotational, dilation-free displacements (BARRON ET AL., 1994; BRUHN ET AL., 2005). With the unknown velocities (or displacements, if $\partial t = 1$) $U = \partial X/\partial t$ and $W = \partial Z/\partial t$, the optical flow is $V = [U, W]^T$. The optical flow constraint in Eq. 7.1.2 describes an ill-posed problem with a single linear equation in two unknowns, i.e. U and W (HORN AND SCHUNCK, 1981). This problem is known as the *aperture problem*, which describes that V can be computed in the direction of image gradients only, but the computation along an iso-brightness contour is precluded (HORN AND SCHUNCK, 1981). A way to constrain V is to consider a group of pixels instead of single pixels with the assumption of certain motion behavior within the group.

Subsequently, the basic concepts of LUCAS AND KANADE (1981) and HORN AND SCHUNCK (1981), based on the above described optical flow constraint are presented. Additionally, the Farnebäck method, which is another technique to provide dense velocity fields, is introduced. All methods are implemented in the OpenCV[1] and therefore widely used in the computer vision community.

7.1.1 LUCAS-KANADE METHOD

The basic assumption of the Lucas-Kanade method is the constancy of displacements in the neighborhood of a regarded pixel. This assumption is reasonable for motion of rigid obstacles. Equation 7.1.2 may be rewritten as:

$$\frac{\partial I(X_i, yZ_i)}{\partial X}U + \frac{\partial I(X_i, Z_i)}{\partial Z}W = -\frac{\partial I(X_i, Z_i)}{\partial t} \tag{7.1.3}$$

with $i = 1 \ldots n$ and n the number of neighboring pixels considered. Obviously, the basic optical flow constraint becomes over-determined. LUCAS AND KANADE (1981) propose to solve this problem iteratively using a least-square optimization and a weighting function $\mathbb{W}$ to account for different contribution of each pixel. $\mathbb{W}$ is typically selected as a Gaussian function. BARRON ET AL. (1994) specify the solution to this problem as:

$$A^T \mathbb{W} A V = A^T \mathbb{W} b \tag{7.1.4}$$

[1] All methods are also implemented in the Matlab® computer vision toolbox. OpenCV is an open-source computer vision and machine learning software library (BRADSKI AND KAEHLER, 2008). OpenCV is natively written in C++, but APIs for Python, Java and Matlab are also available.

with

$$A = \begin{bmatrix} I_{X,1} & I_{Z,1} \\ I_{X,2} & I_{Z,2} \\ \vdots & \vdots \\ I_{X,n} & I_{Z,n} \end{bmatrix} \quad , \quad \mathbb{W} = \begin{bmatrix} W_1 & 0 & \cdots & 0 \\ 0 & W_2 & \ddots & \vdots \\ \vdots & \ddots & \ddots & 0 \\ 0 & \cdots & 0 & W_n \end{bmatrix} \quad \text{and} \quad b = - \begin{bmatrix} I_{t,1} \\ I_{t,2} \\ \vdots \\ I_{t,n} \end{bmatrix} \quad .$$

I_X and I_Z are the brightness gradients in X and Z directions I_t is the derivative with respect to time. Apparently, a solution for the optical flow V with

$$V = \left[A^T \mathbb{W} A \right]^{-1} A^T \mathbb{W} b \tag{7.1.5}$$

requires the matrix $M = \left[A^T \mathbb{W} A \right]$ to be invertible. Eigenvalues equal (or practically close) to zero must indicate an edge or a uniform region (ZHANG AND CHANSON, 2017). TOMASI AND KANADE (1991) specify the following physical meanings of eigenvalues:

- Two small eigenvalues: roughly constant intensity profile within a window (uniform region).
- One large, one small eigenvalue: unidirectional pattern (edge).
- Two large eigenvalues: corners or salt-and-pepper-texture.

In conclusion, TOMASI AND KANADE (1991) suggest to consider a threshold for eigenvalues to select only features which are suitable for tracking. Based on this concept, different corner detectors are available (e.g. HARRIS AND STEPHENS, 1988; SHI AND TOMASI, 1994) which can be easily combined with the Lucas-Kanade method. Figure 7.1.1 shows the detected features using a Shi-Tomasi-Detector for exemplary, seeded water flow (i.e. the previously considered case of a wave propagating from left tor right over a submerged plate, compare Section 3.1). The number of features is indirectly specified by an Euclidean distance of 20 px. The figure suggests that the Lucas-Kanade method in combination with a Shi-Tomasi corner detector may be useful for flow visualization (ZHANG AND CHANSON, 2017) rather than for flow field estimation due to the random selection of tracer particles.

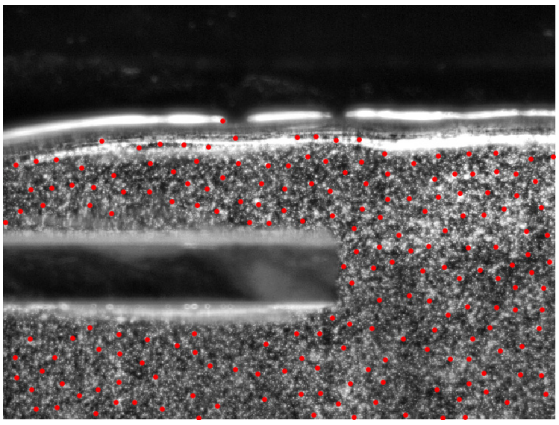

Figure 7.1.1: Detected features to track with the Lucas-Kanade method obtained with a Shi-Tomasi corner detector

7.1.2 HORN-SCHUNCK METHOD

In contrary to LUCAS AND KANADE (1981), HORN AND SCHUNCK (1981) assume that brightness patterns vary smoothly in a global context, i.e. within the entire image. To account for this additional constraint, HORN AND SCHUNCK (1981) consider a smoothing term, given by the magnitude of optical flow gradients, and propose to minimize the error function

$$E = \int\int \left[(I_X U + I_Z W + I_t)^2 + \alpha \left(|\nabla U|^2 + |\nabla W|^2 \right) \right] \mathrm{d}X\mathrm{d}Z \tag{7.1.6}$$

and thus to minimize the difference between the flow field at a pixel and the local average around it (LUCAS, 1984). $\nabla = (\partial/\partial X, \partial/\partial Z)$ is the spatial gradient and α is a weighting factor for the smoothing term. It is noteworthy that for image areas, where the brightness gradient is zero, the smoothing term fills in averaged velocity data from the neighboring pixels and thus yield a dense velocity field.

HORN AND SCHUNCK (1981) show that Eq. 7.1.6 may be approximated by

$$(\alpha + I_X^2 + I_Z^2)(U - \bar{U}) = -I_X(I_X\bar{U} + I_Z\bar{W} + I_t) \tag{7.1.7}$$

$$(\alpha + I_X^2 + I_Z^2)(W - \bar{W}) = -I_Z(I_X\bar{U} + I_Z\bar{W} + I_t) \tag{7.1.8}$$

with $\bar{U}$, $\bar{W}$ the average velocities in X- and Z-direction in the neighborhood of a considered pixel. However, solving this pair of equations by standard techniques, e.g. Gaussian elimination, may be very costly. Therefore, HORN AND SCHUNCK (1981) suggest to consider its product representation, e.g. by Gauss-Seidel (GOLUB

AND VAN LOAN, 2013), which yields

$$U^{n+1} = \bar{U}^n - \frac{I_X \left(I_X \bar{U}^n + I_Z \bar{W}^n + I_t \right)}{\alpha + I_X^2 + I_Z^2} \tag{7.1.9}$$

$$W^{n+1} = \bar{W}^n - \frac{I_Z \left(I_X \bar{U}^n + I_Z \bar{W}^n + I_t \right)}{\alpha + I_X^2 + I_Z^2} \tag{7.1.10}$$

These equations need to be solved iteratively with n the iteration number. Special attention is required for the determination of the intensity derivatives. Eventually, more robust methods of numerical differentiation than the originally proposed first-order differences should be considered, e.g. a four-point central differences method as applied by BARRON ET AL. (1994).

LUCAS (1984) rates the Horn-Schunck method to be based on a fairly weak assumption. Several derivatives of the Horn-Schunck method have been proposed in the past, but, as highlighted by SUN ET AL. (2010), the classical approach still performs well when benchmarked against newer formulations. A comprehensive overview is presented in SUN ET AL. (2010), WEDEL AND CREMERS (2011) and FORTUN ET AL. (2015). Although not developed for application to fluid flows in its original context, it must be emphasized that the global smoothing is of significant benefit for the motion of continuous patterns, such as water with seeding particles or aerated flows. The Horn-Schunck method will be further discussed in the subsequent Sections 7.2 and 7.3 which demonstrate its application to different types of flow.

7.1.3 FARNEBÄCK METHOD

As presented before, classical methods for the determination of the optical flow have been proposed by HORN AND SCHUNCK (1981), yielding a dense velocity field (with information for every pixel), and LUCAS AND KANADE (1981) providing sparse velocity data at selected locations only. Numerous more advanced approaches have been developed in the recent past. One of these novel techniques was introduced by FARNEBÄCK (2003) assuming that the pixel intensity in a pixel neighborhood can be approximated by a quadratic polynomial:

$$I_1(X, Z) \approx \begin{bmatrix} X \\ Z \end{bmatrix} A_1 \begin{bmatrix} X & Z \end{bmatrix} + b_1^T \begin{bmatrix} X & Z \end{bmatrix} + c_1 \tag{7.1.11}$$

$$I_2(X + U, Z + W) = \begin{bmatrix} X + U \\ Z + W \end{bmatrix} A_2 \begin{bmatrix} X + U & Z + W \end{bmatrix} + b_1^T \begin{bmatrix} X + U & Z + W \end{bmatrix} + c_2 \tag{7.1.12}$$

with 1 and 2 the indices related to image 1 and image 2, A a symmetric matrix, b a vector and c a constant. By a simple polynomial expansion, FARNEBÄCK (2003) shows that the unknown displacement vector may be determined as:

$$\begin{bmatrix} U \\ V \end{bmatrix} = -0.5 A_1^{-1} (b_2 - b_1) \tag{7.1.13}$$

thus, requiring A_1 to be invertible. It must be noted that Eq. 7.1.13 holds only for absolute pixel intensity conservation ($A_1 = A_2$), i.e. an ideal condition which is rarely met in practice. By consequence, the symmetric matrix in Eq. 7.1.13 may be replaced by $0.5(A_1 + A_2)$ as a reasonable approximation. Eq. 7.1.13 can be solved pixelwise. However, FARNEBÄCK (2003) describes the results to be affected by noise and proposes to solve Eq. 7.1.13 for an ensemble of pixels within a neighborhood while applying a weighting function for the pixels involved. This step is reasonable if it is assumed that the displacement field is only slowly varying. Eq. 7.1.13 turns then into a more complex minimization problem which needs to be solved iteratively. For more detailed information, the reader is referred to the original literature (FARNEBÄCK, 2003). One drawback of this technique is that the local polynomials are likely exposed to spatial variance, thus involving some error which increases for large displacements.

7.1.4 IMAGE PYRAMIDS

All presented approaches suffer from the assumption of small displacements. Large displacements may remain unresolved or incorrect motion may be obtained. To overcome this issue, a multi-resolution approach, i.e. a so-called image pyramid, can be employed. The image pyramid is a set of images, including an original image at full resolution and a certain number of downsampled, blurred images with different resolutions. A downsampling factor of 2 is commonly chosen. The optical flow is first estimated at the coarsest level. The resulting a priori displacement is then upsampled to next finer resolution and used to unwarp the next image. Fractional pixel locations are determined by interpolation (ATCHESON ET AL., 2009). This image pyramid technique is illustrated in Fig. 7.1.2. Depending on the original image resolution, a total number of 3 to 5 five pyramid levels may be reasonable as the loss of information in the coarsest level can be significant and cause difficulties in computing the optical flow (ATCHESON ET AL., 2009). BUNG AND VALERO (2016B) demonstrate the significant influence on the quality of results. More detailed information on the image pyramid technique can be found in ADELSON ET AL. (1984) and BURT AND ADELSON (1983).

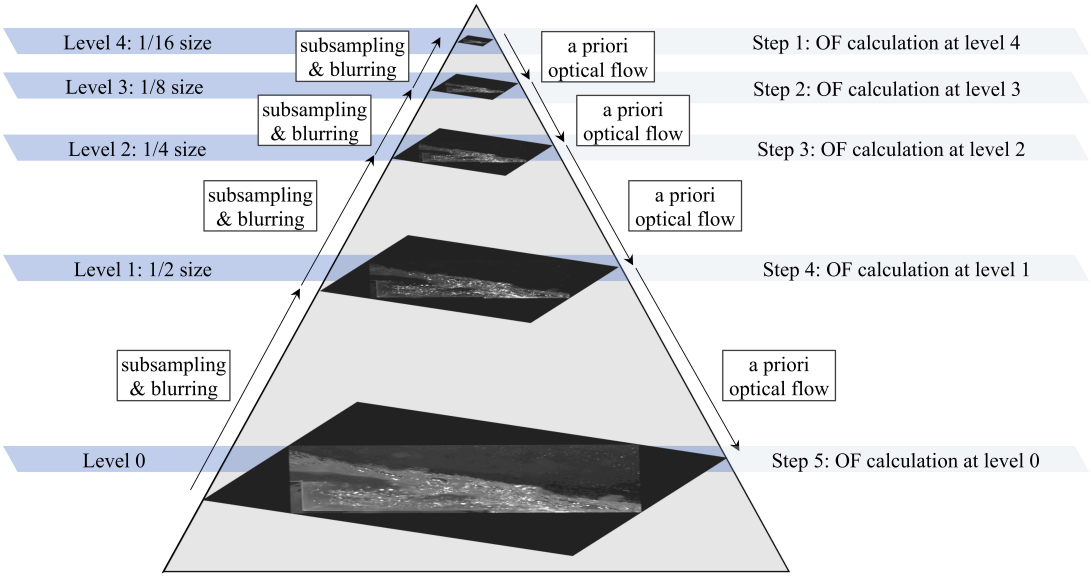

Figure 7.1.2: Exemplary procedure of building an image pyramid (here: with 5 pyramid levels and a downsampling factor of 2) and calculating optical flow using a priori data from coarser image levels

7.2 APPLICATION OF THE OPTICAL FLOW METHOD TO VELOCITY DETERMINATION IN HYDRAULIC STRUCTURE MODELS

Authors: Daniel B. Bung; Daniel Valero
Conference: 6th International Symposium on Hydraulic Structures, Portland
Year: 2016

Abstract: Optical flow estimation is used in Computer Vision for detection of moving obstacles in a sequence of images. The optical flow (OF) is defined as the displacement of brightness patterns between two sequent images. In this paper, this method is applied to high-speed images taken in hydraulic structure models for determination of velocity fields. Water is seeded with tracer particles in two cases and is self-aerated in a third case. It will be shown that the OF method gives valuable results that compare well to other velocity measurements, e.g. by Particle Image Velocimetry. The OF method is generally more time-consuming compared to PIV, but an advantage is given by the density of information when using a so-called global method, as velocity information is obtained at every pixel location.

Keywords: Optical flow, Particle Image Velocimetry, imaging techniques, velocity estimation

7.2.1 INTRODUCTION

Physical modeling of hydraulic structures is still a common technique to elaborate flow patterns, water depths, flow velocities, turbulence, etc.. Flow velocities are typically measured by means of intrusive probes, such as anemometers for 1D and ADVs for 3D point measuring in clear water (ASCE, 2000) and dual-tip conductivity or fiber-optical probes in bubbly flows (FELDER AND CHANSON, 2015). A drawback of these probes is the limitation to a single point (i.e. the velocity is obtained as a local value) and the inevitable perturbation of the flow.

If one is interested in instantaneous 2D (or 3D) flow fields, Particle Image Velocimetry (PIV) is a widely accepted technique based on cross-correlation of subsequent frames from a video, which is captured with either a standard or high-speed camera depending on the expected flow velocity (ADRIAN AND WESTERWEEL, 2011). To visualize the flow, a tracer material needs to be added to the water. Subsequent frames are divided into so-called interrogation windows of user-defined sizes and 2D cross-correlation in spatial or frequency domain is performed to find the most probable displacements of particles within these windows by using different peak finding methods. The method is thus an integral approach yielding a single, statistically determined velocity information for each interrogation window.

Another imaging technique which may be applied to experimental fluid mechanics is given by the optical flow method (OF). Coming from the computer vision field, it is not yet well-known in the community. To date, this method is mainly used in fields like video compression (motion estimation to predict intermediate frames) or vehicle navigation (autonomous car driving) as reported by FORTUN ET AL. (2015). A first approach for optical flow estimation was presented by HORN AND SCHUNCK (1981), defining the optical flow as the movement of brightness (intensity) patterns in a sequence of images. OF aims to approximate a 2D motion or velocity field, which is a projection of generally 3D velocities of surface points onto the imaging surface from spatio-temporal patterns of image intensity. In order to relate the movement of brightness patterns to the movement of an object, it is assumed that the brightness of a moving pixel in the pattern remains constant during the movement. The Horn-Schunck method is a global method attempting to minimize a global energy function. In addition, local methods have been developed based on optimization of local energy-like expression. For instance, LUCAS AND KANADE (1981) assume a small, constant optical flow within a neighborhood. By consequence, this method does not allow the determination of optical flow within a region of uniform intensity. Local methods can only provide sparse flow fields in contrast to global methods, which provide dense flow fields with velocity information at every point. Since its original formulation, several improvements and further developments on this basic idea of the optical flow method have been presented and give surprisingly good results although the basic assumption of brightness constancy may be unrealistic in many applications due to shading effects or changes in illumination.

In some recent studies, the Horn-Schunck approach was applied to fluid flows using particle images obtained from PIV measurements (LIU ET AL., 2015; LIU AND SHEN, 2008). CORPETTI ET AL. (2006) confirm a good agreement with PIV data implementing an approach to account for the continuity equation as well as divergence and vorticity structures of the flow. LIU ET AL. (2015) state that OF, as a differential approach, is more suitable to images with continuous patterns so that single particles used for PIV are not the best case for OF.

This paper aims to test the optical flow method to the field of hydraulic structures modeling for 1) clear water flows being seeded with particles and 2) aerated flows.

7.2.2 METHODOLOGY

The constancy of brightness $I(X, Z, t)$ of a moving pixel with pixel coordinates X and Z at time t may be expressed as:

$$\frac{\mathrm{d}I}{\mathrm{d}t} = \frac{\partial I}{\partial t} + \frac{\partial I}{\partial X}\frac{\partial X}{\partial t} + \frac{\partial I}{\partial Z}\frac{\partial Z}{\partial t} \tag{7.2.1}$$

with I_t the temporal derivative, I_X and I_Z the spatial image derivatives in X and Z direction and U and W the unknown spatial displacements in X and Z directions between two sequent frames. Eq. 7.2.1 may be rewritten as:

$$I_t + I_X U + I_Z W = 0 \tag{7.2.2}$$

Equation 7.2.2 is the so-called spatial term. In order to solve this ill-posed problem (1 equation, 2 variables), a second constraint, i.e. a data term, is required. HORN AND SCHUNCK (1981) assumed that neighboring points have a similar velocity by reducing the square of the gradients of the optical flow velocity. Thus, the following objective function needs to be minimized:

$$E = \int\int \left[(I_X U + I_Z W + I_t)^2 + \alpha \left(|\nabla U|^2 + |\nabla W|^2 \right) \right] \mathrm{d}X\mathrm{d}Z \tag{7.2.3}$$

where $\nabla = (\partial/\partial X, \partial/\partial Z)$ is the spatial gradient and α a smoothing factor for the spatial term. This minimization yields (BRUHN ET AL., 2005):

$$\begin{aligned} \alpha \Delta U - \left(I_X I_t + I_X^2 U + I_X I_Z W \right) &= 0 \\ \alpha \Delta W - \left(I_Z I_t + I_Z^2 W + I_X I_Z U \right) &= 0 \end{aligned} \tag{7.2.4}$$

where ΔU is the spatial Laplace operator over U defined by the scalar product $\nabla \cdot \nabla U$. At image locations with low information from pixel derivatives, no reliable local flow estimate is possible. The Laplace operator fills in information from the neighborhood, α works then as a diffusion coefficient for U and W.

For this paper, an open-source MATLAB® toolbox for optical flow determination developed by SUN ET AL. (2010) is employed. This toolbox implements several different OF methods besides the classical Horn-Schunck method given above as well as different additional image processing techniques, which were developed in the recent past and known to likely improve the results. BUNG AND VALERO (2016B) showed that this toolbox can give valuable results in highly aerated flows on stepped spillways when using the air bubbles as seeding. A similar approach was introduced by RYU ET AL. (2005) and applied by BUNG (2011C), LEANDRO ET AL. (2014), and BUNG AND VALERO (2015) using the Bubble Image Velocimetry (BIV) technique, an adapted Particle Image Velocimetry (PIV) technique using the bubbles instead of tracer particles. In order to demonstrate the general applicability of OF to water flows around hydraulic structures, all investigations are limited to the basic Horn-Schunck scheme.

In detail, three test cases are investigated:

1. Dam-break flow being observed in a 30 cm wide flume with an initial water depth of 40 cm in the reservoir (images taken from OERTEL AND BUNG (2012B)); images of the seeded flow are taken with a high-speed camera at 900 fps and

1280 × 576 px resolution; the OF method is compared to PIV.

2. Wave propagation over a submerged plate (installed at 6 cm below the still water level) being modeled in a 30 cm wide wave flume for a wave height $H = 4$ cm, a wave period $T = 1$ s, and a water depth of 30 cm (images taken from BUNG ET AL. (2008)); the water is again seeded with particles, and images are taken with a high-speed camera with only 256 × 256 px resolution at 500 fps; OF is compared to numerical results from a Large Eddy Simulation.

3. Slightly aerated flow over a stepped spillway with 50 cm width, 6 cm step height, 1V:2H slope, and a specific discharge $q = 0.07$ m^2/s; the high-speed video is captured at 732 fps and a resolution of 1920 × 1200 px on step 5, which was found to be the inception point of surface self-aeration by BUNG (2011A) (the same setup has been previously used in BUNG AND VALERO (2016B) for OF determination for fully aerated flow); water is not seeded in this experiment and, hence, OF is performed on transported air bubbles; OF is compared to BIV results.

MatPIV in its latest version 1.61 is employed for calculation of PIV- and BIV-based velocity fields. MatPIV (SVEEN, 2004) is another open-source toolbox for MATLAB®, which applies a classical PIV technique allowing variation of several parameter settings, e.g. interrogation window size, window overlap, and different filtering methods for smoothing of the velocity field. The reader may note that the studies were conducted by use of simple halogen spotlights being installed in front of the inspection window and above the flumes. It is acknowledged that the presented results are likely affected by sidewall effects as the applied illumination does not allow to define a thin measuring plane as laser sheets usually do. Thus, particles and bubbles near the sidewall are taken into account as well as those in the rear. This fact may also lead to some distortion affecting the results. Moreover, it is pointed out that 3D flow fields are reduced to 2D for all methods.

7.2.3 RESULTS

7.2.3.1 DAM BREAK FLOW

This case is analyzed with both methods, OF and PIV using MatPIV. As PIV is a well-established method in hydraulic engineering, this technique is applied to compare and assess the OF capabilities. The PIV calculations are performed with quadratic interrogation windows and 50 % overlap. Although MatPIV generally includes several filter options to improve results, all calculations are carried out without any filtering and smoothing.

Figure 7.2.1 illustrates the first high-speed image, which was recorded at $t = 0.50$ s after the gate release. In physical scale, the image is roughly 90 cm wide, yielding a

pixel density of ~14 px/cm. In combination with the subsequent frame being recorded 1/900 s later, velocities are determined by both imaging techniques and compared to velocity profiles that were visually extracted from the images. For this purpose, four sections of the images were selected with a width of 16 px each, namely at $x = -7$ cm (section 1), $x = 8$ cm (section 2), $x = 23$ cm (section 3), and $x = 38$ cm (section 4) where the gate axis defines the zero position $x = 0$ cm (see Fig. 7.2.1). Particles within these sections were tracked by eye from one frame to the next, and their displacements were noted. Due to the high density of particles, displacement data were obtained with an average distance of roughly 4 px along the water column (e.g. 38 data points were obtained in section 3, where the water depth was given by 160 px).

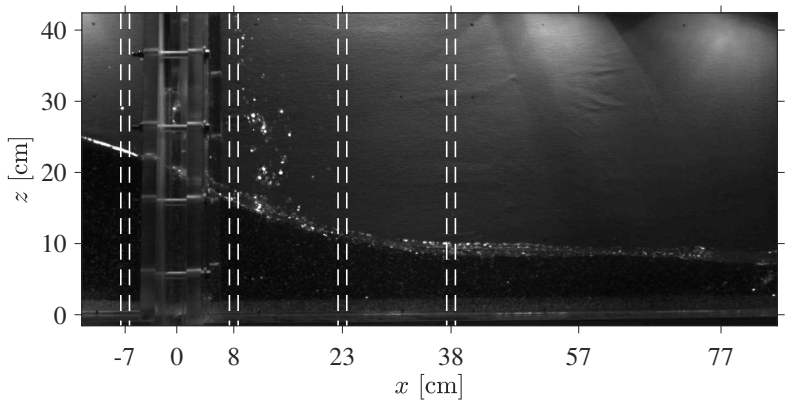

Figure 7.2.1: High-speed frame at $t = 0.50$ s after gate opening (from OERTEL AND BUNG (2012B))

The main parameters influencing the quality of calculated results within the two image processing techniques are given by the number of iterations in each warping step for OF and the interrogation window size for PIV. In order to quantify these influences, both parameters have been systematically varied and the resulting mean error defined by

$$\text{meanerror} = \frac{1}{n}\sum_{i}^{n}\frac{vel_{im,i} - vel_{vis,i}}{vel_{vis,i}} \tag{7.2.5}$$

has been determined. In Eq. 7.2.5, n is the total number of visually detected data points in a section, $vel_{vis,i}$ is the i^{th} visually determined velocity magnitude and $vel_{im,i}$ the velocity magnitude in the same elevation from each imaging technique. Using a median filter of size 12×12 px for smoothing of the dense data in OF, the mean errors in Fig. 7.2.2 were obtained. PIV calculations were run using a multiple approach with three different decreasing interrogation window sizes, i.e. the final pass was run with half of the initial window size.

Obviously, both imaging methods produce results of similar accuracy if settings are properly chosen. In section 1 with relatively low velocities, the mean error in PIV is

about 0.217 for an initial interrogation window size of 32 × 32 px while it is 0.157 for 15 iterations in OF. The reader may note that the mean error decreases in negligible order for a higher number of iterations. In section 4 with higher flow velocities, both techniques reach the same accuracy with a mean error of 0.103 for PIV using again a 32 × 32 px initial window and 0.110 for OF using again 15 iterations. While a clear decreasing trend of the mean error is found in OF with increasing number of iterations, a critical interrogation window size is found in PIV giving the highest accuracy. This fact may be explained by particle displacements being larger than the final interrogation window size when smaller windows are considered. Particles are then no more available in the second frame for cross-correlation.

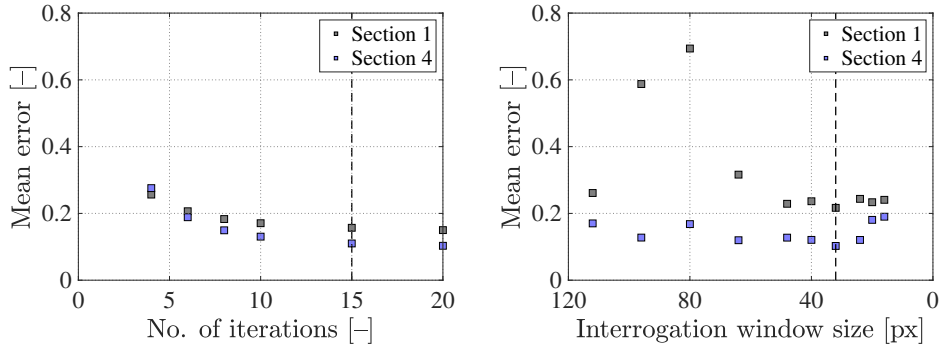

(A) Optical flow **(B)** Particle Image Velocimetry

Figure 7.2.2: Sensitivity of image processing techniques to parameter settings (number of iterations for OF, interrogation window size for PIV), exemplarily for section 1 and 4; dashed lines for selected settings

Figure 7.2.3 shows the resulting velocity magnitude profiles for sections 1 to 4 using the above detected optimal settings, i.e. 15 iterations for OF and 32 × 32 px for PIV. In order to avoid spurious velocities above the water surface line due to local brightness patterns (Fig. 7.2.1), dry areas have been masked before processing. PIV and visual data have been smoothed with a moving average filter in order to get a comparable filtering as it was used for OF. It is found that the velocity data from both techniques compare fairly well. For sections 2 and 4, the differences are very small while for section 1 and 3, some deviation is noted, namely better prediction by OF in section 1 and by PIV in section 3. In any case, PIV supports the calculated shape of the velocity profile. It is observed that both PIV and OF show a lack in accuracy close to the boundaries where an unnatural decrease of velocity is obtained. This decrease may be explained by the smoothing in OF and the overlap of the interrogation window to non-moving areas (masking may support avoiding this error).

Figure 7.2.4 presents the complete velocity magnitude fields. It must be noted that, for better readability, the OF result displays only every 25th vector, while the PIV result includes every 3rd vector to ease comparison of both plots. In the OF result, some spurious vectors appear in the air region due to fluctuation in the illumination. Those

vectors can be eliminated by some image preprocessing, which was not done in the present study. The PIV result shows less spurious vectors.

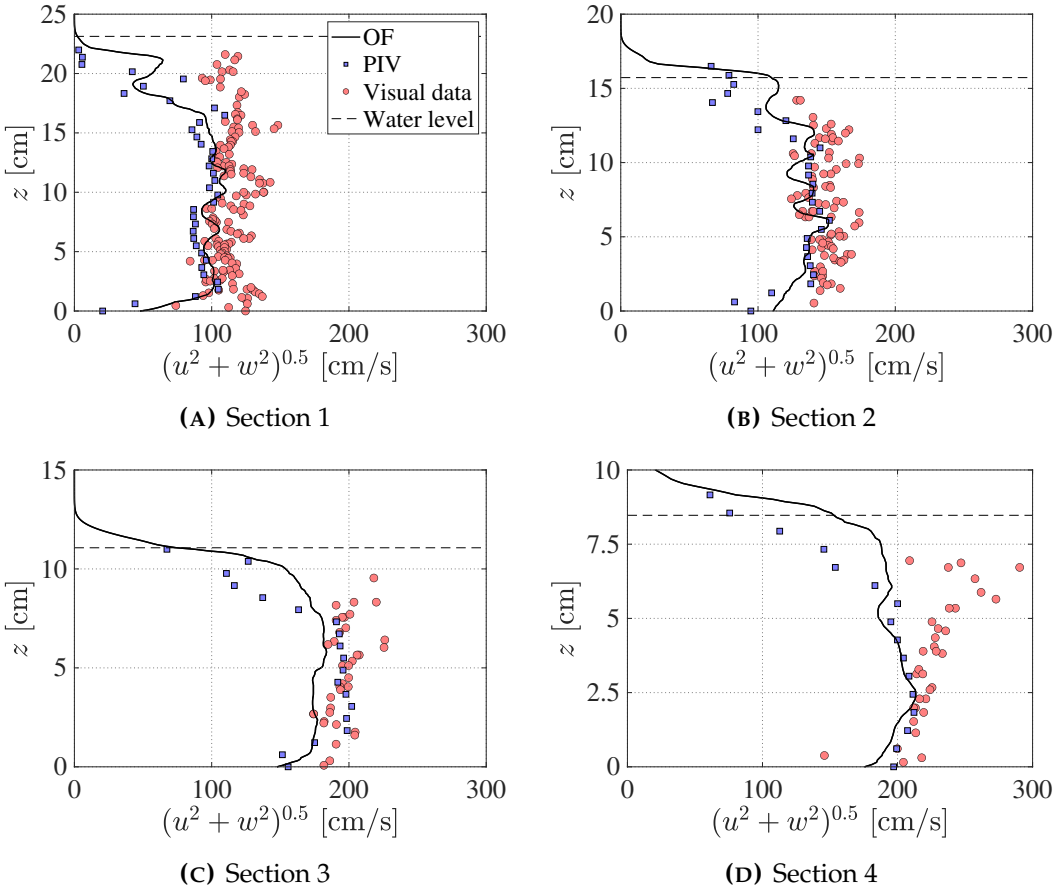

(A) Section 1 **(B)** Section 2

(C) Section 3 **(D)** Section 4

Figure 7.2.3: Velocity magnitude profiles extracted from image processing techniques in comparison to visually determined velocities for four sections (OF data obtained by 15 iterations, PIV data obtained with an interrogation window of 32 × 32 px, note the different scaling of the z-axis)

Processing times for OF (Table 7.2.1) and PIV (Table 7.2.2) are given below. The calculations were performed on a Laptop with a 3.1 GHz Dual-Core Intel i7 processor, 16 GB RAM, and a SSD hard disk. Accordingly, the calculation time in OF takes 28 times the time needed for PIV using the optimal settings (highlighted in gray). However, the absolute time is still acceptable with ~3 minutes regarding the much higher information density obtained by OF, i.e. 65 times more velocity vectors. Depending on the purpose of a given study, this denser information may be of benefit, e.g. for a vortex flow. However, it is pointed out that the performed averaging (median filter of size 12 × 12 px) is relatively time-consuming. Comparative processing of this case without filtering took only 123.0 s.

Table 7.2.1: Calculation time for different iteration numbers in OF method (2 to 20 iterations) and resulting size of the velocity field

Method	**OF 2**	**OF 4**	**Of 6**	**OF 8**	**OF 10**	**OF 15**	**OF 20**
Time (s)	29	52	75	100	133	184	240
VF size (px × px)	1280 × 576						

Table 7.2.2: Calculation time for different initial interrogation window size in PIV method (112 × 112 px to 16 × 16 px) and resulting size of the velocity field (the final calculation pass used 50 % of the given interrogation window size)

Method	**PIV 112**	**PIV 96**	**PIV 80**	**PIV 64**	**PIV 48**	**PIV 40**	**PIV 32**	**PIV 24**	**PIV 20**	**PIV 16**
Time (s)	3	4	6	4	6	8	7	11	16	19
VF size	19	23	27	35	47	56	71	95	114	143
(px × px)	×	×	×	×	×	×	×	×	×	×
	44	42	63	79	105	127	159	212	255	319

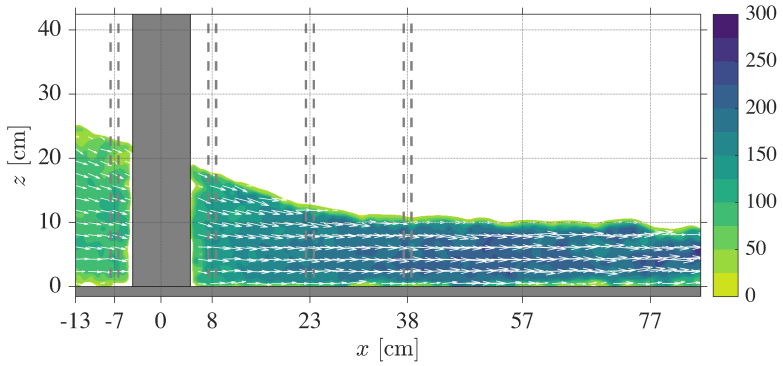

(A) Optical flow for 15 iterations (every 25th vector displayed)

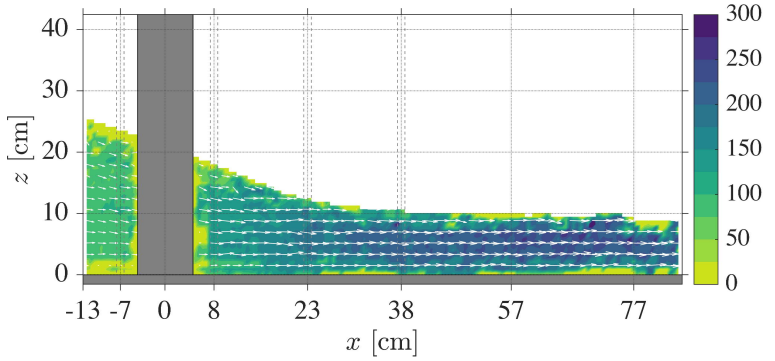

(B) Particle Image Velocimetry for 32 × 32 px initial interrogation window size (every 3rd vector displayed)

Figure 7.2.4: Resulting velocity magnitude fields (in cm/s)

7.2.4 WAVE BREAKING AT ARTIFICIAL REEF

In order to evaluate the performance of the OF method, a regular wave propagating over a submerged plate is investigated in the following. Figure 7.2.5 shows the images taken from the high-speed video at six instants over the wave period of 1 s (left column) as well as the results from OF (center column) in comparison with numerical results from a 2D LES simulation obtained by FLOW-3D (right column).

The field of view is limited to the rear end of the submerged plate. The high-speed images cover a range of ~23 × 23 cm with a resolution of 256 × 256 px. The pixel density, i.e. ~11 px/cm, is thus comparable to the previous test case and the same mean averaging filter size of 12 × 12 px is selected. The time $t = 0$ s was chosen as the moment where the backflow above the plate is just about to set in. Thus, the water is in rest in this moment, and only a small vortex being generated at the end of a wave cycle is still present. A mesh with 5 mm cell size was chosen to resolve the directly simulated large vortices in the LES model.

The flow field in this test case is characterized by several small-scale vortex structures being transported around the plate as well as some aeration after the wave breaking. Generally, the flow velocities, which are obtained by optical flow, are in good agreement with the numerical solution. The very complex flow fields consisting of forwards and backwards directed particle displacements are well represented. Moreover, the small vortices at the end of the plate are in good agreement regarding their size and location. It has to be noted that a relatively small interrogation window size would be required to detect these vortex structures with a PIV technique. The OF calculation time for each frame pair was about 10 s on the same computer as in the test case 1 due to the low image resolution. It was found again that the OF method is sensitive to illumination changes leading to high number of spurious vectors above the water surface. For a better readability and comparability, these regions have been masked in the OF result plots.

7.2.5 AERATED STEPPED SPILLWAY FLOW

In this section, OF application to slightly aerated flows (with a mean air concentration of 20 %) is tested. Therefore, a high-speed recording of a stepped spillway flow is used. The video is captured with a frame rate of 732 fps and a full resolution of 1920 × 1200 px. Two frames were extracted from the video and rotated by 26.6° to align the pseudo-bottom (connecting the step edges) with the horizontal. The images were cropped to the field of interest, i.e. one single step, yielding an image size of 1270 × 1100 px (Fig. 7.2.6(A)). As the investigated step represents the inception point of self-aeration, clear water is found at the upstream end of the step while flow at the downstream end is aerated. The pixel density is about 90 px/cm in this study, much higher than in the previous cases.

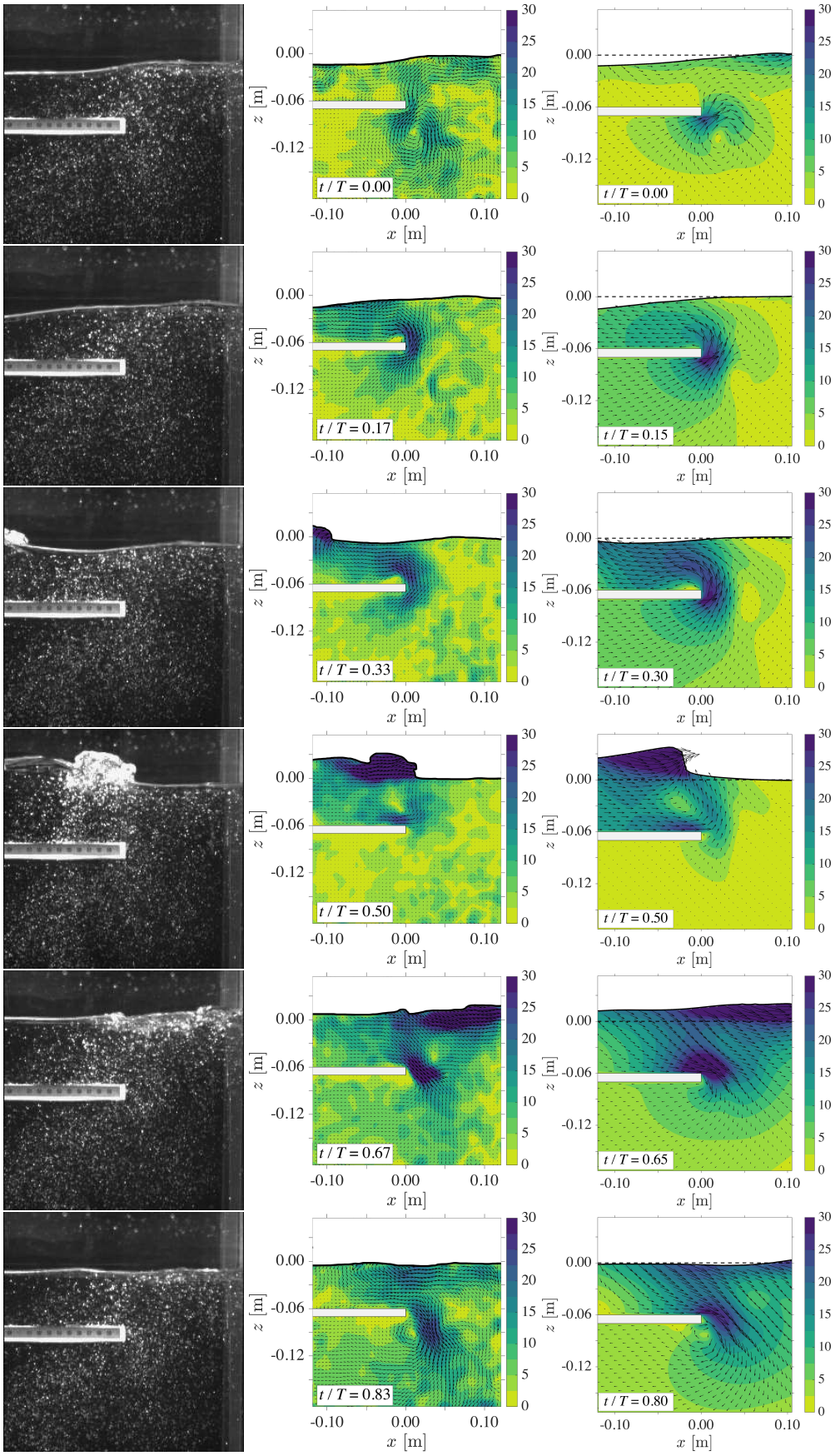

Figure 7.2.5: Velocity magnitude fields over one wave period (top to bottom) at the rear end of the submerged plate (in cm/s) obtained from high-speed video frames (left, from BUNG ET AL. (2008) using OF method (center) in comparison to LES simulation (right), note that spurious vectors in OF results have been masked above the free surface

A simple OF estimation as it was performed in the first two cases was found to not provide useful results. For this reason, the image pyramid technique is considered, which is an incremental multi-resolution method. This method is used to apply a single filter to a set of images instead of using different filters to a single image (ADELSON ET AL., 1984; BURT AND ADELSON, 1983). Herein, the original image size is reduced by a specified factor yielding a blurred (low-pass filtered) copy of the image when upscaled to its original size. Repeating this step several times, a set of images of different sizes are obtained, forming a pyramid when illustrated above each other. In fact, this pyramid is the spatial-frequency domain of the image. Each level is downsampled from its nearest finer level. The optical flow is estimated at a coarse level in a first step. The coarse scale displacement is then used to correct the sequence at the next finer level (warping) (SUN ET AL., 2010). The total displacement is then the sum of all increments, resulting in higher accuracy for large displacements (BRUHN ET AL., 2005).

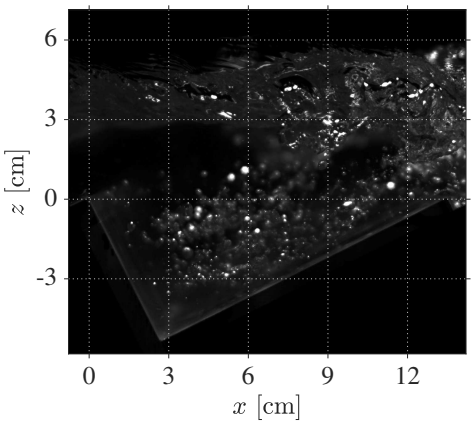

(A) High-speed frame captured at step 5, i.e. the inception point of self-aeration with C_{mean} = 20 %, flow direction from left to right

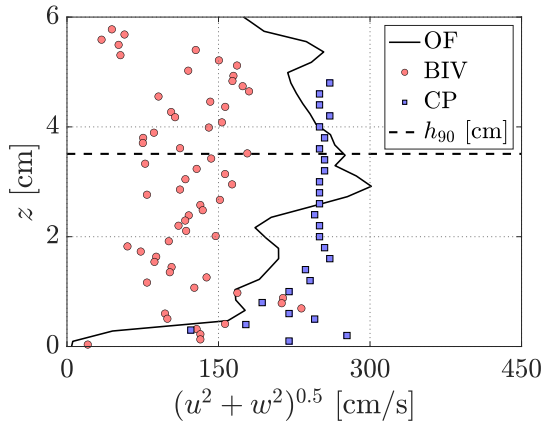

(B) Velocity profile obtained by OF method compared to BIV and conductivity probe data (CP) from the centerline (h_{90} is the elevation with a time-averaged air concentration of 90 %)

Figure 7.2.6: Optical flow method in slightly aerated stepped spillway flows

Naturally, the image pyramid technique is even more time-consuming than the basic Horn-Schunck scheme. For the given sequence of the stepped spillway, the total calculation time was 817.2 s using five pyramid levels with a downsampling factor of 2.5, which yields a minimum image size of 13 × 11 px. The results are illustrated in Fig. 7.2.6(B) in comparison to data from a conductivity probe. This data was gathered by BUNG (2011A) in the centerline of a 30 cm wide flume with identical step height, slope and specific discharge. Moreover, an exemplary BIV result is included. For BIV, an interrogation window size of 32 × 32 px with 75 % overlap was applied. The results show that the OF method can give valuable results even in aerated flows,

which is known to be difficult by imaging techniques (BUNG, 2011C). While BIV commonly tends to provide too low velocities (BUNG AND VALERO, 2015), OF is a more robust method in aerated flow analysis.

7.2.6 CONCLUSIONS

It was shown that the optical flow method is fully capable to determine 2D velocity fields in hydraulic structure models. When choosing a global method, e.g. the Horn-Schunck method used in the present paper, a dense velocity field is obtained. Velocity information is then given for every pixel. The calculation time is much longer compared to a classical PIV calculation. However, PIV results are typically of lower resolution and do not allow the determination of such dense velocity fields, except with additional interpolation. The calculation time for OF is still bearable on modern computers and may be reasonable when detection of small-scale rotational flow structures is of interest.

The OF method was successfully applied to seeded and aerated flows although OF, as a differential approach, should be better suitable for continuous objects than for small particles. Moreover, OF is much more sensitive to local illumination changes as it is a differential approach compared to PIV as an integral approach.

In case of aerated flows, calibration of the data is still recommended. Particularly, application of an image pyramid technique helps to improve the results. Application to other types of aerated flows is planned for future research. A detailed benchmark with direct velocity measurements near the wall using an intrusive probe may help in assessing accuracy of the presented method.

7.3 OPTICAL FLOW ESTIMATION IN AERATED FLOWS

Authors: Daniel B. Bung; Daniel Valero
Journal: Journal of Hydraulic Research 54(5)
Year: 2016

Abstract: Optical flow estimation is known from computer vision where it is used to determine obstacle movements through a sequence of images following an assumption of brightness conservation. This paper presents the first study on application of the optical flow method to aerated stepped spillway flows. For this purpose, the flow is captured with a high-speed camera and illuminated with a synchronized LED light source. The flow velocities, obtained using a basic Horn-Schunck method for estimation of the optical flow coupled with an image pyramid multi-resolution approach for image filtering, compare well with data from intrusive conductivity probe measurements. Application of the Horn-Schunck method yields densely populated flow field data sets with velocity information for every pixel. It is found that the image pyramid approach has the most significant effect on the accuracy compared to other image processing techniques. However, the final results show some dependency on the pixel intensity distribution, with better accuracy found for grey values between 100 and 150.

Keywords: Aerated flow, flow velocity, imaging technique, optical flow, stepped spillway

7.3.1 INTRODUCTION

Aerated flows occur in different hydraulic engineering phenomena. A typical example is spillway aerated flows where self-aeration takes place when the growing turbulent boundary layer reaches the free surface (WOOD ET AL., 1983). Entrained air creates a flow bulking further downstream leading to increased water levels. Knowing the residual energy at the spillway toe is of particular importance for design of downstream energy dissipaters. The residual energy is directly linked to the friction factor and thus to the flow velocity (CHANSON, 2002B).

Traditionally, flow parameters in aerated spillway flows are measured by intrusive dual-tip probes, based on a conductivity or optical fiber principle (CHANSON, 2002A; FELDER AND CHANSON, 2015). However, non-intrusive imaging techniques have gained attention in the recent past (e.g. AMADOR ET AL., 2006; BUNG, 2013). In fact, BUNG (2011C) and LEANDRO ET AL. (2014) showed that these techniques can be applied to estimate velocity fields using a high-speed camera. These studies were based on bubble image velocimetry (BIV), which applies the well-known particle image velocimetry (PIV) method to aerated flows, using the bubbles as tracer particles. To avoid safety and accuracy issues associated with laser reflections from bubble surfaces, with BIV the flow is illuminated using white light instead of the

laser sheet. BIV was found to underestimate the flow velocity measured using intrusive measurements by approximately 20 %. To date, it is not clear if these differences are due to the imaging technique or wall effects. BUNG AND VALERO (2015) showed that the results from BIV can be improved by preprocessing the images and applying different image filtering techniques. However, resulting velocities were still found to be biased low, particularly in the highly aerated region near the free surface.

Optical flow (OF) is defined as the movement of brightness (intensity) patterns in a sequence of images. This technique does not differentiate between movement arising from a moving obstacle (or fluid) observed by a stationary viewer or from a moving viewer observing a stationary object. The Horn-Schunck optical flow estimation method (HORN AND SCHUNCK, 1981) belongs to the so-called global methods which attempt to minimize a global error function (see Section 3). Global methods provide dense flow field data sets, thus providing velocity information at every image pixel, as they can even determine the optical flow within a region of uniform intensity. However, it must be noted that the assumption of the brightness conservation implicitly requires the following preconditions to produce reasonable results (HORN AND SCHUNCK, 1981):

- variation in brightness due to illumination changes must be avoided and the incident illumination must be uniform across the moving obstacle;
- variation in brightness due to shading effects must be avoided – this is only possible for flat surfaces;
- reflectance must vary smoothly with no spatial discontinuities in order to allow the image brightness to be differentiable; and
- obstacles must not occlude one another.

FLEET AND WEISS (2005) stated that it is remarkable that the brightness constancy assumption works well in practice although it can be considered as unrealistic. In this regard, it must be noted that the application of the optical flow concept to date is mainly found in fields such as video compression (motion estimation to predict intermediate frames), microscopy (information about cell deformation) or vehicle navigation (autonomous car driving) according to FORTUN ET AL. (2015). In some recent studies, the Horn-Schunck method was applied to particle images obtained from PIV measurements, and thus to fluid flows (LIU ET AL., 2015; LIU AND SHEN, 2008). CORPETTI ET AL. (2006) found a good agreement with PIV results using a more sophisticated approach that accounted for the continuity equation as well as divergence and vorticity structures of the flow. LIU ET AL. (2015) stated that OF, as a differential approach, is more suitable to images with continuous patterns, so that single particles used for PIV are not the best case for OF. However, they found that

OF is able to extract velocity fields with considerably higher spatial resolution and improved accuracy when parameter settings are carefully selected.

The present study aims to test the applicability of the optical flow concept to a common hydraulic modeling problem such as velocity measurements in aerated flows. To achieve this objective, the sensitivity to image properties and data analysis settings will be analyzed, employing the data for a stepped spillway flow captured with a high-speed camera. This type of flow is characterized by white water due to strong air entrainment with increasing air content from the bottom to the surface. The basic Horn-Schunck method (which will be described in Section 7.3.3) is applied and coupled with image processing techniques. It will be shown that this new method may help obtain valuable data of the flow field.

7.3.2 EXPERIMENTAL SETUP

High-speed images were gathered on a stepped spillway model of 174 cm drop height and 50 cm width. The investigated specific discharge was set to 0.07 m^2/s, the step height was 6 cm and the chute angle was 26.6° (1V:2H). The spillway was part of a closed water conduit where water was pumped into a head tank before being conveyed into an approaching channel of 1m length. Discharge was controlled by a frequency regulator and checked with an inductive flow meter. Due to the given combination of discharge and geometry, a skimming flow regime was established where water flows above the pseudo-bottom formed by the step edges (CHANSON, 2002B). One flume sidewall was made of clear acrylic glass to allow flow visualization; the opposite sidewall consisted of black PVC sheeting to enhance image contrast.

Videos were captured with a system consisting of a Motion-Scope Miro M120 camera (LaVision, Germany) with a resolution of 1920 × 1200 px and a sample rate of 732 Hz, a 50 mm f/1.4 AF-D lens (Nikon, Japan), and a synchronized LED light source installed in front of the sidewall. Due to the applied light source, a constant illumination, which is needed for the application of the OF method, was ensured. The camera was set up in front of step 21, which was located in the fully developed, quasi-uniform flow region (BUNG, 2011A). The distance to the sidewall was about 60 cm and the camera was focusing on the front plane. It must be noted that the light source caused some reflection in the acrylic sheeting, so that the frames were cropped to a size of 1600 × 1200 px (Fig. 7.3.1).

Velocity data from an intrusive double-tip conductivity probe for $x = 13.4$ cm and $z > 0$ cm (see Fig. 7.3.1) was taken from an earlier study published in BUNG (2011A) where the probe was installed in the centerline of a similar, 30 cm wide flume for the same specific discharge, step height, slope and step number. It is acknowledged that differences in flow velocities due to wall effects in the current study are very

likely. KRAMER (2004) showed that the velocity near the sidewall is approximately 15 % lower than at the centerline for self-aerated flow in a 50 cm wide model of a smooth invert chute. LOPES ET AL. (2015) noticed some alternation of cavity flow pattern in the 50 cm wide flume which did not occur in the 30 cm wide flume of BUNG (2011A) for the given setup. However, BUNG (2011A) found that the velocity profiles for $z > 0$ cm in the 30 cm wide flume compare well with the data from wider flumes, e.g. with data of GONZALEZ (2005). Thus, comparison of OF results with the conductivity probe data is possible.

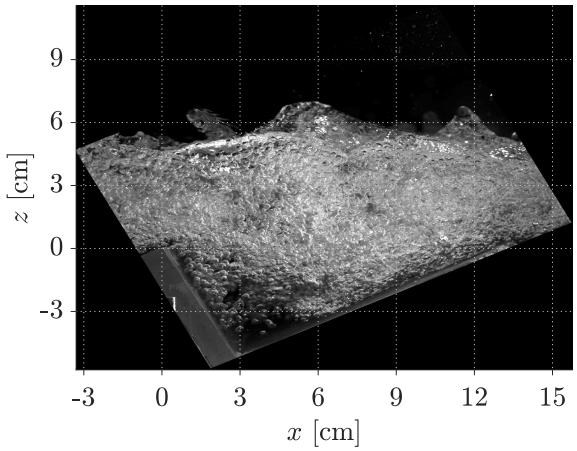

Figure 7.3.1: A frame captured by the high-speed camera with 732 Hz at step 21, rotated by 26.6° and cropped to a resolution of 1600 × 1200 px, flow from left to right

7.3.3 OPTICAL FLOW AND IMAGE PROCESSING TECHNIQUES

In order to relate the movement of brightness patterns to the movement of an object, the classical Horn-Schunck method assumes that the brightness $I(X, Z, t)$ of a pixel with the image coordinates X and Z at the time t in the pattern remains constant during the movement:

$$\frac{\mathrm{d}I}{\mathrm{d}t} = 0 \tag{7.3.1}$$

Equation (1) can be expanded as:

$$\frac{\partial I}{\partial t} + \frac{\partial I}{\partial X}\frac{\partial X}{\partial t} + \frac{\partial I}{\partial Z}\frac{\partial Z}{\partial t} = 0 \tag{7.3.2}$$

Written in a compact form, it yields:

$$I_t + I_X U + I_Z W = 0 \tag{7.3.3}$$

where I_X and I_Z are the spatial image brightness derivatives in X and Z direction, I_t is the temporal derivative, and U and W are the unknown spatial displacements in X

and Z directions between two sequent frames. Apparently, it is not possible to solve the movement of the particles with this constraint alone as it is an ill-posed problem with two unknowns, hence a second constraint is needed.

Based on the assumption that neighboring points have similar velocities, HORN AND SCHUNCK (1981) modified Eq. 7.3.3 to create an error function E, featuring the addition of a "gradient constraint equation" or "data term", which reduces the square of the gradients of the optical flow velocity, as shown in Eq. 7.3.4:

$$E = \int\int \left[(I_X U + I_Z W + I_t)^2 + \alpha \left(|\nabla U|^2 + |\nabla W|^2 \right) \right] \mathrm{d}X\mathrm{d}Z \tag{7.3.4}$$

In Eq. 7.3.4, $\nabla = (\partial/\partial X, \partial/\partial Z)$ is the spatial gradient and α is a scaling factor for the spatial term. Larger values for α will result in smaller flow gradients and thus smoother flow fields.

In addition to the basic method, image filtering techniques may enhance the quality of results. One of the most common techniques in image processing, particularly in optical flow, is an incremental multi-resolution technique based on the so-called pyramid method. This method applies a single filter to a set of images instead of using different filters to a single image (ADELSON ET AL., 1984; BURT AND ADELSON, 1983). For this purpose, the original image size is reduced by a certain factor resulting in a blurred (low-pass filtered) copy of the image when upscaled to its original size. By repeating this step several times, a set of images with different sizes is obtained forming a pyramid when illustrated above each other. This pyramid is the spatial-frequency domain of the image and each level is downsampled from its nearest finer level. Optical flow is first estimated at a coarse level. The coarse scale displacement is then used to correct the sequence at the next finer level (warping) (SUN ET AL., 2010). The total displacement is then the sum of all motion increments resulting in a higher accuracy for flow with large displacements (BRUHN ET AL., 2005).

Some techniques found in the literature utilize median filtering of incremental optical flow estimation to remove outliers or structure texture decomposition (RUDIN ET AL., 1992). According to SUN ET AL. (2010), no single optimal method is suitable for all optical sequences. Instead, an appropriate optical method must be selected for each individual sequence. The review papers of e.g. FORTUN ET AL. (2015) or SUN ET AL. (2010) give further descriptions of optical flow techniques.

For the present study, a MATLAB® toolbox developed and presented by SUN ET AL. (2010) was used. This toolbox was written to benchmark recent advances in optical flow methods against the classical Horn-Schunck method. As a result, SUN ET AL. (2010) found that the standard Horn-Schunck method is surprisingly competitive when appropriately implemented. The toolbox implements several methods and optimization parameters. However, only a few selected parameters related to the classical formulation will be varied in this study (namely the image pyramid settings

and median filter size) to analyze the general applicability of the optical flow method to aerated flows in hydraulic engineering. A link to the download site can be found in SUN ET AL. (2010).

7.3.4 RESULTS

As an initial point of reference, a case absent of any additional processing technique was analyzed. Therefore, the standard Horn-Schunck method with 10 iterations (to minimize the objective function in Eq. 7.3.4) was applied to the data visualized in Fig. 7.3.1. The streamwise velocity distribution $u(z)$ presented in Fig. 7.3.2(A), which includes negative velocity values, appears unrealistic. For clarity, the h_{90} water level (i.e. the elevation where the air concentration was measured to be 90 % with the conductivity probe) is included in the figure. This characteristic level is mostly referred to for spillway design purposes. From Fig. 7.3.2(A) it could be concluded that the optical flow technique is not suitable for the determination of flow velocities for the present problem.

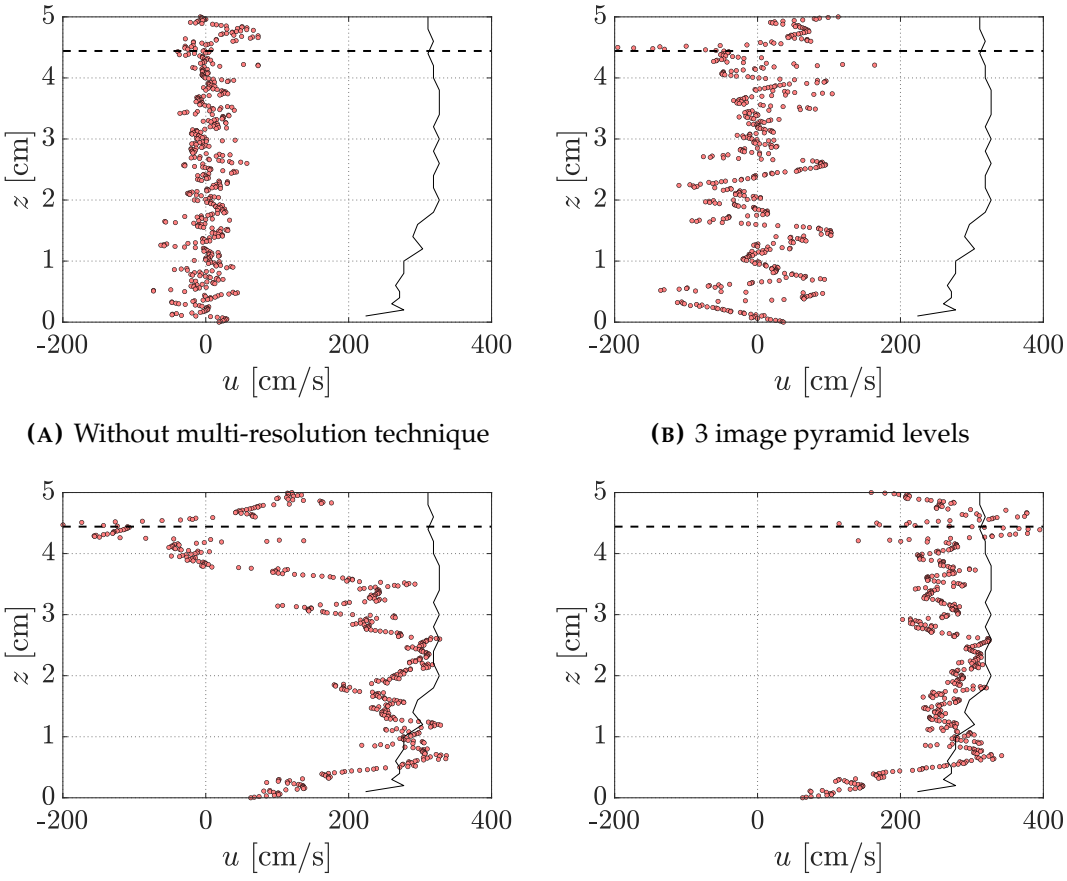

(A) Without multi-resolution technique

(B) 3 image pyramid levels

(C) 5 image pyramid levels

(D) 7 image pyramid levels

Figure 7.3.2: Instantaneous velocity profiles at the downstream step edge ($x = 13.4$ cm), obtained with Horn-Schunck method

Figures 7.3.2(B)-7.3.2(D) show the extracted velocity profiles based on three, five and seven pyramid imaging levels, respectively. The downsampling factor was fixed to 2 so that the minimum image size was approximately 25 × 19 px for the highest number of levels. It must be noted that the maximum displacement between two frames was approximately 40 px in the original image. As expected, applying the multi-resolution technique has significant influence on the optical flow results. A number of three pyramid levels still involves a large scatter, while five pyramid levels give better results. However, significant deviations, particularly above $z = 3$ cm, can still be noted. With seven pyramid levels, this deviation is further reduced. An increase of pyramid levels larger than seven was found not to give better accuracy.

Thus, image resolutions below 25 × 19 px within the pyramid do not improve the results. This finding is in agreement with SUN ET AL. (2010), supporting a final image size of 20-30 px for OF applied for obstacle movements. The question may arise as to whether similar results could be obtained by using smaller initial image sizes with lower numbers of pyramid levels leading to a similar final image size. To address this question, a comparative optical flow calculation was performed with an initial image size of 1000 × 750 px and five levels with a downsampling factor of 2.5, leading to an identical minimum image size of 25 × 19 px. Compared to data presented in Fig. 7.3.2(C), the results with a five-level pyramid was found to be much more robust and deviations to results from the seven-levels pyramid with higher resolution for the original image (Fig. 7.3.2(D)) were small. Based on the flow fields evaluated in this study, it may be concluded that a reasonably large original image combined with a reasonably large final image size is needed for OF application.

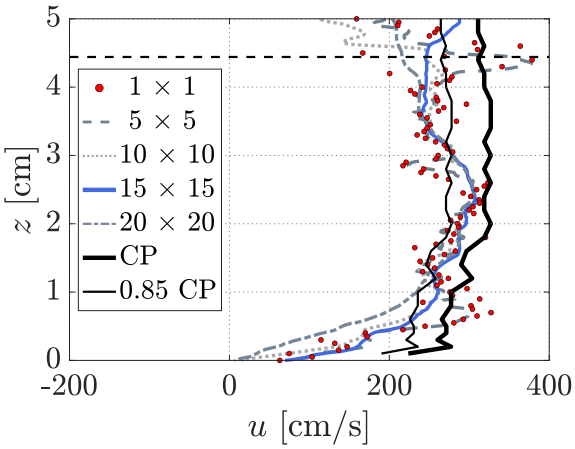

Figure 7.3.3: Instantaneous velocity profiles at the downstream step edge ($x = 13.4$ cm) for median-filtered cases compared to non-filtered data from Fig. 7.3.2(D) (note that only every fifth data point is plotted for better legibility) and conductivity probe data (CP, from the centerline)

Another technique is the application of a median filter for each pixel in every warping step to remove outliers. SUN ET AL. (2010) suggest a filter size of 5 × 5 px. Figure 7.3.3

illustrates the velocity profiles for the following filter sizes: 5×5, 10×10, 15×15 and 20×20 px compared to the non-filtered results from Fig. 7.3.2(D). As expected, the filtering makes the velocity profile smother. Indeed, a filter size of 5×5 px and 10×10 px still results in a scattering shape. The filter size of 15×15 px gives better results while a larger-scale filtering tends to result in higher differences compared to the conductivity probe profile. In order to evaluate the results with regard to wall effects, an additional curve is included in Fig. 7.3.3 representing 85 % of the centerline velocity and thus giving an estimate of flow velocities near the sidewall due to wall friction according to KRAMER (2004). The resulting flow field for the 15×15 px filter size is illustrated in Fig. 7.3.4.

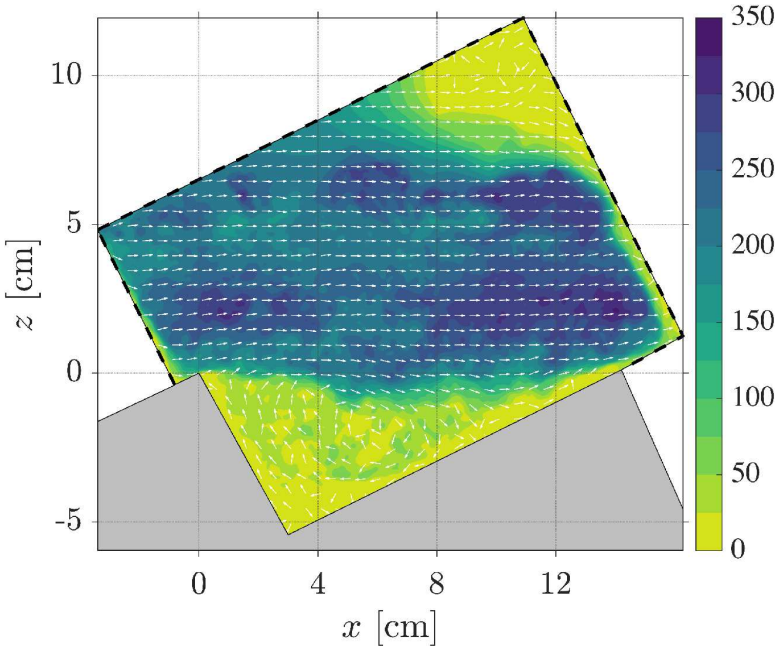

Figure 7.3.4: Instantaneous velocity field (in cm/s) for 15×15 px median filter size (note that only every 50^{th} vector is plotted for better legibility, vectors are plotted with unit length to visualize the cavity vortex), flow from left to right

It is acknowledged that the video frames, which were chosen for processing, give more accurate results compared to the majority of other frame pairs. The OF method is found to give reasonable velocity field results; however, larger deviations, relative to the conductivity probe data, occur in the flow region close to the pseudo-bottom. Investigating the image density distribution in Fig. 7.3.1 in more detail, one may note that most pixels at the examined location (i.e. at $x = 13.4$ cm) have an intensity in the range of 100 to 150 while lower intensities are found close to the pseudo-bottom (i.e. at $z \approx 0$ cm). Interestingly, similar deviations between the OF velocity and the conductivity probe data were found for other frames in flow regions with strong light reflections of air bubbles (high intensities). Such strong reflections did not occur in the present frames. As a consequence, an optimum range of pixel intensities seems

to be necessary to obtain results with a higher quality when applying the OF method to aerated flows. Figure 7.3.5 supports this hypothesis as it shows the pixel intensity I for 100 frame pairs related to the particular relative velocity difference $v_{\text{diff,rel}}$ at the same elevation. The figure shows that the smallest deviations (0 to 25 %) are found for pixel intensities between 100 and 150. On the other hand, a much higher uncertainty is found for low pixel intensities of about 50. The same tendency is given for a high I, but there are not enough data in this range to assure this finding.

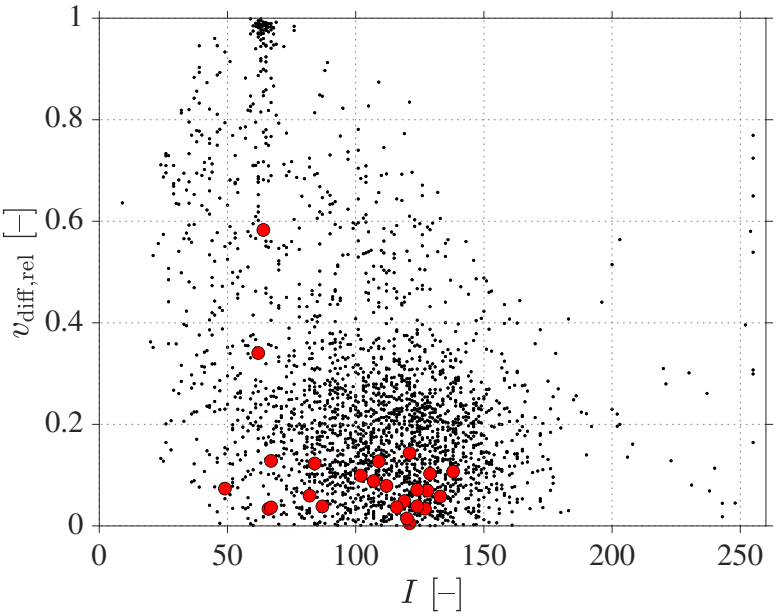

Figure 7.3.5: Relative (dimensionless) velocity difference $v_{\text{diff,rel}}$ versus pixel intensity I above the downstream edge (x = 13.4 cm) for 100 frame pairs (note that the values for the presented frame are marked with red markers)

7.3.5 SUMMARY AND CONCLUSION

In the present study, the applicability of the optical flow method to aerated chute flows using a basic Horn-Schunck method has been demonstrated. OF is an imaging technique based on tracking the location of individual pixels through displacement (as would be also done by visual inspection). By comparison, PIV/BIV represent an integral and statistical approach. OF produces dense flow field data sets with velocity information for every pixel when the Horn-Schunck method is chosen.

It was shown that reasonable results can be obtained with a coupled application of a multi-resolution approach in form of the image pyramid technique. The resulting velocity data showed good agreement to data from an intrusive conductivity probe (obtained in the centerline of a different installation). A reasonable coarse image resolution in the range of 25 px was found to be optimum while the original fine resolution was of lower significance. At this point, additional investigations are

required. Instead of capturing the flow with full spatial resolution and the maximum sample rate of 732 Hz, a lower image size with higher temporal resolution may help to improve the results.

Furthermore, it seems that the method's robustness depends on the pixel intensity distribution. In the present study, a synchronized LED illumination was used to ensure a constant illumination. However, due to the bubble dynamics it was not possible to keep the pixel intensity at a specific location constant over time, which is the basic (although unrealistic) assumption as discussed above. Moreover, some local brightness patterns cannot be avoided as the light source needs to be installed beside the camera yielding to non-uniform illumination over the field of view.

CHAPTER 8

DISCUSSION

8.1 CAPACITIES AND LIMITATIONS OF BIV AND OPTICAL FLOW

The previous sections demonstrated the application of imaging techniques to velocity determination in laboratory conditions. Both, the PIV/BIV and the OF method, provide information on instantaneous velocity fields. PIV is a well-accepted method in hydraulic laboratories and in fluid mechanics laboratories in general. It has been tested and validated in numerous studies that can be found in the literature. PIV can be easily extended to 3D using stereoscopic setups or to volumetric flow fields using multiple cameras. It was shown that PIV can provide valuable data, even when relatively simple setups with halogen or LED illuminations are employed. The use of laser illumination is oftentimes a critical issue in laboratories as special care for safety aspects is required. In air-water flows, laser illumination is not possible due to undesired reflections of the laser. In this case, halogen or LED lights are typically chosen.

It was shown that PIV performs fairly well with this simple setup for seeded clear-water flows (it is noted that all investigated test cases represent almost ideal, two-dimensional flows). The accuracy of BIV, however, strongly depends on the local void fraction. Intense calibration efforts can help to improve the estimated velocities. In addition, image preprocessing may be employed. However, calibration and filtering settings depend on the investigated flow case, illumination, camera settings etc.. Thus, intrusive velocity data are required to validate imaging results. This may be challenging for most laboratories as the only reliable instrumentation in highly aerated flows, i.e. two-tip void fraction probes (which are typically custom-made solutions), are not widely available. Another significant drawback of the PIV/BIV approach is its limitation in spatial resolution. Small-scale turbulent flow structures may remain undetected due to insufficient spatial (or temporal) resolution. Certainly, in some applications, high-resolution velocity fields are not mandatory. Large-scale PIV (LSPIV), for instance, aims at the estimation of discharges in natural rivers through determination of surface velocity distributions (DI CRISTO, 2011; HANSEN ET AL., 2019; LEGLEITER ET AL., 2017; MORGENSCHWEIS, 2018; TAURO ET AL.,

2017). LSPIV may perform reasonably well with low spatial resolution. However, similar studies based on OF techniques have been also presented in the recent past (KHALID ET AL., 2017; TAURO ET AL., 2018). In this context, it is noteworthy that CAO ET AL. (2020) recently applied another computer vision technique to estimate surface velocities in rivers, i.e. airborne feature matching.

As highlighted before, the optical flow approach can provide dense velocity fields with velocity data at every pixel. OF, as a differential approach, is generally more suitable for continuous patterns which may be of benefit for application in highly aerated flows. One drawback is the higher computation cost which even increases when a multi-resolution approach is used.

Since the publication of the previously presented papers in the year 2016, several studies have been presented in the literature, e.g. ZHANG AND CHANSON (2018A) and ZHANG AND CHANSON (2018B) using the Lucas-Kanade and Farnebäck method, respectively, in aerated stepped spillway flows. OERTEL AND SÜFKE (2019) confirm a good agreement between PIV and OF based on Horn-Schunk optical flow estimation methods for dam-break flows. SHI ET AL. (2020) tested all three methods applied to a breaking surge and conclude that Farnebäck performs best. SHI ET AL. (2020) confirm higher discrepancies between intrusively measured flow velocities and the OF results for regions near the air-water boundaries of the roller. In order to reduce these discrepancies in stepped spillway flows, KRAMER AND CHANSON (2019) propose a filtering method and show that flow velocities in the upper flow region can be significantly improved. These selected publications highlight the interest for optical flow methods in the hydraulic engineering community. More applications and further developments may be expected in the future to improve the performance independently of investigated flow conditions.

To the best of the author's knowledge, stereoscopic methods have not been applied to fluid problems yet. However, for optical flow determination of moving obstacles, combination of disparity and optical flow have shown promising results for 3D motions. In the computer vision community, it is then referred to as Scene Flow estimation (MENZE ET AL., 2018; SCHUSTER ET AL., 2018). Consequently, similar approaches should be tested to fluid motion in near future.

The subsequent sections directly compare the performance of both techniques (BIV and OF) for air-water flows. Calculation times, the influence of image resolution and the number of frames are evaluated. Moreover, the capacity of optical flow to estimate turbulence fields is discussed. Finally, a benchmark with synthetic particle images as proposed by BUNG AND VALERO (2017) is presented, highlighting the superior performance of OF for highly turbulent, non-aerated flows.

8.2 IMAGE PROCESSING TECHNIQUES FOR VELOCITY ESTIMATION IN HIGHLY AERATED FLOWS: BUBBLE IMAGE VELOCIMETRY VS. OPTICAL FLOW

Authors: Daniel B. Bung; Daniel Valero
Conference: 4th European IAHR Congress, Liege
Year: 2016

Abstract: Measuring of flow velocities in aerated flows is known to be difficult in physical models. Application of classical anemometers or ADV probes is limited to low air concentration. Thus, highly aerated flows are commonly investigated by use of intrusive needle probes (conductivity or optical fiber) which allow determination of both, air concentration and velocity, as well as related parameters (e.g. bubble chord lengths and turbulence). In the recent past, non-intrusive image processing techniques have gained more attraction. In the present paper, Bubble Image Velocimetry and Optical Flow methods are applied to aerated stepped spillway flows using high-speed cameras with different resolution to highlight capabilities and limitations of both methods. Results show that optical flow is capable to give results of at least the same accuracy as Bubble Image Velocimetry. A higher image resolution enhances the quality of the results. The dense velocity information being obtained by optical flow may help to carry out investigations on turbulence in future.

Keywords: Aerated flow, imaging processing, optical flow, Bubble Image Velocimetry

8.2.1 INTRODUCTION

In hydraulic engineering, the hydraulic performance of weirs and spillways is commonly elaborated by means of hydraulic modeling during early design stages. Herein, energy dissipation potential is a key feature which is closely linked to the flow velocity and friction factor. Performing of velocity measurements is mostly difficult due to self-aeration of the water. Classical velocity probes, e.g. anemometers or Acoustic Doppler Velocimeters (ADV) become less accurate or even unsuitable in highly aerated flows (MATOS ET AL., 2002). Alternatively, intrusive conductivity or fiber-optical probes are commonly employed (BOES, 2000; BUNG, 2011A; CHANSON, 2002A; FELDER AND CHANSON, 2015). However, these probes are known to be expensive and very sensitive to damages due to very fine tips.

In the recent past, non-intrusive imaging techniques have been adopted to such highly aerated spillway flows in several laboratory studies. The advantage of these imaging studies is given by the flow velocity fields which are directly obtained. In contrary, intrusive needle probes yield time-averaged, local velocity (and air concentration) data only. Most of these non-intrusive studies were based on the

so-called Bubble Image Velocimetry (BIV) technique which was introduced by RYU ET AL. (2005) for impinging waves. BIV is the application of a common Particle Image Velocimetry (PIV) method to bubbly flows using bubbles as tracers. BUNG (2011C) first demonstrated the applicability of this technique to stepped spillway flows with high air concentrations. These results were later improved by LEANDRO ET AL. (2014) applying a complex calibration method. BUNG AND VALERO (2015) showed that some image preprocessing and filtering may also help to improve the results compared to data from a conductivity probe. Anyway, all studies showed that BIV tends to underestimate the conductivity probe data in order of up to 20 %.

Another imaging technique that has recently been applied to highly aerated flows (BUNG AND VALERO, 2016B) as well as to slightly aerated flows and particle images for PIV (BUNG AND VALERO, 2016A) is given by the so-called optical flow (OF). This method is known in the computer vision community and is applied to different fields like autonomous car-driving or video compression (FORTUN ET AL., 2015). The optical flow is defined as the movement of brightness (intensity) patterns through a sequence of images (HORN AND SCHUNCK, 1981). It is assumed that the brightness of a moving pixel is conserved through a set of images. While the Horn-Schunck method is a global method, local methods (e.g. LUCAS AND KANADE, 1981), consider a constant optical flow within a close neighborhood. Thus, local methods do not allow to determine a movement within a region of uniform intensity leading to sparse velocity fields. Global methods, in contrary, yield dense velocity fields with velocity information at every image pixel. Although several improvements of the classical Horn-Schunck method have been presented since its original formulation, BUNG AND VALERO (2016A, B) showed that the original method gives good results when applied to hydraulic engineering problems. Similar results were identified by CORPETTI ET AL. (2006), LIU ET AL. (2015) and LIU AND SHEN (2008).

The present paper aims to compare the results from BIV with those from OF for two different image resolutions and quantify and discuss their differences.

8.2.2 METHODOLOGY

Both imaging techniques are applied to high-speed video frames which are taken at two different stepped spillway models. Both models are set up with 1V:2H slope, 6 cm step height and similar inflow conditions. The flumes are built with Plexiglas sidewalls to allow visual inspection and with a black PVC rear wall to enhance the contrast. The specific discharge is set to 0.07 m^2/s.

The first experimental setup consists of a 30 cm wide flume with a total drop height of 2.34 m. Videos are captured with a KSV instruments high-speed camera, type HiSiS 2000, with a resolution of 256 × 256 px and a sample rate of 1220 fps. The camera is installed at 50 cm distance of the sidewall and the flow field is illuminated

with halogen spot lights with a total power of 1,300 W (installed above the flume and in front of the Plexiglas sidewall). Discharge is controlled with a flap valve and an inductive flow meter. Measurements are limited to step 28 in the fully-developed flow region. Figure 8.2.1(A) shows an exemplary frame. Please note that this frame is cropped to the field of interest and rotated to align the pseudo-bottom formed by the step edges with the horizontal. The pixel density is ~14 px/cm. The reader may note the strong blurring of the image.

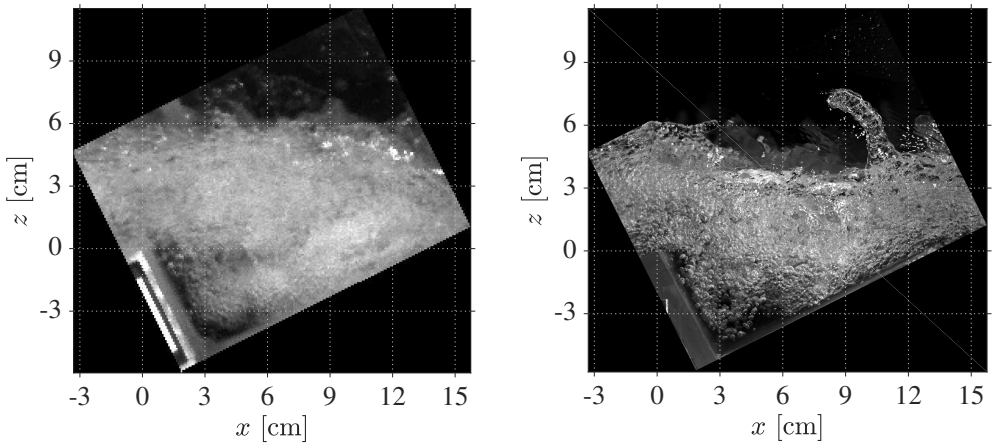

(A) Low-resolution high-speed frame captured at step 28 in setup 1 (pixel intensity is ~14 px/cm)

(B) High-resolution high-speed frame captured at step 28 in setup 2 (pixel intensity is ~103 px/cm)

Figure 8.2.1: Extracted high-speed frames from both setups, flow direction from left to right

The second installation consists of a 50 cm wide flume with a total drop height of 1.74 m. Videos are recorded with MotionScope Miro M120 camera provided by LaVision with a resolution of 1920 × 1200 px and a sample rate of 732 Hz. The camera is installed at 60 cm of the sidewall. The video is captured at step 21 in the quasi-uniform flow region (BUNG AND VALERO, 2016B) using a synchronized LED illumination installed in front of the flume. The discharge is controlled with use of a frequency-regulated pump and an inductive flow meter. Figure 8.2.1(B) shows an extracted video frame (again rotated and cropped to the field of interest). The pixel density is here ~103 px/cm.

Determination of velocity fields is conducted using MatPIV (SVEEN, 2004) in its latest version 1.6.1 for BIV. MatPIV is an open-source Matlab® toolbox allowing to set several filters like a signal-to-noise ratio filter (SNR) as well as local and global filters to be applied with user-defined thresholds. For OF, another open-source Matlab® toolbox, developed by SUN ET AL. (2010), is used. This toolbox was written to benchmark recent advances in optical flow methods against the classical Horn-Schunck scheme which was found to be still competitive when appropriately implemented. This classical Horn-Schunck method, which will be described in the next section, is used in the present study and combined with an image processing

From: Sustainable hydraulics in the era of global change - Proceedings of the 4th IAHR European Congress (Liege, 2016), Eds: S. Erpicum; B. Dewals; P. Archambeau; M. Pirotton, Copyright (2016) by CRC Press. Reproduced with permission from Taylor & Francis Group.

technique to improve the results. All results will be compared to conductivity probe data which were obtained in the centerline of setup 1 (BUNG, 2009). It is acknowledged that wall effects are very likely, but assumed to be small (cmp. LEANDRO ET AL., 2014). Another drawback of these imaging techniques is that no clear measuring plane can be defined as no laser sheet is applied as in standard PIV setups. The reader may note that application of such laser systems is not possible in highly aerated flows due to strong reflections and uncontrolled redirection of the laser light.

8.2.3 IMAGING TECHNIQUES

8.2.3.1 BUBBLE IMAGE VELOCIMETRY

Displacements in Bubble Image Velocimetry (BIV) or Particle Image Velocimetry (PIV), respectively, are generally determined by performing a two-dimensional cross-correlation analysis of the image intensity matrices of two subsequent frames:

$$R(x,z) = \int\int I_1(X,Z) I_2(X+\Delta x, Z+\Delta z) \mathrm{d}X \mathrm{d}Z \tag{8.2.1}$$

In Eq. 8.2.1, I_1 and I_2 denote the pixel intensities of two images, X and Z the pixel coordinates and Δx and Δz the increment to the second frame. This cross-correlation function is characterized by a peak value which represents the best correlation and thus the most likely displacement U and W in X and Z direction. In order to obtain a complete displacement field, images are commonly divided into multiple interrogation windows, which may also overlap, and Eq. 8.2.1 is solved for each window.

Speed-up of the cross-correlation may be achieved when transferring the images into their frequency domain (i.e.: Fast Fourier Transformation or FFT). According to the correlation theorem, correlation in the spatial domain is equivalent to multiplication in the frequency domain. An inverse FFT then yields the spatial cross-correlation.

In any case, it is pointed out that for each interrogation window, a single displacement vector is obtained. Denser displacement or velocity fields thus require a high number of interrogation windows whereby the minimum window size is limited as particles must not leave the window from one image to the next. Additionally, when applying a FFT cross-correlation, displacements larger then half of the window size lead to aliasing, i.e. the correlation peak is folded back into the correlation plane but appears on the opposite side (SVEEN, 2004). Alternatively, higher sample rates could be chosen (technically limited) to allow for reducing interrogation window sizes and obtain denser velocity fields.

8.2.3.2 OPTICAL FLOW

In order to determine the movement of brightness patterns, or the movement of an object, respectively, the classical Horn-Schunck method basically assumes the conservation of brightness $I(X, Z, t)$ of a moving pixel with the image coordinates X and Z at the time t:

$$\frac{\mathrm{d}I}{\mathrm{d}t} = 0 \tag{8.2.2}$$

Equation 8.2.2 may be expanded to

$$\frac{\partial I}{\partial t} + \frac{\partial I}{\partial X}\frac{\partial X}{\partial t} + \frac{\partial I}{\partial Z}\frac{\partial Z}{\partial t} = 0 \tag{8.2.3}$$

or be written in a compact form as

$$I_t + I_X U + I_Z W = 0 \tag{8.2.4}$$

where I_X and I_Z are the spatial image brightness derivatives in X and Z direction and I_t is the temporal derivative. U and W are the unknown spatial displacements in X and Z direction, respectively. Equation 8.2.4 is an ill-posed problem with 2 unknowns, requiring a second constraint to be solved.

HORN AND SCHUNCK (1981) assumed that neighboring points have a similar velocity. A so-called "gradient constraint equation" or "data term" was proposed by reducing the square of the gradients of the optical flow velocity. With this assumption, Eq. 8.2.4 can be substituted by the following objective function

$$E = \int\int \left[(I_X U + I_Z W + I_t)^2 + \alpha \left(|\nabla U|^2 + |\nabla W|^2 \right) \right] \mathrm{d}X\mathrm{d}Z \tag{8.2.5}$$

where E is the error functional to minimize, $\nabla = (\partial/\partial X, \partial/\partial Z)$ is the spatial gradient and α a scaling factor for the spatial term. Larger values for α will result in smaller flow gradients and thus smoother flow fields.

Additional image filtering techniques are known to improve the results. As shown by BUNG AND VALERO (2016B, A), incremental multi-resolution techniques based on the so-called pyramid method help to enhance the results when OF is applied to aerated flows. In principle, this method applies a single filter to a set of images instead of using different filters to a single image (ADELSON ET AL., 1984; BURT AND ADELSON, 1983). For this purpose, the original image size is reduced resulting in a blurred (low-pass filtered) copy of the image when again upscaled to its original size. When this step is repeated multiple times, a set of images with different sizes is obtained forming a pyramid when illustrated one above the other. This pyramid may be regarded as the spatial-frequency domain of the image. The image pyramid method then downsamples each level from its nearest finer level and the optical flow

From: Sustainable hydraulics in the era of global change - Proceedings of the 4th IAHR European Congress (Liege, 2016), Eds: S. Erpicum; B. Dewals; P. Archambeau; M. Pirotton, Copyright (2016) by CRC Press. Reproduced with permission from Taylor & Francis Group.

is first estimated at a coarse level. The coarse scale displacement is used afterwards to correct the sequence at the next finer level (warping) (SUN ET AL., 2010). The total displacement is then given by the summation of all motion increments. According to BRUHN ET AL. (2005), this method results in higher accuracy for flow with large displacements.

SUN ET AL. (2010) state that there is no optimal method which is suitable for any arbitrary sequence. Instead, a suitable method needs to be chosen for a given sequence. The reader is referred to the review papers of e.g. FORTUN ET AL. (2015) or SUN ET AL. (2010) that give further descriptions of optical flow techniques.

8.2.4 RESULTS

8.2.4.1 LOW-RESOLUTION FRAMES

Velocity fields from the low-resolution images have been presented by LEANDRO ET AL. (2014) applying a complex calibration scheme with variation of different filter settings and interrogation window sizes. In order to obtain smoother velocity fields, multiple BIV calculations were performed using a series of subsequent images and the median velocity field was assumed to be representative (cmp. BUNG, 2011C). It was found that the best results were obtained when using 800 frames in total and an interrogation window size of 16×16 px with 75 % overlap (the displacement between two frames is about 5 px). In the current study, the settings from this calibration are adopted leading to the BIV velocity field in 8.2.2.

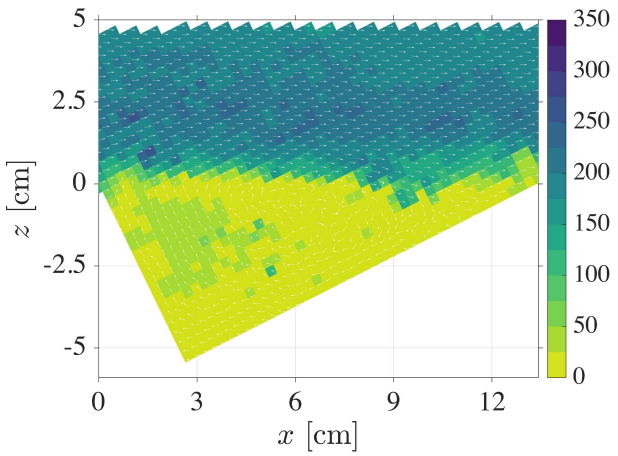

Figure 8.2.2: BIV velocity magnitude field (in cm/s) after calibration according to LEANDRO ET AL. (2014), median result from 800 frame pairs (note that the vectors have been normalized to better visualize the step niche vortex, flow from left to right)

Figure 8.2.3 compares the BIV velocity profile which was extracted at the upstream step edge with the results from OF. For this purpose, OF results will be also averaged

over a varied number of frame pairs. In order to evaluate the required number of frame pairs, median velocities from 10, 50, 200 and 800 OF calculations will be compared. The conductivity probe data is included for completeness. The image pyramid technique is applied with 4 levels and an image size reduction of 50 % between each level. The minimum image size is thus 16 × 16 px. Smaller image sizes are known to not significantly improve the results (BUNG AND VALERO, 2016B; SUN ET AL., 2010). A maximum of 10 iterations is set for each level and pixel to solve Eq. 8.2.5.

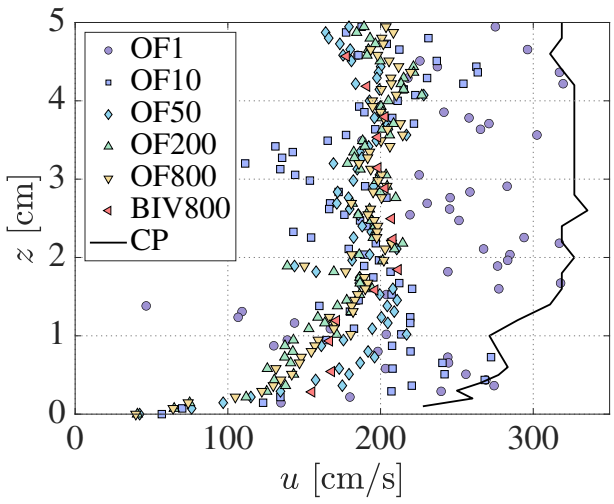

Figure 8.2.3: Velocity profiles at upstream edge ($x = 0$ cm) from OF calculations with 1, 10, 50, 200 and 800 frame pairs compared to the BIV results from Fig. 8.2.2 and the conductivity probe data (CP) for the low-resolution frames

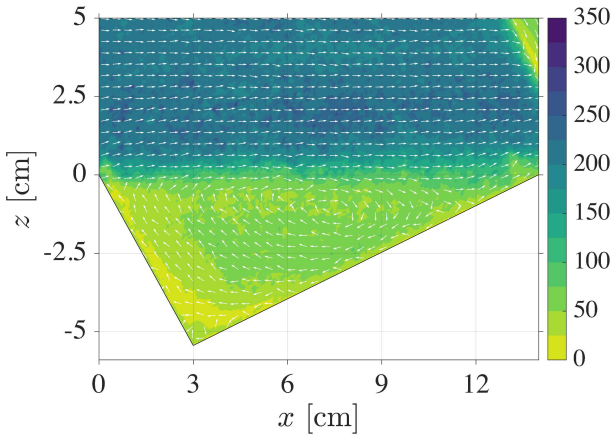

Figure 8.2.4: Median OF velocity magnitude field (in cm/s) using 200 low-resolution frame pairs (note that the vectors have been normalized to better visualize the step niche vortex, every 5th vector is displayed for better legibility, flow from left to right).

Figure 8.2.3 shows that BIV and OF give similar results when median data from the same number of frame pairs is taken into account. OF results converge after roughly 200 frame pairs. It is noted that OF gives higher velocities with only a single frame pair which are then closer to the conductivity probe data. However, significant scattering is found. For more frame pairs, velocities increase up to ~200 cm/s and compare well with BIV. Both methods significantly underestimate the CP data.

The complete velocity field from OF using 200 frame pairs is presented in Fig. 8.2.4. As expected, this velocity field appears much smoother than the BIV result in Fig. 8.2.2. While the stagnation point on the horizontal step surface is found at the same position, the core of the step niche vortex is slightly shifted downstream. Another difference is found at the shear region at the pseudo-bottom ($z = 0$) which is again smoother compared to the BIV results although the median is determined using much less frames in OF.

8.2.4.2 HIGH-RESOLUTION FRAMES

In order to evaluate the sensitivity of velocity fields to initial image quality, similar BIV and OF calculations are performed with images from setup 2. BIV is carried out with an interrogation window size of 80 × 80 px (the maximum pixel displacement is ~40 px) with 75 % overlap. OF is performed with 7 image pyramid levels taking into account the median of 5, 20, 50 and 100 frame pairs while BIV is again limited to the maximum frame number.

Figure 8.2.5 presents the extracted velocity profiles from both imaging techniques. It is found that BIV and OF results compare fairly well for the same number of frames. OF tends to give some higher flow velocities, particularly in lower flow elevations and thus more accurate results. Interestingly, a decrease of median flow velocity is found for increasing number of frames. This trend was not clearly apparent in Fig. 8.2.3.

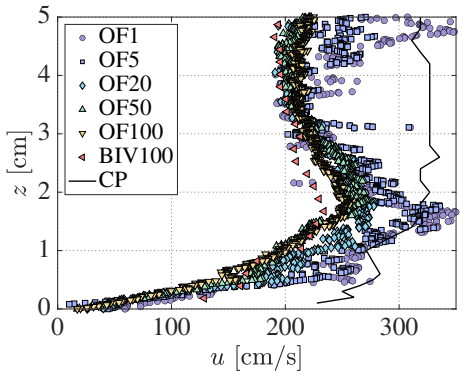

Figure 8.2.5: Velocity profiles at upstream step edge ($x = 0$ cm) from OF calculations with 1, 5, 20, 50 and 100 frame pairs compared to the BIV results with 100 frame pairs and the conductivity probe data (CP) for the high-resolution frames

Figure 8.2.6 presents the complete velocity field from OF using 100 frames. Both, Fig. 8.2.5 and Fig. 8.2.6(A), show the high density of data being obtained by the OF method. Figure 8.2.6(B) illustrates the BIV results. Apparently, OF and BIV results compare fairly well again.

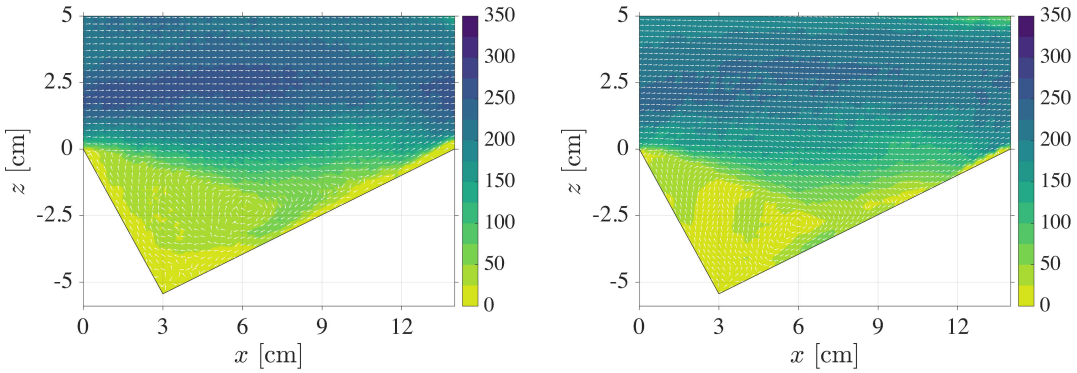

(A) OF (only every 25th vector is displayed for better legibility)

(B) BIV

Figure 8.2.6: Median velocity magnitude fields (in cm/s) using 100 high-resolution frame pairs (note that the vectors have been normalized to better visualize the step niche vortex, flow from left to right)

8.2.5 DISCUSSION AND OUTLOOK

It was shown that the OF method is capable to give velocity data with the same or even higher accuracy as the BIV method. It must be noted that PIV is a statistical and integral approach which is generally better suitable to finite particles. As stated by LIU ET AL. (2015), OF, as a differential approach in contrary, is better suitable to images with continuous patterns which are also found in aerated flows. However, in higher elevations where the air concentration is very high, homogeneous pixel intensity with low intensity gradients and strong blurring is typically found, yielding a high deviation to the conductivity probe data which was recorded at the channel centerline. Additionally, wall effects and the known characteristic of intrusive needle probe to overestimate flow velocities may also enhance this deviation.

A noticeable advantage of the applied Horn-Schunck method is given by the high-density data. Calculation time is consequently higher than for BIV with the same frame number when high-resolution frames are chosen (by a factor of 50). For low-resolution frames, calculation effort increase is almost negligible. However, the authors believe that this high data density could be useful for determination of small-scale turbulence structures. Therefore, future work is intended to better understand the sensitivity to different parameter settings. Some exemplary results on

From: Sustainable hydraulics in the era of global change - Proceedings of the 4th IAHR European Congress (Liege, 2016), Eds: S. Erpicum; B. Dewals; P. Archambeau; M. Pirotton, Copyright (2016) by CRC Press. Reproduced with permission from Taylor & Francis Group.

velocity fluctuations u_{fluct}, w_{fluct} and turbulence intensity Tu defined by

$$u_{\text{fluct}} = \frac{\text{rms}(u)}{\text{median}(u)} \tag{8.2.6}$$

$$w_{\text{fluct}} = \frac{\text{rms}(w)}{\text{median}(w)} \tag{8.2.7}$$

$$\text{Tu} = \frac{\sqrt{\text{rms}(u)^2 + \text{rms}(w)^2}}{\text{median}(u^2 + w^2)} \tag{8.2.8}$$

based on the flow velocities u in x-direction and w in z-direction, respectively, are given in Fig. 8.2.7 showing the related profiles at the upstream step edge ($x = 0$ cm). The results are compared to experimental data for Tu by AMADOR ET AL. (2006) obtained with PIV in the non-aerated flow of a stepped spillway with 1V:0.8H, 5 cm step height and 0.11 m^2/s specific discharge. Experimental data is limited to the boundary layer region. The elevation is normalized by h_{90}, i.e. the water level with an air concentration of 90 %. Apparently, the shape of the turbulence intensity distribution compares fairly well with the experimental data. Higher turbulence intensities in the current study may be explained by the high aeration and the air-water interaction. It is also observed that the vertical velocity fluctuations w_{fluct} are much more intense than u_{fluct}. However, the reader may note that the absolute fluctuations are of one magnitude smaller than those in x-direction (not illustrated). The complete velocity fluctuation field in x-direction is presented in Fig. 8.2.8. Significant turbulence is found within the shear layer developing downstream of the step edge.

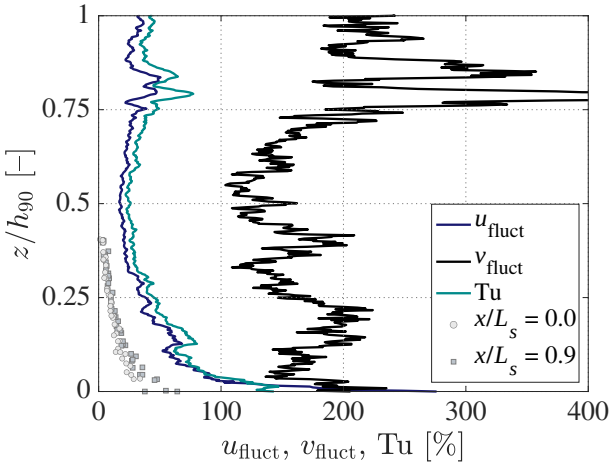

Figure 8.2.7: Velocity fluctuations u_{fluct} and w_{fluct} and turbulence intensity Tu from OF calculation with 100 high-resolution frames (lines) and AMADOR ET AL. (2006) for non-aerated region (markers).

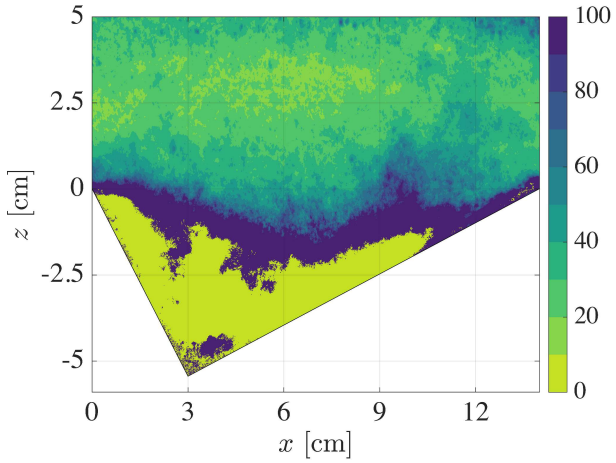

Figure 8.2.8: Velocity fluctuation u_{fluct} (in %) in x-direction according to Eq. 8.2.6 from OF calculation with 100 high-resolution frames

8.2.6 SUMMARY AND CONCLUSIONS

A comparative study of Bubble Image Velocimetry and optical flow for non-intrusive velocity determination in highly aerated stepped spillway flows has been conducted. It was found that both methods give similar results while OF tends to be more accurate than BIV. However, the deviation of both imaging methods compared to intrusive measurements with a conductivity probe is still significant. Further studies using different OF schemes will be conducted in future to analyze potential improvements. It was found that some improvement may be obtained using high-resolution images. However, OF requires much more calculation time which may be reasonable as a dense velocity field is obtained when a global method, such as the Horn-Schunck method, is employed. It was shown that this high data density may be useful to investigate small-scale structures. When a high sample rate is used, turbulence intensity may be determined with the OF approach and complete turbulence intensity fields can be obtained. More research on this capability is required in near future.

8.3 BENCHMARKING WITH SYNTHETIC IMAGES

8.3.1 GENERAL REMARKS

In order to further test the accuracy of the Optical Flow method against the widely accepted PIV method, the idea may come up to compare both to canonical flows (where analytical solutions are available) reproduced in the laboratory. In such case, the velocity fields would be subject to particle slip and other sources of error (ADRIAN AND WESTERWEEL, 2011) yielding velocity differences and inescapable mistakes in the experimental facilities. To overcome this issue, BUNG AND VALERO (2017) presented a new synthethic particle image generator[1] (SPG). This tool provides the exact velocity of each particle. Special attention is put on the accurate generation of the velocity fields to ensure that conclusions apply to different types of flows.

8.3.2 SYNTHETIC PARTICLE IMAGE GENERATION

In SPG, particles can be generated with different fraction rates f_p, i.e. the ratio between particles area and total image area. Their center location is then randomly initialized considering a uniform distribution. Particle radii are also randomly generated by assuming a normal distribution and specifying a mean and standard variation (r_m and r_{std}, correspondingly). Negative radii are avoided by taking the absolute values of the generated sample. Pixels within the particle radius are assigned 1.0 whereas the partially filled pixels receive a fractional value. Additionally, a "shadow" mask, modeled as white noise, is applied which aims to reproduce the pixel errors commonly happening for real cameras. Non-uniform illumination effects are also considered by this shadow mask by assuming a normal distribution with center s_m and standard deviation s_{std} for pixel intensities. Values larger than 255 are restricted in order to keep image values as integers between 0 and 255. An exemplary generated image is shown in Fig. 8.3.1.

[1]This synthetic particle image generator is part of FlowCV, an open-source toolbox for computer vision methods applied to turbulent flows and is primarily based on OpenCV libraries (Python 2.7). Further important libraries are NumPy for scientific computing (VAN DER WALT ET AL., 2011) and Matplotlib for postprocessing (HUNTER, 2007). FlowCV is distributed under the GNU GPLv3 license and is freely available at https://github.com/FlowCV.

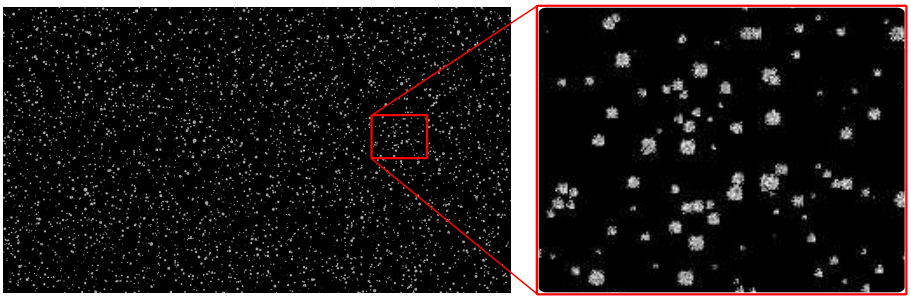

Figure 8.3.1: Synthetic image generated for $f_p = 0.05$, $r_m = 2.5$ px, $r_{std} = 1.25$ px, $s_m = 170$, $s_{std} = 40$ and high-resolution (HD).

8.3.3 STOCHASTIC PARTICLE DISPLACEMENT: SIMULATING ISOTROPIC TURBULENCE

Particles displacement $(x_2 - x_1)$ can be computed by integrating the instantaneous velocity of a particle between t_1 and t_2:

$$x_2 = x_1 + \int_{t_1}^{t_2} u \mathrm{d}t \tag{8.3.1}$$

with u the instantaneous velocity in the x-coordinate, which can be expressed in terms of its mean and fluctuating component as:

$$u = \overline{u} + u' \tag{8.3.2}$$

being $\overline{u}$ the expected value of u and u' the instantaneous fluctuation. For $\overline{u}$, many experimental and analytical solutions exist (e.g. boundary layer flow, mixing region, wake), which can be found in classic literature of fluid mechanics (e.g. POPE, 2000; WHITE, 2006). In SPG, it becomes necessary to simulate the behavior of u' by defining a realistic turbulent velocity for each particle.

For this purpose, the Langevin equation can be used, which was first proposed as a stochastic model for the velocity of a particle subject to Brownian movement (LANGEVIN, 1908). The stochastic process u^* generated by the Langevin equation is known as Ornstein-Uhlenbeck process and its probability density function is governed by the Fokker-Planck equation (POPE, 2000). Thereby, the instantaneous quantity u' is modeled by means of a stochastic differential equation for $u^*(u'(x, y, z, t) \approx u^*)$:

$$\mathrm{d}u^*(t) = -u^*(t)\frac{\mathrm{d}t}{T_L} + \left(\frac{2\sigma^2}{T_L}\right)^{1/2} \mathrm{d}W(t) \tag{8.3.3}$$

where T_L is the time scale defined by the Lagrangian velocity autocorrelation function

Selected contents from: Managing water for sustainable development: Learning from the past for the future - Proceedings of the 37th IAHR World Congress (Kuala Lumpur, 2017), Ed: A. Ghani. Reproduced with permission from IAHR.

$\rho(s) = \exp(-s/T_L)$ as:

$$T_L = \int_0^\infty \rho(s)\mathrm{d}s \tag{8.3.4}$$

In the stochastic differential equation (Eq. 8.3.3), σ is a measurement of the velocity fluctuation scale and $W(t)$ represents a Wiener process. Equation 8.3.3 can be approximated by the following finite difference equation (POPE, 2000):

$$\mathrm{d}u^*(t+\Delta t) = u^*(t) - u^*(t)\frac{\Delta t}{T_L} + \left(\frac{2\sigma^2\Delta t}{T_L}\right)^{1/2}\xi(t) \tag{8.3.5}$$

where $\xi(t)$ is a standardized Gaussian random variable (mean zero and unit standard deviation). Eq. 8.3.5 represents a diffusion equation which is consistent with KOLMOGOROV (1941) hypotheses for the turbulence inertial subrange, thus:

$$\tau_\eta \ll \Delta t \ll T_L \tag{8.3.6}$$

with τ_η the Kolmogorov time scale. It can be then demonstrated that, instead of the two parameters σ and T_L, Eq. 8.3.3 can be written in terms of the turbulent kinetic energy $k = 3/2\sigma^2$, its dissipation $\epsilon = 4k/(3C_0T_L)$ and a model coefficient C_0 (POPE, 2000):

$$\mathrm{d}u^*(t) = -\frac{3}{4}C_0\frac{\epsilon}{k}u^*(t)\mathrm{d}t + (C_0\epsilon)^{1/2}\,\mathrm{d}W(t) \tag{8.3.7}$$

While the choice of C_0 value is not completely clear (POPE, 1994, 2000), LIEN AND D'ASARO (2002) studied a broad range of DNS and experimental results concluding that $C_0 = 6 \pm 0.5$ is consistent. Consequently, $C_0 = 6.0$ may be considered as a reasonable value. In the FlowCV toolbox by BUNG AND VALERO (2017), $\overline{u}$ and $\overline{w}$ (i.e. the mean velocities in x- and z-direction, T_L and σ can be specified for particle generation. Exemplary results are illustrated in Fig. 8.3.2.

Selected contents from: Managing water for sustainable development: Learning from the past for the future - Proceedings of the 37th IAHR World Congress (Kuala Lumpur, 2017), Ed: A. Ghani. Reproduced with permission from IAHR.

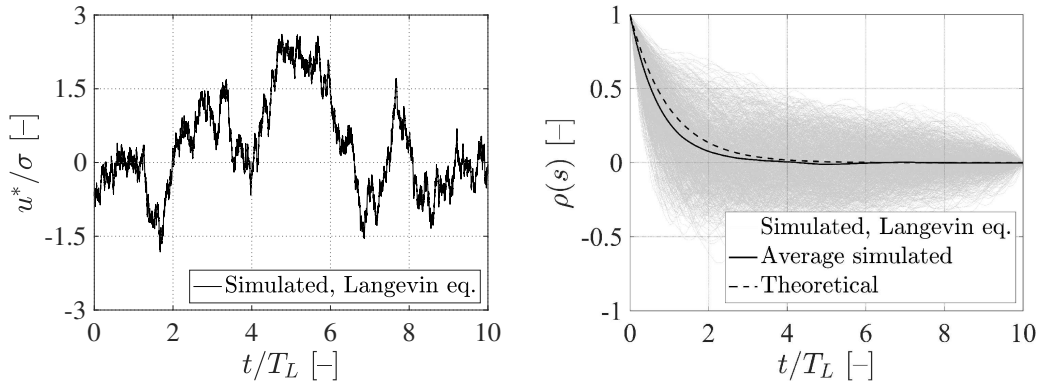

(A) Exemplary u^* generated with Eq. 8.3.5 for one particle

(B) Autocorrelation of 1,000 generated particles

Figure 8.3.2: Exemplary particle generation results

8.3.4 CASE STUDIES

Equation 8.3.1 has been integrated, both for x- and z-direction, by using a fourth order Runge-Kutta method as described by WHITE (2006). A mean velocity $\overline{u}$ of 5 px/frame is assumed for each case and the velocity fluctuation u' is modelled using Eq. 8.3.7 for each particle and time step. The separation time Δt is chosen small enough to satisfy Eq. 8.3.6 and the Courant-Friedrich-Lewy (CFL) condition (HIRSCH, 2007). Main features of the synthetic velocity fields can be found in Table 8.3.1, altogether with the corresponding turbulence intensity Tu.

Table 8.3.1: Turbulence information on the generated particles synthetic images

Case	$\overline{u}$ **[px/frame]**	$\overline{w}$ **[px/frame]**	k **[px^2/frame^2]**	ϵ **[px^2/frame^3]**	Tu **[%]**	**Resolution [px × px]**
U01	Uniform (5.0)	Null	0.375	0.017	10.0	1920 × 1080
U02	Uniform (5.0)	Null	3.375	0.150	30.0	1920 × 1080
U03	Uniform (5.0)	Uniform (5.0)	18.75	0.833	50.0	1920 × 1080

8.3.5 PROCESSING

For each of the specified cases, two frames have been generated using a particle fraction $f_p = 0.05$, a mean particle radius $r_m = 2.5$ px with a standard deviation $r_{std} = 1.25$ px. The mean pixel intensity was $s_m = 170$ with a standard deviation of $s_{std} = 40$ (an exemplary particel image with identical parameters was presented in Fig. 8.3.1). In order to illustrate the velocity magnitude fields from the synthetic images, the generated, sparse velocity data has been interpolated in both directions (see Figs. 8.3.3(A), 8.3.4(A) and 8.3.5(A).

For evaluation of the Optical Flow, results are compared to the Particle Image Velocimetry (PIV) method. For this study, a multiple FFT analysis was conducted with the open-source Matlab® toolbox PIVlab (THIELICKE AND STAMHUIS, 2014A) using interrogation window sizes of 64, 32, 16 and 8 px and 50 % overlap. The multiple window size technique, similar to the image pyramid in OF, helps to minimize the loss of information due to particle displacement (THIELICKE AND STAMHUIS, 2014B).

The Optical Flow has been determined using the Horn-Schunck method as introduced in Sections 7.2 and 7.3. With respect to the previous studies, an image pyramid with five levels was applied without further sensitivity analysis. The filter length was set to 3 px in both directions to better compare the results to the PIV method for which filtering is unavoidable as the displacement found by correlation is, approximately, an average over the particles (ADRIAN AND WESTERWEEL, 2011), but to still adequately capture turbulent flow structures as any filter smoothes the flow field and dampens turbulence.

8.3.6 RESULTS

Resulting velocity fields are shown in Figs. 8.3.3 to 8.3.5. As PIV data is obtained with a resolution of 480 × 270 data points, 2D interpolation is required for illustration.

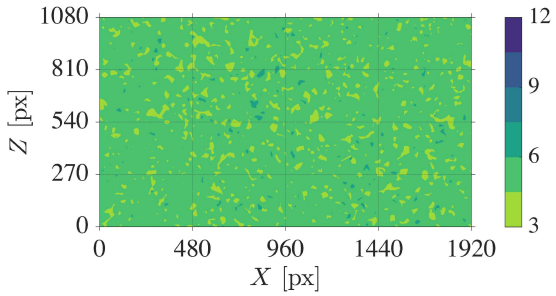

(A) Synthetic Particle Generator (SPG, for reference)

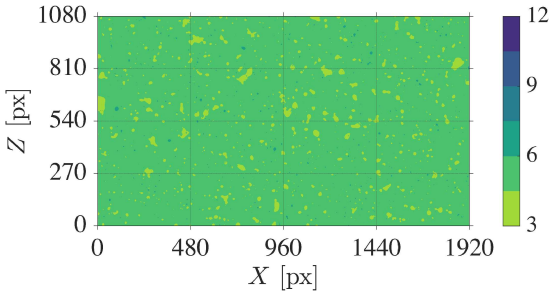

(B) Optical Flow (OF)

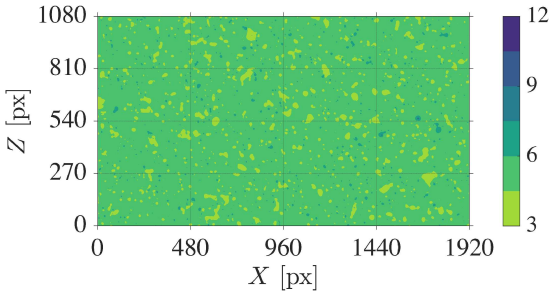

(C) Particle Image Velocimetry (PIV)

Figure 8.3.3: Resulting velocity magnitude fields for Case U01 (in px/frame), flow direction from left to right

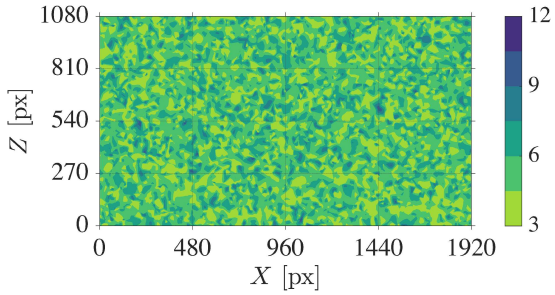

(A) Synthetic Particle Generator (SPG, for reference)

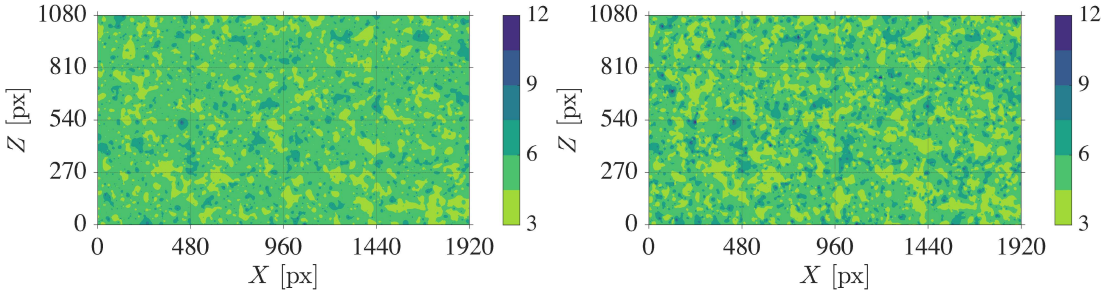

(B) Optical Flow (OF)

(C) Particle Image Velocimetry (PIV)

Figure 8.3.4: Resulting velocity magnitude fields for Case U02 (in px/frame), flow direction from left to right

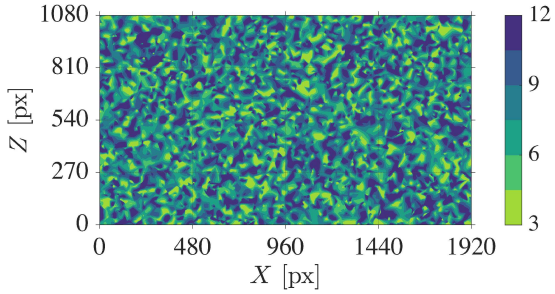

(A) Synthetic Particle Generator (SPG, for reference)

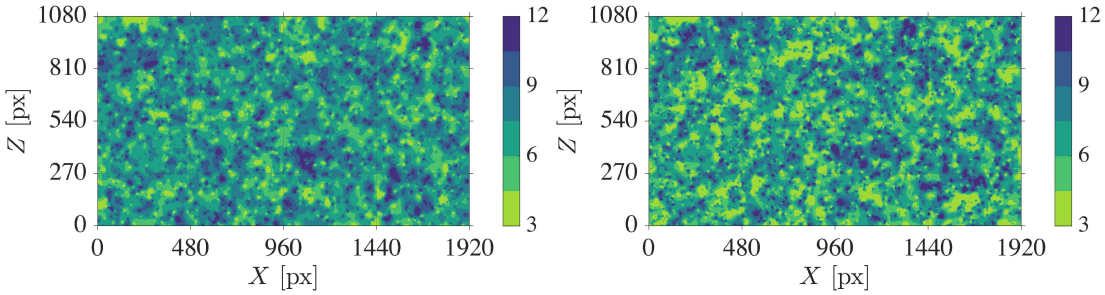

(B) Optical Flow (OF)

(C) Particle Image Velocimetry (PIV)

Figure 8.3.5: Resulting velocity magnitude fields for Case U03 (in px/frame), flow direction from upper left to lower right

The velocity fields suggest that both imaging techniques, OF and PIV, tend to underestimate the real flow velocities as originally generated by the SPG, independently from turbulence intensity. Interestingly, the PIV results seem to have larger deviation from the synthetic data than the OF results for the 2D flow case (Case U03). For 1D flows (Case U01 and U02), both flow fields show similar velocity magnitudes. This finding is supported by Figs. 8.3.6(A), 8.3.6(B) and 8.3.6(C), illustrating the normalized histograms with bin widths of 0.1 px/frame[2], and thus the relative probability of the velocity magnitudes for all cases. While the originally generated, normal distribution of velocities is well reproduced for the lower turbulent cases with almost identical mean value, the PIV data becomes slightly positively skewed for highest turbulence. Both imaging techniques show steeper distributions than the SPG, i.e. the variance of detected velocity magnitudes is smaller. This could be a consequence of the filtering as it was discussed above.

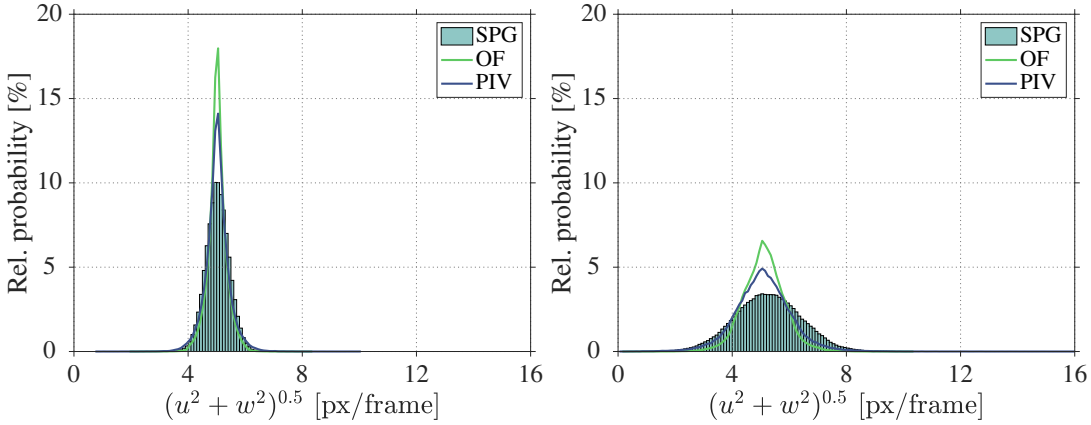

(A) Histogram (Case U01)

(B) Histogram (Case U02)

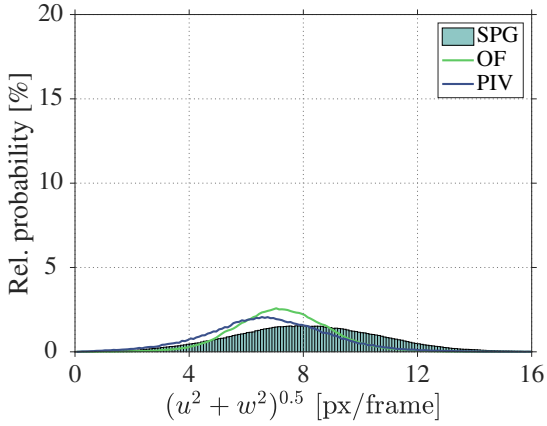

(C) Histogram (Case U03)

Figure 8.3.6: Normalized histograms (relative probability) of velocity magnitudes as generated bs Synthethic Particle Generator (SPG) or determined by Optical Flow (OF) and Particle Image Velocimetry (PIV)

[2]Sub-pixel resolution in PIV is typically achieved by interpolation of the cross-correlation peak function assuming a Gaussian distribution (ADRIAN AND WESTERWEEL, 2011).

Selected contents from: Managing water for sustainable development: Learning from the past for the future - Proceedings of the 37th IAHR World Congress (Kuala Lumpur, 2017), Ed: A. Ghani. Reproduced with permission from IAHR.

Figure 8.3.7 illustrates the accuracy of OF and PIV compared to the synthetic data.

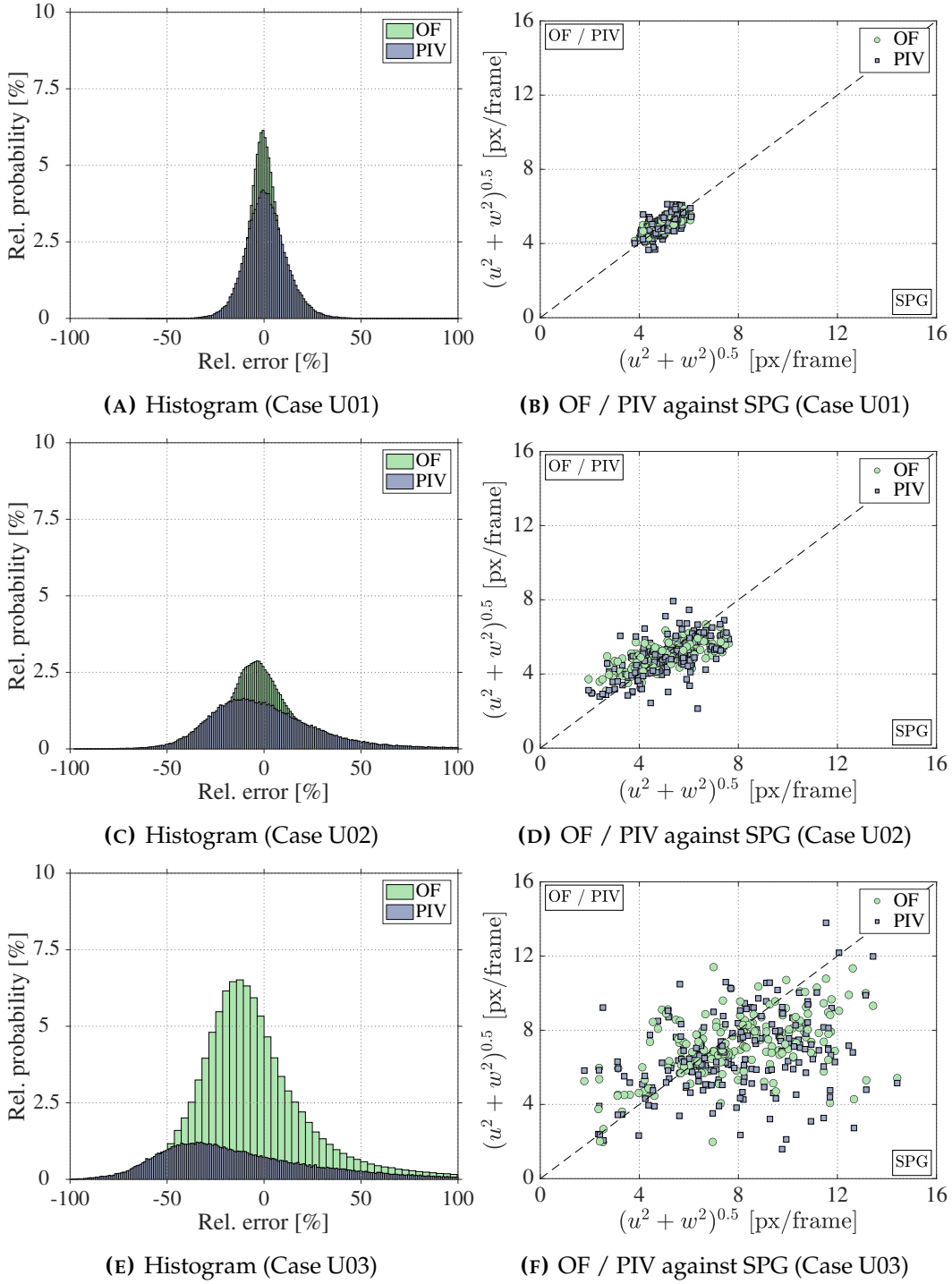

(A) Histogram (Case U01)

(B) OF / PIV against SPG (Case U01)

(C) Histogram (Case U02)

(D) OF / PIV against SPG (Case U02)

(E) Histogram (Case U03)

(F) OF / PIV against SPG (Case U03)

Figure 8.3.7: Expected accuracy from both imaging techniques (i.e. OF and PIV), left: normalized histograms (relative probability) of the relative error, right: comparison of 200 randomly selected velocities data points with identical pixel coordinates from OF / PIV and SPG

Figures 8.3.7(A), 8.3.7(C) and 8.3.7(E) show the normalized histograms or relative probability, respectively, of the relative error of velocity vectors calculated in each

method, i.e.:

$$\mathrm{ERR}_{\mathrm{OF/PIV}} = \frac{\mathrm{VEL}_{\mathrm{OF/PIV}} - \mathrm{VEL}_{\mathrm{SPG}}}{\mathrm{VEL}_{\mathrm{SPG}}} * 100 \tag{8.3.8}$$

where $\mathrm{VEL}_{\mathrm{OF/PIV}}$ is the instantaneous velocity magnitude for a specific pixel and $\mathrm{VEL}_{\mathrm{SPG}}$ is the corresponding generated velocity magnitude. The relative error is found to be normally distributed for PIV data (as it is known from the literature, see e.g. CAMERON AND ADMIRAAL (2017)) as well as for OF data, although a slight positive skewness is found for both techniques for larger turbulence. This finding supports again the conclusion that PIV as well as OF tend to underestimate the real velocities. While the mean error from both methods is almost null for low turbulence (Case U01), it becomes larger for PIV than for OF with increasing Tu. For Case U03, OF has a mean error of about -2 % with a peak at -13 %. PIV has a mean error of -9 % with a peak at -34 %.

Figures 8.3.7(B), 8.3.7(D) and 8.3.7(F) show the absolute calculated velocities in comparison to the generated velocities for 200 randomly selected velocity vectors with identical pixel coordinates. In agreement with previously discussed results, an increase of data scattering is found for increasing turbulence. This scatter tends to be larger for PIV than for OF.

8.3.7 CONCLUSIONS

The performances of the Optical Flow method and the well-accepted Particle Image Velocimetry technique have been tested against synthetically generated particle images using the FlowCV toolbox (BUNG AND VALERO, 2017). This approach is common in the PIV community. Different turbulence intensity levels have been investigated. It was found that the OF method may provide data of similar accuracy for low turbulence levels. For increasing turbulence intensity, OF was found to perform even better than PIV. It is acknowledged that the accuracy of the PIV method strongly depends on the employed PIV algorithm as well as the image quality (e.g. particle density) and findings described herein must not be generalized (CAMERON AND ADMIRAAL, 2017). In any case, it may be concluded that OF is a suitable technique for hydraulic laboratory investigations, for discrete particle images as well as for more complex textures as involved by aerated flows (as demonstrated before). It is worth to note that even for relatively simple, uniform flow, both methods tend to underestimate the real velocities. Discrepancies, as found in case of aerated flows, may thus be assumed to be caused by the general method instead of the particular, more complex flow case. Future investigations need to be carried out to optimize available OF methods for fluid flows applications. The reader may note that other OF methods, e.g. the Farnebäck method, showed a similar accuracy in comparison to synthetic data from the employed particle generator (BUNG AND VALERO, 2017).

PART IV

CLOSURE

CHAPTER 9

SUMMARY AND CONCLUSIONS

Data collection plays an important role in hydro-environment engineering. On the one hand, it is mandatory for safe design of water infrastructure in practice, e.g. by monitoring existing hydraulic structures or optimizing these structures by means of physical modeling in early design stages. In fundamental research, on the other hand, accurate measurements are necessary to gain better understanding of flow phenomena and to improve numerical models which became a standard tool in the last two decades, complementary to classical physical modeling. The continuous development of new, more sophisticated measuring techniques helps to achieve these goals.

In this thesis, recent advances in imaging techniques applied to hydraulic engineering problems were presented. It has been demonstrated that the classical Particle Image Velocimetry (PIV) can also be used for velocity field determination in aerated flows, profiting from the bubble-induced image texture for image processing. In the literature, it is referred to as Bubble Image Velocimetry (BIV), a method wich was limited to flows with low aeration and as a complementary technique to PIV before. The presented studies in this thesis first applied this method to fully aerated flows. Indeed, the basic integral approach (i.e. local cross-correlation of pixel intensity distributions in subsequent images) was found to better perform with discrete particle images. However, particularly for flow regions with moderate aeration (e.g. close to the bottom in aerated spillway flows), BIV was found to provide data with reasonable accuracy. In regions of very high void fractions, the performance is limited but can still be improved by preceding image processing and implementation of sophisticated calibration algorithms. In any case, potential wall effects need to be considered for accuracy evaluation as for any imaging techniques employed through sidewalls.

It was further demonstrated that, beyond this classical approach, modern computer vision methods may provide additional, relevant information. Computer vision is a subdiscipline of Artificial Intelligence and aims at the automatic interpretation of images and videos by e.g. detection of image features, such as edges and corners, by calculating range maps of an image allowing for 3D reconstruction of the scene or by identification of moving obstacles and estimation of their velocities. Computer vision is found in many engineering applications to date. However, in hydraulic engineering

and research, it is not widespread so far. Indeed, it is pointed out that, at the time of publication of the individual studies, most concepts were novel in this discipline. The presented paper collection, however, underlines their suitability to measure the most relevant hydraulic flow features, i.e. flow depth and velocity.

As it was shown, edge detection methods can be employed for extraction of water suface lines and thus provide instantaneous 2D information. In the presented case of aerated chute flows, additional challenges arise due to the three-dimensional, highly turbulent flow which impedes unequivocal interpretation of extracted lines. But still, it could be shown that this method can give relevant further insight. In detail, flow depths were found that significantly exceeded typical, characteristic water levels from phase detection measurements, which are commonly regarded as idealized water depth. Edge detection from images has become a common approach nowadays, mainly in coastal engineering laboratory studies, where wave propagation in channels involve almost ideal 2D water surfaces.

Aerated flows at hydraulic structures, however, are generally three-dimensional. In order to account for this additional difficulty, depth cameras can be a low-cost, easy-to-use alternative to edge detection, yielding instantaneous depth maps with high spatial and temporal resolution. The presented study on the application of a RGB-D camera, employing a stereo depth technique, intended to investigate if such consumer-grade device is capable to accurately measure the free surface of a highly turbulent hydraulic jump. Surprisingly, it was found that the achieved accuracy was similar to classical instrumentation previously used in comparable studies. Resulting data can provide detailed information on turbulent flow structures in future. A similar study has not been performed before. Thus, conclusions must not be generalized but require additional investigations which are planned for near future. However, it may be assumed that depth cameras can bring air-water flow research a significant step forward.

Another computer vision technique, applied and discussed in this thesis, is the optical flow (OF) method. Again, this method has not been applied to hydraulic engineering problems before. As demonstrated herein, it can be used for determination of flow velocity fields, although originally developed for recognition of moving obstacles within a series of images. It was shown that, in terms of accuracy, OF can compete with the classical PIV/BIV method, with the important benefit of yielding dense velocity fields. The dense velocity data may be helpful for detection of small-scale turbulent structures. However, velocity calculation is much more time-consuming than for PIV/BIV. Optical flow methods have not yet been optimized for fluids application (only a few attempts have been made in the past, e.g. by implementing mass conservation concepts), demanding additional research. In any case, OF-based velocity estimation has gained a lot of interest in recent years and it may be expected that, in the hydraulics community, it will achieve similar relevance as the well-accepted PIV method.

CHAPTER 10

FUTURE RESEARCH NEEDS

Although this thesis presented numerous studies on the application of imaging techniques to hydraulic engineering problems, several aspects still require more research to better understand or to improve results. Moreover, presented methods have been limited to laboratory environments. Exploration of potential transfer to field applications, particularly for novel computer vision methods, will be an important next step. To date, very limited studies on field application have been published in the literature. Consequently and given the conclusions of the individual, previously presented studies, following research needs can be identified:

- It was shown that edge detection methods can be employed to extract surface levels in laboratory flumes. Particularly, in highly turbulent, three-dimensional flows, interpretation of surface levels is vague as waves in the background may adulterate the results. Combination with depth camera measurements can help to identify background artefacts from sidewall videos.
- Some studies on application of edge detection methods to gauge water levels in natural water bodies have been presented in the literature. Yet, this application may be improved and eventually, combined with determination of surface velocities by use of optical flow methods to allow for discharge estimation. Furthermore, depth cameras may also be applied to measure water levels in the field by identifying the intersection line of the reflective water surface with fixed obstacles, e.g. bridge piers, within the range maps. For potential field applications, it is interesting to note that, during the time of writing of this thesis, new customer-grade depth cameras became available which allow for measuring longer ranges of approximately 20 m by extending the baseline of both camera sensors.
- Nowadays, high-performance customer-grade camcorders are available which allow for taking videos with up to 12k resolution and frame rates in the order of 200 fps. With such devices, it may be worth to test if identification of individual bubbles, e.g. by application of edge detection methods, may be accomplished to more accurately (and with less calibration effort) measure air concentration from sidewall videos.

- Depth cameras are a very promising option for measurement of turbulent free-surface properties. The presented study, however, was limited to interpretation of centerline data in order to compare this new instrument to classical devices. In a next step, rectification of the depth images and interpretation of the 3D data should be performed. Such study may be interesting for different types of aerated flow, e.g. spillways and hydraulic jumps. Identification of turbulent length and time scales from depth cameras may provide important information to improve understanding of aerated flows and the performance of numerical models. In this context, a comparison with void fraction data will help to better understand, which level a depth camera really detects. For the latter, a systematic investigation with different degrees of aeration will be helpful.

- For velocity estimation by means of optical flow, the Farnebäck method was found to be most effective in terms of accuracy and computation time. However, this method is still not optimized for application to fluid flows. The quadratic polynomial to approximate the intensity distribution in a pixel neighborhood, which is considered in the original approach, may be improved to better account for different types of flow. Application to fluids is more challenging than the original purpose, i.e. to estimate velocities of moving objects. Particularly, in presence of high air concentrations, a modification of this polynomial may be justified.

- Besides all these potential improvements and future applications, a still remaining task is to enhance the accuracy of velocities from optical flow (and also from Bubble Image Velocimetry) in regions of high void fractions. It was shown that deviations in the order of up to 20 % occur, almost regardless of image preprocessing and filtering. The performance of optical flow strongly depends on image quality. Higher image resolutions, as proposed above, could help to increase accuracy. Anyway, it is believed that unavoidable, time-dependent light reflections at air bubbles, which violate the assumption of constant illumination, are mainly responsible for this significant error. Self-learning methods to optimize results, potentially in real-time, will be challenging, yet interesting to implement. Contrast enhancement is generally helpful. However, so far only a spatial histogram equalization has been performed on individual video frames, without accounting for histograms of subsequent images. An extension of histogram equalization to the time domain may be considered in future. Once the time-averaged velocities are met with sufficient accuracy, research can be extended to analyze turbulence properties.

BIBLIOGRAPHY

Aberle, J. (2017). "Water depth." *Experimental Hydraulics: Methods, Instrumentation, Data Processing and Management, Vol. II: Instrumentation and Measurement Techniques*, J. Aberle, C. D. Rennie, D. M. Admiraal, and M. Muste, eds., IAHR Monograph, CRC Press, Leiden, The Netherlands, Chapter 6.2.2.

Aberle, J. and Järvelä, J. (2015). "Hydrodynamics of vegetated channels." *Rivers – physical, fluvial and environmental processes*, P. M. Rowinski and A. Radecki-Pawlik, eds., Springer, 519–541.

Aberle, J., Rennie, C. D., Admiraal, D. M., and Muste, M. (2017). *Experimental Hydraulics: Methods, Instrumentation, Data Processing and Management*, Vol. II: Instrumentation and measurement techniques. CRC Press, Leiden, The Netherlands.

Adelson, E., Anderson, C. H., Bergen, J. R., Burt, P. J., and Ogden, J. (1984). "Pyramid methods in image processing." *RCA Engineer*, 29(6), 33–41.

Adrian, R. J. and Westerweel, J. (2011). *Particle Image Velocimetry*. Cambridge University Press.

Ahmed, T., Shim, J., Jeong, J. H., and Duan, J. G. (2017). "Advanced signal processing of sonar measurement for bridge scour monitoring." *Proceedings of the World Environmental and Resources Congress*, ASCE, 93–100.

Allamano, P., Croci, A., and Laio, F. (2015). "Toward the camera rain gauge." *Water Resources Research*, 51, 1744–1757.

Amador, A., Sánchez-Juny, M., and Dolz, J. (2006). "Characterization of the nonaerated flow region in a stepped spillway by piv." *Journal of Fluid Engineering*, 128, 1266–1273.

Amador, A., van der Graaf, G., Sánchez-Juny, M., Dolz, J., Sánchez-Tembleque, F., and Puertas, J. (2004). "Characterization of the flow field in a stepped spillway by PIV." *12th International Symposium on Applications of Laser Techniques*.

André, S. (2004). "High velocity aerated flows on stepped chutes with macro-roughness elements." Ph.D. thesis, EPF Lausanne, Lausanne.

ASCE (2000). *Hydraulic modeling: concepts and practice*, Vol. 7 of *ASCE manuals and reports on engineering practice*. American Society of Civil Engineers, Reston, USA.

ASCE (2007). *Measurement of Oxygen Transfer in Clean Water ASCE 2-06*. American Society of Civil Engineers, Reston, USA.

Atcheson, B., Heidrich, W., and Ihrke, I. (2009). "An evaluation of optical flow algorithms for background oriented schlieren imaging." *Experiments in Fluids*, 46, 467–476.

Aureli, F. and Mignosa, P. (2002). "Rapidly varying flows due to levee-breaking." *Proceedings of the International Conference on Fluvial Hydraulics (River Flow)*, D. Bousmar and Y. Zech, eds., Louvain-La-Neuve, 459–466.

Avery, S. T. and Novak, P. (1978). "Oxygen transfer at hydraulic structures." *Journal of the Hydraulics Division*, 104(HY11), 1521–1540.

Bandini, F. (2017). "Hydraulics and drones: observations of water level, bathymetry and water surface velocity from Unmanned Aerial Vehicles." Ph.D. thesis, Technical University of Denmark, Lyngby, Denmark.

Barnard, S. T. and Fischler, M. A. (1982). "Computational stereo." *ACM Computing Surveys*, 14(4).

Barron, J. L., Fleet, D. J., and Beauchemin, S. S. (1994). "Performance of optical flow techniques." *International Journal of Computer Vision*, 12(1), 43–77.

Bazaraa, M. S., Sherali, H. D., and Shetty, C. M. (1993). *Nonlinear programming*. Wiley.

Bell, T., Li, B., and Zhang, S. (2016). "Structured light techniques and applications." *Wiley Encyclopedia of Electrical and Electronics Engineering*, Wiley. https://doi.org/10.1002/047134608X.W8298.

Bhola, P. K., Nair, B. B., Leandro, J., Rao, S. N., and Disse, M. (2019). "Flood inundation forecasts using validation data generated with the assistance of computer vision." *Journal of Hydroinformatics*, 21(2), 240–256.

Boes, R. M. (2000). "Zweiphasenströmung und Energieumsetzung an Großkaskaden." Ph.D. thesis, ETH Zurich, Zurich.

Boes, R. M. and Hager, W. H. (2003). "Hydraulic design of stepped spillways." *Journal of Hydraulic Engineering*, 129(9), 671–679.

Boiten, W. (2005). *Hydrometry*. IHE Delft Lecture Notes. A. A. Balkema.

Bradski, G. and Kaehler, A. (2008). *Learning OpenCV – Computer Vision with the OpenCV Library*. O'Reilly.

Brasington, J. (2017). "Terrestrial laser scanning: Topographic measurement & modelling." *Experimental Hydraulics: Methods, Instrumentation, Data Processing and Management, Vol. II: Instrumentation and Measurement Techniques*, J. Aberle, C. D. Rennie, D. M. Admiraal, and M. Muste, eds., IAHR Monograph, CRC Press, Leiden, The Netherlands, Chapter 4.2.2.1.

Brenner, C., Apperl, B., and Schulz, K. (2015). "Integration von Orthofotos in die Abschätzung des Hochwasserschadenspotenzials." *Österreichische Wasser- und Abfallwirtschaft*, 67, 412–421.

Bruhn, A., Weickert, J., and Schnörr, C. (2005). "Lucas/Kanade meets Horn/Schunck: Combining local and global optic flow methods." *International Journal of Computer Vision*, 61(3), 211–231.

Buffi, G., Manciola, P., Grassi, S., Barberini, M., and Gambi, A. (2017). "Survey of the Ridracoli dam: UAV-based photogrammetry and traditional topographic techniques in the inspection of vertical structures." *Geomatics, Natural Hazards and Risk*, 8(2), 1562–1579.

Bung, D. B. (2009). "Zur selbstbelüfteten Gerinneströmung auf Kaskaden mit gemäßigter Neigung." Ph.D. thesis, University of Wuppertal, Wuppertal.

Bung, D. B. (2010). "A comparative study of self-aerated stepped spillway and smooth invert chute flow: The effect of step-induced macro-roughness." *Chinese-German joint symposium on hydraulic and ocean engineering (CG JOINT 2010)*, Y. Wang, ed., 451–456.

Bung, D. B. (2011a). "Developing flow in skimming flow regime on embankment stepped spillways." *Journal of Hydraulic Research*, 49(5), 639–648.

Bung, D. B. (2011b). "Fließcharakteristik und Sauerstoffeintrag bei selbstbelüfteten Gerinneströmungen auf Kaskaden mit gemäßigter Neigung." *Österreichische Wasser- und Abfallwirtschaft*, 3-4/2011, 76–81.

Bung, D. B. (2011c). "Non-intrusive measuring of air-water flow properties in self-aerated stepped spillway flow." *34th IAHR World Congress*, Brisbane.

Bung, D. B. (2012). "Sensitivity of phase detection techniques in aerated chute flows to hydraulic design parameters." *2nd European IAHR Congress*, Munich.

Bung, D. B. (2013). "Non-intrusive detection of air-water surface roughness in self-aerated chute flows." *Journal of Hydraulic Research*, 51(3), 322–329.

Bung, D. B., Hildebrandt, A., Oertel, M., Schlenkhoff, A., and Schlurmann, T. (2008). "Bore propagation over a submerged horizontal plate by physical and numerical simulation." *Proceedings of the 31st International Conference on Coastal Engineering (ICCE)*, Hamburg, 3542–3553.

Bung, D. B. and Oertel, M. (2019). "Wave breaking over a submerged plate: Optical flow, LES and RANS." *E-proceedings of the 38th IAHR World Congress*, 3690–3698.

Bung, D. B., Sun, Q., Meireles, I., Matos, J., and Viseu, T. (2012). "USBR type III stilling basin performance for steep stepped spillways." *4th IAHR Symposium on Hydraulic Structures*, Porto.

Bung, D. B. and Valero, D. (2015). "Image processing for bubble image velocimetry in self-aerated flows." *36th IAHR World Congress*, The Hague.

Bung, D. B. and Valero, D. (2016a). "Application of the optical flow method to velocity determination in hydraulic structure models." *6th International Symposium on Hydraulic Structures (IAHR)*, Portland, 240–249.

Bung, D. B. and Valero, D. (2016b). "Optical flow estimation in aerated flows." *Journal of Hydraulic Research*, 54(5), 575–580.

Bung, D. B. and Valero, D. (2017). "FlowCV - An open-source toolbox for computer vision applications in turbulent flows." *37th IAHR World Congress*, Kuala Lumpur.

Burt, P. J. and Adelson, E. H. (1983). "The Laplacian pyramid as a compact image code." *IEEE Transactions on Communications*, 31(4), 532–540.

Butkiewicz, T. (2014). "Low-cost coastal mapping using Kinect v2 time-of-flight cameras." *Proceedings of the Oceans Conference*, 1–9.

Cain, P. (1978). "Measurements within self-aerated flow on a large spillway." Ph.D. thesis, University of Canterbury, Christchurch.

Cameron, S. and Admiraal, D. M. (2017). "Particel image velocimetry (PIV)." *Experimental Hydraulics: Methods, Instrumentation, Data Processing and Management, Vol. II: Instrumentation and Measuring Techniques*, J. Aberle, C. D. Rennie, D. M. Admiraal, and M. Muste, eds., CRC Press, Leiden, The Netherlands, Chapter 3.7.2.4.

Cao, L., Weitbrecht, V., Li, D., and Detert, M. (2020). "Airborne feature matching velocimetry for surface flow measurements in rivers." *Journal of Hydraulic Research* https://doi.org/10.1080/00221686.2020.1818309.

Carfagni, M., Furferi, R., Governi, L., Santarelli, C., Servi, M., Uccheddu, F., and Volpe, Y. (2019). "Metrological and critical characterization of the Intel D415 stereo depth camera." *Sensors*, 19(3), 489.

Carvalho, R. F. and Amador, A. T. (2008). "Flow field over a stepped spillway: Physical and numerical approach." *3rd International Symposium on Hydraulic Structures (IAHR)*, Nanjing.

Caviedes-Voullième, D., Juez, C., Murillos, C., and García-Navarro, P. (2014). "2D dry granular free-surface flow over complex topography with obstacles. Part I: experimental study using a consumer-grade RBG-D sensor." *Computer & Geosciences*, 73, 177–197.

Chachereau, Y. and Chanson, H. (2011). "Free-surface fluctuations and turbulence in hydraulic jumps." *Experimental Thermal and Fluid Science*, 35(6), 896–909.

Chanson, H. (1993). "Stepped spillway flows and air entrainment." *Canadian Journal of Civil Engineering*, 20(3), 422–435.

Chanson, H. (1996). *Air Bubble Entrainment in Free-Surface Turbulent Shear Flows*. Academic Press, San Diego, USA.

Chanson, H. (2002a). "Air-water measurements with intrusive phase-detection probes: Can we improve their interpretation?." *Journal of Hydraulic Engineering*, 128(3), 252–255.

Chanson, H. (2002b). *The Hydraulics of Stepped Chutes and Spillways*. A. A. Balkema, Lisse, Niederlande.

Chanson, H. (2004). "Unsteady air-water flow measurements in sudden open channel flows." *Experiments in Fluids*, 37(6), 899–909.

Chanson, H. (2007). "Bubbly flow structure in hydraulic jump." *European Journal of Mechanics - B/Fluids*, 26(3), 367–384.

Chanson, H. (2009). "Application of the method of characteristics to the dam break wave problem." *Journal of Hydraulic Research*, 47(1), 41–49.

Chanson, H. (2015). *Energy dissipation in hydraulic structures*. CRC Press, EH Leiden.

Chanson, H. and Brattberg, T. (2000). "Experimental study of the air-water shear flow in a hydraulic jump." *International Journal of Multiphase Flow*, 26(4), 583–607.

Chanson, H. and Felder, S. (2010). "Turbulence measurements in air-water self-aerated flows: Basic analysis and results." *7th International Conference on Multiphase Flow (ICMF 2010)*, Tampa.

Chanson, H. and Toombes, L. (2001). "Experimental investigations of air entrainment in transition and skimming flows down a stepped chute." *Report No. CE158*, The University of Queensland, Brisbane.

Chanson, H. and Toombes, L. (2002). "Air-water flows down stepped chutes: Turbulence and flow structure observations." *International Journal of Multiphase Flow*, 28, 1737–1761.

Chanson, H. and Toombes, L. (2004). "Hydraulics of stepped chutes: The transition flow." *Journal of Hydraulic Research*, 42(1), 43–54.

Chen, Y. and Han, D. (2016). "Big data and hydroinformatics." *Journal of Hydroinformatics*, 18(4), 599–614.

Chowdhury, M. R., Hall, R. L., and Pesantes, E. (1997). "Flow-induced vibration experiments for a 1:25-scale-model flat wicket gate." *Report No. SL-97-4*, U.S. Army Corps of Engineers, Waterways Experiment Station, Louisville.

Chua, L. H. C. and Holz, K.-P. (2005). "Hybrid neural network - finite element river flow model." *Journal of Hydraulic Engineering*, 131(1), 52–59.

Cipolla, R., Battiato, S., and Farinella, G. M. (2010). *Computer Vision - Detection, recognition and reconstruction*. Springer, Berlin.

Corpetti, T., Heitz, D., Arroyo, G., Memin, E., and Santa-Cruz, A. (2006). "Fluid experimental flow estimation based on an optical-flow scheme." *Experiments in Fluids*, 40(1), 80–97.

Cosgrove, W. J. and Loucks, D. P. (2015). "Water management: Current and future challenges and research directions." *Water Resources Research*, 51, 4823–439.

Davies, E. R. (2018). *Computer Vision - Principles, algorithms, applications, learning*. Elsevier, London.

Di Cristo, C. (2011). "Particle imaging velocimetry and its applications in hydraulics: A state-of-the-art review." *Experimental Methods in Hydraulic Research*, P. M. Rowinski, ed., Springer, 49–66.

Dorschel, J. (2015). *Praxishandbuch Big Data*. Springer Gabler, Wiesbaden.

Douglas, S., Cornett, A., and Nistor, I. (2020). "Image-based measurement of wave interactions with rubble mound breakwaters." *Journal of Marine Science and Engineering*, 8(6), 472.

Drazin, P. G. (2002). *Introduction to hydrodynamic stability*. Cambridge University Press.

Dressler, R. F. (1952). "Hydraulic resistance effect upon the dambreak functions." *Journal of Research of the National Bureau of Standards*, 49(3), 217–225.

Du, H., Li, M., and Meng, J. (2017). "Study of fluid edge detection and tracking method in glass flume based on image processing technology." *Advances in Engineering Software*, 112, 117–123.

Dunn, P. F. (2010). *Measurement and data analysis for engineering and science*. CRC Press, Boca Raton.

Eltner, A., Elias, M., Sardemann, H., and Spieler, D. (2018). "Automatic image-based water stage measurement for long-term observations in ungauged catchments." *Water Resources Research*, 54(12), 10362–10371.

Erpicum, S., Crookston, B., Bombardelli, F., Bung, D. B., Felder, S., Mulligan, S., Oertel, M., and Palermo, M. (2020). "Hydraulic structures engineering: An evolving science in a changing world." *WIRE's Water* https://doi.org/10.1002/wat2.1505.

Ervine, D. A. and Falvey, H. T. (1987). "Behaviour of turbulent water jets in the atmosphere and in plunge pools." *Proceedings of the Institution of Civil Engineers (ICE)*, Vol. 83, Telford Services, 295–314.

Essery, I. T. S., Tebutt, T. H. Y., and Rasaratnam, S. K. (1978). "Design of spillways for re-aeration of polluted waters." *Report No. 72*, Construction Industry Research and Information Association (CIRIA), Birmingham.

Farnebäck, G. (2003). "Two-frame motion estimation based on polynomial expansion." *13th Scandinavian Conference, SCIA 2003*, Halmstad.

Felder, S. and Chanson, H. (2015). "Phase-detection probe measurements in high-velocity free-surface flows including a discussion of key sampling parameters." *Experimental Thermal and Fluid Science*, 61, 66–78.

Felder, S., Guenther, P., and Chanson, H. (2012). "Air-water flow properties and energy dissipation on stepped spillways: A physical study of several pooled stepped configurations." *Report No. CH87/12*, The University of Queensland, Brisbane.

Felder, S., Hohermuth, B., and Boes, R. M. (2019). "High-velocity air-water flows downstream of sluice gates including selection of optimum phase-detection probe." *International Journal of Multiphase Flows*, 116, 203–220.

Ferreira, R. and Aleixo, R. (2017). "Laser-Doppler velocimetry anemometry." *Experimental Hydraulics: Methods, Instrumentation, Data Processing and Management, Vol. II: Instrumentation and Measurement Techniques*, J. Aberle, C. D. Rennie, D. M. Admiraal, and M. Muste, eds., IAHR Monograph, CRC Press, Leiden, The Netherlands, Chapter 3.6.

Ferreira da Silva, A. M. and Yalin, M. S. (2017). *Fluvial processes*. CRC Press, London.

Fleet, D. J. and Weiss, Y. (2005). *Handbook of mathematical models in computer vision*. Springer, Chapter Optical flow estimation, 237–257.

Fortun, D., Bouthemy, P., and Kervrann, C. (2015). "Optical flow modeling and computation: A survey." *Computer Vision and Image Understanding*, 134, 1–21.

Gallup, D., Frahm, J.-M., Mordohai, P., and Pollefeys, M. (2008). "Variable baseline/resolution stereo." *IEEE Computer Society Conference on Computer Vision and Pattern Recognition (CVPR)*, Anchorage.

Giancola, S., Valenti, M., and Sala, R. (2018). *A Survey on 3D Cameras: Metrological Comparison of Time-of-Flight, Structured-Light and Active Stereoscopy Technologies*. Springer.

Golub, G. H. and van Loan, C. F. (2013). *Matrix computations*. The Johns Hopkins University Press, Baltimore.

Gonzalez, C. A. (2005). "An experimental study of free-surface aeration on embankment stepped chutes." Ph.D. thesis, The University of Queensland, Brisbane.

Gonzalez, R. C. and Woods, R. E. (2018). *Digital Image Processing*. Pearson, New York.

Gonzalez, R. C., Woods, R. E., and Eddins, S. L. (2009). *Digital image processing using Matlab*. Gatesmark Publishing.

Goodfellow, I., Bengio, Y., and Courville, A. (2016). *Deep learning*. MIT Press, Cambridge.

Goring, D. G. and Nikora, V. I. (2002). "Despiking acoustic Doppler velocimeter data." *Journal of Hydraulic Engineering*, 128(1), 117–126.

Govindaraju, R. S. (2000). "Artificial neural networks in hydrology. I: Preliminary concepts." *Journal of Hydrologic Engineering*, 5(2), 115–123.

Gruen, A. (2012). "Development and status of image matching in photogrammetry." *The Photogrammetric Record*, 27(137), 36–57.

Grunnet-Jepsen, A., Sweetser, J. N., Winder, P., Takagi, A., and Woodfill, J. (2019a). "Projectors for D400 series depth cameras. Retrieved February 1, 2020, from https://dev.intelrealsense.com/docs/projectors.

Grunnet-Jepsen, A., Sweetser, J. N., and Woodfill, J. (2018). "Best known methods for tuning Intel® Realsense™ depth cameras D415 and D435 v1.9. Retrieved July 26, 2019, from https://www.intel.com/content/dam/support/us/en/documents/emerging-technologies/intel-realsense-technology/BKMs_Tuning_RealSense_D4xx_Cam.pdf.

Grunnet-Jepsen, A., Sweetser, J. N., and Woodfill, J. (2019b). "Subpixel linearity improvement for Intel® Realsense depth camera D400 series. Retrieved February 1, 2020, from https://dev.intelrealsense.com/docs/white-paper-subpixel-linearity-improvement-for-intel-realsense-depth-cameras.

Grunnet-Jepsen, A., Sweetser, J. N., and Woodfill, J. (2019c). "Tuning depth cameras for best performance. Retrieved February 1, 2020, from https://dev.intelrealsense.com/docs/tuning-depth-cameras-for-best-performance.

Guimarães, P. V., Ardhuin, F., Bergamasco, F., Leckler, F., Filipot, J.-F., Shim, J.-S., Dulov, V., and Benetazzo, A. (2020). "A data set of sea surface stereo images to resolve space-time wave fields." *Scientific Data*, 7(1), 145.

Hager, W. H. (1992). *Energy disspators and hydraulic jump*. Kluwer Academic.

Hager, W. H. (1993). "Classical hydraulic jump: free surface profile." *Canadian Journal of Civil Engineering*, 20(3), 536–539.

Hansen, I., Satzger, C., Peña-Haro, S., and Lüthi, B. (2019). "Kamerabasierte Durchflussmessung in offenen Kanälen und Flüssen." *Wasserwirtschaft*, 7-8, 12–15.

Harris, C. and Stephens, M. (1988). "A combined corner and edge detector." *4th Alvey Vision Conference*, Manchester, 147–151.

Heller, V. (2011). "Scale effects in physical hydraulic engineering models." *Journal of Hydraulic Research*, 49(3), 293–306.

Herschy, R. W. (2009). *StreamfLow measurement*. Routledge, New York.

Hirsch, C. (2007). *Numerical computation of internal & external flows*, Vol. 1: Fundamentals of Computational Fluid Dynamics. Butterworth-Heinemann, Burlington, MA.

Hirt, C. W. and Nichols, B. D. (1981). "Volume of fluid (vof) method for the dynamics of free boundaries." *Journal of Computational Physics*, 39(1), 201–225.

Horn, B. K. P. and Schunck, B. G. (1981). "Determining optical flow." *Artificial Intelligence*, 17, 185–203.

Hughes, S. A. (1993). *Physical Models and Laboratory Techniques in Coastal Engineering*, Vol. 7 of *Advanced Series on Ocean Engineering*. World Scientific Publishing, Singapur.

Hunt, B. (1982). "Asymptotic solution for dam-break problem." *Journal of the Hydraulics Division*, 108(HY1), 115–126.

Hunter, J. D. (2007). "Matplotlib: A 2d graphics environment." *Journal of Computing Science and Engineering*, 9, 90–95.

ICOLD (1996). *Vibrations of hydraulic equipment for dams: review and recommendations*, Vol. 102. International Commission on Large Dams / Committee on Hydraulics for Dams, Paris.

Kähler, C. J., Astarita, T., Vlachos, P. P., Sakakibara, J., Hain, R., Discetti, S., La Foy, R., and Cierpka, C. (2016). "Main results of the 4th international PIV challenge." *Experiments in Fluids*, 57:97.

Kanade, T. and Okutomi, M. (1991). "A stereo matching algorithm with an adaptive window: theory and experiment." *Proceedings of the IEEE International Conference on Robotics and Automation*.

Khalid, M., Pénard, L., and Mémin, E. (2017). "Application of optical flow for river velocimetry." *37th IEEE International Symposium on Geoscience and Remote Sensing (IGARSS)*, Fort Worth, TX.

Killen, J. M. (1968). "The surface characteristics of self-aerated flow in steep channels." Ph.D. thesis, University of Minnesota, Minnesota.

Kimmoun, O. and Branger, H. (2007). "A particle image velocimetry investigation on laboratory surf-zone breaking waves over a sloping beach." *Journal of Fluid Mechanics*, 588, 353–397.

Kobus, H. (1980). *Hydraulic modelling*, Vol. 7. German Association for Water Resources and Land Improvement (DVWK), Paul Parey, Hamburg.

Kobus, H. (1984). *Symposium on scale effects in modelling hydraulic structures*. Hydraulic Engineering Institute, University of Stuttgart, Stuttgart.

Kobus, H. (1985). *An Introduction to Air-Water-Flows in Hydraulics*, Vol. 61. Hydraulic Engineering Institute, University of Stuttgart, Stuttgart.

Kolmogorov, A. N. (1941). "The local structure of turbulence in incompressible viscous fluid for very large reynolds numbers." *Doklady Akademii Nauk SSSR*, 30, 301–305.

Kramer, K. (2004). "Development of aerated chute flow." Ph.D. thesis, ETH Zurich, Zurich.

Kramer, M. and Chanson, H. (2019). "Optical flow estimations in aerated spillway flows: Filtering and discussion on sampling parameters." *Experimental Thermal and Fluid Science*, 103, 318–328.

Kramer, M., Chanson, H., and Felder, S. (2019a). "Can we improve the non-intrusive characterization of high-velocity air-water flows? application of LIDAR technology to stepped spillways." *Journal of Hydraulic Research*, 58(2), 350–362.

Kramer, M., Hohermuth, B., Valero, D., and Felder, S. (2020). "Best practices for velocity estimations in highly aerated flows with dual-tip phase-detection probes." *International Journal of Multiphase Flow*, 126, 103228.

Kramer, M. and Valero, D. (2020). "Turbulence and self-similarity in highly-aerated shear flows: the stable hydraulic jump." *International Journal of Multiphase Flow*, 129.

Kramer, M., Valero, D., Chanson, H., and Bung, D. B. (2019b). "Towards reliable turbulence estimations with phase-detection probes: an adaptive window cross-correlation technique." *Experiments in Fluids*, 60, 2.

Kucukali, S. and Chanson, H. (2008). "Turbulence measurements in the bubbly flow region of hydraulic jumps." *Experimental Thermal and Fluid Science*, 33(1), 41–53.

Lachat, E., Macher, H., Gonzalez-Aguilera, D., Akca, D., Müller, R., and Thenkabail, P. S. (2015). "Assessment and calibration of a RBG-D camera (Kinect v2 sensor) towards a potential use for close-range 3D modelling." *Remote Sensing*, 7(10), 13070–13097.

Langevin, P. (1908). "Sur la théorie du movement brownien." *Comptes Rendus de l'Academie des Sciences*, 146, 530–533.

Lauber, G. and Hager, W. H. (1998a). "Experiments to dambreak wave: Horizontal channel." *Journal of Hydraulic Research*, 36(3), 291–307.

Lauber, G. and Hager, W. H. (1998b). "Experiments to dambreak wave: Sloping channel." *Journal of Hydraulic Research*, 36(5), 761–773.

Laurien, E. and Oertel, H. (2018). *Numerische Strömungsmechanik*. Springer.

Leandro, J., Bung, D. B., and Carvalho, R. (2014). "Measuring void fraction and velocity fields of a stepped spillway for skimming flow using non-intrusive methods." *Experiments in Fluids*, 55(5).

Leandro, J., Carvalho, R., Chachereau, Y., and Chanson, H. (2012). "Estimating void fraction in a hydraulic jump by measurements of pixel intensity." *Experiments in Fluids*, 52, 1307–1318.

Legleiter, C., Kinzel, O., and Nelson, J. (2017). "Remote measurement of river discharge using thermal particle image velocimetry (PIV) and various sources of bathymetric information." *Journal of Hydrology*, 554, 490–506.

Lemmin, U. (2017). "Acoustic backscattering instruments (ABIs) for fine-scale flow measurements." *Experimental Hydraulics: Methods, Instrumentation, Data Processing and Management, Vol. II: Instrumentation and Measurement Techniques*, J. Aberle, C. D. Rennie, D. M. Admiraal, and M. Muste, eds., IAHR Monograph, CRC Press, Leiden, The Netherlands, Chapter 3.2.

Lennon, J. M. and Hill, D. F. (2006). "Particle image velocity measurements of undular and hydraulic jumps." *Journal of Hydraulic Engineering*, 132(12), 1283–1294.

Li, L. (2014). "Time-of-Flight camera - An introduction." *Technical White Paper SLOA190B*, Texas Instruments.

Lien, R.-C. and D'Asaro, E. A. (2002). "The Kolmogorov constant for the Lagrangian velocity spectrum and structure function." *Physics of Fluids*, 14(12), 4456–4459.

Lin, C., Hsieh, S.-C., Kuo, K.-J., and Chang, K.-A. (2008). "Periodic oscillation caused by a flow over a vertical drop pool." *Journal of Hydraulic Engineering*, 134(7), 948–960.

Lin, C., Hsieh, S. C., Lin, I. J., Chang, K. A., and Raikar, R. V. (2012). "Flow property and self-similarity in steady hydraulic jumps." *Experiments in Fluids*, 53(5), 1591–1616.

Liu, M., Rajaratnam, N., and Zhu, D. Z. (2004). "Turbulence structure of hydraulic jumps of low froude numbers." *Journal of Hydraulic Engineering*, 130(6), 511–520.

Liu, T., Merat, A., Makhmalbaf, M. H. M., Fajardo, C., and Merati, P. (2015). "Comparison between optical flow and cross-correlation methods for extraction of velocity fields from particle images." *Experiments in Fluids*, 56(8).

Liu, T. and Shen, L. (2008). "Fluid flow and optical flow." *Journal of Fluid Mechanics*, 614, 253–291.

Lopes, P., Bung, D. B., Leandro, J., and Carvalho, R. F. (2015). "The effect of cross-waves in physical stepped spillway models." *Proceedings of the 36th IAHR World Congress*, The Hague.

Lucas, B. D. (1984). "Generalized image matching by the method of differences." Ph.D. thesis, Carnegie-Mellon University, Pittsburgh.

Lucas, B. D. and Kanade, T. (1981). "An iterative image registration technique with an application to stereo vision." *Proceedings of imaging understanding workshop*, 121–130.

Matos, J. (2000). "Hydraulic designs of stepped spillways over rcc dams." *Hydraulics of Stepped Spillways*, H.-E. Minor and W. H. Hager, eds., International Workshop on Hydraulics of Stepped Spillways (IAHR), Zurich, A. A. Balkema, 187–194.

Matos, J., Frizell, K.-H., André, S., and Frizell, K. W. (2002). "On the performance of velocity measurement techniques in air-water flows." *Proceedings of the Hydraulic Measurements & Experimental Methods Conference: EWRI-ASCE / IAHR*, T. L. Wahl, C. A. Pugh, K. A. Oberg, and T. B. Vermeyen, eds., Estes Park.

McKeon, B. J. (2007). "Pressure-based velocity measurements." *Springer Handbook of Experimental Fluid Mechanics*, C. Tropea, A. L. Yarin, and J. F. Foss, eds., Springer, Berlin, Chapter 5.1.

Meireles, I., Matos, J., and Frizell, K. (2007). "Measuring air entrainment and flow bulking in skimming flow over steeply sloping stepped chutes." *Hydraulic Measurements and Experimental Methods Conference*, E. Cowen, ed., EWRI/ASCE & IAHR, Lake Placid.

Menze, M., Heipke, C., and Geiger, A. (2018). "Object scene flow." *Journal of Photogrammetry and Remote Sensing*, 140, 60–76.

Milly, P. C. D., Betancourt, J., Falkenmark, M., Hirsch, R. M., Kundzewicz, Z. W., Lettenmaier, D. P., and Stouffer, R. J. (2008). "Stationarity is dead: Whither water management?." *Science*, 319(5863), 573–574.

Misra, S. K., Kirby, J. T., Brocchini, M., Veron, F., Thomas, M., and Kambhamettu, C. (2008). "The mean and turbulent flow structure of a weak hydraulic jump." *Physics of Fluids*, 20(3).

Molfetta, M. G., Bruno, M. F., Pratola, L., Rinaldi, A., Morea, A., Preziosa, G., Di Risio, M., and Mossa, M. (2020). "A sterescopic system to measure water waves in laboratories." *Remote Sensing*, 12, 2288.

Montano, L. and Felder, S. (2020). "LIDAR observations of free-surface time and length scales in hydraulic jumps." *Journal of Hydraulic Engineering*, 146(4).

Montano, L., Li, R., and Felder, S. (2018). "Continuous measurements of time-varying free-surface profiles in aerated hydraulic jumps with a lidar." *Experimental Thermal and Fluid Science*, 93, 379–397.

Montes, J. S. (1998). *Hydraulics of open channel flow*. ASCE, Reston.

Morgenschweis, G. (2018). *Hydrometrie, Theorie und Praxis der Durchflussmessung in offenen Gerinnen*. Springer, Heidelberg.

Mossa, M. (1999). "On the oscillating characteristics of hydraulic jumps." *Journal of Hydraulic Research*, 37(4), 541–558.

Mossa, M. and Tolve, U. (1998). "Flow visualization in bubbly two-phase hydraulic jump." *Journal of Fluid Engineering*, 120, 160–165.

Murillo, R. E. (2006). "Experimental study of the development flow region on stepped chutes." Ph.D. thesis, University of Manitoba, Manitoba.

Murzyn, F. and Chanson, H. (2009a). "Free-surface fluctuations in hydraulic jumps: Experimental observations." *Experimental Thermal and Fluid Science*, 33(7), 1055–1064.

Murzyn, F. and Chanson, H. (2009b). "Non intrusive measurement technique for dynamic free-surface characteristics in hydraulic jumps." *Proceedings of the 33rd IAHR Congress: Water Engineering for a Sustainable Environment*, Vancouver.

Murzyn, F., Mouaze, D., and Chaplin, J. R. (2007). "Air-water interface dynamic and free surface features in hydraulic jumps." *Journal of Hydraulic Research*, 45(5), 697–685.

Nilsson, N. J. (2009). *Artificial Intelligence: A new synthesis*. Morgan Kaufmann, San Francisco.

Noack, M., Schmid, G., Beckers, F., Haun, S., and Wieprecht, S. (2018). "PHOTOSED-PHOTOgrammetric sediment erosion detection." *Geosciences*, 8(7), 243.

Oertel, M. and Bung, D. B. (2012a). "Characeristics of cross-bar block ramp flows." *4th IAHR Symposium on Hydraulic Structures*, Porto.

Oertel, M. and Bung, D. B. (2012b). "Initial stage of two-dimensional dam-break waves: Laboratory vs. VOF." *Journal of Hydraulic Research*, 50(1), 89–97.

Oertel, M. and Schlenkhoff, A. (2008). "Flood wave propagation and flooding of underground facilities." *Proceedings of River Flow Conference*, Izmir, 595–600.

Oertel, M. and Süfke, F. (2019). "Two-dimensional dam-break wave analysis: PIV vs. optical flow." *Journal of Hydraulic Research*, 58(2), 326–334.

Ohtsu, I., Yasuda, Y., and Takahashi, M. (2004). "Flow characteristics of skimming flows in stepped channels." *Journal of Hydraulic Engineering*, 130(9), 860–869.

Otsu, N. (1979). "A threshold selection method from gray-level histograms." *IEEE Transactions on Systems, Man, and Cybernetics*, (9(1)), 62–66.

Ozmen-Cagatay, H. and Kocaman, S. (2010). "Dam-break flows during initial stage using SWE and RANS approaches." *Journal of Hydraulic Research*, 48(5), 603–611.

Pagliara, S. and Palermo, M. (2015). "Scour problems downstream of low-head hydraulic structures." *Rivers – physical, fluvial and environmental processes*, P. M. Rowinski and A. Radecki-Pawlik, eds., Springer, 99–119.

Pegram, G. G. S., Officer, A. K., and Mottram, S. R. (1999). "Hydraulics of skimming flow on modeled stepped spillways." *Journal of Hydraulic Engineering*, 125(5), 500–510.

Pfister, M. and Chanson, H. (2012). "Discussion on Scale effects in physical hydraulic engineering models." *Journal of Hydraulic Research*, 50(2), 244–246.

Pfister, M. and Hager, W. H. (2011). "Self-entrainment of air in stepped spillways." *International Journal of Multiphase Flow*, 37, 99–107.

Pizer, S. M., Amburn, E. P., Austin, J. D., Cromartie, R., Geselowitz, A., Greer, T., Romeny, B. H., Zimmerman, J. B., and Zuiderveld, K. (1987). "Adaptive histogram equalizaton and its variations." *Computer Vision, Graphics, and Image Processing*, (39), 355–368.

Pope, S. B. (1994). "Lagrangian pdf methods for turbulent flows." *Annual Review of Fluid Mechanics*, 26, 23–63.

Pope, S. B. (2000). *Turbulent Flows*. Cambridge University Press.

Prewitt, J. M. S. (1970). "Object enhancement and extraction." *Picture Processing and Psychopictorics*, B. S. Lipkin and A. Rosenfeld, eds., Academic Press, New York.

Rajaratnam, N. (1962). "An experimental study of air entrainment characteristics of the hydraulic jump." *Journal of the Institution of Engineers (India)*, 42, 247–273.

Rajaratnam, N. (1967). "Hydraulic jumps." *Advances in Hydroscience*, 197–280.

Rao, N. S. L. and Kobus, H. (1975). *Characteristics of self-aerated free-surface flows*, Vol. 10 of *Water and Waste Water Current Research and Practice*. Erich Schmidt, Berlin.

Rao, N. S. L., Seetharamiah, K., and Gangadharaiah, T. (1970). "Characteristics of self-aerated flows." *Journal of the Hydraulics Division*, 96(HY2), 331–355.

Resch, F., Leutheusser, H., and Alemum, S. (1974). "Bubbly two-phase flow in hydraulic jump." *Journal of the Hydraulics Division*, 100, 137–149.

Riester, J. B., Bajura, R. A., and Schwarz, S. H. (1980). "Effects of water temperature and salt concentration on the characteristics of horizontal buoyant submerged jets." *Journal of Heat Transfer*, 102, 557–562.

Ritter, A. (1892). "Die Fortpflanzung der Wasserwelle." *Zeitschrift Verein Deutscher Ingenieure*, 36(2), 947–954.

Roger, S., Dewals, B. J., Erpicum, S., Schwanenberg, D., Schüttrumpf, H., Köngeter, J., and Pirotton, M. (2009). "Experimental and numerical investigations of dike-break induced flows." *Journal of Hydraulic Research*, 47(3), 349–359.

Rudin, L. I., Osher, S., and Fatemi, E. (1992). "Nonlinear total variation based noise removal algorithms." *Physica D: Nonlinear Phenomena*, 60(1-4), 259–268.

Ruff, J. F. and Frizell, K. H. (1994). "Air concentration measurements in highly-turbulent flow on a steeply-sloping chute." *Hydraulic Engineering '94 (Proceedings of the 1994 Conference)*, G. V. Cotroneo and R. R. Rumer, eds., Vol. 2, Buffalo, New York, American Society of Civil Engineers, 999–1003.

Ruhnau, P., Kohlberger, T., Schnörr, C., and Nobach, H. (2005). "Variational optical flow estimation for particle image velocimetry." *Experiments in Fluids*, 38, 21–32.

Ryu, Y., Chang, K.-A., and Lim, H.-J. (2005). "Use of bubble image velocimetry for measurement of plunging wave impinging on structure and associated greenwater." *Measurement Science and Technology*, 16(10), 1945–1953.

Savic, D. (2019). "Aritficial intelligence - how can water planning and management benefit from it?." *IAHR White Papers*, 1/2019.

Scharr, H. (2000). "Optimale Operatoren in der digitalen Bildverarbeitung." Ph.D. thesis, Ruprecht-Karls-University, Heidelberg, Germany.

Schlurmann, T. and Bung, D. B. (2012). "Experimental investigation of flow-induced radial gate vibrations at Lower Subansiri dam." *6th Chinese-German Joint Symposium on Hydraulic and Ocean Engineering*, Keelung.

Schuster, R., Bailer, C., WasenmÃ¼ller, O., and Stricker, D. (2018). "Combining stereo disparity and optical flow for basic scene flow." *Proceedings of the 5th Commercial Vehicle Technology Symposium – CVT 2018*, K. Berns, ed., Wiesbaden, Springer.

Seong, J. H., Song, M. S., Nunez, D., Manera, A., and Kim, E. S. (2019). "Velocity refinement of PIV using global optical flow." *Experiments in Fluids*, 60, 174.

Shi, J. and Tomasi, C. (1994). "Good features to track." *9th IEEE Conference on Computer Vision and Pattern Recognition*, Seattle.

Shi, R., Leng, X., and Chanson, H. (2020). "On optical flow techniques applied to breaking surges." *Flow Measurement and Instrumentation*, 72, 101710.

Soares-Frazão, S. (2007). "Experiments of dam-break wave over a triangular bottom sill." *Journal of Hydraulic Research*, 45(Extra issue), 19–26.

Soares-Frazão, S. and Zech, Y. (2007). "Experimental study of dambreak flow against an isolated obstacle." *Journal of Hydraulic Research*, 45(Extra issue), 27–36.

Sobel, I. E. (1970). "Camera models and machine perception." Ph.D. thesis, Stanford University, Palo Alto.

Sonka, M., Hlavac, V., and Boyle, R. (2015). *Image processing, analysis and machine vision*. Cengage Learning.

Sriram, V., Sannasiraj, S. A., Sundar, V., Schlenkhoff, A., and Schlurmann., T. (2010). "Quantification of phase shift in the simulation of shallow water waves." *International Journal for Numerical Methods in Fluids*, 62(12), 1381–1410.

Stansby, P. K., Chegini, A., and Barnes, T. C. D. (1998). "The initial stages of dam-break flow." *Journal of Fluid Mechanics*, 374, 407–424.

Straub, L. G. and Anderson, A. G. (1958). "Experiments on selfaerated flow in open channels." *Journal of the Hydraulics Division*, 84(HY7), 1890–1–1890–35.

Sun, D., Roth, S., and Black, M. J. (2010). "Secrets of optical flow estimation and their principles." *IEEE conf. on computer vision and pattern recognition (cvpr)*.

Sveen, J. K. (2004). *An introduction to MatPIV v1.6.1*. Deptartment of Mathematics, Mechanics and Applied Mathematics, University of Oslo, Oslo.

Sveen, J. K. (2013). "14 - laser doppler anemometry (lda) and particle image velocimetry (piv) for marine environments." *Subsea Optics and Imaging*, J. Watson and O. Zielinski, eds., Woodhead Publishing Series in Electronic and Optical Materials, Woodhead Publishing, 353–379e.

Tauro, F., Piscopia, R., and Grimaldi, S. (2017). "Streamflow observations from cameras: Large-scale particle image velocimetry or particle tracking velocimetry?." *Water Resources Research*, 10, 374–394.

Tauro, F., Tosi, F., Mattoccia, S., Toth, E., Piscopia, R., and Grimaldi, S. (2018). "Optical tracking velocimetry (OTV): Leveraging optical flow and trajectory-based filtering for surface streamflow observations." *Remote Sensing*, 10, 1–24.

Thielicke, W. and Stamhuis, E. J. (2014a). "PIVlab - Time-resolved digital particle image velocimetry tool for matlab (version 2.31).

Thielicke, W. and Stamhuis, E. J. (2014b). "PIVlab - Towards user-friendly, affordable and accurate digital particle image velocimetry in Matlab." *Journal of Open Research Software*, 2(1).

Thorwarth, J. (2008). "Hydraulisches Verhalten von Treppengerinnen mit eingetieften Stufen - Selbstinduzierte Abflussinstationaritäten und Energiedissipation." Ph.D. thesis, RWTH Aachen, Aachen.

Tomasi, C. and Kanade, T. (1991). "Detection and tracking of point features." *Report No. CMU-CS-91-132*, School of Computer Science, Pittsburgh.

Toombes, L. and Chanson, H. (2005). "Air-water mass transfer on a stepped waterway." *Journal of Environmental Engineering*, 131(10), 1377–1386.

Toombes, L. and Chanson, H. (2007). "Surface waves and roughness in self-aerated supercritical flow." *Environmental Fluid Mechanics*, 7(3), 259–270.

Toombes, L. and Chanson, H. (2008). "Flow patterns in nappe flow regime down low gradient stepped chutes." *Journal of Hydraulic Research*, 46(1), 4–14.

Tropea, C., Scarano, F., Westerweel, J., Cavone, A. A., Meyers, J. F., Lee, J. W., and Schodl, R. (2007). "Particle-based techniques." *Springer Handbook of Experimental Fluid Mechanics*, C. Tropea, A. L. Yarin, and J. F. Foss, eds., Springer, Berlin, Chapter 5.3.

Turner, J. S. (1966). "Jets and plumes with negative or reversing buoyancy." *Journal of Fluid Mechanics*, 26, 779–792.

Ullman, S. (1979). "The interpretation of structure from motion." *Proceedings of the Royal Society of London.*, Vol. 203 of *Series B, Biological Sciences*, 405–426.

Valero, D. (2018). "On the fluid mechanics of self-aeration in open channel flows." Ph.D. thesis, University of Liège, Liège.

Valero, D. and Bung, D. B. (2018a). "Artificial Neural Networks and pattern recognition for air-water flow velocity estimation using a single-tip optical fibre probe." *Journal of Hydro-environment Research*, 19, 150–159.

Valero, D. and Bung, D. B. (2018b). "Reformulating self-aeration in hydraulic structures: turbulent growth of free surface perturbations leading to air entrainment." *International Journal of Multiphase Flow*, 100, 127–142.

Valero, D. and Bung, D. B. (2018c). "Vectrino profiler spatial filtering for shear flows based on the mean velocity gradient equation." *Journal of Hydraulic Engineering*, 144(7), 04018037.

Valero, D., Chanson, H., and Bung, D. B. (2020). "Robust estimators for free surface turbulence characterization: A stepped spillway application." *Flow Measurement and Instrumentation*.

Van der Walt, S., Colbert, S. C., and Varoquaux, G. (2011). "The numpy array: A structure for efficient numerical computation." *Journal of Computing Science and Engineering*, 13, 22–30.

VDI (2012). "Optical 3-D measuring systems - Optical systems based on area scanning. VDI/VDE 2634 Blatt 2.

Viollet, P.-L. (2007). *Water engineering in ancient civilizations*. IAHR Monograph Series. IAHR, Madrid.

Wahl, T. L. (2003). "Discussion of "Despiking acoustic Doppler velocimeter data" by Derek G. Goring and Vladimir I. Nikora." *Journal of Hydraulic Engineering*, 129(6), 484–487.

Wang, H. (2014). "Turbulence and air entrainment in hydraulic jumps." Ph.D. thesis, The University of Queensland, Brisbane.

Wang, H. and Chanson, H. (2015). "Experimental study of turbulent fluctuations in hydraulic jumps." *Journal of Hydraulic Engineering*, 141(7).

Wedel, A. and Cremers, D. (2011). *Stereo scene flow for 3D motion analysis*. Springer.

White, F. M. (2006). *Viscous fluid flow*. McGraw-Hill.

Whitham, G. B. (1955). "The effects of hydraulic resistance in the dam-break problem." *Proceedings of the Royal Society A*, 227, 399–407.

Wilhelms, S. C. and Gulliver, J. S. (2005). "Bubbles and waves description of self-aerated spillway flow." *Journal of Hydraulic Research*, 43(5), 522–532.

Wood, I. R. (1983). "Uniform region of self-aerated flow." *Journal of Hydraulic Engineering*, 109(3), 447–461.

Wood, I. R., Ackers, P., and Loveless, J. (1983). "General method for critical point on spillways." *Journal of Hydraulic Engineering*, 109(2), 308–312.

Yang, C., Lin, B., Jiang, C., and Liu, Y. (2010). "Predicting near-field dam-break flow and impact force using a 3d model." *Journal of Hydraulic Research*, 48(6), 784–792.

Yasuda, Y. and Ohtsu, I. (1999). "Flow resistance of skimming flows in stepped channels." *Hydraulic Engineering for Sustainable Water Resources Management at the Turn of the Millenium*, number XXVIII in IAHR Congress, Graz.

Zhang, D., Heery, B., O'Neil, M., Little, S., O'Connor, N. E., and Regan, F. (2019a). "A low-cost smart sensor network for catchment monitoring." *Sensors*, 19(10), 2278.

Zhang, G. and Chanson, H. (2017). "Application of local optical flow methods to high-velocity air-water flows: Validation and application to skimming flows on stepped chutes." *Report No. CH105/17*, The University of Queensland, Brisbane.

Zhang, G. and Chanson, H. (2018a). "Application of local optical flow methods to high-velocity free-surface flows: Validation and application to stepped chutes." *Experimental Thermal and Fluid Science*, 90, 186–199.

Zhang, G. and Chanson, H. (2018b). "Application of optical flow methods to aerated skimming flows above triangular and trapezoidal step cavities." *Journal of Hydraulic Research*, 57(4), 488–497.

Zhang, G., Valero, D., Bung, D. B., and Chanson, H. (2018). "On the estimation of free-surface turbulence using ultrasonic sensors." *Flow Measurement and Instrumentation*, 60, 171–184.

Zhang, L., Fu, X., and Duan, J. (2017). "A surface-based hiding function linking flume and field data." *Science China Technological Sciences*, 60, 1560–1569.

Zhang, Z., Zhou, Y., Liu, H., and Gao, H. (2019b). "In-situ water level measurement using nir-imaging video camera." *Flow Measurement and Instrumentation*, 67, 95–106.

Zollhöfer, M. (2019). "Commodity RGB-D sensors: Data acquisition." *RGB-D Image Analysis and Processing*, P. L. Rosin, Y. Lai, L. Shao, and Y. Liu, eds., Springer.